
DIPARTIMENTO DI FISICA "G. OCCHIALINI"

DOTTORATO DI RICERCA IN FISICA E ASTRONOMIA
CICLO XXIX

# Electroweak and strong next-to-leading-order corrections to $HV$ and $HVj$ production at hadron colliders

Granata Federico

matr. 708650

Tutor: Prof. Carlo Oleari

Coordinatore: Prof. Marta Calvi

Anno Accademico 2015-16

# Contents

# Introduction

After the discovery of the Higgs boson at the CERN Large Hadron Collider (LHC) [1, 2], the first results from the 13 TeV Run of the LHC show that accurate predictions for processes that involve the production of this particle are fundamental, in order to measure its properties and to further investigate the phenomenon of electroweak symmetry breaking. A high degree of precision allows to look for signals of new physics, particularly in the high-energy tails of some kinematic distributions, where discrepancies from the Standard Model predictions could show up.

At the energies reached by the LHC, the dominant perturbative corrections are given by the QCD sector of the Standard Model, where the first perturbative order (NLO) gives contributions of the order of 20-30% to the typical cross sections, that can exceptionally reach 100% for processes like Higgs boson production through gluon fusion. The contribution coming from NLO electroweak (EW) corrections, instead, is rather mild on the integrated cross sections, basically because of the smallness of the electromagnetic coupling constant with respect to the strong one. Nevertheless, the impact of this sector can become relevant when inspecting some kinematic quantities, like the high-energy tails of some transverse-momentum distributions. Moreover, electroweak corrections play an important role in the study of the nature of dark matter and in its indirect detection. Indeed, dark-matter candidates can decay into Standard Model particles, or they can be revealed at colliders as missing transverse momentum. In the context of supersymmetry searches, instead, processes like vector bosons plus jets production are irreducible and important backgrounds for many supersymmetric processes. A precise knowledge of the high-energy tails of Standard Model events, including electroweak corrections, is then essential in order to test the validity of these models.

The electroweak sector has several differences with respect to QCD, in the structure of both the real and the virtual contributions to cross sections. Since in QED and QCD the virtual and real corrections involve the exchange of massless particles, they are separately divergent, and only their sum is finite. In these theories, then, the inclusion of real corrections is mandatory. When considering weak corrections, instead, because of the exchange of massive bosons, all the contributions to the NLO cross section are finite. Moreover, the radiated massive particles would decay, giving final states that can be experimentally distinguished from the leading-order ones. There are no technical reasons, then, to include the real emission of $W$ and $Z$ bosons in a computation where the weak virtual corrections are considered. On the other hand, the inclusion of photon emission is unavoidable in order to cancel the singularities of the corresponding virtual diagrams. The consequence of considering virtual electroweak corrections is the appearance of logarithms that involve ratios of different scales, and that can be large in particular kinematic regions [3–7]. These corrections become relevant starting from energies of order 1 TeV, where they are known to give sizable negative contributions to the high-energy tails of some transverse-momentum distributions. Indeed, they can reach 40-50% with a partonic center-of-mass energy of a few TeV, thus becoming larger in magnitude than the NLO QCD corrections. It has been proven in refs. [8–10] that, in the

limit in which all the kinematic invariants involved are of the same order and much greater than the electroweak scale, the structure of the electroweak virtual corrections is universal: it can then be computed once and for all and applied to the desired processes. The one-loop electroweak corrections in this high-energy limit are called electroweak Sudakov corrections: they are much faster to compute with respect to the complete ones, since they consist in universal functions that multiply leading-order matrix elements, and can be used to obtain a next-to-leading logarithmic (NLL) approximation of the complete virtual corrections at a reduced computational cost.

In this thesis we present the combined QCD+EW corrections to $HV$ and $HVj$ production, where $V = W, Z$. The associated production of a Higgs boson with a vector boson is very important, since it allows to study the $H \to b\bar{b}$ decay channel, that has the highest branching ratio in the Higgs boson mass region, and the $HVV$ coupling. The second relevant process analyzed is the associated production with a vector boson and a jet, $HVj$, that has the same properties of $HV$ and contributes to the background for Beyond Standard Model events.

In order to fully simulate hadronic events and to compare theoretical predictions with the experimental data, the parton-level processes must be interfaced to a parton-shower generator, that describes further collinear radiation down to the hadronic scale. The precision needed for the LHC studies requires the hard event to be described at least at NLO accuracy, before matching it to the parton shower. At present, both the $HV$ and $HVj$ processes are described at NLO+PS QCD accuracy in `MC@NLO` [11] and in the `POWHEG` [12] framework. The NLO+PS accuracy in the electroweak sector is instead missing.

The aim of this thesis is the description of the $HV$ and $HVj$ associated production processes at NLO+PS QCD+EW accuracy. The structure of this thesis is the following: in Chap. 1 we review the main production and decay modes of the Higgs boson, we summarize the results of the analyses, performed at the LHC, that led to the discovery of this particle, and we describe the state of the art in theoretical predictions. Chapter 2 is dedicated to the description of some extensions of the `POWHEG BOX` [13, 14] that are useful for the processes under study. This program, one of the most commonly used tools to obtain theoretical predictions for comparisons with the experimental data, is a Monte Carlo event generator with NLO accuracy, that can be interfaced to parton-shower generators according to the `POWHEG` method [15]. Recently, an important improvement has been introduced: the implementation of a resonance-aware subtraction scheme [16]. The resulting code is the `POWHEG BOX RES`, that allows a better description of processes in which the radiation could come from the decay of a resonance, like photons emitted from the leptons coming from the vector-boson decay, or gluons emitted from bottom quarks in top decay. In addition to QCD radiation, photon radiation was introduced in the `POWHEG BOX` for the first time in ref. [17], in which NLO QCD+EW corrections to $W$ boson production were computed. The leptons coming from the decay of the vector boson were considered as massive, and the treatment of photon radiation from massive charged particles was implemented correspondingly. In this thesis, instead, the charged leptons are considered as massless: we then describe the modifications introduced in the `POWHEG BOX RES` to generate photon radiation from final-state massless charged particles. In Chap. 3 we describe the high-energy limit of the electroweak one-loop corrections, and we report the general formulae that allow to obtain the Sudakov NLL corrections to a given process. These formulae are applied to the $HV$ and $HVj$ production processes in Chap. 4, distinguishing between the production of transverse and longitudinal vector bosons, since they behave in a different way in the high-energy limit. Finally, in Chap. 5, we present numerical predictions and kinematic distributions for the associated production of a Higgs boson with a leptonically-decaying vector boson and eventually a jet, in proton-proton collisions at a center-of-mass energy of 13 TeV, obtained with the `POWHEG BOX RES`. We mainly focus on

observables that are sensitive to electroweak corrections. For each process ($HW$, $HZ$, $HWj$ and $HZj$), we first compare fixed-order NLO results: we analyze the differences between the NLO EW corrections and their NLL approximation, and the impact of the electroweak sector on the QCD results. Then, we compare NLO+PS events at QCD and QCD+EW accuracy. We conclude by comparing the NLO+PS QCD+EW predictions for $HV$ production with those for $HVj$ production. The latter are obtained by including the `MiNLO` [18, 19] prescription of choosing scales and attaching Sudakov form factors to underlying-Born configurations. This allows us to have a $HVj$ generator that has NLO accuracy both for $HV$ inclusive quantities and for $HVj$ ones. We can then compare directly $HV$ and $HVj$ distributions and see how scale variations affect them. In App. A we list some useful group-theoretical quantities that have been used in the calculation of the Sudakov corrections, and in App. B we compute these correction factors for the $HW$ and $HZ$ associated production processes.

# Chapter 1

# The associated production of a Higgs boson with a vector boson

In 2012 the ATLAS and CMS Collaborations at the CERN Large Hadron Collider (LHC) reported the observation of a new particle with a mass of approximately 125 GeV [1, 2] that, within the present accuracy, presented all the characteristics of the Standard Model (SM) Higgs boson. The mass was confirmed by later measurements [20–22]: thanks to this discovery the main missing ingredient for the validation of the Standard Model is now in place.

The discovery of the Higgs boson is fundamental in order to understand the electroweak symmetry breaking (EWSB). Within the Standard Model, EWSB is achieved through the Brout-Englert-Higgs mechanism [23–25], which predicts the existence of a neutral scalar particle, commonly known as the Higgs boson. While the Standard Model does not predict the value of its mass, the production cross sections and decay branching ratios of the Higgs boson can be precisely calculated, once the mass is known. Therefore, precision measurements of the properties of this newly discovered particle are fundamental to verify whether it is fully responsible for EWSB and whether there are potential deviations from the SM predictions.

In this chapter we review the main production and decay modes of the Higgs boson, and we summarize the results of the analyses, performed at the LHC, that led to the discovery of this particle. The $H \to b\bar{b}$ decay channel, that has the highest branching ratio for a 125 GeV Higgs boson, turns out to be very promising at the LHC when the Higgs boson is produced via associated production with a vector boson. For this reason we then focus on this process, studying its importance in the experimental analysis and in Beyond Standard Model (BSM) searches, and describing the state of the art in theoretical predictions.

## 1.1 Production modes and decay channels

The Higgs boson is a fundamental ingredient of the Standard Model. It is predicted by spontaneous electroweak symmetry breaking, the solution proposed in 1964 by Higgs, Brout and Englert to explain how the Standard Model particles acquire their physical mass. This model allows to introduce mass terms for gauge bosons and fermions in the SM Lagrangian without violating the unitarity and the renormalizability of the theory. As a result of this phenomenon, particles acquire mass by interacting with the Higgs boson. The Higgs boson couples to vector bosons with a coupling proportional to the square of their mass, and it couples to fermions through Yukawa-type interactions, with a coupling proportional to the mass of the fermion itself. The coupling to photons or gluons occurs only through a loop of massive particles. Since the masses of the Standard Model particles are well known from

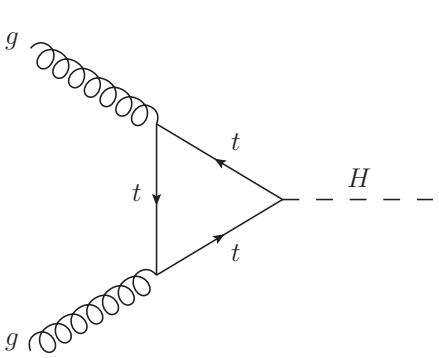


(a) Gluon fusion.

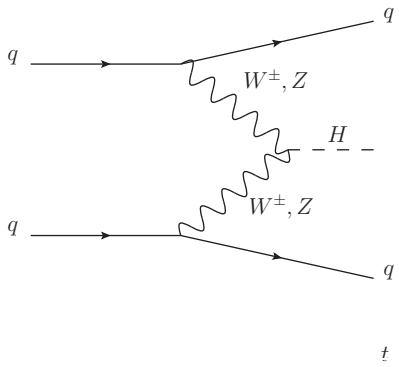


(b) Vector boson fusion.

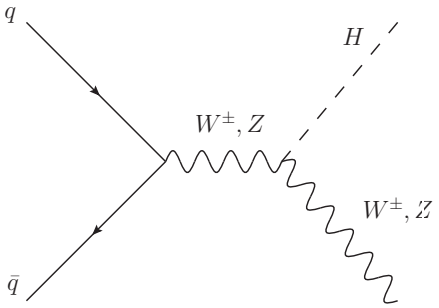


(c) Associated production with a vector boson.

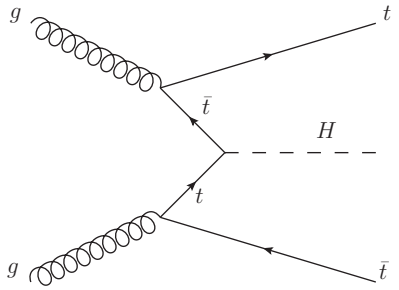


(d) Associated production with a $t\bar{t}$ pair.

Figure 1.1: Main contributions to the production of a Higgs boson at a hadron collider.

experiments, these couplings can be accurately tested.

The production modes and decay channels of the Higgs boson, then, preferably involve couplings to heavy particles. The four main processes through which a Higgs boson can be produced at a hadron collider are the gluon fusion, the vector boson fusion, the associated production with a vector boson and the associated production with a $t\bar{t}$ pair. A sample of the Feynman diagrams for these processes is depicted in fig. 1.1, while fig. 1.2, taken from ref. [26], shows the corresponding total cross sections for a 125 GeV Higgs boson at different center-of-mass energies.

The dominant production process in the LHC energy range is by gluon fusion, shown in fig. 1.1 (a): the same process could be realized with a loop of bottom quarks, but it is suppressed because of the lower mass of the fermion involved. This process is sensitive to a fourth generation of quarks: since the Higgs boson coupling to fermions is proportional to their mass, including a new generation of heavy quarks would change drastically the cross section.

The second relevant contribution, reported in fig. 1.1 (b), comes from the vector-boson fusion channel (VBF). The process involving two $W$ bosons is enhanced with respect to the one with two $Z$ bosons because the latter has a smaller coupling to fermions. Looking at fig. 1.2 we see that, in the whole energy range considered, the cross section for this process is about one order of magnitude smaller than the gluon fusion one. Nevertheless, this channel is very interesting because the presence of two spectator jets with high invariant mass in the forward region provides a powerful tool to tag the signal events and discriminate the background.

Another important process is the associated production with a vector boson, $HV$, in fig. 1.1 (c): the cross section is smaller than in the VBF channel, but the vector boson can be identified quite easily if it decays leptonically. At the Tevatron, this was the main searching

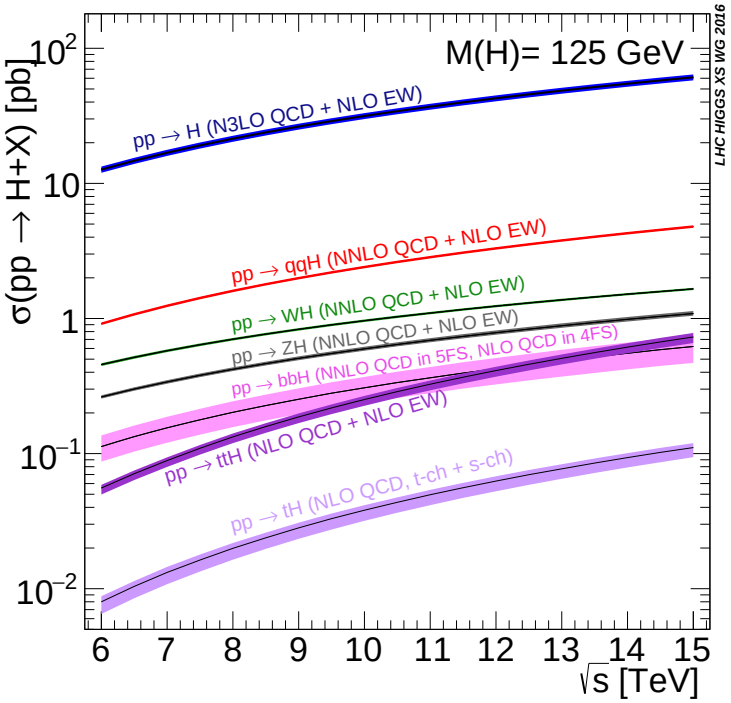


Figure 1.2: Total theoretical cross section for different Higgs production processes, as a function of the accelerator center-of-mass energy. The bands indicate the theoretical uncertainties, and the labels the accuracy of the computation.

channel in the low-mass region. At the LHC, instead, this channel has been considered less promising, because of larger backgrounds. However, some studies [27] have indicated that at large transverse momenta, employing modern jet reconstruction and decomposition techniques, the associated production channel is a promising searching mode.

Finally, the last relevant process is the associated production with heavy quarks, shown in fig. 1.1 (d). Even if the cross section is more than two orders of magnitude smaller than the dominant one, this channel can give important information on the Yukawa coupling of the Higgs boson to heavy quarks. The cross section for $b\bar{b}H$ production is comparable to that of $t\bar{t}H$ and, for center-of-mass energies smaller than 13 TeV, even larger, thanks to the available phase space.

Moving to the decay channels, fig. 1.3, also taken from ref. [26], shows the branching ratios of the Higgs boson in the mass window around its physical mass. In this region the fermionic decay channels play an important role: in particular, the channel $H \to b\bar{b}$ has the highest branching ratio (58% for $M_H = 125$ GeV) since the $b$ quark is the heaviest particle that can be produced on shell. However, the most promising decay channels for the Higgs boson do not depend only on the corresponding branching ratios, but also on the capability of detecting the signal while rejecting the background. For this reason, $H \to b\bar{b}$ is not accessible if the Higgs boson is produced through gluon fusion, since it would give a fully hadronic final state that cannot be easily resolved in the background. For the same reason, even the VBF production channel is only marginally accessible. The associated production $HV$, instead, thanks to the leptonic decay of the vector boson, allows the $H \to b\bar{b}$ decay mode to be studied, although the production process has a smaller cross section. Being able to study this channel is very important, because it gives the possibility to measure the Yukawa coupling of the Higgs boson to down-type fermions.

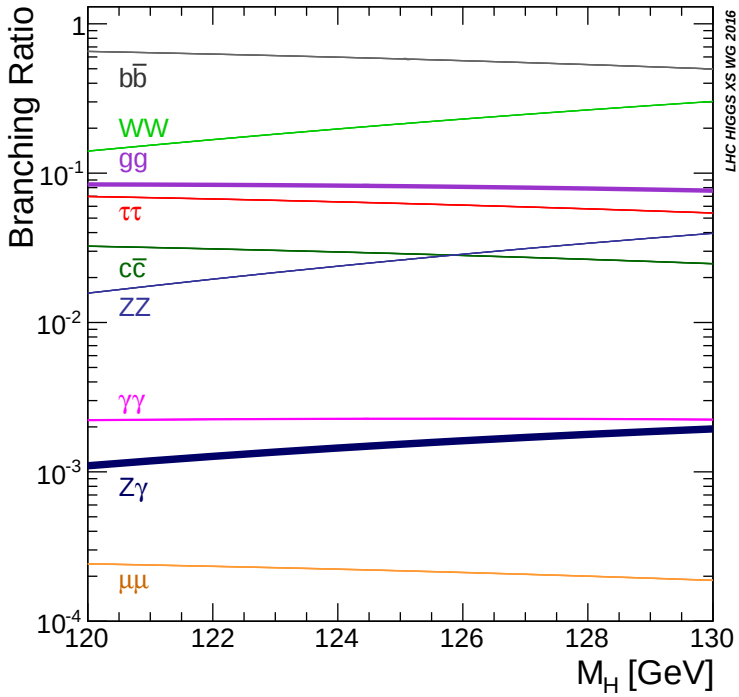


Figure 1.3: Branching ratios of the Higgs boson in the mass region around 125 GeV.

Among the bosonic decay channels, the one that has the highest branching ratio is the $H \to WW^*$ channel. Even if the $W$ boson is much heavier than the $b$ quark, with $M_H \sim 125$ GeV at least one of the vector bosons has to be produced off shell, thus decreasing the branching ratio. This channel is very important when coupled to the VBF or $HV$ production modes, since it allows to deeply investigate the coupling of the Higgs boson to vector bosons. The same considerations can be applied for the decay into a pair of $Z$ bosons.

Another relevant decay channel is $H \to \gamma\gamma$, that occurs through a closed loop. Although the branching ratio is roughly three orders of magnitude smaller than the dominant one, it gives a very clear experimental signature: a bump over the extrapolated background into the signal region, in correspondence with the invariant mass of the two photons. For this reason, it played the main role in the Higgs boson search.

## 1.2 Experimental results

The analysis of the experimental data from the LHC Run 1 was based on the datasets of proton-proton collisions, with integrated luminosities of up to 4.7 fb$^{-1}$ at $\sqrt{s} = 7$ TeV and 20.3 fb$^{-1}$ at $\sqrt{s} = 8$ TeV recorded by the ATLAS detector, 5.1 fb$^{-1}$ at $\sqrt{s} = 7$ TeV and up to 19.7 fb$^{-1}$ at $\sqrt{s} = 8$ TeV recorded by the CMS detector, in 2011 and 2012. The first data collected during the LHC Run 2, at $\sqrt{s} = 13$ TeV, allow initial measurements with comparable precision. This analysis was focused mainly on five channels: three bosonic decay modes, $H \to \gamma\gamma$, $H \to WW^* \to 2l2\nu$, $H \to ZZ^* \to 4l$, and two fermionic ones, $H \to b\bar{b}$ and $H \to \tau^-\tau^+$. Together they account for approximately 88% of all decays of a SM Higgs boson at $M_H \sim 125$ GeV. The hadronic decays of the vector bosons have been excluded, because of the high background.

The discovery of the Higgs boson was based primarily on the mass peaks observed in

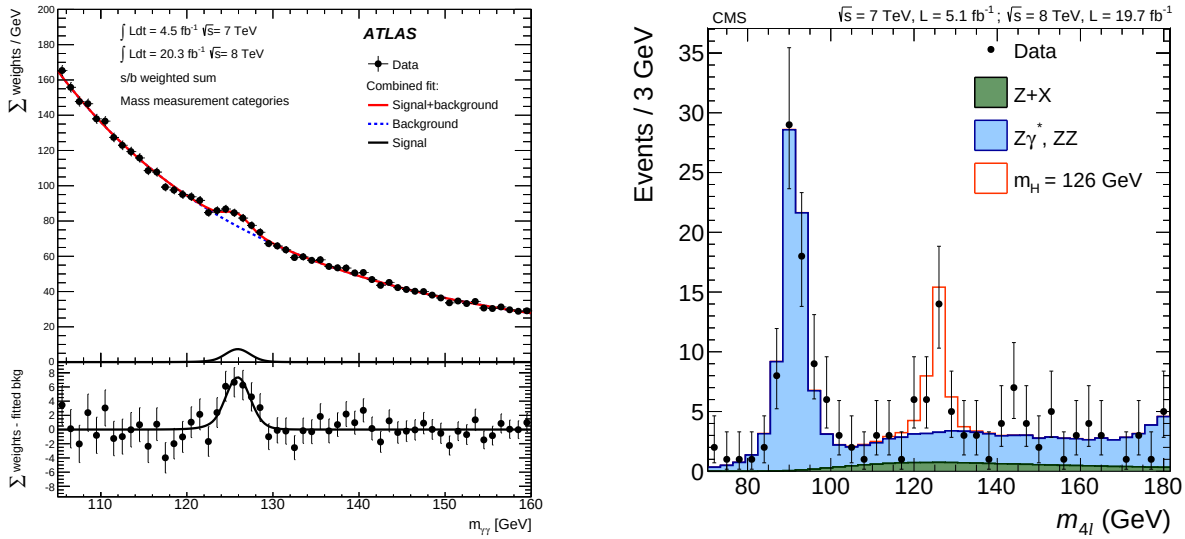


Figure 1.4: ATLAS distribution of the diphoton reconstructed mass (left), and CMS distribution of the four-lepton reconstructed mass (right).

the $H \to \gamma\gamma$ and $H \to ZZ^* \to 4l$ channels. These decay modes play a special role due to their high sensitivity and the excellent mass resolution of the reconstructed diphoton and four-lepton final state. In particular, $H \to \gamma\gamma$, shown on the left-hand side of fig. 1.4, is characterized by a narrow resonant signal peak above a large falling continuum background, containing many events. $H \to ZZ^* \to 4l$, instead, on the right-hand side of fig. 1.4, gives only a few tens of signal events per experiment, but it has very little background.

The Higgs boson was discovered by combining the measurements performed in these bosonic decay modes. The results on the mass determination are taken from ref. [28], that summarizes the analyses performed by the ATLAS and CMS Collaborations. These results are reported in fig. 1.5, while their combination gives

$$M_H = 125.09 \pm 0.21\,(\text{stat}) \pm 0.11\,(\text{syst})\,\text{GeV}. \tag{1.1}$$

The uncertainties are dominated by the statistical error, even when the Run 1 data sets of ATLAS and CMS are combined: nevertheless, the experimental accuracy will rapidly increase during the next years, when the full data sample of the Run 2 will be available.

The $H \to WW^* \to 2l2\nu$ channel has not been included in the mass measurement, since the presence of neutrinos in the final state gives a relatively poor mass resolution. The same resolution problems hold for the two fermionic decay modes $H \to b\bar{b}$ and $H \to \tau^-\tau^+$, that moreover suffer from large background contributions and then have lower sensitivity.

Nevertheless, obtaining information on the fermionic decay channels is very important in order to test the Higgs boson coupling to all of the Standard Model particles: combining the results coming from $H \to b\bar{b}$ and $H \to \tau^-\tau^+$, both the collaborations have published evidence for the decay of the Higgs boson into fermions [29–31]. The best way to distinguish the signal over the background is to look for these decay channels when the Higgs boson is produced via associated production with a vector boson. Even if the cross section for the $HW$ and $HZ$ processes is smaller than the gluon fusion and VBF ones, they are still interesting channels. The only other relevant process that allows to analyze the decay of the Higgs boson into a pair of bottom quarks is the associated production with a $t\bar{t}$ pair, but it has an even smaller cross section and presents a fully hadronic final state. For the associated production $HV$,

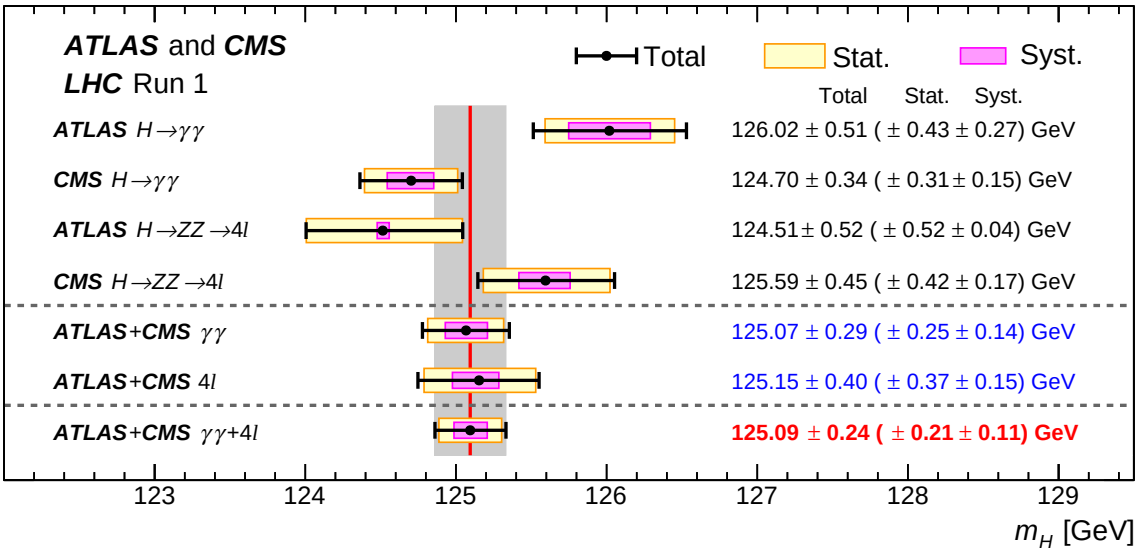


Figure 1.5: Measurements of the Higgs boson mass from the individual analyses of ATLAS and CMS, and from the combined analysis. The systematic, statistical and total uncertainties are indicated. The red vertical line represents the central value of the combined measurement, while its total uncertainty is reported in the gray shaded column.

instead, a method to reduce the background has been proposed in ref. [27]: the proposal was to investigate $HV$ production in a boosted regime, in which both the Higgs boson and the vector boson have large transverse momentum ($p_T \gtrsim 200$ GeV). In this phase space region the cross section is a small fraction of the total one (about 5%), but the intermediate virtual vector boson that produces the $HV$ pair must have a very high virtuality. It will then be produced in the central region, and the transversely boosted kinematics of the Higgs boson and of the vector boson ensures that their decay products will have sufficiently large transverse momentum to be tagged. As a consequence, the signal-over-background ratio can be significantly improved, and also the $HZ \to H\nu\bar{\nu}$ channel becomes visible because of the large missing transverse momentum. Moreover, in the context of BSM searches, $HV$ production with high invariant mass provides the leading source of irreducible background for the detection of exotic new particles decaying into an $HV$ pair.

When the cuts for the boosted products are applied, this becomes one of the most promising channels to constrain the Yukawa coupling of the Higgs boson to the bottom quark. It is very useful also for studying the $H \to \tau^-\tau^+$ decay channels, particularly if the $\tau$ leptons decay hadronically, because the leptonic decay products of the vector boson satisfy the trigger requirements with high efficiency.

An important part of the analysis has focused on the determination of the signal strength $\mu_{i,f}$, that is one of the most common parameters for comparing theory expectations with experimental results. The signal strength is defined as the ratio of the measured Higgs boson rate $i \to H \to f$ with respect to its Standard Model prediction,

$$\mu_{i,f} = \frac{\sigma_i \times \mathrm{BR}_f}{(\sigma_i \times \mathrm{BR}_f)_{\mathrm{SM}}}, \tag{1.2}$$

where $\sigma$ denotes the cross section for the production mode $i$, and BR is the branching ratio for its decay into $f$. This parameter represents a measure of potential deviations from the Standard Model predictions, under the assumption that the Higgs boson production and

decay kinematics do not change appreciably from the theoretical expectations.

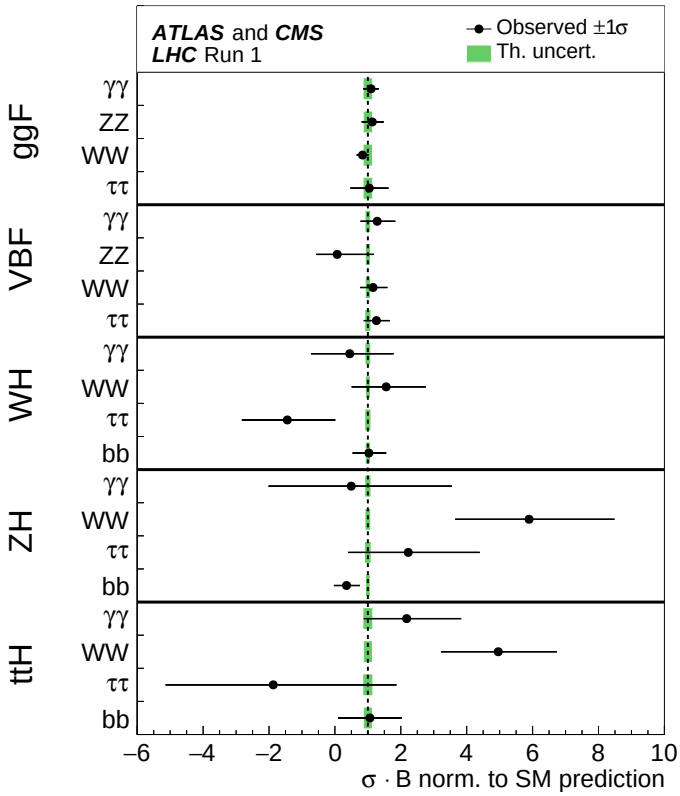


Figure 1.6: Signal strength for each specific channel $i \to H \to f$. The error bars indicate the $1\sigma$ intervals, while the green bands represent the theoretical uncertainties. Not all the decay channels are reported for each production process, either because they are not measured with meaningful precision or they are not measured at all, as for the $H \to b\bar{b}$ channel in gluon fusion or in VBF.

Figure 1.6, taken from ref. [32], shows the combined ATLAS and CMS results for the signal strengths of the various production and decay processes. The combination of the ATLAS and CMS analyses gives the following results,

$$\mu_{HW,b\bar{b}} = 1.0 \pm 0.5, \tag{1.3}$$

$$\mu_{HZ,b\bar{b}} = 0.4 \pm 0.4, \tag{1.4}$$

$$\mu_{t\bar{t}H,b\bar{b}} = 1.1 \pm 1.0. \tag{1.5}$$

As expected, the last result has bigger uncertainties, because of the background that makes this process harder to detect. Nevertheless, these experimental results show a good agreement with the Standard Model predictions. Combining all $i \to H \to f$ measurements it is possible to obtain a global signal strength for Higgs boson production and decay,

$$\mu = 1.09^{+0.11}_{-0.10} = 1.09^{+0.07}_{-0.07}\,(\text{stat})^{+0.09}_{-0.08}\,(\text{syst}). \tag{1.6}$$

The systematic uncertainty is slightly bigger than the statistical one, mainly because of the large uncertainty in the gluon fusion cross section. The overall result is however consistent with the theoretical predictions within less than $1\sigma$.

The associated production and VBF processes turn out to be very useful even in the search for anomalous couplings of the Higgs boson. These processes, indeed, provide direct

access to the coupling $HVV$: due to the highly off-shell nature of the propagator in $HV$ production, small anomalous couplings can lead to significant modifications of cross sections and kinematic distributions. In particular, the $HV$ invariant mass is highly sensitive to anomalous $HVV$ couplings. Probing this coupling in the region where the virtuality of the virtual gauge boson is far off shell can show sensitivity to the presence of higher-dimensional effective operators, beyond the limit that can be tested from the determination of the branching ratios $H \to VV$. Moreover, if the Higgs boson decays into fermions, the associated production process $HV$ allows to test also anomalous Yukawa couplings. Since the masses of down-type fermions can be obtained through different mechanisms in BSM theories [33], it is of great importance to study the coupling of the Higgs boson to bottom quarks in order to establish its nature.

Assuming the validity of the SU(2) custodial symmetry and a universal scaling of the fermion couplings relative to the Standard Model predictions, the observations have been compared with the expectations for the Higgs boson by fitting two parameters $\kappa_V$ and $\kappa_F$. These are common scaling factors for the couplings to massive vector bosons and to fermions, respectively. Other analyses have been performed, distinguishing between $\kappa_W$ and $\kappa_Z$, and among the various possible fermions, but the results are consistent with the hypothesis of a common factor for bosons and another one for fermions. In this analysis, no BSM effects have been accounted for, in the theoretical predictions. Figure 1.7, taken from ref. [32], shows

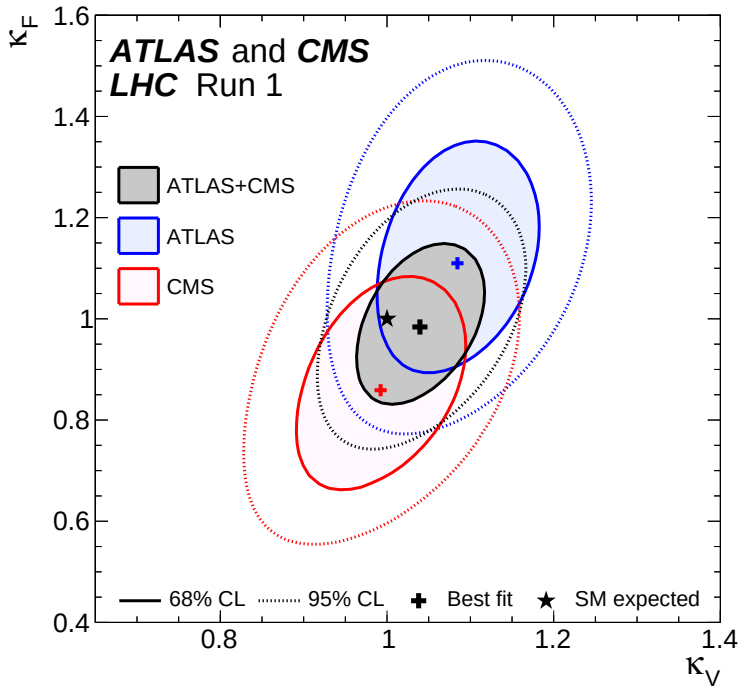


Figure 1.7: Results of 2D likelihood scans for the $\kappa_V$ and $\kappa_F$ parameters performed by the ATLAS and CMS Collaborations, and their combination. The crosses indicate the best-fit values, the contours show the 68% and 95% CL regions, and the star represents the Standard Model values $(\kappa_V, \kappa_F) = (1, 1)$.

the 2D likelihood scan over the $(\kappa_V, \kappa_F)$ parameter space, with the 68% and 95% CL regions. Both for the single experimental analyses and for the combined results the Standard Model expectation, $(\kappa_V, \kappa_F) = (1, 1)$, lies within the 68% CL region defined by the data. Because of the way these compatibility tests are constructed, any significant deviation from $(1, 1)$ would not have a straightforward interpretation within the Standard Model and would imply BSM

physics. The best fits, with the corresponding uncertainties, are reported in tab. 1.1.

| | ATLAS | CMS |
|---|---|---|
| $\kappa_V$ | $1.09 \pm 0.07$ | $1.01 \pm 0.07$ |
| $\kappa_F$ | $1.11 \pm 0.16$ | $0.87^{+0.14}_{-0.13}$ |

Table 1.1: Best-fit values and uncertainties for the scaling factors $\kappa_V$ and $\kappa_F$.

Summarizing, the analysis of the 2011 and 2012 datasets has investigated the Higgs boson production and decay properties: the results obtained are consistent with the Standard Model expectations, with no significant deviations in the measurement of both the signal strength and the coupling of the Higgs boson to the other particles. The results from the LHC Run 2, with a center-of-mass energy of 13 and 14 TeV, will significantly decrease the statistical uncertainties, leading to much more precise results.

## 1.3 Theoretical accuracy

In order to perform accurate comparisons between the experimental data and the theoretical predictions, it is fundamental to reduce as much as possible the theoretical uncertainties. For all of the reasons explained in this chapter, the associated production of a Higgs boson with a vector boson that decays leptonically is a very interesting process. To fully exploit this channel it is then important to have accurate theoretical predictions for the production cross section and for the associated distributions.

The next-to-next-to-leading order (NNLO) QCD corrections to the $HV$ inclusive cross section have been known for many years [34]. In recent years, a fully differential NNLO calculation of $HV$ production has been presented in refs. [35, 36], while in refs. [37, 38] also the next-to-leading order (NLO) corrections to the decay of the Higgs boson into a $b$-quark pair have been considered, and combined with the NNLO corrections to the production process. Moreover, the role played by gluon-induced contributions to the associated production $HZ$ has been studied in ref. [39], in which they have been calculated at NLO. The results obtained show that, while NNLO corrections to the inclusive cross section are quite small, of the order of 1-2%, their impact can increase substantially when cuts are imposed on the decay products and on differential distributions.

In refs. [40, 41], NLO electroweak (EW) corrections have been studied: even if quite small at the level of the total cross section, they can give sizable contributions in the high-energy tails of some differential distributions. These outcomes will be explained in detail in Chap. 3. These corrections have then been implemented in the public code `HAWK` [42], that gives the possibility to combine NLO QCD and EW corrections. `VH@NNLO` [43], instead, allows to compute the inclusive cross section for $HV$ production at NNLO QCD + NLO EW accuracy.

All of these results come from fixed-order computations. In order to fully simulate a hadronic event and to compare theoretical predictions with experimental data, the parton-level processes have to be interfaced to a parton-shower generator, that describes further collinear radiation down to the hadronic scale. The precision needed for the LHC studies requires the hard event to be described at least at NLO accuracy, before matching it to the parton shower: this level of accuracy is usually called NLO+PS. The associated production of a Higgs boson with a vector boson, matched with a parton shower generator, has been implemented in `MC@NLO` [11] and in the `POWHEG BOX` [12] framework. The latter also includes

NLO+PS predictions for $HV + 1$ jet ($HVj$): the $HVj$ simulations have been implemented using the Multiscale improved NLO (`MiNLO`) approach [18], that will be described in Sec. 2.5.

In ref. [19] it was shown that, for processes where a colourless system $X$ is produced in hadronic collisions, it is possible to simulate both $X$ and $X+1$ jet production simultaneously at NLO+PS accuracy, without introducing any external merging scale. It was then shown in refs. [19, 44] that, with a merged generator of $X$ and $X + 1$ jet, and the NNLO differential cross section for $X$ production, it is possible to build a NNLO+PS accurate generator for $X$ production. This approach was used to build, in ref. [45], a NNLO+PS generator for $HW$ production.

Summing up, the accuracy reached in the QCD sector is high enough to comply with the experimental results that are coming from the LHC Run 2. In the electroweak sector, instead, the NLO+PS accuracy is still missing.

Since one of the goals of the ongoing LHC Run is to show, if present, signals of new physics, a precise knowledge of the production cross sections is mandatory. One of the main BSM searches concerns the Supersymmetric extensions of the Standard Model (SUSY). This symmetry predicts the existence of a superpartner for every Standard Model particle: to every boson is associated a fermion with the same mass and internal quantum numbers (apart from spin), and vice-versa. Since supersymmetric particles have not been observed yet, if SUSY exists it must be necessarily a spontaneously broken symmetry. These particles would then have a higher mass with respect to their Standard Model partners and this would explain the fact that, up to now, the LHC has not discovered them. Many supersymmetric particles could be produced and detected at the LHC: the main production channels are squark-antisquark, gluino-squark and gluino-gluino pairs, if they are light enough to be produced. Typical squark and gluino decays contain isolated leptons and jets, and they produce a stable Lightest Supersymmetric Particle (LSP), if an R-parity conserving SUSY model is assumed. Since the LSP cannot be detected, missing transverse momentum will be observed in the detector. Therefore, the typical experimental signature of a supersymmetric event consists of multiple jets, isolated leptons and missing transverse momentum.

This signature can be obtained with Standard Model processes in several ways: for example $W+$ jets events with leptonic decay of the $W$ boson, or the production of $t\bar{t}$ pairs in which both quarks decay into $Wb$ pairs, and then one vector boson decays leptonically while the other one decays hadronically. Even if the cross section is much lower, $HWj$ production too can contribute to the background, if the Higgs boson decays into a $b\bar{b}$ pair and the $W$ boson decays leptonically. It is therefore important to study also this process with high accuracy. These production processes are important by themselves, since they allow to study the coupling of the Higgs boson to vector bosons and to $b$ quarks. At present, the $HVj$ process is described at NLO+PS accuracy in QCD, while both electroweak NLO+PS and QCD NNLO+PS are missing.

For all of these reasons, this thesis is dedicated to the implementation of the associated production of a Higgs boson with a vector boson and eventually a jet, at NLO+PS accuracy, in the `POWHEG BOX`, considering both QCD and EW corrections. The leptonic decay of the vector boson has been fully taken into account: for the $Z$ production processes we have considered only the decay of the vector boson into charged leptons. Although in the rest of the work we will refer to these processes with the shorthand notations $HV$ and $HVj$, we have computed the amplitudes for these processes with full spin and decay correlations of the final-state leptons.

# Chapter 2

# The POWHEG BOX RES framework

The POWHEG BOX [13, 14] is a Monte Carlo event generator with NLO accuracy that can be interfaced to parton shower generators according to the POWHEG method [15]. It is one of the most commonly used tools to obtain theoretical predictions for comparisons with the experimental data. Within this framework, the hard event can be described at NLO+PS accuracy, while the subsequent part of the shower is left to a Monte Carlo parton shower program that supports the Les Houches Interface for User Generated Processes, such as Pythia [46] or Herwig [47], up to the formation of hadrons.

Since its release, the POWHEG BOX has undergone many extensions and modifications that improved the precision and the efficiency of this generator. All the information and the instructions for downloading this program can be found at http://powhegbox.mib.infn.it.

This chapter is dedicated to the description of the modifications that are relevant for the implementation of $HV$ and $HVj$ at NLO+PS QCD+EW accuracy in the POWHEG BOX.

## 2.1 The treatment of resonances

When QED or QCD corrections are included in a fixed-order computation, the appearance of soft and collinear divergences cannot be avoided, because of the exchange of massless particles. Nevertheless, considering infrared-safe observables these divergences cancel between the virtual and real corrections as a consequence of generalizations of the KLN theorem [48, 49], and the result is finite.

One of the methods to expose the cancellation of the singularities is the *subtraction method*. Calling $\Phi_B$ and $\Phi_R$ the Born and real phase spaces, a generic NLO cross section can be written as

$$d\sigma^{\mathrm{NLO}} = \big[B(\Phi_B) + V(\Phi_B)\big]\, d\Phi_B + R(\Phi_R)\, d\Phi_R, \tag{2.1}$$

where $B$, $V$ and $R$ represent the Born, virtual and real cross sections. The mean value of an infrared-safe observable can then be obtained from

$$\langle \mathcal{O} \rangle = \int \mathcal{O}\, d\sigma^{\mathrm{NLO}} = \int \big[B(\Phi_B) + V(\Phi_B)\big]\, \mathcal{O}(\Phi_B)\, d\Phi_B + \int R(\Phi_R)\, \mathcal{O}(\Phi_R)\, d\Phi_R. \tag{2.2}$$

Assuming that soft and collinear divergences are treated in dimensional regularization, $d\Phi_B$ and $d\Phi_R$ are evaluated in $D = 4 - 2\epsilon$ dimensions. In this way, the singularities associated to the emission of soft and/or collinear particles appear as poles in $\epsilon$.

In order to implement the subtraction method, a parametrization of the real phase space is introduced,

$$\Phi_R = \Phi_R\left(\Phi_B, \Phi_{\mathrm{rad}}\right), \qquad d\Phi_R = d\Phi_B\, d\Phi_{\mathrm{rad}}, \tag{2.3}$$

where $\Phi_{\rm rad}$ represents three variables that describe the emission of the extra particle involved in the real corrections. The real phase space must be parametrized in such a way that it matches the Born one in the limit of soft/collinear emission. Then, one introduces an approximation of the real cross section, $R_s$, with the same behaviour of $R$ in the soft and collinear limits. Equation (2.2) can then be rewritten as

$$\begin{aligned}\langle\mathcal{O}\rangle &= \int\left[B(\Phi_B)+V(\Phi_B)+\int d\Phi_{\rm rad}\,R_s(\Phi_B,\Phi_{\rm rad})\right]\mathcal{O}(\Phi_B)\,d\Phi_B \\ &\quad+\int\left[R(\Phi_B,\Phi_{\rm rad})\mathcal{O}(\Phi_B,\Phi_{\rm rad})-R_s(\Phi_B,\Phi_{\rm rad})\mathcal{O}(\Phi_B)\right]d\Phi_B\,d\Phi_{\rm rad}. \qquad (2.4)\end{aligned}$$

This formula is identical to the previous one, having just added and subtracted a contribution. Nevertheless, in the square bracket of the first term, the soft and collinear divergences arising from the integration of $R_s$ over the radiation phase space cancel with the ones coming from the virtual cross section. Furthermore, thanks to the infrared-safety property of $\mathcal{O}$, the divergences in the second square bracket cancel at integrand level, being $R_s$ the singular approximation of $R$. This term can then be integrated in $D=4$ dimensions through numerical methods. The cancellation of the singularities in the first term, instead, can be obtained analytically once and for all. In fact, defining the soft-virtual contribution as

$$V_{\rm sv}(\Phi_B)=\lim_{\epsilon\to 0}\left[V(\Phi_B)+\int R_s(\Phi_B,\Phi_{\rm rad})\,d\Phi_{\rm rad}\right], \qquad (2.5)$$

that is finite by construction, eq. (2.4) becomes

$$\begin{aligned}\langle\mathcal{O}\rangle &= \int\left[B(\Phi_B)+V_{\rm sv}(\Phi_B)\right]\mathcal{O}(\Phi_B)\,d\Phi_B \\ &\quad+\int\left[R(\Phi_B,\Phi_{\rm rad})\mathcal{O}(\Phi_B,\Phi_{\rm rad})-R_s(\Phi_B,\Phi_{\rm rad})\mathcal{O}(\Phi_B)\right]d\Phi_B\,d\Phi_{\rm rad}, \qquad (2.6)\end{aligned}$$

and also the first integral can be evaluated numerically in four dimensions.

Many formulations of this method have been proposed, that differ in the parametrization of $R_s$. For example, in its original implementation, the `POWHEG BOX` used both the Catani-Seymour [50] and the Frixione-Kunszt-Signer [51] subtraction schemes.

The general formulas for the full NLO cross section derived according to the `POWHEG` method can be found in eqs. (4.13), (4.16) and (4.17) of ref. [13]. We report them here for completeness,

$$\begin{aligned}d\sigma &= \sum_{f_b}\bar{B}^{f_b}(\Phi_B)\,d\Phi_B\left\{\Delta^{f_b}(\Phi_B,p_{T,\rm min}^2)\right. \\ &\quad\left.+\sum_{\alpha_r\in\{\alpha_r|f_b\}}\frac{\left[R(\Phi_R)\,\Delta^{f_b}(\Phi_B,k_T^2)\,\theta(k_T-p_T^{\rm min})\,d\Phi_{\rm rad}\right]_{\alpha_r}^{\bar{\Phi}_B^{\alpha_r}=\Phi_B}}{B^{f_b}(\Phi_B)}\right\}. \qquad (2.7)\end{aligned}$$

The function $\bar{B}^{f_b}(\Phi_B)$ is the NLO inclusive cross section at fixed underlying-Born flavour configuration $f_b$ and kinematics $\Phi_B$,

$$\begin{aligned}\bar{B}^{f_b}(\Phi_B) &= \left[B(\Phi_B)+V_{\rm sv}(\Phi_B)\right]_{f_b}+\sum_{\alpha_r\in\{\alpha_r|f_b\}}\int\left\{\left[R(\Phi_R)-R_s(\Phi_R)\right]d\Phi_{\rm rad}\right\}_{\alpha_r}^{\bar{\Phi}_B^{\alpha_r}=\Phi_B} \\ &\quad+\sum_{\alpha_\oplus\in\{\alpha_\oplus|f_b\}}\int\frac{dz}{z}\,G_\oplus^{\alpha_\oplus}(\Phi_{B,\oplus})+\int\frac{dz}{z}\,G_\ominus^{\alpha_\ominus}(\Phi_{B,\ominus}). \qquad (2.8)\end{aligned}$$

The real contributions are separated into terms labelled by the index $\alpha_r$: each of them denotes a flavour structure and a singular region. With the notation $\alpha_r \in \{\alpha_r | f_b\}$ we group together all the real singular contributions that have $f_b$ as underlying Born flavour. The square brackets with subscript $\alpha_r$ and superscript $\bar{\Phi}_B^{\alpha_r} = \Phi_B$ mean that everything inside refers to the particular real contribution labelled by $\alpha_r$, and has underlying-Born kinematics equal to $\Phi_B$. The factors $G_{\oplus}^{\alpha_{\oplus}}$ and $G_{\ominus}^{\alpha_{\ominus}}$, instead, are needed to obtain the complete cancellation of the initial-state collinear singularities.

Finally, $\Delta^{f_b}(\Phi_B, p_T^2)$ is the Sudakov form factor,

$$\Delta^{f_b}(\Phi_B, p_T^2) = \exp\left\{ - \sum_{\alpha_r \in \{\alpha_r | f_b\}} \int \frac{\left[ R(\Phi_R)\, \theta(k_T(\Phi_R) - p_T)\, d\Phi_{\rm rad} \right]_{\alpha_r}^{\bar{\Phi}_B^{\alpha_r} = \Phi_B}}{B^{f_b}(\Phi_B)} \right\}. \tag{2.9}$$

It corresponds to the probability that no emission occurs with transverse momentum $k_T$ bigger than $p_T$, that is a function of the kinematics variables of the particular singular region considered. This factor is used to generate the hardest radiation according to the POWHEG method [15]. Looking at eq. (2.7), then, the first term represents the probability that no resolvable emissions occur down to the scale $p_T^{\rm min}$, that is the scale at which QCD becomes non perturbative, while the second one corresponds to the probability of evolving down to the scale $k_T$ without emissions and then emitting a parton with transverse momentum $k_T$ (which is required, through the $\theta$ function, to be larger than $p_T^{\rm min}$).

In the generation of the events, it is possible to separate the real cross section into a finite and a singular part, using the `flg_withdamp` option as explained in Sec. 5 of ref. [14], and exponentiating only the singular part. In the context of this thesis, this feature has not been used.

The subtraction schemes employed in the POWHEG BOX, however, have not been thought having in mind the production of radiation from resonances. As described in detail in ref. [16], with processes that involve decaying resonances, a possible source of problems arises when the mapping (2.3) is performed. This mapping is constructed in such a way that, in the collinear limit, the so-called underlying-Born configuration is obtained by appropriately merging the two collinear particles. In order to preserve the masses of the external particles, some momentum reshuffling is needed, and this operation does not necessarily preserve the virtuality of the intermediate resonances. The typical difference in the resonance virtuality between the original real kinematics and the reconstructed Born-like one is of order $m^2/E$, where $m$ and $E$ are the invariant mass and the energy of the merged-partons system, respectively.

In this way, the cancellation between the real contribution $R$ and the subtraction term $R_s$ will be effective only if the condition $m^2/E \ll \Gamma$ is satisfied, being $\Gamma$ the width of the resonance. As $\Gamma$ decreases, the convergence becomes more problematic, getting completely spoiled in the zero-width limit. In order to overcome this problem, it would be desirable to have a subtraction method that preserves the mass of the resonance in the subtraction terms.

Further problems arise in the generation of radiation, performed according to a Sudakov form factor of the form

$$\Delta(p_T^2) = \exp\left[ - \int \frac{R(\Phi_B, \Phi_{\rm rad})}{B(\Phi_B)}\, \theta\big(k_T(\Phi_{\rm rad}) - p_T\big) d\Phi_{\rm rad} \right]. \tag{2.10}$$

The upper limit of the integration is dictated by the maximum transverse momentum allowed for the radiation in the process under study. The mapping that connects the real phase space to $\Phi_B$ and $\Phi_{\rm rad}$ is the same used in the NLO subtraction: for this reason, also in this case the virtuality of the resonance will not be preserved. In the $R/B$ ratio, then, the two terms will

not be on the resonance peak at the same time unless the condition $m^2/E \ll \Gamma$ is satisfied, and this can yield large ratios that violate the collinear approximation. Moreover, when the NLO calculation is interfaced to a Monte Carlo shower program, radiation should have a well-defined resonance assignment, according to which the Monte Carlo generator should be instructed to preserve the mass of the resonance.

In order to solve these problems, in ref. [16] it is explained that the different subprocesses contributing to the cross section have to be separated into terms with a definite resonance history. Each term has a resonance peak only in a single resonance cascade chain, and the mapping of the real phase space into an underlying-Born configuration is defined in such a way that the virtuality of the resonance is preserved. When the algorithm looks for particles that can give rise to a collinear singularity, then, it must consider only pairs originating from the same resonance, or from the production process. This procedure constitutes the main extension of the `POWHEG BOX`. The resulting code is the `POWHEG BOX RES` [16], that is the resonance-aware version of the original program. The main modifications deal with the subtraction method: instead of simply separating the real cross section into a sum of terms that are singular in a specific kinematic region, each of these terms must also become associated to a particular resonance history. To this end, when the partonic structure of the different (Born and real) subprocesses is set up by the user, a subroutine automatically generates all the relevant resonance histories for every subprocess. In this way, the full Born flavour structure is no more represented by the only array `flst_born(j,iborn)`: its resonance information is stored in the `flst_bornres(j,iborn)` array too. The index `iborn` labels a particular Born flavour structure, while `j` runs over the external legs and the internal resonances. The entries in the `flst_born` array represent the flavour code of the particle (that coincides with the PDG code [33], except for gluons that are labeled by 0). In `flst_bornres`, instead, the value of `j` represents pointers that allow to reconstruct the resonance structure. These pointers contain 0 for particles generated at the production stage, while for particles coming from the decay of a resonance the corresponding entry is the position of the mother resonance in the list.

A big difference with respect to the original `POWHEG BOX` implementation arises here: since a given process admits several resonance structures, the flavour lists can have different lengths. The index `j` does not run anymore from 1 to `nlegborn`: for every subprocess its upper limit is given by the corresponding value stored in the array `flst_bornlength(iborn)`, that contains the length of each flavour list. At the end, an array `flst_bornresgroup(iborn)` is used to group together all the Born flavour configurations that share the same resonance structure, so that they can be integrated together with the same importance sampling. The values of this array label the resonance structure group of the Born flavour structure `iborn`. The number of different Born resonance structures is then saved in the variable `flst_nbornresgroup`. Similar arrays are defined and filled for the real subprocesses.

These operations are performed automatically in the `init_processes` subroutine by the subroutines `build_resonance_histories` and `buildresgroups`. The user only has to provide the list of contributing flavour structures of the Born and real subprocesses, and the power of the electroweak and strong couplings of the Born amplitude, stored in the variables `res_powew` and `res_powst`.

Once the resonance structure is filled, the separation of the real cross section into singular regions can be performed. To each term, a weight is associated that makes it dominant only in a specific resonance region. Then, the subtraction procedure has been adapted so that, for each of these terms, the mapping of the real to the underlying-Born configuration does not change the virtuality of the resonance. To obtain this result, in case of radiation coming from the decay of a resonance, the subtraction procedure is applied in the resonance center-of-mass

frame. In this way, neither the momentum of the resonance nor that of all the particles that do not come from its decay are altered. For particles radiated from the production process, instead, the subtraction method remains unchanged.

The two main problems of the standard subtraction methods are thus solved: both in the calculation of the NLO cross section and in the generation of radiation the mass of the resonance is preserved, and the radiation has a well-defined resonance assignment, so that also the Monte Carlo shower algorithm can preserve its virtuality.

### 2.1.1 Resonance histories for the $HV$ and $HVj$ processes

To further clarify the mechanism of resonance assignments, we apply it to the processes relevant for this thesis. The Born level resonance structures for the $HV$ and $HVj$ processes are very simple. We focus on the processes involving a $W^-$ boson: the $W^+$ and $Z$ boson cases can be described in the same way. The Feynman diagram for $HW^-$ production, with

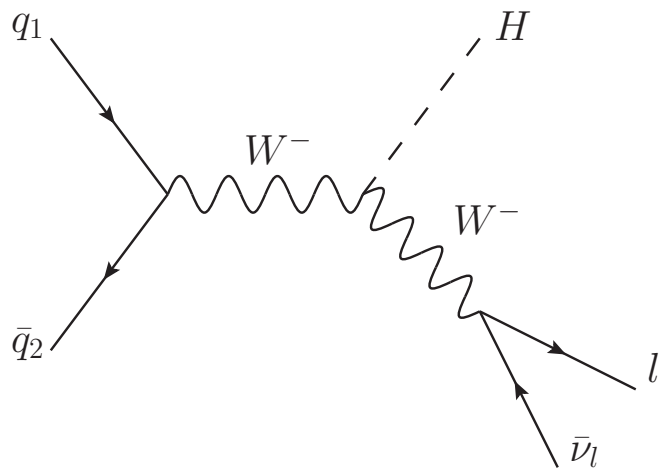


Figure 2.1: Feynman diagram for the associated production of a Higgs boson and a $W^-$ boson that decays leptonically.

leptonic decay of the vector boson, is depicted in fig. 2.1. The resonance histories can thus be described by the arrays

```
flst_born(:,iborn)    = [i, j, -24, -24, 25, 11, -12],
flst_bornres(:,iborn) = [0, 0,   0,   3,  3,  4,   4],
```

for all the relevant choices of initial parton flavours `i`, `j`. The resonance assignment in `flst_bornres` means that:

- the third particle in the `flst_born` array, that is a $W^-$ boson, is produced by the initial-state partons;
- the fourth and the fifth particle come from the decay of the third one, that is the aforementioned $W^-$ boson;
- the two leptons come from the fourth particle in the list, the $W^-$ boson just before its decay.

For $HW^-j$ production the Born structure is very similar. There is one more parton in the final state, with respect to $HW$ production: since it comes from the production stage, its resonance assignment is set to 0,

```
flst_born(:,iborn)    = [i, j, -24, -24, 25, 11, -12, k],
flst_bornres(:,iborn) = [0, 0,   0,   3,  3,  4,   4, 0],
```

for the relevant choices of `i`, `j` and `k`. The length of the Born processes is then always the same (i.e. 7 in $HW^-$ and 8 in $HW^-j$), and only one resonance group is present, so that `flst_nbornresgroup = 1`.

When setting up the real subprocesses, the resonance-aware machinery becomes very important. As for the Born structures, we describe the $HW^-$ case, all the other processes work in the same way. Although this thesis is focused on the implementation of the associated production processes at NLO+PS QCD+EW accuracy, it is also possible to obtain predictions that consider QCD and EW corrections separately. The flag that controls this possibility is `qed_qcd`, that has to be set in the `POWHEG BOX RES` input file. If one wants to include only QCD corrections, `qed_qcd` must be set to 0: in this case the radiated parton can come only from the initial state. We then have one resonance history: the arrays `flst_real` and `flst_realres` have the same form of the Born arrays for $HW^-j$ production. If one considers only electroweak corrections, instead, by setting `qed_qcd` to 1, the radiated particle is a photon, that can be emitted by every charged particle. For the subprocess

```
flst_real(:,ireal)    = [i, j, -24, -24, 25, 11, -12, 22],
```

we can then have two resonance assignments:

```
flst_realres(:,ireal) = [0, 0, 0, 3, 3, 4, 4, 0],
flst_realres(:,ireal) = [0, 0, 0, 3, 3, 4, 4, 4].
```

The first one corresponds to photon emission from the initial-state partons, while in the second one the photon comes from the decay of the $W^-$ resonance. In this case, then, we have `flst_nrealresgroup = 2`. Both these resonance structures are considered by the `POWHEG BOX RES` during the subtraction procedure, and they are treated in different ways, in order to preserve the resonance virtuality when the photon comes from the $W$ boson decay.

Finally, by setting the flag `qed_qcd` to 2, both QCD and QED corrections are included, and all the subprocesses are implemented.

To obtain a complete NLO electroweak result, also the processes with an incoming photon should be included in the computation, together with the real emission of $W$ and $Z$ bosons. For the photon-initiated processes, although many PDF sets include the electromagnetic evolution, the photon density is very small, of order $\alpha$, and it multiplies a process of order $\alpha$ with respect to the leading-order one. For this reason, we decided to leave out the photon-initiated processes. The real emission of $W$ and $Z$ bosons, instead, has not been considered for reasons that will be explained in Chap. 3.

## 2.2 The inclusion of photon radiation

If we are including electroweak corrections, as we have just seen, we have to consider the emission of a photon. Photon radiation was introduced in the `POWHEG BOX` for the first time in ref. [17], in which NLO QCD+EW corrections to $W$ boson production were computed. Then, this procedure was extended in the context of $Z$ boson production in ref. [52]. In

these articles, the leptons coming from the decay of the vector boson were considered as massive, and the treatment of photon radiation from massive charged particles was implemented correspondingly. In this thesis, instead, both quarks and charged leptons are considered as massless: for this reason we have modified the code so that it can generate also photon radiation from massless charged particles.

The first relevant change is in the structure of the soft and virtual counterterms, needed to compute the soft-virtual contribution to the NLO cross section of eq. (2.5). Photon emission, however, is similar to gluon emission from quarks: the counterterms can then be easily obtained from the QCD case with minor efforts.
Adapting the factors $\gamma_q$ and $\gamma'_q$ in eqs. (2.95) and (2.96) of the original POWHEG paper [13],

$$\gamma_q = \frac{3}{2} C_F^2, \qquad \gamma'_q = \left(\frac{13}{2} - \frac{2}{3}\pi^2\right) C_F^2, \tag{2.11}$$

for the exchange of a photon we obtain

$$\gamma_f^{\text{EM}} = \frac{3}{2} Q_f^2, \qquad \gamma_f^{'\text{EM}} = \left(\frac{13}{2} - \frac{2}{3}\pi^2\right) Q_f^2, \tag{2.12}$$

where $f$ denotes the flavour of the emitting particle. We can immediately see that, while the original terms have a physical significance only for coloured particles, due to the presence of $C_F$, the factors in eq. (2.12) are valid for every charged particle, since they involve the electric charge of the emitter. At this point, the counterterm for final-state QED radiation from massless particles can be obtained straightforwardly from the results for QCD radiation from massless quarks, that is already implemented. For every final-state charged massless particle one soft-virtual term is added, with the same structure of the QCD case but with $\gamma_q$ and $\gamma'_q$ substituted by $\gamma_f^{\text{EM}}$ and $\gamma_f^{'\text{EM}}$, respectively.

The second important modification to the code involves the upper-bounding function used in the generation of radiation according to the POWHEG Sudakov form factor. This function is used to generate photon radiation using the highest-bid method. As explained in the original paper, several upper-bounding functions have been implemented in the POWHEG BOX, for initial- and final-state QCD radiation. These functions correspond to the upper bound of the $R/B$ ratio of eq. (2.10): they catch the divergent behaviour of the real cross section in the singular region, and they include one power of the strong coupling constant, evaluated at the transverse momentum of the emitting parton, $\alpha_s(k_T^2)$. Since QED and QCD radiation share many similarities, in order to obtain the functions for photon emission we can repeat the procedure for the QCD case, described in Apps. C and D of ref. [14], starting from the same upper-bounding functions but using a fixed-valued electromagnetic coupling constant $\alpha$ instead of a running $\alpha_s(k_T^2)$. We proceed in this way since the running of $\alpha$ is negligible in the energy range considered, and in the limit of zero momentum transfer we have $\alpha \to 1/137$.

We start from describing final-state radiation. The form of the upper-bounding function we have used is

$$U(\xi, y) = N \frac{\alpha}{\xi(1-y)}, \tag{2.13}$$

in which $N$ is a normalization factor, $\xi$ is the fraction of the emitter energy carried by the emitted particle, and $y = \cos\theta$ is related to the angle between the emitter and the radiated particle. As in QCD, the soft and collinear final-state singularities correspond to $\xi \to 0$ and $y \to 1$, respectively. This function is used to generate $p_T$ uniformly in

$$\Delta(p_T^2) = \exp\left[-\int U(\xi, y)\, \theta(k_T - p_T)\, d\xi\, dy\, d\phi\right], \tag{2.14}$$

in which $d\xi\, dy\, d\phi$ is a parametrization of the radiation phase space $d\Phi_{\rm rad}$ of eq. (2.10). The variable $k_T$ entering the theta function can be related to the integration variables through

$$k_T^2 = \frac{s}{2}\,\xi^2(1-y), \tag{2.15}$$

being $s$ the partonic center-of-mass energy squared. The integration ranges of $\xi$, $y$ and $\phi$ are given by

$$0 \le \xi \le \xi_{\rm max} = 1 - \frac{M_{\rm rec}^2}{s}, \qquad -1 \le y \le 1, \qquad 0 \le \phi < 2\pi, \tag{2.16}$$

where $M_{\rm rec}$ is the mass of the system recoiling against the emitter and emitted particles. Trading $y$ for $k_T^2$ through eq. (2.15) we get

$$y = 1 - \frac{2k_T^2}{\xi^2 s} \longrightarrow dy = -\frac{2}{\xi^2 s} dk_T^2, \qquad 0 \le k_T^2 \le s\xi^2. \tag{2.17}$$

Taking the logarithm of eq. (2.14), we then obtain

$$\begin{aligned} -\log\Delta(p_T^2) &= \int_0^{\xi_{\rm max}} d\xi \int_{-1}^{1} dy \int_0^{2\pi} d\phi\; N\,\frac{\alpha}{\xi(1-y)}\,\theta(k_T - p_T) \\ &= 2\pi\alpha N \int_0^{\xi_{\rm max}} d\xi \int_{\xi^2 s}^{0} \left(-dk_T^2\right) \frac{1}{\xi k_T^2}\,\theta(k_T - p_T). \end{aligned} \tag{2.18}$$

Since $k_T^2$ depends on $\xi$, the theta function restricts the integration ranges for both $k_T^2$ and $\xi$, giving

$$-\log\Delta(p_T^2) = 2\pi\alpha N \int_{\sqrt{p_T^2/s}}^{\xi_{\rm max}} \frac{d\xi}{\xi} \int_{p_T^2}^{s\xi^2} \frac{dk_T^2}{k_T^2} = \frac{\pi\alpha N}{2}\log^2\frac{\xi_{\rm max}^2 s}{p_T^2}. \tag{2.19}$$

At this point, the procedure for the generation of radiation proceeds in the standard way, generating a random number $r$ and solving the equation $r = \Delta(p_T^2)$. In the implementation, this equation is translated into $\log r = \log\Delta(p_T^2)$, and solved numerically for $p_T$. Once $p_T$ is generated, $\xi$ is generated uniformly in $\log\xi$ within the limits

$$\sqrt{\frac{p_T^2}{s}} \le \xi \le \xi_{\rm max}, \tag{2.20}$$

$y$ is obtained through

$$y = 1 - \frac{2p_T^2}{s\xi^2}, \tag{2.21}$$

and $\phi$ is generated uniformly in $[0, 2\pi)$. The simplification with respect to the QCD case comes from the fact that, considering a fixed coupling constant, the dependence of the integrand function on $k_T^2$ is much simpler.

When generating initial-state radiation, if we consider combined QCD+EW corrections, photon emission always occurs in competition with gluon emission: for this reason, the upper-bounding function for QCD radiation has to be used. Including only QED radiation, instead, the QCD function would make the generation of radiation extremely inefficient. For this reason, we have implemented a procedure for generating initial-state photon radiation in a more efficient way. We remind that this option is used only if the flag `qed_qcd` is set to 1, otherwise the presence of QCD radiation forces the use of the corresponding upper-bounding function.

The upper-bounding function for QED initial-state radiation can be obtained from the QCD one exactly as we have done in the previous case, i.e. by using $\alpha$ instead of $\alpha_s(k_T^2)$,

$$U(x,y) = N\,\frac{\alpha}{(1-x)(1-y^2)}, \tag{2.22}$$

having defined $x = 1-\xi$, so that the singular limit is reached when $x \to 1$ and $y \to \pm 1$. The $k_T$ variable can be related to $x$ and $y$ through

$$k_T^2 = \frac{s_b}{4x}(1-x)^2(1-y^2), \tag{2.23}$$

being $s_b$ the center-of-mass energy of the underlying Born. As for the final-state case, we will trade $y$ for $k_T$ in performing the integral. Since the range of $U(x,y)$ must cover the range of the radiation variables for the given underlying-Born configuration, a practical restriction for the integration variables is

$$\rho \le x \le 1, \qquad \rho = \frac{s_b}{S}, \tag{2.24}$$

$$k_T^2 \le k_{T,\max}^2, \qquad k_{T,\max}^2 = s_b\,\frac{(1-\bar{x}_\oplus^2)(1-\bar{x}_\ominus^2)}{(\bar{x}_\oplus+\bar{x}_\ominus)^2}. \tag{2.25}$$

In these formulae, $S$ is the energy of the incoming hadrons, and $\bar{x}_{\circledast}$ are the momentum fractions of the incoming partons after radiation. We want to generate $p_T$ uniformly according to eq. (2.14): to this end, writing $y$ in terms of $k_T^2$ we obtain

$$|y| = \sqrt{1 - \frac{4x}{(1-x)^2}\,\frac{k_T^2}{s_b}}, \tag{2.26}$$

so that

$$dy = \mp\,\frac{2x}{s_b(1-x)}\,\frac{dk_T^2}{\sqrt{(1-x)^2 - 4xk_T^2/s_b}}. \tag{2.27}$$

Defining $a = k_T^2/s_b$, the zeros of the square root are located at

$$x_\pm = \left(\sqrt{1+a} \pm \sqrt{a}\right)^2, \tag{2.28}$$

with $x_+ > 1$ and $x_- < 1$. The presence of the square root further restricts the integration interval for $x$: since its argument must be positive, $x$ can take values only in the interval $(-\infty, x_-] \cup [x_+, +\infty)$. The integration range of $x$ is then reduced from $\rho$ to $x_-$. The upper-bounding function, rewritten in terms of $k_T^2$, becomes

$$U(x,k_T^2) = N\alpha\,\frac{s_b(1-x)}{4xk_T^2}, \tag{2.29}$$

and we obtain

$$\begin{aligned} -\log\Delta(p_T^2) &= 2\pi\alpha N \int_{p_T^2}^{k_{T,\max}^2} \frac{dk_T^2}{k_T^2} \int_\rho^{x_-} \frac{dx}{\sqrt{(x_+-x)(x_--x)}} \\ &= 2\pi\alpha N \int_{p_T^2}^{k_{T,\max}^2} \frac{dk_T^2}{k_T^2}\,\log\frac{\sqrt{x_+-\rho}+\sqrt{x_--\rho}}{\sqrt{x_+-\rho}-\sqrt{x_--\rho}}. \end{aligned} \tag{2.30}$$

Since $x_+$ and $x_-$ depend on $k_T^2$, and since we are looking for an upper bound, we can simplify the integrand by noting that

$$\log \frac{\sqrt{x_+ - \rho} + \sqrt{x_- - \rho}}{\sqrt{x_+ - \rho} - \sqrt{x_- - \rho}} \leq \log \frac{\sqrt{x_+} + \sqrt{x_-}}{\sqrt{x_+} - \sqrt{x_-}} = \frac{1}{2} \log \left(1 + \frac{s_b}{k_T^2}\right). \tag{2.31}$$

At this point the integration can be easily performed analytically, leading to

$$\begin{aligned} -\log \Delta(p_T^2, ) \leq -\log \tilde{\Delta}(p_T^2) &= \pi\alpha N \int_{p_T^2}^{k_{T,\max}^2} \frac{dk_T^2}{k_T^2} \log \left(1 + \frac{s_b}{k_T^2}\right) \\ &= \pi\alpha N \left[\mathrm{Li}_2 \left(-\frac{s_b}{k_{T,\max}^2}\right) - \mathrm{Li}_2 \left(-\frac{s_b}{p_T^2}\right)\right]. \end{aligned} \tag{2.32}$$

The procedure of generation of radiation now works in the same way as the QCD case, generating $p_T$ according to $\tilde{\Delta}(p_T^2)$ by solving $\log r = \log \tilde{\Delta}(p_T^2)$, and then using the veto method to obtain $p_T$ distributed according to $\Delta(p_T^2)$. At the end, all the other variables are obtained through the relations introduced in this derivation.

Thanks to these improvements, QED radiation can now be generated consistently and efficiently, both in the massive- and in the massless-emitter case. NLO electroweak corrections can then be included in the `POWHEG BOX RES`, provided that the matrix elements for the virtual and real corrections are supplied.

## 2.3 The automated generation of matrix elements with `OpenLoops`

In the last years, many progresses have been made in the field of automated matrix element generation. One of these generators is `OpenLoops` [53], based on fast numerical recursion relations for the generation of tree and one-loop scattering amplitudes [54]. Combined with the OPP reduction method [55] implemented in `CutTools` [56] and the scalar one-loop library `OneLOop` [57], or with the tensor integral reduction methods [58–60] implemented in `COLLIER` [61], the employed recursion allows to achieve very high CPU performance and a high degree of numerical stability. Indeed, the small fraction of numerically-unstable one-loop matrix elements is automatically detected and rescued through re-evaluation with `CutTools` in quadruple precision.

In order to take advantage of these features in the `POWHEG BOX RES`, a general process-independent interface between the `POWHEG BOX RES` and `OpenLoops` has been developed [62]. This interface allows for a straightforward implementation of many NLO processes, generating QCD or electroweak corrections. It is obtained through a FORTRAN90 module called `openloops_powheg`. Internally, the `POWHEG BOX RES`+`OpenLoops` framework automatically compiles, loads and manages all the required `OpenLoops` amplitude libraries.

The interface provides three subroutines, with the same structure as the `POWHEG BOX` subroutines `setborn`, `setreal` and `setvirtual`. These are `openloops_born`, `openloops_real` and `openloops_virtual`. The subroutines `openloops_borncolour`, `openloops_realcolour` and `openloops_init` are provided, too. The former two supply the required colour information, returning a colour flow for the Born and real matrix elements, in the large colour limit, on a probabilistic basis. The latter includes the synchronization of all the parameters between the `POWHEG BOX RES` and `OpenLoops`, and has to be called at the end of the `init_processes` subroutine.

Several OpenLoops internal options can be changed directly from the input file of the POWHEG BOX RES. In particular, it is possible to switch between the tensor-integral reduction methods implemented in COLLIER and the OPP reduction methods implemented in CutTools. The default behaviour uses COLLIER, while inserting the line

```
olpreset  1
```

in the input file, the program uses the reduction via CutTools. In a similar way, the insertion of the line

```
olverbose OpenLoops_verbosity_level
```

allows to select the verbosity level of OpenLoops. While all the relevant input parameters are automatically passed to OpenLoops during the POWHEG BOX RES initialization procedure, further parameters can be set directly through the routine

```
set_parameter (parameter,value)
   character(*), intent(in) :: parameter
   TYPE, intent(in) :: value
```

Here, TYPE can be an integer, double or character type, according to the parameter that has to be set. For example, if the user wants to change the value of the Higgs boson mass to 200 GeV, the following call has to be performed:

```
call set_parameter ("h_mass", 200d0)
```

The OpenLoops amplitude libraries for a given process, in the POWHEG BOX RES+OpenLoops framework, can be obtained by running the script generate_process.py, available in the POWHEG-BOX-RES/OpenLoopsStuff directory, with the following arguments:

```
./generate_process.py library_name -order_ew=m -order_qcd=n -name=dir_name
```

Here, library_name corresponds to the OpenLoops amplitude library of the desired process, a list of which can be found on the official website [53], while m and n denote the order of the Born cross section in terms of powers of the electromagnetic and strong coupling constants, $\mathcal{O}(\alpha^m \alpha_s^n)$. This execution builds a rudimentary POWHEG BOX process structure in the directory POWHEG-BOX-RES/dir_name. For example, the call

```
./generate_process.py pphlnj -order_ew=3 -order_qcd=1 -name=HWj
```

yields the structure for a NLO+PS generator including all required tree level and one-loop amplitudes for $pp \to HW(\to l\nu) + 1$ jet production with QCD corrections. At this point, the user only has to provide the list of contributing flavour structures and the powers of the electroweak and strong couplings of the Born amplitude, as explained in Sec. 2.1.

Currently NLO QCD corrections to any Standard Model process are supported by this interface, while electroweak corrections will be available soon. In the context of this thesis, we have used a dedicated interface, provided by the authors of OpenLoops, to obtain the matrix elements for the electroweak virtual and real corrections to the $HV$ and $HVj$ processes. The Born, Born-correlated and real QCD amplitudes in $HVj$ processes have instead been obtained through the automatic interface [63] to MadGraph [64, 65]. All the other contributions have been computed analytically.

## 2.4 The optimization of the virtual corrections

The computation of virtual electroweak corrections is the most CPU-demanding part of the calculation. For this reason, the best way to improve the efficiency of the generator is to minimize the number of calls to the virtual part of the cross section, taking care not to spoil the statistical accuracy of the complete result. Two different strategies can be adopted, depending on what part of the simulation a user is interested in.

If one needs to compute fixed NLO results, this minimization can be achieved by evaluating the virtual and real contributions with independent statistical accuracies. In the `POWHEG BOX RES` there is the possibility to separate the virtual cross section from the rest, in such a way that it can be computed with an accuracy that matches the one of the real contribution, thus saving computer time. More specifically, the code can be run twice. In the first run, the flag `novirtual` is set to 1 in the `POWHEG BOX RES` input file: in this way, no call to the calculation of the virtual corrections and of the soft-virtual terms is done, and the corresponding distributions do not contain these contributions. The code is then rerun by using the same importance-sampling grids computed in the first run, with the flag `virtonly` set to 1, `novirtual` set to 0 and with lower statistics with respect to the previous run. The virtual contributions are thus called fewer times with respect to the Born and real ones. Finally, the kinematic distributions obtained in the two steps can be combined.

All the NLO results presented in this thesis have been obtained by applying this procedure.

If instead one is interested in generating Les Houches events, it is more convenient to avoid the computation of the virtual corrections for the large number of events that are vetoed during the generation. This can be done, provided that one renounces to generating events with constant weight. The events are generated with settings such that the virtual cross section is not included: then, through a reweighting procedure, one can recompute the complete weight associated to a given event. In this way, the virtual contribution is computed only once for each event, instead of several tens of times, thus reducing dramatically the running time of the code.

In order to do so, one first generates events with the flag `novirtual` set to 1. Then, the following lines are added to the input file:

```
rwl_add 1
rwl_file '-'
<initrwgt>
<weight id='xx'> some reweight info </weight>
<weight id='yy'> some reweight info </weight>
...
</initrwgt>
```

For each `<weight` line, a new weight is generated and added to the event. These weights are all computed with the inclusion of the virtual corrections, and with the information stored in this line. This option can also be used to perform scale variations: in this case, the first run is performed with the central-scale values, and in the subsequent runs the scaling factors are varied.

In this thesis we have used a slightly different variant of this reweighting procedure: the interested reader can find all the details in Chap. 5.

## 2.5 The MiNLO procedure

One of the most problematic issues of QED and QCD calculations is the fact that, being forced to adopt a perturbative expansion, the appearance of unphysical renormalization and factorization scales $\mu_R$ and $\mu_F$ is unavoidable. The dependence of the results on these scales would vanish only when considering all the terms of the expansion, a task that cannot be fulfilled at all. These scales are then used to estimate the theoretical uncertainty associated to a fixed-order computation, usually by varying them by a factor of two around a "central" value.

The main problem related to the appearance of renormalization and factorization scales is that their "central" value is not fixed by the theory, and could be determined by requiring either the perturbative corrections to be small or the scale sensitivity to be minimized. Indeed, a "wrong" choice would give rise to large logarithms involving the ratio between these scales and the characteristic scales of the process, thus leading to sizable unphysical corrections.

If we consider for example a Drell-Yan process, a reasonable scale choice is the intermediate vector-boson mass. With more complex and exclusive processes, like $V+$jets production, more scale choices are possible: the higher the final-state multiplicity, the bigger the number of possible choices becomes. It would thus be desirable to have a method for suggesting the central scales starting from the kinematics of the process under consideration, rather than on a posteriori studies.

In the context of leading order matrix element - parton shower (MEPS) merging algorithms, a method for assigning the renormalization and factorization scales has been proposed in refs. [66–68]. In the so-called CKKW formalism, the kinematic configuration of the process is associated with the most probable branching history by means of a jet clustering algorithm. The relative transverse momentum at each branching defines the renormalization scale for the corresponding factor of $\alpha_s$ at the vertex, while the factorization scale is associated with the MEPS matching scale. Also the Sudakov form factors are included, in order to account for the large double logarithms that arise when the clustered event contains well separated scales. This procedure incorporates all the large logarithms associated with rendering the event exclusive with respect to the radiation above the MEPS merging scale, that is the scale beneath which the parton shower algorithms are used to populate the remaining phase space.

The partons are recursively recombined according to a $k_T$-clustering algorithm, in order to reconstruct the most likely branching history. At each vertex $i$ a nodal scale $q_i$ is assigned, equal to the relative transverse momentum at which the clustering has taken place. In addition, a resolution scale $Q_0$ is assigned, meaning that the cross section is interpreted as being inclusive for all radiation below this value. The procedure ends when no more clusterings are possible: the remaining particles form the primary system, to which is assigned a scale equal to its invariant mass $Q$.

At this point, the CKKW cross section is obtained by taking the tree-level matrix element, with the strong couplings associated at each node evaluated at the corresponding scale $q_i$. The remaining powers of the coupling constant, associated to the primary system, are evaluated at the scale $Q$. At next-to-leading logarithmic (NLL) accuracy the Sudakov form factor can be written as

$$\Delta_f(Q_1^2, Q_2^2) = \exp\left\{ -\int_{Q_1^2}^{Q_2^2} \frac{dq^2}{q^2} \left[ A_f\left(\alpha_s\left(q^2\right)\right) \log\frac{Q_2^2}{q^2} + B_f\left(\alpha_s\left(q^2\right)\right) \right] \right\}, \tag{2.33}$$

where $f = q, g$, and the functions $A_f$ and $B_f$ have a perturbative expansion in terms of

constant coefficients,

$$A_f(\alpha_s) = \sum_{i=1}^{\infty} A_{f,i}\, \alpha_s^i, \qquad B_f(\alpha_s) = \sum_{i=1}^{\infty} B_{f,i}\, \alpha_s^i. \tag{2.34}$$

To each intermediate line involving a parton $f$ that connects the nodes $i$ and $j$ is assigned a Sudakov form factor

$$\frac{\Delta_f(Q_0^2, q_i^2)}{\Delta_f(Q_0^2, q_j^2)} = \Delta_f(q_j^2, q_i^2). \tag{2.35}$$

This factor represents the probability that no branching occurs between the scales $q_i$ and $q_j$. External lines have a Sudakov form factor equal to $\Delta_f(Q_0^2, q_k^2)$, where $k$ is the node connected to the external line. At the end, the factorization scale is set to $Q_0$.

Thanks to eq. (2.34), the Sudakov form factor can be expanded in powers of the strong coupling constant, according to

$$\Delta_f(Q_1^2, Q_2^2) = 1 + \Delta_f^{(1)}(Q_1^2, Q_2^2) + \mathcal{O}\left(\alpha_s^2\right). \tag{2.36}$$

In this formula, $\Delta_f^{(1)}(Q_1^2, Q_2^2)$ represents the effective NLO correction that is included in the Born term when the CKKW prescription is used. Each event, reweighted to include these Sudakov form factors and scale assignments, is then passed to a Monte Carlo parton shower generator, with the requirement that no radiation is generated above $Q_0$, so that this region is governed by the exact tree-level matrix element, and the remaining phase space is filled by the shower.

Since the `POWHEG BOX` is an event generator with NLO accuracy, it is necessary to adapt the calculation of NLO cross sections so that the Born term is evaluated with the scales and Sudakov form factors prescribed by the CKKW formalism, while the full result maintains formal NLO accuracy. Moreover, the accuracy near the Sudakov regions must be comparable to that of the corresponding tree-level calculation in the adopted CKKW scheme.

This result has been obtained in refs. [18, 19]. The procedure, called `MiNLO` for Multi-scale improved NLO, includes the choice of the scales appearing in the coupling constants associated with the Born level and with the NLO (virtual and real) corrections. Since the NLO virtual correction already includes the $\mathcal{O}(\alpha_s)$ expansion of the Sudakov form factor, a term $\Delta_f^{(1)}(Q_1^2, Q_2^2)$ has to be subtracted for each Sudakov form factor included. To this end, after performing the clustering and evaluating the coupling constants at the corresponding nodal scales, the Born term in the inclusive cross section for the computation of the underlying-Born kinematics (the so-called $\bar{B}$ function in the `POWHEG BOX` method) is modified according to

$$B \to B \times \left[1 - 2\sum_j \Delta_{f_j}^{(1)}(Q^2, q_{n_j}^2)\right], \tag{2.37}$$

where the index $j$ runs over the Born-level final-state partons.

### 2.5.1 `MiNLO` in the *HVj* generators

When the `MiNLO` procedure has been proposed, it has been applied to the production of a Higgs, $W$ or $Z$ boson plus one or two jets. Indeed, in ref. [19] it was shown that, by applying this procedure to the NLO production of a colourless object in association with one jet, it is possible to reach NLO accuracy for quantities that are inclusive in the production of the colour-neutral system, i.e. when the associated jet is not resolved. We refer to this as the

improved MiNLO. Since the $HVj$ process can be interpreted as the production of a jet and a virtual colourless vector boson, that decays into an $HV$ pair, the improved MiNLO approach can be applied also to this case. For this process, the two relevant energy scales entering the process are the invariant mass of the virtual vector boson, $M_{HV} = (p_H + p_V)^2$, and its transverse momentum, $k_T$. The inclusion of the Sudakov form factors and the assignment of scales for the couplings modifies the $\bar{B}$ function of eq. (2.8), giving

$$\begin{aligned}\bar{B}\left(\Phi_B\right) \;=\; & \alpha_s(k_T^2)\,\Delta_q^2(M_{HV}^2,k_T^2) \\ & \times\left\{B(\Phi_B)\big[1-2\Delta_q^{(1)}(M_{HV}^2,k_T^2)\big]+V(\Phi_B)+\int d\Phi_{\rm rad}\,R(\Phi_B,\Phi_{\rm rad})\right\}. \quad (2.38)\end{aligned}$$

In this equation, one power of $\alpha_s$ has been stripped off from the Born, virtual and real contributions, and it has been explicitly written in front, with its scale dependence. The improved MiNLO procedure requires for the factorization scale, and for the scale at which the remaining power of $\alpha_s$ in $V$, $R$ and $\Delta_q^{(1)}$ is evaluated, to be again $k_T$. In the definition of $\Delta_q(M_{HV}^2,k_T^2)$, the coefficients $A_{q,1}$, $A_{q,2}$, $B_{q,1}$ and $B_{q,2}$ have to be included in order to preserve NLO accuracy. Their value for the present case is given by (see refs. [69–71])

$$\begin{aligned}A_{q,1} \;=\; & \frac{1}{2\pi}\,C_F, \qquad A_{q,2}=\frac{1}{4\pi^2}\,C_F\left[\left(\frac{67}{18}-\frac{\pi^2}{6}\right)C_A-\frac{5}{9}\,n_f\right], \qquad B_{q,1}=-\frac{3}{4\pi}C_F, \\ B_{q,2} \;=\; & \frac{1}{2\pi^2}\left[\left(\frac{\pi^2}{4}-\frac{3}{16}-3\zeta_3\right)C_F^2+\left(\frac{11}{36}\,\pi^2-\frac{193}{48}+\frac{3}{2}\,\zeta_3\right)C_FC_A\right. \\ & \left.+\left(\frac{17}{24}-\frac{\pi^2}{18}\right)C_Fn_f\right]+4A_{q,1}^2\zeta_3. \quad (2.39)\end{aligned}$$

The $\mathcal{O}(\alpha_s)$ expansion of the Sudakov form factor is instead given by

$$\Delta_q^{(1)}(M_{HV}^2,k_T^2)=\alpha_s\left(k_T^2\right)\left[-\frac{1}{2}A_{q,1}\log^2\frac{k_T^2}{M_{HV}^2}+B_{q,1}\log\frac{k_T^2}{M_{HV}^2}\right]. \quad (2.40)$$

With these inclusions, events generated according to eq. (2.38) have NLO accuracy for distributions inclusive in the $HV$ production, and also for distributions inclusive in the $HV+1$ jet production. This generator can then replace the $HV$ one, since it has the same NLO accuracy, and in addition it is NLO accurate in the production of the hardest jet.

# Chapter 3

# The high-energy limit of the NLO electroweak corrections

An efficient comparison between theoretical expectations and experimental results requires high precision, both in the detector performance and in the computation of collider observables. At hadron colliders like the LHC the dominant higher-order corrections to a tree-level process come from QCD corrections. Nowadays NLO QCD corrections are completely automatized. Several frameworks are available: `MC@NLO` [72] and its extensions, the `POWHEG BOX` [13–15] and its resonance-aware extension [16], `SHERPA` [73] and many more. They are often interfaced to automated matrix-element generators, that provide the one-loop amplitudes. The `POWHEG BOX` can be interfaced to `GoSam` [74] and `OpenLoops` [54]. Other generators that are commonly used are `BlackHat` [75], `RECOLA` [76] and `MadGraph5_aMC@NLO` [77]. All of these frameworks allow the computation of NLO cross sections matched with a parton shower algorithm.

To increase the theoretical precision in the computation of observables, the next step is to consider NNLO QCD corrections, of order $\alpha_s^2$ with respect to the leading-order process. For typical LHC processes, this kind of corrections gives contributions that can reach 10%, thus improving the precision in a non-negligible way. However, the drawback is that these corrections are in general very complicated to calculate: indeed, the NNLO contributions to the cross section for a given process involve multi-loop diagrams, and final states with high multiplicity.

Since the search for new physics needs to proceed with precision at the highest possible level, also the electroweak sector plays an important role. In fact, as in principle it is not known how new physics could manifest itself, one has to look for even small deviations from the Standard Model predictions. The electromagnetic coupling constant is very small if compared to the strong one, since $\alpha_s(M_Z) \simeq 0.119$, while $\alpha(M_Z) \simeq 1/128 = 0.008$. For this reason, looking only at the value of the coupling constants, the electroweak contribution is expected to be more than ten times smaller than the QCD one. While this reasoning has some physical soundness for inclusive quantities, for exclusive distributions things can be different. In fact, for several processes, the NLO EW corrections turn out to give contributions comparable to the NNLO QCD ones. Moreover, they are known to alter the shape of some important distributions, like the $W$ boson transverse mass in the TeV region or the $Z$ boson mass [78], thus affecting their determination. Finally, even if the effect of the electroweak corrections is rather mild on the integrated cross sections, they usually give sizable negative contributions in the high-energy tails of some transverse-momentum distributions. Indeed, in these kinematic regions, they can reach 40-50% [79, 80] with a partonic center-of-mass energy of a few TeV, thus becoming larger in magnitude than the NLO QCD corrections.

The importance of considering also NLO EW corrections comes from the fact that these energy ranges can be reached by the LHC.

For all of these reasons, both the theoretical and the experimental communities agree on the importance of the inclusion of electroweak corrections, as can be seen by examining the Les Houches wishlist, in tabs. 1 - 3 of ref. [80], where the state of the art of several Standard Model processes and the desired accuracy in the theoretical computations are shown. It appears clear that, together with NNLO QCD corrections, also NLO EW corrections play an important role in all the relevant final-state topologies (namely Higgs boson, jets, heavy-quark and EW gauge boson production).

## 3.1 The Sudakov logarithms

The high-energy tails of some transverse-momentum distributions receive sizable corrections from the electroweak sector because at high energies electroweak corrections are dominated by double and single logarithms of the typical energy scale of the process over the mass of the electroweak bosons $M_V$, with $V = W, Z$. These are called Sudakov logarithms [3–7]. The leading contributions, double-logarithmic corrections, are proportional to $\alpha \log^2(s/M_V^2)$, in which $\sqrt{s}$ is the partonic center-of-mass energy, while the subleading ones are proportional to $\alpha \log(s/M_V^2)$. These logarithms are the result of the emission of virtual or real massive gauge bosons from the external particles, and they stand for the soft and collinear singularities that would appear if the exchanged bosons were massless. For this reason they are called mass singularities. $M_V$ plays the role of infrared (IR) regulator for the singularities of loop diagrams, like the infinitesimal photon mass $\lambda$ usually introduced to regularize the IR singularities appearing in massless gauge theories. The high-energy regime $\sqrt{s} \gg M_V$ corresponds to the IR regime of the electroweak theory, where the gauge-boson masses can be neglected if compared to the other energy scales.

The electroweak sector has many differences with respect to QCD, in the structure of both the real and the virtual contributions to the cross section. Soft and collinear emissions of real massless particles give rise to divergences, that cancel the ones coming from one-loop corrections providing a finite result. In the electroweak case the situation is different for two reasons. First, even if the masses of the $W$ and $Z$ bosons act as IR cutoffs in one-loop corrections, they are physical parameters. There is no technical reason, then, for including the contribution coming from the radiation of an extra massive gauge boson. This represents a big difference with respect to the other theories, in which the singularities coming from the virtual corrections are regularized by introducing arbitrary regulators, that are canceled only when the IR-divergent real contributions are included in the calculation. This is precisely the case of photon emission, for which one introduces an infinitesimal mass $\lambda$. All the logarithms involving this parameter, that would diverge when taking the limit $\lambda \to 0$, cancel when summing the virtual and real contributions in the unresolved region, so that the result remains finite.

Another motivation to exclude real emissions of $W$ and $Z$ bosons, even if they contribute at the same perturbative order, comes from the fact that, being unstable particles, they subsequently decay. This leads to different final states in the detectors, that can be experimentally distinguished, not being degenerate with the leading-order ones.

If, however, real weak corrections were included, one could naively expect a complete cancellation of the Sudakov logarithms, just like in the case of photon emission. In the electroweak case, instead, the non-abelian structure of the gauge group leads to a mismatch between virtual and real contributions, as long as one does not sum over the non-abelian

charges of the external particles. The mismatch is a violation of the Bloch-Nordsieck theorem [81–84], that states that observables which are inclusive over soft final states are IR safe. This violation is due to the non-abelian nature of the electroweak charges in the initial state. The same phenomenon occurs in QCD, however in this case it has no physical consequences because of the colour averaging of the initial partonic states, needed in QCD since the colour charges do not exist as free asymptotic states. In the electroweak case the weak isospin charge of the initial state is fixed, and no averaging is performed: this leads to the non-cancellation of the Sudakov logarithms.

The origin of this non-cancellation can be understood by considering, for example, fully inclusive $e^+e^-$ annihilations. Virtual corrections are related to the cross section $\sigma_{e^+e^-}$. The same holds for the real corrections that involve the emission of a photon or a $Z$ boson. However, the emission of a $W$ boson changes the isospin of the incoming electron, turning it into a neutrino. The corresponding corrections are thus related to the cross section $\sigma_{e^+\nu_e}$, and they do not cancel the virtual contributions. An average over the different possible isospin states ($\sigma_{e^+e^-}, \sigma_{e^+\nu_e}, \sigma_{\bar{\nu}_e e^-}, \sigma_{\bar{\nu}_e \nu_e}$) would lead to a full cancellation of the logarithms [85]. Nevertheless, at hadron colliders this averaging is not possible because different weak isospin states receive different weights from the parton distribution functions.

In ref. [86] the role of weak boson emission and the compensation between virtual and real corrections were studied for several LHC processes. The result was that, as expected, the real cross section becomes important at high energies and compensates the negative contribution coming from the virtual corrections. However, this compensation is never exact, and in some cases, the real cross section is even bigger than the virtual one.

In refs. [87–91], the real emission of weak bosons was treated in analogy with QED or QCD: all the tree level diagrams with the emission of an extra $W$ or $Z$ boson were considered, with the gauge boson produced on shell and integrated over the full phase space. The result was a significant cancellation between real and virtual corrections, though still incomplete due to Bloch-Nordsieck violations. In refs. [79, 92], instead, the decay of the extra boson was investigated when the final states were degenerate with the leading-order ones, for both Standard Model and BSM processes. Also in these cases the cancellation between virtual and real contributions turned out to be only partial, and dependent on the process and on the event selections.

Electroweak virtual corrections are much more involved than the QCD ones, because they receive contributions from a wider set of particles ($\gamma$, $W$, $Z$, $H$), many of which are massive and interact with the colorless sector too (leptons, for example). However, in the high-energy regime, in the limit in which all the kinematic invariants are of the same order and much bigger than the electroweak scale, and for processes that are not mass-suppressed at high energies (the so-called Sudakov limit), the leading part of the one-loop corrections is universal [8]. It depends only on the flavour and on the kinematics of the external particles: it can thus be computed in a process-independent way and written as a sum of universal functions that multiply tree-level matrix elements. This approximation can be very helpful, since the calculation of the full electroweak corrections is computationally demanding. In the Sudakov limit, the universality of the leading part of the electroweak corrections allows to develop general algorithms [9, 10, 93] for the fast calculation of these contributions, that catch the main part of the corrections. The bulk of the corrections can then be obtained with a reduced computational cost, while the non-logarithmic part is process-dependent, and requires to be computed for every desired process. Since this approximation includes the dominant and the subdominant logarithmic terms, the level of accuracy reached considering these corrections is next-to-leading-logarithmic (NLL).

The leading-logarithmic part of the corrections comes from the exchange of soft-collinear

gauge bosons between pairs of external particles, and gives a negative contribution. The subleading part, instead, arises when soft or collinear gauge bosons are exchanged. It is often positive, and tends to compensate the leading term. It is for this reason that the tails of typical $p_T$ distributions receive negative contributions from the electroweak corrections.

Since these logarithms correspond to the singular behaviour of the loop integrals, the logarithmic structure of the corrections shares the same features as the one emerging from the IR limit of QED and QCD in mass regularization. The factorization properties of the Sudakov corrections over the tree-level matrix element are instead similar to the ones of the QCD corrections, because of the non-abelian structure of the underlying gauge groups, SU(3) for QCD and SU(2) $\times$ U(1) for the electroweak theory. Nevertheless, there are some differences between the two IR limits, related to the nature of the weak charges and to the spontaneous symmetry breaking of the electroweak sector.

In fact, spontaneous symmetry breaking implies that the masses of the $W$ and the $Z$ bosons are physical parameters. For this reason, even if at high energies $M_W$ and $M_Z$ act as IR regulators for the loop diagrams, their values cannot be set to zero: one-loop weak corrections are thus always IR-finite, even if they can be very large because of the leading logarithms. Another consequence of electroweak symmetry breaking is that also the scalar sector enters the computation of the corrections, both because the collinear factorization is based on the Becchi-Rouet-Stora invariance [94] of the Standard Model and because of the Goldstone-boson equivalence theorem [95–97] that relates longitudinally polarized gauge bosons to the corresponding Goldstone bosons at high energies.

In this thesis real corrections due to the radiation of massive $W$ and $Z$ bosons are not included: we focus on one-loop virtual contributions, and on their high-energy limit. We consider the limit in which the partonic center-of-mass energy, as well as all the kinematic invariants, are much bigger than the electroweak scale. Furthermore, we must consider only matrix elements that are not mass-suppressed, i.e. matrix elements with mass dimension $d$ that, in the high-energy limit, scale as $E^d$, and neglect all the contributions of order $M_V^n E^{d-n}$.

In this limit, the phenomenon of electroweak symmetry breaking has some consequences. First of all, introducing a weak scale of order $M_W$, spontaneous symmetry breaking creates a gap between this scale and the fictitious photon mass. Because of this gap, electroweak corrections are not symmetric at low energies, where they are usually split into an electromagnetic part, due to photon loops, and the remaining weak part. At high energies, instead, it is more convenient to separate the corrections in a different way, to reflect the SU(2) $\times$ U(1) symmetry. For this reason, the resulting logarithms coming from $\gamma$ and $Z$ boson loops are split into various parts. The contributions corresponding to a fictitious heavy photon and a $Z$ boson with mass $M_W$ are added to $W$ boson loops, determining a symmetric electroweak contribution. The logarithms originating from the gap between the photon mass and the weak scale are instead collected in a pure electromagnetic contribution. Finally, the logarithms originating from the gap between $M_Z$ and $M_W$ are of minor importance and are collected together.

The second consequence is the presence of longitudinal gauge bosons as physical states. These bosons are not present in a symmetric gauge theory, since they represent a characteristic feature of spontaneous symmetry breaking, arising in the Higgs mechanism together with the Higgs boson. In the high-energy limit, above the EWSB scale, longitudinal gauge bosons are related to the unphysical components of the scalar doublet, the Goldstone bosons, by means of the Goldstone-boson equivalence theorem, that will be treated in Sec. 3.3.

In the following sections we summarize the formalism and the results obtained in refs. [8, 9] for the description of the high-energy limit of electroweak one-loop corrections. We first fix

the notation and introduce some concepts useful to derive the universal formulae that describe the Sudakov limit. Then, we report these process-independent correction factors.

## 3.2 Structure of the Sudakov logarithms

We begin by fixing some conventions and notations. The particles involved in a process can be fermions, scalar particles and gauge bosons. Chiral fermions and antifermions are denoted by $f^j_{\kappa,\sigma}$ and $\bar{f}^j_{\kappa,\sigma}$, where $\kappa = L, R$ stands for the chirality, $\sigma = \pm$ denotes the weak isospin, $j = 1, 2, 3$ corresponds to the fermion generation and $f = Q, L$ distinguishes between quarks and leptons. Gauge bosons are denoted by $V^a = A, Z, W^\pm$, and they can be transversely ($V^a_T$) or longitudinally ($V^a_L$) polarized. Finally, scalar particles are denoted by $\Phi_i = H, \chi, \phi^\pm$. $H$ is the Higgs boson, while $\chi$ and $\phi^\pm$ are the Goldstone bosons, that can be used to treat processes with longitudinally polarized gauge bosons ($Z_L, W^\pm_L$) by the Goldstone-boson equivalence theorem. All of these fields are labeled by $\varphi_i$.

We now consider an arbitrary process involving $m$ incoming and $n-m$ outgoing particles with momenta $\tilde{p}_i$,

$$\varphi_1(\tilde{p}_1)\dots\varphi_m(\tilde{p}_m) \to \varphi_{m+1}(\tilde{p}_{m+1})\dots\varphi_n(\tilde{p}_n). \tag{3.1}$$

As a convention we deal with all particles incoming, so that the process can be written as

$$\varphi_1(\tilde{p}_1)\dots\varphi_m(\tilde{p}_m)\,\bar{\varphi}_{m+1}(-\tilde{p}_{m+1})\dots\bar{\varphi}_n(-\tilde{p}_n) \to 0, \tag{3.2}$$

i.e. substituting outgoing particles with the corresponding incoming antiparticles, and reversing their momenta.

Defining now $p_i \equiv \tilde{p}_i$ if the i-th particle in eq. (3.1) is incoming, $p_i \equiv -\tilde{p}_i$ if it is outgoing, the process (3.2) can be written as

$$\varphi_1(p_1)\dots\varphi_m(p_m)\,\bar{\varphi}_{m+1}(p_{m+1})\dots\bar{\varphi}_n(p_n) \to 0, \tag{3.3}$$

and for the matrix element we have

$$\mathcal{M}^{\varphi_1\dots\varphi_n}(p_1\dots p_n) = G^{\underline{\varphi}_1\dots\underline{\varphi}_n}(p_1\dots p_n)\prod_{j=1}^{n} v_{\varphi_j}(p_j). \tag{3.4}$$

The function $G$ is the Green function associated to the process, and the fact that its elements are underlined means that the external legs are truncated. This function is then contracted with the wave functions $v_{\varphi_j}(p_j)$ of the external particles: these are the Dirac spinors if the external particle is a fermion, the polarization vectors for gauge bosons, and 1 if the external particles are scalars.

In order to reach the Sudakov limit, we focus on the following kinematic region: we consider the external legs on shell, and all the other kinematic invariants much larger than the electroweak scale,

$$\left(\sum_{i=1}^{N} p_i\right)^2 \sim s \gg M_W^2, \qquad 1 < N < n-1. \tag{3.5}$$

This request corresponds to a high center-of-mass energy and considerable scattering angles: in this region the matrix elements can be expanded in the small parameters $M_i/\sqrt{s} \ll 1$, where the various $M_i$ represent the mass scales that enter the process. In order to consider

only matrix elements that are not mass-suppressed, we restrict ourselves to the ones that at leading order scale as

$$\mathcal{M}_0^{\varphi_1\dots\varphi_n}(p_1\dots p_n) \sim E^d, \tag{3.6}$$

being $d$ the mass dimension of the matrix element. For the one-loop corrections, defining

$$|r_{kl}| = |(p_k + p_l)^2| \sim |2p_k \cdot p_l| \gg M_W^2, \tag{3.7}$$

we consider only double- and single-logarithmic corrections of order

$$\begin{aligned} \delta^{\mathrm{DL}}\mathcal{M}^{\varphi_1\dots\varphi_n}(p_1\dots p_n) &\sim E^d L, \\ \delta^{\mathrm{SL}}\mathcal{M}^{\varphi_1\dots\varphi_n}(p_1\dots p_n) &\sim E^d l, \end{aligned} \tag{3.8}$$

where $L$ and $l$ are the double and single logarithms

$$L = L(|r_{kl}|, M_i^2) \equiv \frac{\alpha}{4\pi}\log^2\frac{|r_{kl}|}{M_i^2}, \qquad l = l(|r_{kl}|, M_i^2) \equiv \frac{\alpha}{4\pi}\log\frac{|r_{kl}|}{M_i^2}. \tag{3.9}$$

In this way, we neglect contributions of order $M_W^n\, E^{d-n} L$, $M_W^n\, E^{d-n}\, l$ and $\alpha E^d$, the latter because they are constant with respect to the leading-order matrix element.

In order to make the results as symmetric as possible we relate the energy-dependent part of the logarithms to the scales $s$ and $M_W$. We then write all the logarithms in terms of

$$L(s) \equiv L(s, M_W^2) = \frac{\alpha}{4\pi}\log^2\frac{s}{M_W^2}, \qquad l(s) \equiv l(s, M_W^2) = \frac{\alpha}{4\pi}\log\frac{s}{M_W^2}, \tag{3.10}$$

and logarithms of mass ratios and ratios of invariants. Finally, we collect together all the double-logarithmic contributions proportional to $L(s)$ and $l(s)\log(|r_{kl}|/s)$, and the single-logarithmic contributions proportional to $l(s)$, that make up the main part of the corrections. They can be thought of as the part of the corrections that originates from above the electroweak scale.

We do not include $\alpha\log(M_Z^2/M_W^2)$ terms, since $M_W \sim M_Z$, apart from the contributions proportional to $l(s)\log(M_Z^2/M_W^2)$ which grow with the energy. We also neglect pure angular contributions of type $\alpha\log^2(|r_{kl}|/s)$ and $\alpha\log(|r_{kl}|/s)$, since, in the Sudakov limit, all the kinematic invariants are of the order of $s$.

In this limit, it has been shown in refs. [8–10] that the virtual one-loop corrections assume the general form

$$\begin{aligned} \delta\mathcal{M}^{\varphi_1\dots\varphi_n}(\{\lambda_i\},\, p_1\dots p_n) &= \sum_{\lambda_i} \delta\lambda_i \,\frac{\partial\mathcal{M}_0^{\varphi_1\dots\varphi_n}}{\partial\lambda_i}(\{\lambda_i\},\, p_1\dots p_n) \\ &+ \sum_{\varphi_{1'}\dots\varphi_{n'}} \mathcal{M}_0^{\varphi_{1'}\dots\varphi_{n'}}(\{\lambda_i\},\, p_1\dots p_n)\, \delta^{\varphi_1\dots\varphi_n}_{\varphi_{1'}\dots\varphi_{n'}}(\{\lambda_i\},\, p_1\dots p_n). \end{aligned} \tag{3.11}$$

The first term is the contribution related to the renormalization $\delta\lambda_i$ of the dimensionless parameters $\lambda_i$ that appear in the matrix element. The second term contains contributions that factorize in momentum space into leading-order matrix elements multiplied by universal correction factors, $\delta^{\varphi_1\dots\varphi_n}_{\varphi_{1'}\dots\varphi_{n'}}$. These are tensors with $\mathrm{SU}(2) \times \mathrm{U}(1)$ indices that can be associated to single external particles or to pairs of them. The dimensionless correction factors, together with the running of the coupling constants, can be evaluated in a completely process-independent way keeping the dominant $L(s)$ and $l(s)$ terms. The SU(2) transformed matrix elements $\mathcal{M}_0^{\varphi_{1'}\dots\varphi_{n'}}$, instead, are process-dependent.

It can be proven [8] that mass singularities arise in one-loop diagrams from a restricted set of Feynman diagrams, in specific regions of the loop momentum, namely from diagrams with virtual gauge bosons coupled to the external legs in the momentum regions in which these bosons are soft and/or collinear to the external legs. The factorization of these contributions is a consequence of gauge symmetry, in particular of the charge-conservation relations and the Ward identities of the electroweak theory. The result is a set of logarithmic corrections that, grouped together, take the form

$$\delta\mathcal{M} = \delta^{\mathrm{LSC}}\mathcal{M} + \delta^{\mathrm{SSC}}\mathcal{M} + \delta^{\mathrm{C}}\mathcal{M} + \delta^{\mathrm{PR}}\mathcal{M}. \tag{3.12}$$

The first two terms correspond to the double-logarithmic contributions: they originate from one-loop diagrams in which soft-collinear gauge bosons are exchanged between pairs of external legs. The leading part $\delta^{\mathrm{LSC}}$ consists of angular-independent double logarithms like $L(s)$, while the subleading part $\delta^{\mathrm{SSC}}$ contains the angular-dependent contributions proportional to $l(s)\log(|r_{kl}|/s)$. The other terms are instead single-logarithmic contributions. The factor $\delta^{\mathrm{C}}$ contains collinear or soft single logarithms, originating from the renormalization of the asymptotic fields, from corrections to processes involving longitudinal gauge bosons, and from the emission of collinear virtual gauge bosons from the external legs. $\delta^{\mathrm{PR}}$ collects instead the contributions of ultraviolet origin, related to the renormalization of the dimensionless parameters.

These NLL corrections can be further grouped in $\delta^{\mathrm{DL}} = \delta^{\mathrm{LSC}} + \delta^{\mathrm{SSC}}$ and in $\delta^{\mathrm{SL}} = \delta^{\mathrm{C}} + \delta^{\mathrm{PR}}$. In the following sections we report the analytic formulae for these correction factors. In the derivation of the results, some group-theoretical quantities are involved, such as the electric charge $Q$ of the external particles, their weak isospin $T^a$, or the electroweak Casimir $C^{\mathrm{ew}}$: their values can be found in App. A. We introduce some shorthand notations: with $s_W$ and $c_W$ we refer to $\sin\theta_W$ and $\cos\theta_W$, respectively, where $\theta_W$ is the Weinberg angle.

## 3.3 The Goldstone-boson equivalence theorem

In order to obtain the structure of eq. (3.12) for the one-loop electroweak corrections, one of the fundamental requests is to neglect mass-suppressed matrix elements. However, this approach is not applicable to processes that involve longitudinal gauge bosons $V_L^a = Z_L, W_L^{\pm}$. To understand the reason, we consider a process with a longitudinal gauge boson and $n$ other external particles,

$$V_L^a(q)\,\varphi_1(p_1)\ldots\varphi_n(p_n) \to 0. \tag{3.13}$$

The matrix element is given by

$$\mathcal{M}^{V_L^a\varphi_1\ldots\varphi_n}(q,\,p_1\ldots p_n) = \epsilon_L^{\mu}(q)\,G_{\mu}^{\underline{V_L^a}\,\underline{\varphi}_1\cdots\underline{\varphi}_n}(q,\,p_1\ldots p_n)\prod_{j=1}^{n} v_{\varphi_j}(p_j), \tag{3.14}$$

in which the amputated Green function $G$ is contracted with the Dirac spinors and with the longitudinal polarization vector

$$\epsilon_L^{\mu}(q) = \frac{q^{\mu}}{M_{V^a}} + \mathcal{O}\left(\frac{M_{V^a}}{q^0}\right), \tag{3.15}$$

with $q^0 = E_{V^a} \gg M_{V^a}$. We immediately see that the matrix element contains mass terms in the denominator: in this case, then, it appears clear that the contributions of order $M_{V^a}^n\,E^{d-n}$ cannot be neglected.

However, in the high-energy limit the dominant part of the longitudinal polarization vector is proportional to the momentum of the gauge boson: for this reason the matrix element can be simplified using the electroweak Ward identities. These relations connect amputated Green functions involving longitudinal gauge bosons with amputated Green functions involving the corresponding Goldstone bosons. The result is the Goldstone-boson equivalence theorem (GBET) [95, 96], and can be stated as

$$\mathcal{M}^{V_L^a\,\varphi_1\dots\varphi_n}(q,p_1\dots p_n) = i^{(1-Q_{V^a})}A^{V^a}\mathcal{M}^{\Phi_a\,\varphi_1\dots\varphi_n}(q,p_1\dots p_n) + \mathcal{O}\left(ME^{d-1}\right). \tag{3.16}$$

The factor

$$A^{V^a} = 1 + \delta A^{V^a} \tag{3.17}$$

consists of a trivial lowest-order contribution and a loop part, that enters the computation of the single-logarithmic corrections associated to the external particles, contained in $\delta^{\mathrm{C}}$.

In 1985 this theorem was generalized to matrix elements involving more than one longitudinal boson. The proof can be found in ref. [97], the result is that the substitution of eq. (3.16) applies to each of the $m$ bosons involved, and the original matrix element becomes

$$\begin{aligned}\mathcal{M}^{V_L^{a_1}\dots V_L^{a_m}\,\varphi_1\dots\varphi_n}(q_1\dots q_m,\,p_1\dots p_n) &= \prod_{k=1}^{m} i^{(1-Q_{V^{a_k}})}A^{V^{a_k}} \\ &\times \mathcal{M}^{\Phi_{a_1}\dots\Phi_{a_m}\,\varphi_1\dots\varphi_n}(q_1\dots q_m,\,p_1\dots p_n) + \mathcal{O}\left(ME^{d-1}\right).\end{aligned} \tag{3.18}$$

Thanks to this theorem, at leading order the matrix element can be rewritten as

$$\mathcal{M}_0^{V_L^{a_1}\dots V_L^{a_m}\,\varphi_1\dots\varphi_n} = \prod_{k=1}^{m} i^{(1-Q_{V^{a_k}})}\mathcal{M}_0^{\Phi_{a_1}\dots\Phi_{a_m}\,\varphi_1\dots\varphi_n} + \mathcal{O}\left(ME^{d-1}\right), \tag{3.19}$$

while the one-loop corrections split up into two parts, as

$$\delta\mathcal{M}^{V_L^{a_1}\dots V_L^{a_m}\,\varphi_1\dots\varphi_n} = \sum_{k=1}^{m}\delta A^{V^{a_k}}\mathcal{M}_0^{V_L^{a_1}\dots V_L^{a_m}\,\varphi_1\dots\varphi_n} + \prod_{k=1}^{m} i^{(1-Q_{V^{a_k}})}\delta\mathcal{M}^{\Phi_{a_1}\dots\Phi_{a_m}\,\varphi_1\dots\varphi_n}, \tag{3.20}$$

which means that the corrections to the GBET are combined with the corrections to the matrix element involving Goldstone bosons.

## 3.4 Double-logarithmic corrections

The double-logarithmic corrections originate from those loop diagrams in which virtual gauge bosons $V^a = A, Z, W^\pm$ are exchanged between pairs of external legs. The logarithmic contributions come from the integration region in which the exchanged bosons are soft and collinear to one of the external particles. Like in QCD, the integrals can be computed using the eikonal approximation, that consists in neglecting all mass terms and setting the momentum of the gauge boson to zero. It can be shown that these contributions are the only ones that are not mass-suppressed in the eikonal limit: for example, the exchange of a fermion between two external lines would give a suppressed contribution due to the Dirac equation for the fermionic spinor and to the identity $\not{p}^2 = p^2 = m_f^2$, that introduces a mass term in the matrix element.

The detailed derivation of the results can be found in ref. [8]. Here we sketch the procedure and list the resulting formulae. Considering the exchange of a virtual gauge boson $V^a$ between

two external legs $k$ and $l$, the one-loop corrections evaluated in eikonal approximation turn out to be

$$\begin{aligned}\delta^{\rm DL}\mathcal{M}^{\varphi_1\dots\varphi_n} &= \sum_{k=1}^{n}\sum_{l<k}\sum_{V^a=A,\,Z,\,W^\pm}\sum_{\varphi_{k'},\,\varphi_{l'}} I^{V^a}_{\varphi_{k'}\varphi_k}\, I^{\bar V^a}_{\varphi_{l'}\varphi_l}\,\mathcal{M}_0^{\varphi_1\dots\varphi_{k'}\dots\varphi_{l'}\dots\varphi_n} \\ &\quad\times\frac{\alpha}{4\pi}\left[\log^2\frac{|r_{kl}|}{M^2_{V^a}}+2\sum_{m=k,\,l} I_C(M_{\varphi_m},M_{V^a},M_{\varphi_{m'}})\right],\end{aligned} \tag{3.21}$$

where the integral

$$I_C(M_1,M_{V^a},M_2)=-\int_0^1\frac{dx}{x}\,\log\left(1+\frac{M_2^2-M_{V^a}^2-M_1^2}{M_{V^a}^2-i\epsilon}\,x+\frac{M_1^2}{M_{V^a}^2-i\epsilon}\,x^2\right) \tag{3.22}$$

gives large logarithms only if the mass of the soft gauge boson $V^a$ is much smaller than one of the other masses. This happens in the case of photon exchange diagrams, and with weak-boson exchanges in which one of the particles $\varphi_m,\varphi_{m'}$ is a top quark or a Higgs boson.

The eikonal approximation applies to external chiral fermions, transverse gauge bosons and Higgs bosons. Because of the longitudinal polarization vectors, matrix elements involving longitudinal gauge bosons have to be expressed in terms of matrix elements involving the corresponding Goldstone bosons, using the GBET, according to eq. (3.19). Since the one-loop corrections to the GBET do not involve double-logarithmic contributions, we can apply this theorem in its leading-order form,

$$\delta^{\rm DL}\mathcal{M}^{V_L^{a_1}\dots V_L^{a_m}\,\varphi_1\dots\varphi_n}=\prod_{k=1}^{m} i^{(1-Q_{V^{a_k}})}\delta^{\rm DL}\mathcal{M}^{\Phi_{a_1}\dots\Phi_{a_m}\,\varphi_1\dots\varphi_n}. \tag{3.23}$$

By inspecting eq. (3.21) we note that the $\log^2(|r_{kl}|/M^2_{V^a})$ terms are angular-dependent, since they contain the invariant $r_{kl}$. In order to make the result as symmetric as possible, we can split these contributions into

$$\log^2\frac{|r_{kl}|}{M^2_{V^a}}=\log^2\frac{s}{M^2_{V^a}}+2\log\frac{s}{M^2_{V^a}}\log\frac{|r_{kl}|}{s}+\log^2\frac{|r_{kl}|}{s}. \tag{3.24}$$

The last term can be neglected if all the invariants are of the same order. In this way we can separate the leading soft-collinear contributions from the subleading ones, that depend upon the angles between the involved momenta.

### 3.4.1 Leading soft-collinear contributions

Using some charge-conservation relations in the high-energy limit, that follow from the SU(2) × U(1) global symmetry, the angular-independent leading soft-collinear corrections in eq. (3.21) can be written as a single sum over external legs. Evaluating the sum over the gauge bosons, and keeping the angular-independent part in eq. (3.24), these corrections become

$$\delta^{\rm LSC}\mathcal{M}^{\varphi_1\dots\varphi_n}=\sum_{k=1}^{n}\sum_{\varphi_{k'}}\delta^{\rm LSC}_{\varphi_{k'}\varphi_k}\,\mathcal{M}_0^{\varphi_1\dots\varphi_{k'}\dots\varphi_n}, \tag{3.25}$$

in which the correction factors take the form

$$\begin{aligned}\delta^{\rm LSC}_{\varphi_{k'}\varphi_k} &= -\frac{\alpha}{8\pi}C^{\rm ew}_{\varphi_{k'}\varphi_k}\log^2\frac{s}{M_W^2}+\delta_{\varphi_{k'}\varphi_k}\left[\frac{\alpha}{4\pi}(I^Z_{\varphi_k})^2\log\frac{s}{M_W^2}\log\frac{M_Z^2}{M_W^2}\right. \\ &\quad\left.+\delta^{\rm LSC,h}_{\varphi_k}-\frac{1}{2}Q^2_{\varphi_k}L_{\rm em}(s,\lambda^2,m^2_{\varphi_k})\right].\end{aligned} \tag{3.26}$$

The first term represents the double-logarithmic symmetric electroweak part, proportional to the electroweak Casimir $C^{\text{ew}}$ that can be found in eq. (A.13). This term is always negative, and diagonal except in the case of neutral gauge bosons, where some mixing happens due to the non-diagonal components $C^{\text{ew}}_{AZ}$ and $C^{\text{ew}}_{ZA}$. The factor

$$L_{\text{em}}(s,\lambda^2,m_\varphi^2) = \frac{\alpha}{4\pi}\left[2\log\frac{s}{M_W^2}\log\frac{M_W^2}{\lambda^2} + \log^2\frac{M_W^2}{\lambda^2} - \log^2\frac{m_\varphi^2}{\lambda^2}\right] \tag{3.27}$$

contains logarithms of electromagnetic origin, that diverge when taking the limit of the photon mass $\lambda \to 0$. Finally, $\delta^{\text{LSC,h}}_{\varphi_k}$ is relevant only if one of the particles $\varphi_k$, $\varphi_{k'}$ is a heavy quark, a Higgs boson or a longitudinal gauge boson:

$$\delta^{\text{LSC,h}}_{t_L} = \frac{\alpha}{4\pi}\left[\frac{(3c_W^2 - s_W^2)^2}{72 s_W^2 c_W^2}\log^2\frac{m_t^2}{M_Z^2} + \frac{1}{2s_W^2}\log^2\frac{m_t^2}{M_W^2}\right], \tag{3.28}$$

$$\delta^{\text{LSC,h}}_{b_\kappa} = \delta_{\kappa L}\frac{\alpha}{4\pi}\frac{1}{2s_W^2}\log^2\frac{m_t^2}{M_W^2}, \tag{3.29}$$

$$\delta^{\text{LSC,h}}_{t_R} = \frac{\alpha}{4\pi}\frac{2s_W^2}{9c_W^2}\log^2\frac{m_t^2}{M_Z^2}, \tag{3.30}$$

$$\delta^{\text{LSC,h}}_{H} = \frac{\alpha}{4\pi}\left[\frac{1}{4s_W^2 c_W^2}\log^2\frac{M_H^2}{M_Z^2} + \frac{1}{2s_W^2}\log^2\frac{M_H^2}{M_W^2}\right], \tag{3.31}$$

$$\delta^{\text{LSC,h}}_{\phi^\pm} = \frac{\alpha}{4\pi}\frac{1}{4s_W^2}\log^2\frac{M_H^2}{M_W^2}, \tag{3.32}$$

$$\delta^{\text{LSC,h}}_{\chi} = \frac{\alpha}{4\pi}\frac{1}{4s_W^2 c_W^2}\log^2\frac{M_H^2}{M_Z^2}. \tag{3.33}$$

### 3.4.2 Subleading soft-collinear contributions

The second term of eq. (3.24) maintains a sum over the possible pairs of external legs, and constitutes the subleading part of the corrections,

$$\delta^{\text{SSC}}\mathcal{M}^{\varphi_1\dots\varphi_n} = \sum_{k=1}^{n}\sum_{l<k}\sum_{V^a=A,Z,W^\pm}\sum_{\varphi_{k'},\,\varphi_{l'}}\delta^{V^a,\,\text{SSC}}_{\varphi_{k'}\varphi_k\varphi_{l'}\varphi_l}\,\mathcal{M}_0^{\varphi_1\dots\varphi_{k'}\dots\varphi_{l'}\dots\varphi_n}. \tag{3.34}$$

The contributions from the various gauge bosons are:

$$\delta^{A,\,\text{SSC}}_{\varphi_{k'}\varphi_k\varphi_{l'}\varphi_l} = \frac{\alpha}{2\pi}\left[\log\frac{s}{M_W^2} + \log\frac{M_W^2}{\lambda^2}\right]\log\frac{|r_{kl}|}{s}\,I^A_{\varphi_{k'}\varphi_k}\,I^A_{\varphi_{l'}\varphi_l}, \tag{3.35}$$

$$\delta^{Z,\,\text{SSC}}_{\varphi_{k'}\varphi_k\varphi_{l'}\varphi_l} = \frac{\alpha}{2\pi}\log\frac{s}{M_W^2}\log\frac{|r_{kl}|}{s}\,I^Z_{\varphi_{k'}\varphi_k}\,I^Z_{\varphi_{l'}\varphi_l}, \tag{3.36}$$

$$\delta^{W^\pm,\,\text{SSC}}_{\varphi_{k'}\varphi_k\varphi_{l'}\varphi_l} = \frac{\alpha}{2\pi}\log\frac{s}{M_W^2}\log\frac{|r_{kl}|}{s}\,I^\pm_{\varphi_{k'}\varphi_k}\,I^\mp_{\varphi_{l'}\varphi_l}. \tag{3.37}$$

The couplings $I^A$ and $I^Z$ are diagonal, except for $I^Z$ in the neutral scalar sector $(H,\chi)$: this means that also these corrections generally factorize over the original Born matrix element. For the exchange of $W^\pm$ bosons, owing to the non-diagonal matrices $I^\pm$, some contributions coming from SU(2)-transformed Born matrix elements appear. They are generally not related to the original Born matrix element and have to be evaluated explicitly.

## 3.5 Single-logarithmic corrections

The corrections with a single-logarithmic structure originate from the renormalization of the asymptotic states, from the corrections to the GBET, from mass-singular loop diagrams in which a collinear virtual gauge boson is emitted and from the renormalization of the dimensionless parameters that appear in the matrix element. In the derivation of these results, we exploit the renormalization-scale independence of the $S$ matrix and we set the dimensional-regularization scale to $\mu^2 = s$, so that only mass-singular logarithms of type $\log(\mu^2/M_W^2)$ and $\log(s/M_W^2)$ are large.

### 3.5.1 Corrections associated to external particles

The first part of these corrections comes from the collinear limit of loop diagrams in which an external line splits into two internal lines. In this case too, following ref. [8] it can be proven that, in the collinear approximation, we obtain contributions that are not mass-suppressed only if at least one of the internal lines after the splitting is a gauge boson.

These corrections must be added to the mass singularities that originate from the renormalization of the asymptotic fields and from the corrections to the GBET. The contributions associated to external fermions, transverse gauge bosons and Higgs bosons are given by the known field-renormalization constants (FRCs), $\delta Z_{\varphi_k}/2$ for each external leg. For longitudinal gauge bosons, together with the FRCs, we also have to consider the corrections to the GBET $\delta A^{V^a}$ as in eq. (3.17).

The FRCs are fixed such that the fields do not mix and the residua of renormalized propagators are equal to one: this means that the renormalized fields correspond to physical fields, and no extra wave function renormalization constants are required. For this reason the wave function renormalization factors that usually appear on the right-hand side of eq. (3.4) are set to 1.

Taking care of the double counting (for example we have to subtract the soft-collinear part of the result, already included in $\delta^{\mathrm{LSC}}$), also these single-logarithmic contributions can be written as a sum over the external legs,

$$\delta^{\mathrm{C}}\mathcal{M}^{\varphi_1\cdots\varphi_n} = \sum_{k=1}^{n}\sum_{\varphi_{k'}} \delta^{\mathrm{C}}_{\varphi_{k'}\varphi_k}\,\mathcal{M}_0^{\varphi_1\cdots\varphi_{k'}\cdots\varphi_n}, \tag{3.38}$$

with

$$\delta^{\mathrm{C}}_{\varphi_{k'}\varphi_k} = \left(\delta^{\mathrm{WF}}_{\varphi_{k'}\varphi_k} + \delta^{\mathrm{coll}}_{\varphi_{k'}\varphi_k}\right)\Big|_{\mu^2=s}. \tag{3.39}$$

For external Higgs bosons the correction factor reads

$$\delta^{\mathrm{C}}_{HH} = \frac{\alpha}{4\pi}\left[2C^{\mathrm{ew}}_{\Phi}\left(\log\frac{s}{M_W^2} - \log\frac{M_H^2}{M_W^2}\right) - \frac{3}{4s_W^2}\frac{m_t^2}{M_W^2}\left(\log\frac{s}{M_W^2} - \log\frac{m_t^2}{M_W^2}\right)\right]. \tag{3.40}$$

For transverse gauge bosons, instead, we obtain

$$\begin{aligned}\delta^{\mathrm{C}}_{V_T^aV_T^b} = \frac{\alpha}{4\pi}\Bigg[&\frac{1}{2}\left(b^{\mathrm{ew}}_{V^aV^b} + b^{\mathrm{ew}}_{AZ}\,E_{V^aV^b}\right)\log\frac{s}{M_W^2} + \delta_{V^aV^b}\,Q^2_{V^a}\,\log\frac{M_W^2}{\lambda^2}\\ &+ \delta_{V^aV^b}\frac{M^2_{V^a}}{24s_W^2M_W^2}\log\frac{M_H^2}{M_W^2} + T_{V^aV^b}\log\frac{m_t^2}{M_W^2}\Bigg] - \frac{1}{2}\delta_{V^aA}\delta_{V^bA}\,\Delta\alpha(M_W^2).\end{aligned} \tag{3.41}$$

The factors $b^{\mathrm{ew}}_{V^aV^b}$ are given in eqs. (A.36) - (A.39), $E_{V^aV^b}$ is non-vanishing only for the neutral gauge-boson combinations $E_{AZ} = -E_{ZA} = 1$, and the last term $\Delta\alpha(M_W^2)$ corresponds

to the running of the electromagnetic coupling constant from zero momentum transfer to the scale $M_W$,

$$\Delta\alpha(M_W^2) = \frac{\alpha}{3\pi} \sum_{f_\sigma^j \neq t} N_C^f \, Q_{f_\sigma^j}^2 \, \log \frac{M_W^2}{m_{f_\sigma^j}^2}. \tag{3.42}$$

The sum runs over the generations $j = 1, 2, 3$ of leptons and quarks with isospin $\sigma = \pm$, omitting the top quark, and $N_C^f$ is the colour factor. $T_{V^a V^a}$ has components

$$\begin{aligned} T_{WW} &= \frac{1}{2s_W^2}, & T_{ZA} &= 0, & T_{AA} &= \frac{8}{9}, \\ T_{ZZ} &= \frac{9 - 24s_W^2 + 32s_W^4}{36 s_W^2 c_W^2}, & T_{AZ} &= \frac{16s_W^2 - 6}{9 s_W c_W}. \end{aligned} \tag{3.43}$$

The correction factor for external chiral fermions is

$$\delta^{\mathrm{C}}_{f^{j'}_{\kappa,\sigma'} f^j_{\kappa,\sigma}} = \delta_{j'j}\delta_{\sigma'\sigma} \left\{ \frac{\alpha}{4\pi} \left[ \frac{3}{2} C^{\mathrm{ew}}_{f^j_{\kappa,\sigma}} \log \frac{s}{M_W^2} + Q^2_{f^j_{\kappa,\sigma}} \left( \frac{1}{2} \log \frac{M_W^2}{m_f^2} + \log \frac{M_W^2}{\lambda^2} \right) \right] + \delta^{\mathrm{C,h}}_{f^j_{\kappa,\sigma}} \right\}, \tag{3.44}$$

in which the term $\delta^{\mathrm{C,h}}_{f^j_{\kappa,\sigma}}$ is relevant only for external heavy quarks,

$$\delta^{\mathrm{C,h}}_{t_L} = \frac{1}{8s_W^2} \left[ - l(s) \, \frac{m_t^2}{M_W^2} + \frac{\alpha}{4\pi} \log \frac{m_t^2}{M_W^2} \left( \frac{m_t^2}{M_W^2} - \frac{16c_W^4 + 10c_W^2 + 1}{3c_W^2} \right) \right], \tag{3.45}$$

$$\delta^{\mathrm{C,h}}_{t_R} = - l(s) \, \frac{m_t^2}{4s_W^2 M_W^2} + \frac{\alpha}{4\pi} \log \frac{m_t^2}{M_W^2} \left( \frac{m_t^2}{4s_W^2 M_W^2} - \frac{2s_W^2}{3c_W^2} \right), \tag{3.46}$$

$$\delta^{\mathrm{C,h}}_{b_\kappa} = \frac{\delta_{\kappa L}}{8s_W^2} \left[ - l(s) \, \frac{m_t^2}{M_W^2} + \frac{\alpha}{4\pi} \log \frac{m_t^2}{M_W^2} \left( \frac{m_t^2}{M_W^2} - 6 \right) \right]. \tag{3.47}$$

Finally, for longitudinal gauge bosons we have

$$\begin{aligned} \delta^{\mathrm{C}}_{V_L^{a\prime} V_L^a} \;=\; & \delta_{V^{a\prime} V^a} \frac{\alpha}{4\pi} \left[ 2C^{\mathrm{ew}}_{\Phi} \log \frac{s}{M_W^2} - \frac{3}{4s_W^2} \frac{m_t^2}{M_W^2} \left( \log \frac{s}{M_W^2} - \log \frac{m_t^2}{M_W^2} \right) \right. \\ & \left. + \frac{M_{V^a}^2}{8 s_W^2 M_W^2} \log \frac{M_H^2}{M_W^2} + Q^2_{V^a} \log \frac{M_W^2}{\lambda^2} \right]. \end{aligned} \tag{3.48}$$

### 3.5.2 Logarithms from parameter renormalization

The last source of logarithmic corrections comes from the renormalization of the parameters that appear in the considered matrix element. These corrections can be obtained from

$$\delta^{\mathrm{PR}} \mathcal{M}^{\varphi_1 \ldots \varphi_n} = \sum_{\lambda_i} \frac{\partial \mathcal{M}_0^{\varphi_1 \ldots \varphi_n}}{\partial \lambda_i} \, \delta\lambda_i \Bigg|_{\mu^2 = s}, \tag{3.49}$$

where $\delta\lambda_i$ are the counterterms that renormalize the bare parameters $\lambda_i$,

$$\lambda_{i,0} = \lambda_i + \delta\lambda_i. \tag{3.50}$$

At high energies and for matrix elements that are not mass-suppressed, the running of the masses in the propagators or in couplings with mass dimension gives only mass-suppressed

contributions. For this reason, we can restrict ourselves to the running of the dimensionless parameters $\lambda_i = g_1, g_2, \lambda_H, \lambda_t$, i.e. the gauge couplings $g_1, g_2$, the Higgs self-coupling $\lambda_H$ and the top-quark Yukawa coupling $\lambda_t$. They represent a convenient set of independent parameters to describe electroweak processes at high energies, but they are not directly related to observable quantities. We then use the parameters $\lambda_i = e, c_W, h_H, h_t$, that involve the electric charge $e$, the cosine of the Weinberg angle $c_W$ and two mass ratios $h_H = M_H^2/M_W^2$ and $h_t = m_t/M_W$. For the renormalization of these parameters the on-shell scheme is adopted [98]. The electric charge is defined in the Thomson limit of Compton scattering, the masses of the gauge bosons and of the top quark are defined as the poles of the propagators of the corresponding physical fields and the Weinberg angle is fixed by $c_W = M_W/M_Z$.

After the parameters have been renormalized, they can be translated into the original set of parameters by the following relations:

$$g_1 = \frac{e}{c_W}, \qquad g_2 = \frac{e}{s_W}, \qquad \lambda_H = \frac{e^2}{2s_W^2}\, h_H, \qquad \lambda_t = \frac{e}{\sqrt{2}s_W}\, h_t. \tag{3.51}$$

The relations for the corresponding counterterms, instead, are

$$\frac{\delta g_1}{g_1} = \frac{\delta e}{e} - \frac{1}{2}\frac{\delta c_W^2}{c_W^2}, \tag{3.52}$$

$$\frac{\delta g_2}{g_2} = \frac{\delta e}{e} - \frac{1}{2}\frac{\delta s_W^2}{s_W^2} = \frac{\delta e}{e} + \frac{c_W^2}{2s_W^2}\frac{\delta c_W^2}{c_W^2}, \tag{3.53}$$

$$\frac{\delta \lambda_H}{\lambda_H} = 2\frac{\delta g_2}{g_2} + \frac{\delta h_H^{\text{eff}}}{h_H}, \tag{3.54}$$

$$\frac{\delta \lambda_t}{\lambda_t} = \frac{\delta g_2}{g_2} + \frac{\delta h_t}{h_t}. \tag{3.55}$$

In the third relation additional effects originating from tadpole renormalization have been absorbed into a redefinition of the counterterm $\delta h_H \to \delta h_H^{\text{eff}}$.

We now list the counterterms for the physical set of parameters, from which one can obtain the single-logarithmic corrections to the desired process according to eq. (3.49):

$$\frac{\delta e}{e} = \frac{1}{2}\left[-\frac{\alpha}{4\pi} b_{AA}^{\text{ew}} \log\frac{\mu^2}{M_W^2} + \Delta\alpha(M_W^2)\right], \tag{3.56}$$

$$\begin{aligned}\frac{\delta c_W^2}{c_W^2} &= \frac{\delta M_W^2}{M_W^2} - \frac{\delta M_Z^2}{M_Z^2} \\ &= \frac{\alpha}{4\pi}\left[\frac{s_W}{c_W} b_{AZ}^{\text{ew}} \log\frac{\mu^2}{M_W^2} + \frac{5}{6c_W^2}\log\frac{M_H^2}{M_W^2} - \frac{9 + 6s_W^2 - 32s_W^4}{18 s_W^2 c_W^2}\log\frac{m_t^2}{M_W^2}\right],\end{aligned} \tag{3.57}$$

$$\begin{aligned}\frac{\delta h_H^{\text{eff}}}{h_H} = \frac{\alpha}{4\pi}\Bigg\{&\left[b_{WW}^{\text{ew}} + \frac{3M_W^2}{s_W^2 M_H^2}\left(1 + \frac{1}{2c_W^4}\right) - 6C_\Phi^{\text{ew}}\right]\log\frac{\mu^2}{M_W^2} + \frac{N_C^t}{3s_W^2}\log\frac{m_t^2}{M_W^2} \\ &+ \frac{3M_H^2}{2s_W^2 M_W^2}\left(\log\frac{\mu^2}{M_W^2} - \log\frac{M_H^2}{M_W^2}\right) + \frac{N_C^t m_t^2}{s_W^2 M_W^2}\left(1 - 2\frac{m_t^2}{M_H^2}\right)\left(\log\frac{\mu^2}{M_W^2} - \log\frac{m_t^2}{M_W^2}\right) \\ &+ \left[\frac{3}{2}C_\Phi^{\text{ew}} + \frac{5}{6s_W^2} - \frac{9M_W^2}{2s_W^2 M_H^2}\left(1 + \frac{1}{2c_W^4}\right)\right]\log\frac{M_H^2}{M_W^2}\Bigg\}.\end{aligned} \tag{3.58}$$

$$\frac{\delta h_t}{h_t} = \frac{\alpha}{4\pi}\left\{\frac{1}{2}\,b^{\rm ew}_{WW}\,\log\frac{\mu^2}{M_W^2} + \left[\frac{3+2N_C^t}{8s_W^2}\,\frac{m_t^2}{M_W^2} - \frac{3}{2}\left(C^{\rm ew}_{t_L} + C^{\rm ew}_{t_R}\right)\right]\left(\log\frac{\mu^2}{M_W^2} - \log\frac{m_t^2}{M_W^2}\right) + \left(\frac{1}{2s_W^2} - 2C^{\rm ew}_{\Phi}\right)\log\frac{m_t^2}{M_W^2} + \frac{5}{12s_W^2}\log\frac{M_H^2}{M_W^2}\right\}, \tag{3.59}$$

The renormalization of the Weinberg angle is obtained combining the renormalization factors for the masses of the vector bosons,

$$\frac{\delta M^2_{V^a}}{M^2_{V^a}} = -\frac{\alpha}{4\pi}\left[(b^{\rm ew}_{V^aV^a} - 4C^{\rm ew}_{\Phi})\log\frac{\mu^2}{M_W^2} + \frac{N_C^t}{2s_W^2}\,\frac{m_t^2}{M_W^2}\left(\log\frac{\mu^2}{M_W^2} - \log\frac{m_t^2}{M_W^2}\right) + \frac{5M^2_{V^a}}{6s_W^2M_W^2}\log\frac{M_H^2}{M_W^2} + \frac{2N_C^t}{3}\,T_{V^aV^a}\log\frac{m_t^2}{M_W^2}\right]. \tag{3.60}$$

## 3.6 The leading-pole approximation

In order to derive the one-loop Sudakov electroweak corrections to the associated production of a Higgs boson and a vector boson that decays leptonically, plus eventually a jet, we must make some approximations that regard the virtualities of the particles involved. Denoting by $P_i = q, \bar{q}, g$ a generic parton, the leading-order process can be written as

$$P_1(p_1)\,P_2(p_2) \to H(p_3)\,V(k)\,\Big(P_6(p_6)\Big) \to H(p_3)\,l_1(p_4)\,\bar{l}_2(p_5)\Big(P_6(p_6)\Big), \tag{3.61}$$

where $k = p_4 + p_5$. In $HV$ production, $P_6$ is not present, and the two incoming partons are always a quark-antiquark pair. When considering $HVj$, instead, the additional gluon can be in both the initial or final state.

As outlined in ref. [99], the treatment of processes that involve the production and decay of unstable particles like the vector boson $V$ in eq. (3.61) poses some theoretical problems when considering gauge invariance. In fact, an intermediate gauge boson with momentum $k$ and mass $M_V$ can give rise to poles $1/(k^2 - M_V^2)$ if it is treated as a stable particle. This problem can be resolved by introducing the gauge boson decay width, i.e. by performing the replacement

$$\frac{1}{k^2 - M_V^2} \longrightarrow \frac{1}{k^2 - M_V^2 + i\Gamma_V M_V}. \tag{3.62}$$

The decay width arises naturally when resumming to all orders the imaginary parts of higher-order diagrams that describe the gauge boson self-energy. However, in performing this summation, only a restricted subset of diagrams is included. The results obtained considering incomplete higher-order contributions can thus violate the Ward identities of the theory or retain some gauge dependence.

One way to ensure gauge invariance is to use the pole scheme [99]: in this scheme the complete amplitude is decomposed by expanding it around the poles. Since the physically-observable residues of the poles are by themselves gauge invariant, gauge invariance is not broken if the finite width is taken into account in the pole terms, as in eq. (3.62). This procedure can be viewed as a gauge-invariant prescription for performing an expansion in powers of $\Gamma_V/M_V$. However, there is no unique definition of the residues, since their calculation involves a mapping of off-shell matrix elements with off-shell kinematics to on-shell matrix elements with restricted kinematics. The ambiguity comes from the fact that this mapping is not unique, since one has to specify the variables that must be kept fixed in the mapping. The resulting implementation dependence manifests itself in differences of order

$\mathcal{O}(\Gamma_V/M_V)$. However, when electroweak corrections are taken into account, these differences become subleading since they are multiplied by a factor $\alpha$. The intrinsic error associated to this procedure goes then below 0.1% except far off resonance, where the pole scheme cannot be viewed as an effective expansion in powers of $\Gamma_V/M_V$.

In order to apply the pole scheme to the associated production processes $HV$ and $HVj$, we write the propagator of the unstable gauge boson as a sum over the vector boson polarizations,

$$\frac{1}{k^2 - M_V^2 + i\Gamma_V M_V}\left(-g^{\mu\nu} + \frac{k^\mu k^\nu}{M_V^2}\right) = \sum_{\lambda=-1}^{1} \frac{\epsilon_\lambda^\mu(k)\,\epsilon_\lambda^{*\nu}(k)}{k^2 - M_V^2 + i\Gamma_V M_V}. \tag{3.63}$$

In this way the complete matrix element factorizes into the matrix element for the production of a Higgs boson and a vector boson (plus eventually a jet), multiplied by the intermediate fixed-width propagator and by the matrix element for the decay of the vector boson. This is called leading-pole approximation (LPA),

$$\mathcal{M}_{0,\mathrm{LPA}}^{P_1\bar{P}_2\to Hl_1\bar{l}_2(P_6)} = \frac{1}{k^2 - M_V^2 + i\Gamma_V M_V}\sum_\lambda \mathcal{M}_0^{P_1\bar{P}_2\to HV_\lambda(P_6)}\mathcal{M}_0^{V_\lambda\to l_1\bar{l}_2}. \tag{3.64}$$

The momentum of the vector boson must be projected on shell in order to ensure gauge invariance, both in the production and in the decay subprocesses. In the overall propagator, instead, it retains its original value. The sum runs over the physical helicities of the vector boson.

### 3.6.1 On-shell projection

In order to use the leading-pole approximation, we need to build a mapping that, conserving energy and momentum, projects on shell the momentum of the vector boson and rescales its decay products. We choose to keep fixed the solid angles formed by the vector boson and by one of the leptons.

In the center-of-mass frame of the $HV$ pair, the spatial momenta of the vector boson and of the Higgs boson are equal and opposite, $\vec{k} = -\vec{p}_3$: as a consequence, preserving the solid angle of the vector boson also preserves the direction of the Higgs boson. In this frame the two four-momenta can be written as

$$k = \left(E_V, \vec{k}\right), \qquad p_3 = \left(E_H, -\vec{k}\right). \tag{3.65}$$

The condition that has to be fulfilled, in order to have on-shell bosons and preserve the energy, is

$$\sqrt{s} = E_V^{\mathrm{on}} + E_H^{\mathrm{on}} = \sqrt{|\vec{p}^{\,\mathrm{on}}|^2 + M_V^2} + \sqrt{|\vec{p}^{\,\mathrm{on}}|^2 + M_H^2}, \tag{3.66}$$

where $\vec{p}^{\,\mathrm{on}}$ is a vector with the same direction of $\vec{k}$. This relation, solved for $|\vec{p}^{\,\mathrm{on}}|$, gives

$$|\vec{p}^{\,\mathrm{on}}| = \frac{1}{2\sqrt{s}}\sqrt{[s - (M_V + M_H)^2]\,[s - (M_V - M_H)^2]}, \tag{3.67}$$

and thus

$$E_V^{\mathrm{on}} = \sqrt{|\vec{p}^{\,\mathrm{on}}|^2 + M_V^2} = \frac{s + M_V^2 - M_H^2}{2\sqrt{s}}, \tag{3.68}$$

$$E_H^{\mathrm{on}} = \sqrt{|\vec{p}^{\,\mathrm{on}}|^2 + M_H^2} = \frac{s + M_H^2 - M_V^2}{2\sqrt{s}}. \tag{3.69}$$

Summing up the results, the on-shell projected boson momenta read

$$k^{\text{on}} = \left(E_V^{\text{on}}, \vec{p}^{\,\text{on}}\right), \qquad p_3^{\text{on}} = \left(E_H^{\text{on}}, -\vec{p}^{\,\text{on}}\right). \tag{3.70}$$

At this point we have to rescale the momentum of the decay products, to comply with the on-shell projection just performed. To this end, we choose to keep fixed the direction of the lepton $l(p_4)$: the result can be obtained simply by multiplying the components of its momentum by $\zeta^{\text{on}}$, computed in the following way. Care has to be taken in choosing this rescaling factor such that both the lepton and the antilepton remain massless. In other words, the following relations have to be fulfilled together:

$$\begin{cases} (p_4^{\text{on}} + p_5^{\text{on}})^2 = M_V^2 \\ p_4^{\text{on}} = \zeta^{\text{on}}\, p_4 \\ p_5^{\text{on}} = p_V^{\text{on}} - p_4^{\text{on}} \\ (p_4^{\text{on}})^2 = (p_5^{\text{on}})^2 = 0. \end{cases} \tag{3.71}$$

Combining the first two relations and using the fact that the leptons are massless we get $2\zeta^{\text{on}}\,(p_4 \cdot p_5^{\text{on}}) = M_V^2$. Inserting now the third relation into this one, we finally obtain the rescaling factor

$$\zeta^{\text{on}} = \frac{M_V^2}{2\,(p_4 \cdot p_V^{\text{on}})}. \tag{3.72}$$

For processes that do not involve the production of a jet at Born level, the $HV$ center-of-mass frame coincides with the partonic one. For $HVj$ processes, since the jet recoils against the $HV$ pair, we first have to perform a boost in the center-of-mass frame of the $Hl_1\bar{l}_2$ system, and carry out all the previous steps on the boosted momenta. At the end, we return to the laboratory frame with an inverse boost.

If the center-of-mass energy is smaller than the sum of the vector-boson physical masses, $\sqrt{s} < M_V + M_H$, the argument of the square root in eq. (3.67) becomes negative. In this case, the event has not enough energy even to produce a vector boson and a Higgs boson at rest. For this reason, if this happens we set the whole matrix element of eq. (3.64) to zero.

### 3.6.2 Virtual corrections in the leading-pole approximation

The leading-pole approximation has many advantages in the context of virtual corrections. Apart from providing a gauge invariant answer, it reduces drastically the number of diagrams that have to be computed, since the matrix element splits into components with less particles than the original process. On the other hand, the definition of the LPA is somehow problematic for photon emission diagrams. Photon radiation from the initial and from the final states leads to propagators that become resonant at different locations in the phase space, depending on the photon energy. For this reason, the LPA will be applied only to the virtual corrections, while for the real emissions, for the computation of the counterterms and for the leading-order contributions we use the full matrix elements.

In leading-pole approximation, the electroweak corrections to processes that involve the production and decay of an unstable particle can be divided into two categories: the factorizable corrections and the non-factorizable ones. The former are the ones associated either to the production or to the decay subprocess, while the latter connect these subprocesses. However, for many processes [100–103], the non-factorizable corrections turn out to be very small: the most relevant contributions come from the exchange of soft photons between the

production and decay subprocesses, but they typically give percent-level corrections. For this reason, in this work we neglect them and focus only on the factorizable ones. The corrections to the matrix element (3.64) can then be written as

$$\begin{aligned}\delta\mathcal{M}_{\text{LPA}}^{P_1\bar{P}_2\to Hl_1\bar{l}_2(P_6)} &= \frac{1}{k^2-M_V^2+i\Gamma_V M_V}\sum_\lambda\Big[\delta\mathcal{M}^{P_1\bar{P}_2\to HV_\lambda(P_6)}\,\mathcal{M}_0^{V_\lambda\to l_1\bar{l}_2} \\ &\quad + \mathcal{M}_0^{P_1\bar{P}_2\to HV_\lambda(P_6)}\,\delta\mathcal{M}^{V_\lambda\to l_1\bar{l}_2}\Big], \end{aligned} \tag{3.73}$$

where the various $\delta\mathcal{M}$ denote the virtual corrections to that particular process. Since the decay process involves no high-energy variables, being all of the kinematic quantities of the order of $M_V$, the corresponding virtual corrections vanish in the Sudakov limit. For this reason, we do not consider the term in the second line of eq. (3.73), and we obtain

$$\delta\mathcal{M}_{\text{LPA}}^{P_1\bar{P}_2\to Hl_1\bar{l}_2(P_6)} = \frac{1}{k^2-M_V^2+i\Gamma_V M_V}\sum_\lambda\delta\mathcal{M}^{P_1\bar{P}_2\to HV_\lambda(P_6)}\,\mathcal{M}_0^{V_\lambda\to l_1\bar{l}_2}. \tag{3.74}$$

The virtual contribution to the cross section is given by the interference between this matrix element and $\mathcal{M}_0$, evaluated in leading-pole approximation.

We need then to compute the matrix elements for the production and the decay subprocesses, for both transverse and longitudinal $V$ bosons. The production of a longitudinal gauge boson can be treated using the GBET, substituting it with the corresponding Goldstone boson. For the decay process, instead, we can keep the longitudinal gauge boson, since the GBET applies at high energies and this process does not involve high-energy variables. Moreover, if we used the GBET, the matrix element for the resulting process would contain a vertex $\phi ff'$, that is proportional to the mass of the fermions involved, and thus the contribution would vanish.

# Chapter 4

# The NLO Sudakov corrections to the $HV$ and $HVj$ processes

This chapter is dedicated to the computation of the NLO Sudakov electroweak corrections to the associated production of a Higgs boson with a vector boson and eventually a jet, in leading-pole approximation. We consider only leptonic decays of the vector boson, excluding the $Z \to \nu\bar{\nu}$ channel. In the following we refer to leptons of the first generation, although our results remain valid also for the other generations, as long as these particles are considered as massless. With $u$ and $d$ we denote generic up- and down-type quarks, with no assumptions on their generation, unless specified.

We first describe these processes at leading order, calculating their matrix elements for both transverse and longitudinal vector bosons. Then, we move to the inclusion of one-loop corrections in the high-energy regime, deriving the correction factors from the general formulae described in the previous chapter.

All the group-theoretical quantities involved in the following are listed in App. A, while the detailed derivation of the results can be found in App. B.

## 4.1 The $HW$ associated production

We start from describing the production of a Higgs boson with a $W$ boson that decays into an electron-neutrino pair. Due to the couplings of the $W$ boson, this process involves only left-chiral quarks and leptons

$$d_L(p_1)\,\bar{u}_L(p_2) \to H(p_3)\,W^-(k) \to H(p_3)\,e^-_L(p_4)\,\bar{\nu}_e(p_5), \tag{4.1}$$

$$\bar{d}_L(p_1)\,u_L(p_2) \to H(p_3)\,W^+(k) \to H(p_3)\,e^+_L(p_4)\,\nu_e(p_5). \tag{4.2}$$

We focus only on these two processes, since the ones with the initial-state particles interchanged can be described in the same way, and are related by simple transformations. In leading-pole approximation, we need the matrix elements for the production and decay of both transverse and longitudinal $W$ bosons.

### 4.1.1 Production of a transverse $W^-$ boson

The Feynman diagram for the production of a transverse $W^-$ boson is shown in the left-hand side of fig. 4.1. The process can be written as $d_L(p_1)\,\bar{u}_L(p_2) \to H(p_3)\,W^-_T(k)$ or, making all the particles incoming,

$$d_L(p_1)\,\bar{u}_L(p_2)\,H(-p_3)\,W^+_T(-k) \to 0. \tag{4.3}$$

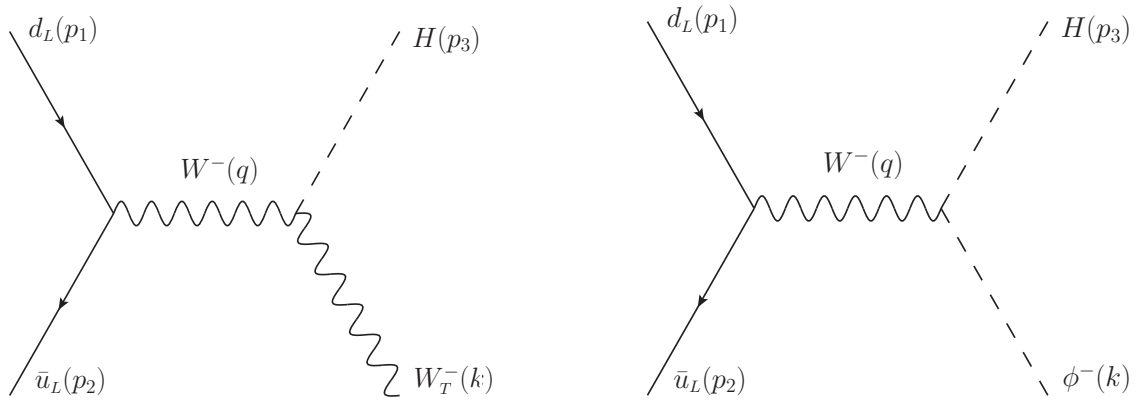


Figure 4.1: Feynman diagram for the associated production of a Higgs boson with a transverse $W^-$ boson (left), and with a $\phi^-$ Goldstone boson (right), at leading order.

Its matrix element can be written as

$$\mathcal{M}_0^{d_L\bar{u}_L H W_T^+} = \frac{e^2}{\sqrt{2}s_W^2}\, M_W\, V_{ud}^{\text{CKM}}\, \frac{A_{T-}}{q^2}, \tag{4.4}$$

where the spinorial part has been grouped in $A_{T-}$ as in eq. (B.7). Here and in the following sections, $q = p_1 + p_2$. The process with exchanged initial particles has the same matrix element apart from the spinorial part, that becomes

$$A'_{T-} = -i\, \bar{v}_L(p_1)\gamma^\mu u_L(p_2)\, \epsilon_\mu^T(-k). \tag{4.5}$$

### 4.1.2 Production of a longitudinal $W^-$ boson

The production of a longitudinal $W^-$ boson has the same structure as for a transverse one. Nevertheless, at high energies this particle has to be substituted by the corresponding Goldstone boson, according to the GBET. The result is shown in the right-hand side of fig. 4.1. The process, with all particles incoming, is

$$d_L(p_1)\, \bar{u}_L(p_2)\, H(-p_3)\, W_L^+(-k) \to 0, \tag{4.6}$$

and the application of the GBET formula in eq. (3.19) turns it into

$$\mathcal{M}_0^{d_L\bar{u}_L H W_L^+} = i^{(1-Q_{W^+})}\mathcal{M}_0^{d_L\bar{u}_L H\phi^+} = \mathcal{M}_0^{d_L\bar{u}_L H\phi^+}. \tag{4.7}$$

The computation of the matrix element gives

$$\mathcal{M}_0^{d_L\bar{u}_L H W_L^+} = \mathcal{M}_0^{d_L\bar{u}_L H\phi^+} = \frac{e^2}{2\sqrt{2}s_W^2}\, V_{ud}^{\text{CKM}}\, \frac{A_{L-}}{q^2}, \tag{4.8}$$

having defined $A_{L-}$ as in eq. (B.47). In this case too, the exchange of the initial-state particles produces a modification only in the spinorial part

$$A'_{L-} = -i\, \bar{v}_L(p_1)\gamma^\mu u_L(p_2)\, (-k + p_3)_\mu. \tag{4.9}$$

By inspecting the results obtained in eqs. (4.4) and (4.8), we see that the former contains a factor $M_W$, coming from the Higgs vertex, that is absent in the longitudinal case. The

transverse matrix element is then mass-suppressed and, at high energies, it should be neglected. Moreover, the universal formulae for the electroweak Sudakov corrections, derived in Chap. 3, are based on some identities that are fulfilled only by matrix elements that, in the high-energy limit, are not mass-suppressed. Therefore, they should not be applied to this process. Nevertheless, several results that contribute to the Sudakov logarithms, like eq. (3.21) or the running-coupling effects, can be applied even to mass-suppressed matrix elements. We can then compute the Sudakov corrections for the production of a transverse $W$ boson, and compare the results with the full electroweak one-loop corrections in order to obtain information about the correctness of this approximation. In Sec. 4.6.3 we study the relevance of the transverse polarization, both at leading order and with the inclusion of electroweak corrections, to understand if can be effectively neglected due to its mass suppression or if it has to be included.

### 4.1.3 Decay of the $W^-$ boson

The matrix element for the decay of a $W^-$ boson has the same form for all the polarizations $\lambda$,

$$\mathcal{M}_0^{W^-_\lambda \to e^- \bar{\nu}_e} = -i \frac{e}{\sqrt{2} s_W} \bar{u}_L(p_4) \gamma^\mu v_L(p_5) \epsilon^\lambda_\mu(k). \tag{4.10}$$

### 4.1.4 Production of a transverse $W^+$ boson

The matrix element for the production of a transverse $W^+$ boson,

$$\bar{d}_L(p_1)\, u_L(p_2)\, H(-p_3)\, W^-_T(-k) \to 0, \tag{4.11}$$

is very similar to the one for the $W^-$ boson, the only relevant change is in the spinorial part, where the quark spinors are interchanged,

$$\mathcal{M}_0^{\bar{d}_L u_L H W^-_T} = \frac{e^2}{\sqrt{2} s_W^2} M_W\, V_{ud}^{\mathrm{CKM}} \frac{A'_{T-}}{q^2}. \tag{4.12}$$

The exchange of the initial-state particles causes the replacement of $A'_{T-}$ with $A_{T-}$.

### 4.1.5 Production of a longitudinal $W^+$ boson

Applying the GBET to the process $\bar{d}_L(p_1)\, u_L(p_2)\, H(-p_3)\, W^-_L(-k) \to 0$ we get, differently from the $W^-$ case,

$$\mathcal{M}_0^{\bar{d}_L u_L H W^-_L} = i^{(1-Q_{W^-})} \mathcal{M}_0^{\bar{d}_L u_L H \phi^-} = -\mathcal{M}_0^{\bar{d}_L u_L H \phi^-}. \tag{4.13}$$

The vertex that involves the Goldstone boson changes sign, so that we obtain once again

$$\mathcal{M}_0^{\bar{d}_L u_L H W^-_L} = -\mathcal{M}_0^{\bar{d}_L u_L H \phi^-} = \frac{e^2}{2\sqrt{2} s_W^2} V_{ud}^{\mathrm{CKM}} \frac{A'_{L-}}{q^2}. \tag{4.14}$$

As for the $W^-$ boson, changing the initial-state particles amounts to using $A_{L-}$ as spinorial part. Again, the transverse matrix element is mass-suppressed with respect to the longitudinal one.

### 4.1.6 Decay of the $W^+$ boson

The decay of a $W^+$ boson is given for all polarizations by

$$\mathcal{M}_0^{W^+_\lambda \to e^+\nu_e} = -i\,\frac{e}{\sqrt{2}s_W}\,\bar{u}_L(p_5)\gamma^\mu v_L(p_4)\,\epsilon^\lambda_\mu(k). \tag{4.15}$$

### 4.1.7 Sudakov electroweak corrections

The Sudakov electroweak corrections can be obtained by applying the procedure described in Secs. 3.4 and 3.5 to the processes under study.

The correction factors containing logarithms of type $\log(M_W^2/\lambda^2)$, which involve the fictitious photon mass $\lambda$, represent the IR-divergent part of the corrections coming from photon-exchange diagrams. In order to obtain a finite result, these contributions should be combined with the soft-collinear singularities of real photon emission. This subtraction procedure is performed in the `POWHEG BOX RES` in dimensional regularization. The `POWHEG BOX RES` requires the finite part of the virtual cross section with a precise normalization factor, as described in eqs. (2.11) and (2.12) of ref. [14]. A mapping of the $\lambda$-logarithms into $\epsilon$ poles is then mandatory, in order to consistently match the Sudakov corrections to the `POWHEG` subtraction. While for processes with massive fermions and without $W$ bosons in the final state this mapping is known,

$$\frac{1}{2}\log^2(\lambda^2) \to \frac{1}{\epsilon^2}, \tag{4.16}$$

it is not entirely clear if an analogous formula holds for the processes under study. For this reason, in the following we do not omit the Sudakov correction factors that contain logarithms of type $\log(M_W^2/\lambda^2)$. Further studies regarding this issue will be performed in the near future, in order to define a matching procedure that allows to obtain correctly matched results.

As will be described in Secs. 4.3.4 and 4.4, for $HZ$ and $HZj$ production a matching can be derived. This matching is approximate in the $HZj$ case, and exact for $HZ$. For the $W$-boson production processes, instead, this procedure is more complicated, due to the presence of charged gauge bosons to which the photon couples. The corresponding results, then, are not precisely matched to the `POWHEG BOX RES`. This is certainly a problem from the theoretical point of view and for the analysis of the NLO results obtained including the Sudakov EW corrections. For the analysis of the showered events in Chap. 5, however, we focus on the results obtained with full QCD+EW accuracy, that contain the complete one-loop electroweak corrections and are thus perfectly matched to the `POWHEG BOX RES`.

The logarithms of type $\log(M_W^2/m_f^2)$, that involve the masses of the light fermions $m_f$, together with the factor $\Delta\alpha(M_W^2)$, are instead relevant only if the on-shell scheme is used, with $\alpha(0)$ as input. As described in Sec. 4.5, in the implementation of these processes we use the $G_\mu$ scheme, that already incorporates these terms in the definition of $\alpha_{G_\mu}$. For these reasons, in both $HV$ and $HVj$ production, we do not consider the $\Delta\alpha(M_W^2)$ term and the logarithms that contain $m_f$.

Moreover, since the bottom quark is considered as massless, we do not include the terms $\delta^{\mathrm{LSC,h}}_{b_\kappa}$ and $\delta^{\mathrm{C,h}}_{b_\kappa}$ in our correction factors.

For processes that involve only four particles, $p_1+p_2+p_3+p_4 \to 0$, some identities relate the kinematic invariants: in particular, $r_{12} = r_{34}$, $r_{13} = r_{24}$ and $r_{14} = r_{23}$. The formula that

describes the subleading soft-collinear corrections, eq. (3.34), simplifies then to

$$\begin{aligned}\delta^{\rm SSC}\mathcal{M}^{\varphi_1\varphi_2\varphi_3\varphi_4} &= \frac{\alpha}{2\pi}\sum_{V^a=A,\,Z,\,W^\pm}\sum_{\varphi_{k'},\varphi_{l'}}\left[\log\frac{s}{M_W^2}+\log\frac{M_W^2}{M_{V^a}^2}\right]\\ &\times\left[\log\frac{|r_{12}|}{s}\left(I^{V^a}_{\varphi_{1'}\varphi_1}I^{\bar V^a}_{\varphi_{2'}\varphi_2}\mathcal{M}_0^{\varphi_{1'}\varphi_{2'}\varphi_3\varphi_4}+I^{V^a}_{\varphi_{3'}\varphi_3}I^{\bar V^a}_{\varphi_{4'}\varphi_4}\mathcal{M}_0^{\varphi_1\varphi_2\varphi_{3'}\varphi_{4'}}\right)\right.\\ &+\log\frac{|r_{13}|}{s}\left(I^{V^a}_{\varphi_{1'}\varphi_1}I^{\bar V^a}_{\varphi_{3'}\varphi_3}\mathcal{M}_0^{\varphi_{1'}\varphi_2\varphi_{3'}\varphi_4}+I^{V^a}_{\varphi_{2'}\varphi_2}I^{\bar V^a}_{\varphi_{4'}\varphi_4}\mathcal{M}_0^{\varphi_1\varphi_{2'}\varphi_3\varphi_{4'}}\right)\\ &\left.+\log\frac{|r_{14}|}{s}\left(I^{V^a}_{\varphi_{1'}\varphi_1}I^{\bar V^a}_{\varphi_{4'}\varphi_4}\mathcal{M}_0^{\varphi_{1'}\varphi_2\varphi_3\varphi_{4'}}+I^{V^a}_{\varphi_{2'}\varphi_2}I^{\bar V^a}_{\varphi_{3'}\varphi_3}\mathcal{M}_0^{\varphi_1\varphi_{2'}\varphi_{3'}\varphi_4}\right)\right]. \quad (4.17)\end{aligned}$$

To obtain these factors, we split them into two components, one coming from the exchange of neutral gauge bosons, the other from the exchange of charged bosons

$$\delta^{\rm SSC}\mathcal{M}^{d_L\bar u_L HW_T^+}=\delta^{\rm SSC,n}\mathcal{M}^{d_L\bar u_L HW_T^+}+\delta^{\rm SSC,\pm}\mathcal{M}^{d_L\bar u_L HW_T^+}. \quad (4.18)$$

We now compute the corrections to the associated production of a Higgs boson and a $W^-$ boson, and we obtain the correction factors for the $W^+$ case from these results.

**Transverse case**

We focus on the process of eq. (4.3), whose matrix element is given in eq. (4.4). In the computation of the single-logarithmic corrections associated to the parameter renormalization, the parameters that have to be renormalized are $e$, $M_W$ and $s_W$. The correction factor for the last one can be obtained from

$$\frac{\partial\mathcal{M}_0}{\partial c_W^2}\,\delta c_W^2=-\frac{\partial\mathcal{M}_0}{\partial s_W^2}\,\delta c_W^2. \quad (4.19)$$

Even if $M_W$ is a dimensional parameter, in this case its renormalization must not be neglected because the original matrix element is mass-suppressed. The corresponding correction factor would indeed give a contribution that scales with energy exactly as the matrix element does.

For the leading soft-collinear contributions we obtain

$$\begin{aligned}\delta^{\rm LSC}\mathcal{M}^{d_L\bar u_L HW_T^+} &= \left\{-\frac{1}{2}L(s)\left[2C_q^{\rm ew}+C_\Phi^{\rm ew}+C_W^{\rm ew}\right]+\delta_H^{\rm LSC,h}\right.\\ &+l(s)\log\frac{M_Z^2}{M_W^2}\left[(I^Z_{d_L})^2+(I^Z_{\bar u_L})^2+(I^Z_H)^2+(I^Z_W)^2\right]-\frac{1}{2}\left[Q_d^2\,L_{\rm em}(s,\lambda^2,m_d^2)\right.\\ &\left.\left.+Q_u^2\,L_{\rm em}(s,\lambda^2,m_u^2)+Q_W^2\,L_{\rm em}(s,\lambda^2,M_W^2)\right]\right\}\mathcal{M}_0, \quad (4.20)\end{aligned}$$

where $C_q^{\rm ew}=C_{d_L}^{\rm ew}=C_{\bar u_L}^{\rm ew}$ and the factors $L_{\rm em}(s,\lambda^2,m_\phi^2)$ and $\delta_H^{\rm LSC,h}$ are given in eqs. (3.27) and (3.31).

Defining $t=(p_1-p_3)^2=r_{13}$ and $u=(p_1-k)^2=r_{14}$, the subleading soft-collinear factors take the form

$$\begin{aligned}\delta^{\rm SSC,n}\mathcal{M}^{d_L\bar u_L HW_T^+} &= \left[2l(s)\left(R_{d_LW^+}\log\frac{|u|}{s}-R_{u_LW^+}\log\frac{|t|}{s}\right)\right.\\ &\left.+\frac{\alpha}{2\pi}\log\frac{M_W^2}{\lambda^2}\left(Q_d\log\frac{|u|}{s}-Q_u\log\frac{|t|}{s}\right)Q_{W^+}\right]\mathcal{M}_0, \quad (4.21)\end{aligned}$$

$$\delta^{\mathrm{SSC},\pm}\mathcal{M}^{d_L\bar{u}_L HW_T^+} = 2l(s)\, s_W \left[\log\frac{|t|}{s}\left(\frac{I^z_{u_L}}{2c_W} - \frac{Q_u}{2s_W} + \frac{I^z_{d_L}}{s^2_W c_W}\right) - \log\frac{|u|}{s}\left(\frac{I^z_{d_L}}{2c_W} - \frac{Q_d}{2s_W} + \frac{I^z_{u_L}}{s^2_W c_W}\right)\right]\mathcal{M}_0. \tag{4.22}$$

$R_{\phi_1\phi_2}$ is a factor related to the charge and to the weak isospin of the involved particles according to

$$R_{\phi_1\phi_2} = Q_{\phi_1}Q_{\phi_2} + I^z_{\phi_1}I^z_{\phi_2}. \tag{4.23}$$

The single-logarithmic corrections associated to external particles read

$$\begin{aligned}\delta^{\mathrm{C}}\mathcal{M}^{d_L\bar{u}_L HW_T^+} = \Bigg\{&\frac{\alpha}{4\pi}\left[\left(\frac{3}{4s^2_W}\frac{m_t^2}{M_W^2} + T_{WW}\right)\log\frac{m_t^2}{M_W^2} + \left(\frac{1}{24s^2_W} - 2C^{\mathrm{ew}}_\Phi\right)\log\frac{M_H^2}{M_W^2}\right] \\ &+ l(s)\left[3C^{\mathrm{ew}}_q + 2C^{\mathrm{ew}}_\Phi + \frac{1}{2}b^{\mathrm{ew}}_{WW} - \frac{3}{4s^2_W}\frac{m_t^2}{M_W^2}\right] \\ &+ \frac{\alpha}{4\pi}\log\frac{M_W^2}{\lambda^2}(Q_d^2 + Q_u^2 + Q_W^2)\Bigg\}\mathcal{M}_0,\end{aligned} \tag{4.24}$$

with $T_{WW}$ and $b^{\mathrm{ew}}_{WW}$ defined respectively in eqs. (3.43) and (A.39). Finally, for the corrections from parameter renormalization we obtain

$$\begin{aligned}\delta^{\mathrm{PR}}\mathcal{M}^{d_L\bar{u}_L HW_T^+} = \Bigg\{&\frac{\alpha}{4\pi}\left[\frac{5}{12s^2_W}\log\frac{M_H^2}{M_W^2} - \left(\frac{9 + 6s^2_W - 32s^4_W}{18s^4_W} + T_{WW} - \frac{3}{4s^2_W}\frac{m_t^2}{M_W^2}\right)\log\frac{m_t^2}{M_W^2}\right] \\ &+ l(s)\left(-\frac{3}{2}b^{\mathrm{ew}}_{WW} + 2C^{\mathrm{ew}}_\Phi - \frac{3}{4s^2_W}\frac{m_t^2}{M_W^2}\right)\Bigg\}\mathcal{M}_0,\end{aligned} \tag{4.25}$$

where we have included the contributions coming from the $W$-boson mass renormalization.

Moving to the process with the initial-state particles interchanged, we can obtain its correction factors from the ones that we have just calculated. Indeed, the spinorial part changes, but this does not influence the structure of the electroweak corrections since they factorize on it. Most of the corrections involve a sum over the external particles: for this reason, the exchange of the position of two particles plays no role, and the contributions remain the same. The only modifications concern the subleading soft-collinear corrections: interchanging the initial-state particles, the kinematic invariants become $|r_{1j}| \leftrightarrow |r_{2j}|$, for $j = 3, 4$, i.e. $t$ becomes $u$ and vice-versa. The subleading soft-collinear corrections can then be obtained from the previous ones, eqs. (4.21) and (4.22), simply by switching $t$ and $u$.

The corrections to the production of a transverse $W^+$ boson turn out to be the same as the ones for $HW_T^-$ production, since all of the group-theoretical quantities that appear in the formulae take the same value for the two kinds of processes considered (for example, $(I^z_{d_L})^2 = (I^z_{\bar{d}_L})^2$, $C^{\mathrm{ew}}_{W^+} = C^{\mathrm{ew}}_{W^-}$).

### Longitudinal case

We now move to the calculation of the corrections to the associated production of a Higgs boson and a longitudinal $W^-$ boson, starting from the process (4.6). By applying the GBET we found that the matrix element for this process is equivalent to the one for the production of a Higgs boson and a $\phi^-$ Goldstone boson. The same equivalence also holds for the one-loop corrections: for this reason we compute $\delta\mathcal{M}^{d_L\bar{u}_L H\phi^+}$. The matrix element has been computed in eq. (4.8): in this case, the parameters that have to be renormalized are only $e$ and $s_W$.

The leading soft-collinear contributions take the form

$$\begin{aligned}\delta^{\rm LSC}\mathcal{M}^{d_L\bar{u}_L H\phi^+} &= \Big\{ -L(s)\left(C_q^{\rm ew}+C_\Phi^{\rm ew}\right)+\delta_H^{\rm LSC,h}+\delta_{\phi^\pm}^{\rm LSC,h} \\ &\quad + l(s)\log\frac{M_Z^2}{M_W^2}\left[(I_{d_L}^Z)^2+(I_{\bar{u}_L}^Z)^2+(I_H^Z)^2+(I_{\phi^+}^Z)^2\right]-\frac{1}{2}\left[Q_d^2\,L_{\rm em}(s,\lambda^2,m_d^2)\right. \\ &\quad \left.+Q_u^2\,L_{\rm em}(s,\lambda^2,m_u^2)+Q_\phi^2\,L_{\rm em}(s,\lambda^2,M_W^2)\right]\Big\}\mathcal{M}_0, \end{aligned} \tag{4.26}$$

while the subleading ones, split according to eq. (4.18), read

$$\begin{aligned}\delta^{\rm SSC,n}\mathcal{M}^{d_L\bar{u}_L H\phi^+} &= \frac{\alpha}{2\pi}\log\frac{M_W^2}{\lambda^2}\left(Q_d\log\frac{|u|}{s}-Q_u\log\frac{|t|}{s}\right)Q_{\phi^+}\mathcal{M}_0 \\ &\quad +2l(s)\left[\log\frac{|t|}{s}\left(iI_{H\chi}^Z I_{d_L}^Z-R_{u_L\phi^+}\right)-\log\frac{|u|}{s}\left(iI_{H\chi}^Z I_{u_L}^Z-R_{d_L\phi^+}\right)\right]\mathcal{M}_0, \end{aligned} \tag{4.27}$$

$$\delta^{\rm SSC,\pm}\mathcal{M}^{d_L\bar{u}_L H\phi^+} = 2l(s)\left[\log\frac{|t|}{s}\left(iI_{H\chi}^Z I_{d_L}^Z-R_{u_L\phi^+}\right)-\log\frac{|u|}{s}\left(iI_{H\chi}^Z I_{u_L}^Z-R_{d_L\phi^+}\right)\right]\mathcal{M}_0. \tag{4.28}$$

In the end, the single-logarithmic corrections are

$$\begin{aligned}\delta^{\rm C}\mathcal{M}^{d_L\bar{u}_L H\phi^+} &= \left\{\frac{\alpha}{4\pi}\left[\frac{3}{2s_W^2}\frac{m_t^2}{M_W^2}\log\frac{m_t^2}{M_W^2}+\left(\frac{1}{8s_W^2}-2C_\Phi^{\rm ew}\right)\log\frac{M_H^2}{M_W^2}\right]\right. \\ &\quad \left.+l(s)\left[3C_q^{\rm ew}+4C_\Phi^{\rm ew}-\frac{3}{2s_W^2}\frac{m_t^2}{M_W^2}\right]+\log\frac{M_W^2}{\lambda^2}(Q_d^2+Q_u^2+Q_\phi^2)\right\}\mathcal{M}_0, \end{aligned} \tag{4.29}$$

$$\delta^{\rm PR}\mathcal{M}^{d_L\bar{u}_L H\phi^+} = \left[\frac{\alpha}{4\pi}\left(\frac{5}{6s_W^2}\log\frac{M_H^2}{M_W^2}-\frac{9+6s_W^2-32s_W^4}{18s_W^4}\log\frac{m_t^2}{M_W^2}\right)-b_{WW}^{\rm ew}l(s)\right]\mathcal{M}_0. \tag{4.30}$$

The correction factors for the process with the initial-state particles interchanged, and the ones for the production of a longitudinal $W^+$ boson, can be obtained by applying the same procedure described in the transverse case.

## 4.2 The *HWj* associated production

The quark-initiated associated production of a Higgs boson with a $W$ boson and a jet is given by the following partonic processes,

$$d_L(p_1)\,\bar{u}_L(p_2)\to H(p_3)\,W^-(k)\,g(p_6)\to H(p_3)\,e_L^-(p_4)\,\bar{\nu}_e(p_5)\,g(p_6), \tag{4.31}$$

$$\bar{d}_L(p_1)\,u_L(p_2)\to H(p_3)\,W^+(k)\,g(p_6)\to H(p_3)\,e_L^+(p_4)\,\nu_e(p_5)\,g(p_6), \tag{4.32}$$

plus the ones with an initial-state particle interchanged with the final-state gluon. We begin by describing the process (4.31): by applying the leading-pole approximation we see that, also for $HWj$ production, we need to distinguish between transverse and longitudinal $W$ bosons. Nevertheless, the results are very similar to the $HW$ case: the only relevant change is the insertion of a gluon along the fermionic line. We first write the fermionic current as

$$S_\kappa^{\mu\nu}=\bar{v}_\kappa(p_2)\left[\gamma^\mu\frac{\not{p}_1-\not{p}_6}{(p_1-p_6)^2}\gamma^\nu+\gamma^\nu\frac{\not{p}_6-\not{p}_2}{(p_6-p_2)^2}\gamma^\mu\right]u_\kappa(p_1), \tag{4.33}$$

in which $\kappa$ labels the chirality of the quarks involved. The processes and its matrix elements, with all particles incoming, are then

$$d_L(p_1)\,\bar{u}_L(p_2)\,H(-p_3)\,W^+_\lambda(-k)\,g(-p_6)\to 0, \tag{4.34}$$

$$\mathcal{M}_0^{d_L\bar{u}_L HW^+_T g} = -\frac{i}{q^2}\frac{e^2}{\sqrt{2}s_W^2}\,M_W\,V_{ud}^{\rm CKM}\,g_s t^a\,S^{\mu\nu}_\kappa\epsilon^T_\mu(-k)\,\epsilon_\nu(-p_6), \tag{4.35}$$

$$\mathcal{M}_0^{d_L\bar{u}_L HW^+_L g} = \mathcal{M}_0^{d_L\bar{u}_L H\phi^+ g} = -\frac{i}{q^2}\frac{e^2}{2\sqrt{2}s_W^2}\,V_{ud}^{\rm CKM}\,g_s t^a\,S^{\mu\nu}_\kappa(-k+p_3)_\mu\,\epsilon_\nu(-p_6), \tag{4.36}$$

being $g_s$ the strong coupling constant and $t^a$ the colour matrix. The matrix element with the initial-state particles interchanged can be obtained by modifying the spinorial part as done in $HW$ production, while the processes with a gluon in the initial state can be described by applying crossing symmetry.

The computation of the Sudakov corrections almost comes for free from the $HW$ case. This is due to the fact that the only added particle, the gluon, is not involved in the electroweak corrections because of its quantum numbers: for this reason many of the corrections, that consist in a sum of radiator functions over the external particles, remain unchanged. In particular, $\delta^{\rm LSC}\mathcal{M}$, $\delta^{\rm C}\mathcal{M}$ and $\delta^{\rm PR}\mathcal{M}$ maintain the same values of $HW$ production for both the transverse and the longitudinal cases. The only change is in $\delta^{\rm SSC}\mathcal{M}$, because with five particles involved the kinematic invariants are not equal one to another anymore. Moreover, when considering processes with the gluon in the initial state, the application of crossing symmetry modifies some of the kinematic invariants $r_{kl}$. For example, in the process $g\bar{u}_L\to HW^-_\lambda\bar{d}_L$ the kinematic logarithm related to the exchange of a vector boson between the two quarks does not involve anymore $r_{12}$, but rather $r_{26}$. By applying crossing symmetry, however, we can use the original correction factors in which we perform the exchange $r_{12}\leftrightarrow r_{26}$. As a result, in these cases $\log(|r_{12}|/s)$ does not vanish anymore. Applying the general formula (3.34) for the subleading soft-collinear corrections, in the transverse case we obtain

$$\begin{aligned}\delta^{\rm SSC,n}\mathcal{M}^{d_L\bar{u}_L HW^+_T g} &= \frac{\alpha}{2\pi}\log\frac{M_W^2}{\lambda^2}\left(\log\frac{|r_{14}|}{s}\,Q_dQ_{W^+}-\log\frac{|r_{24}|}{s}\,Q_uQ_{W^+}-\log\frac{|r_{12}|}{s}\,Q_dQ_u\right)\mathcal{M}_0\\ &\quad+2l(s)\left(\log\frac{|r_{14}|}{s}\,R_{d_LW^+}-\log\frac{|r_{24}|}{s}\,R_{u_LW^+}-\log\frac{|r_{12}|}{s}\,R_{d_Lu_L}\right)\mathcal{M}_0,\end{aligned} \tag{4.37}$$

$$\begin{aligned}\delta^{\rm SSC,\pm}\mathcal{M}^{d_L\bar{u}_L HW^+_T g} &= 2l(s)s_W\left[\log\frac{|r_{23}|}{s}\left(\frac{Q_d}{2s_W}-\frac{I^Z_{d_L}}{2c_W}\right)+\log\frac{|r_{24}|}{s}\,\frac{I^Z_{d_L}}{s_W^2c_W}\right.\\ &\quad\left.-\log\frac{|r_{13}|}{s}\left(\frac{Q_u}{2s_W}-\frac{I^Z_{u_L}}{2c_W}\right)-\log\frac{|r_{14}|}{s}\,\frac{I^Z_{u_L}}{s_W^2c_W}\right]\mathcal{M}_0.\end{aligned} \tag{4.38}$$

For the production of a longitudinal $W^-$ boson, instead, the results are

$$\begin{aligned}\delta^{\rm SSC,n}\mathcal{M}^{d_L\bar{u}_L H\phi^+ g} &= \frac{\alpha}{2\pi}\log\frac{M_W^2}{\lambda^2}\left(\log\frac{|r_{14}|}{s}\,Q_dQ_{\phi^+}\log\frac{|r_{24}|}{s}\,Q_uQ_{\phi^+}-\log\frac{|r_{12}|}{s}\,Q_uQ_d\right)\mathcal{M}_0\\ &\quad+2l(s)\left[-\log\frac{|r_{12}|}{s}\,R_{u_Ld_L}+\log\frac{|r_{14}|}{s}\,R_{d_L\phi^+}-\log\frac{|r_{24}|}{s}\,R_{u_L\phi^+}\right.\\ &\quad\left.+iI^Z_{H\chi}\left(\log\frac{|r_{13}|}{s}\,I^Z_{d_L}-\log\frac{|r_{23}|}{s}\,I^Z_{u_L}+\log\frac{|r_{34}|}{s}\,I^Z_{\phi^+}\right)\right]\mathcal{M}_0,\end{aligned} \tag{4.39}$$

$$\delta^{\mathrm{SSC},\pm}\mathcal{M}^{d_L\bar{u}_L H\phi^+ g} = 2l(s)\left[\log\frac{|r_{23}|}{s}\,R_{d_L\phi^+} - \log\frac{|r_{13}|}{s}\,R_{u_L\phi^+} - iI^Z_{H\chi}\left(\log\frac{|r_{14}|}{s}\,I^Z_{u_L} - \log\frac{|r_{24}|}{s}\,I^Z_{d_L}\right)\right]\mathcal{M}_0. \tag{4.40}$$

The corrections to the process with the exchanged initial particles can be obtained from these ones by transposing $r_{13} \leftrightarrow r_{23}$ and $r_{14} \leftrightarrow r_{24}$. The $W^+$ case has the same leading-order matrix element as the $W^-$, apart from the spinorial component, and the same corrections.

## 4.3 The $HZ$ associated production

By repeating the procedure used in the previous sections we can obtain the Sudakov corrections to the associated production of a Higgs boson and a $Z$ boson. The main difference with respect to the production of a $W$ boson is that the neutral gauge boson couples to both left- and right-handed currents. We use

$$q(p_1)\,\bar{q}(p_2) \to H(p_3)\,Z(k) \to H(p_3)\,e^+(p_4)\,e^-(p_5) \tag{4.41}$$

as working example, and we obtain the results for the process with initial-state particles interchanged in the same way as in the $HW$ case. Since both left- and right-handed particles are involved, we can write the process in leading-pole approximation, making the chiralities $\kappa, \kappa'$ explicit, as

$$\mathcal{M}^{q_\kappa\bar{q}_\kappa\to He^+_{\kappa'}e^-_{\kappa'}}_{0,\mathrm{LPA}} = \frac{1}{k^2 - M_Z^2 + i\Gamma_Z M_Z}\sum_\lambda \mathcal{M}_0^{q_\kappa\bar{q}_\kappa\to HZ_\lambda}\,\mathcal{M}_0^{Z_\lambda\to e^+_{\kappa'}e^-_{\kappa'}}. \tag{4.42}$$

When computing the squared matrix element, the only terms that contribute to the final result are

$$\left|\mathcal{M}^{q\bar{q}\to He^+e^-}_{0,\mathrm{LPA}}\right|^2 = \frac{1}{(k^2 - M_Z^2)^2 + \Gamma_Z^2 M_Z^2}\sum_{\kappa,\,\kappa'}\left|\sum_\lambda \mathcal{M}_0^{q_\kappa\bar{q}_\kappa\to HZ_\lambda}\,\mathcal{M}_0^{Z_\lambda\to e^+_{\kappa'}e^-_{\kappa'}}\right|^2. \tag{4.43}$$

We then need the matrix elements for the production and decay of both transverse and longitudinal $Z$ bosons, with the different chiralities involved.

### 4.3.1 Production of a transverse $Z$ boson

The production of a transverse $Z$ boson, $q(p_1)\,\bar{q}(p_2) \to H(p_3)\,Z_T(k)$, where $q$ stands for both up- and down-type quarks, has the same structure as the $W$ boson case. Making all the particles incoming this process becomes

$$q(p_1)\,\bar{q}(p_2)\,H(-p_3)\,Z_T(-k) \to 0. \tag{4.44}$$

In writing the matrix element we keep track of the quark chirality $\kappa$ in the group-theoretical quantities involved, so that we can describe both the left- and right-handed cases at the same time. The matrix element for this process can then be written as

$$\mathcal{M}_0^{q\bar{q}HZ_T} = \frac{e^2 M_Z}{s_W c_W}\sum_\kappa I^Z_{q_\kappa}\frac{A^\kappa_{TZ}}{q^2}, \tag{4.45}$$

with the spinorial part collected in $A^\kappa_{TZ}$ according to eq. (B.78). The process with exchanged initial particles gives the same matrix element apart from the spinorial part, that becomes

$$A'^\kappa_{TZ} = -i\,\bar{v}_\kappa(p_1)\gamma^\mu u_\kappa(p_2)\,\epsilon^T_\mu(-k). \tag{4.46}$$

### 4.3.2 Production of a longitudinal $Z$ boson

The production of a longitudinal $Z$ boson, with all particles incoming, reads

$$q(p_1)\,\bar{q}(p_2)\,H(-p_3)\,Z_{\scriptscriptstyle L}(-k) \to 0, \tag{4.47}$$

and the application of the GBET formula gives

$$\mathcal{M}_0^{q\bar{q}HZ_L} = i^{(1-Q_Z)}\mathcal{M}_0^{q\bar{q}H\chi} = i\mathcal{M}_0^{q\bar{q}H\chi}. \tag{4.48}$$

The matrix element is

$$\mathcal{M}_0^{q\bar{q}HZ_L} = i\mathcal{M}_0^{q\bar{q}H\chi} = \frac{e^2}{2s_W c_W}\sum_\kappa I^Z_{q_\kappa}\frac{A^\kappa_{LZ}}{q^2}, \tag{4.49}$$

having defined $A^\kappa_{LZ}$ in eq. (B.126). Even in this case, the exchange of the initial-state particles modifies only the spinorial part, turning it into

$$A'^\kappa_{LZ} = -i\,\bar{v}_\kappa(p_1)\gamma^\mu u_\kappa(p_2)\,(-k+p_3)_\mu. \tag{4.50}$$

As we can see by inspecting the results obtained, the mass-suppression of the transverse matrix element manifests itself also for the $Z$ boson case, due to the fact that the topology of the $HW$ and $HZ$ production processes is the same. The comments of Sec. 4.1.2 on the relevance of the transverse polarization also hold for this process.

### 4.3.3 Decay of the $Z$ boson

The matrix element for the decay of a $Z$ boson is the same for all the polarizations $\lambda$, and is made up of two components, one for each lepton chirality $\kappa'$, like for the quark current,

$$\mathcal{M}_0^{Z_\lambda\to e^+e^-} = -ie\sum_{\kappa'} I^Z_{e_{\kappa'}}\,\bar{u}_{\kappa'}(p_5)\gamma^\mu v_{\kappa'}(p_4)\,\epsilon^\lambda_\mu(k). \tag{4.51}$$

### 4.3.4 Sudakov electroweak corrections

#### Transverse case

For the process in eq. (4.44) the matrix element has the form given in eq. (4.45): we thus need to compute the correction factors for left- and right-handed initial state particles, that multiply the corresponding part of the matrix element. The structure of these factors however remains the same both varying the flavour $q$ of the particles involved and considering different chiralities $\kappa$. The corrections coming from parameter renormalization involve the renormalization of $e$, $c_W$ and $M_Z$, that has to be included for the same reasons of $M_W$. In performing the renormalization of the Weinberg angle, we recall that it appears also in the definition of $I^Z_{q_\kappa}$, as in eq. (A.12).

For the process involving $q_\kappa$ and its corresponding antiparticle, the leading soft-collinear corrections read

$$\begin{aligned}\delta^{\rm LSC}\mathcal{M}^{q_\kappa\bar{q}_\kappa HZ_T} \;=\; &\Bigg\{-\frac{1}{2}\,L(s)\left[2C^{\rm ew}_{q_\kappa}+C^{\rm ew}_{\Phi}+C^{\rm ew}_{ZZ}\right]+\delta^{\rm LSC,h}_H\\ &+l(s)\log\frac{M_Z^2}{M_W^2}\left[2\big(I^Z_{q_\kappa}\big)^2+\big(I^Z_H\big)^2\right]-Q_q^2\,L_{\rm em}(s,\lambda^2,m_q^2)\Bigg\}\mathcal{M}_0.\end{aligned} \tag{4.52}$$

The subleading soft-collinear contributions, instead, have a different form for up- and down-type quarks. Moreover, they come only from the exchange of charged bosons, and for this reason they involve only left-handed particles. Defining a common factor

$$F_T^{\rm SSC} = -\frac{c_W(1+c_W^2)}{2s_W^3}\left[\log\frac{|t|}{s}+\log\frac{|u|}{s}\right], \tag{4.53}$$

the corrections for up- and down-type quarks become

$$\delta^{\rm SSC}\mathcal{M}^{u_\kappa\bar{u}_\kappa HZ_T} = \delta_{\kappa L}\, l(s)\,\frac{F_T^{\rm SSC}}{I_{u_\kappa}^Z}\,\mathcal{M}_0, \tag{4.54}$$

$$\delta^{\rm SSC}\mathcal{M}^{d_\kappa\bar{d}_\kappa HZ_T} = -\,\delta_{\kappa L}\, l(s)\sum_{u_i}|V_{u_i d}^{\rm CKM}|^2\,\frac{F_T^{\rm SSC}}{I_{d_\kappa}^Z}\,\mathcal{M}_0, \tag{4.55}$$

in which the sum over the quark generations does not include the top quark, $u_i = u, c$. Moving to the single-logarithmic contributions, we obtain

$$\begin{aligned}\delta^{\rm C}\mathcal{M}^{q_\kappa\bar{q}_\kappa HZ_T} = \Bigg\{&\frac{\alpha}{4\pi}\left[\left(\frac{3}{4s_W^2}\frac{m_t^2}{M_W^2}+T_{ZZ}\right)\log\frac{m_t^2}{M_W^2}+\left(\frac{M_Z^2}{24s_W^2M_W^2}-2C_\Phi^{\rm ew}\right)\log\frac{M_H^2}{M_W^2}\right]\\ &+l(s)\left[3C_{q_\kappa}^{\rm ew}+2C_\Phi^{\rm ew}+\frac{1}{2}b_{ZZ}^{\rm ew}-\frac{3}{4s_W^2}\frac{m_t^2}{M_W^2}\right]+\frac{\alpha}{2\pi}\,Q_q^2\log\frac{M_W^2}{\lambda^2}\Bigg\}\mathcal{M}_0,\end{aligned} \tag{4.56}$$

$$\begin{aligned}\delta^{\rm PR}\mathcal{M}^{q_\kappa\bar{q}_\kappa HZ_T} = \Bigg\{&\frac{\alpha}{4\pi}\left[\left(\frac{5}{6s_W^2}+\frac{5\rho_{q_\kappa}}{6c_W^2}-\frac{5M_Z^2}{12s_W^2M_W^2}\right)\log\frac{M_H^2}{M_W^2}\right.\\ &\left.-\left(\frac{9+6s_W^2-32s_W^4}{18s_W^2}\left(\frac{1}{s_W^2}+\frac{\rho_{q_\kappa}}{c_W^2}\right)+T_{ZZ}-\frac{3}{4s_W^2}\frac{m_t^2}{M_W^2}\right)\log\frac{m_t^2}{M_W^2}\right]\\ &+l(s)\left[-b_{WW}^{\rm ew}+\rho_{q_\kappa}\frac{s_W}{c_W}b_{AZ}^{\rm ew}+2C_\Phi^{\rm ew}-\frac{1}{2}b_{ZZ}^{\rm ew}-\frac{3}{4s_W^2}\frac{m_t^2}{M_W^2}\right]\Bigg\}\mathcal{M}_0,\end{aligned} \tag{4.57}$$

with the flavour- and chirality-dependent factor $\rho_{q_\kappa}$ defined in eq. (B.121).

The process with interchanged initial-state particles gives the same correction factors: to obtain them we should perform a $t \leftrightarrow u$ exchange, but eq. (4.53) is symmetric in these invariants.

### Longitudinal case

We now analyze the production of a longitudinal $Z$ boson, see eq. (4.47), that, as usual, has to be treated according to the GBET, and it gives the matrix element of eq. (4.49): the parameters that have to be renormalized are therefore $e$ and $c_W$.

For the longitudinal case too we consider the corrections to the process involving quarks $q$ with chirality $\kappa$: the leading soft-collinear corrections are

$$\begin{aligned}\delta^{\rm LSC}\mathcal{M}^{q_\kappa\bar{q}_\kappa H\chi} = \Bigg\{&-L(s)\left[C_{q_\kappa}^{\rm ew}+C_\Phi^{\rm ew}\right]+2l(s)\log\frac{M_Z^2}{M_W^2}\left[(I_{q_\kappa}^Z)^2+(I_H^Z)^2\right]\\ &+\delta_H^{\rm LSC,h}+\delta_\chi^{\rm LSC,h}-Q_q^2\,L_{\rm em}(s,\lambda^2,m_q^2)\Bigg\}\mathcal{M}_0.\end{aligned} \tag{4.58}$$

To compute the subleading soft-collinear contributions we define a common factor

$$F_L^{\rm SSC} = -\frac{c_W}{s_W^3}\left[\log\frac{|t|}{s}+\log\frac{|u|}{s}\right], \tag{4.59}$$

and separate the corrections to processes with initial-state up- and down-type quarks according to

$$\delta^{\rm SSC}\mathcal{M}^{u_\kappa\bar{u}_\kappa H\chi} = \delta_{\kappa L}\, l(s)\, \frac{F_L^{\rm SSC}}{I^Z_{u_\kappa}}\, \mathcal{M}_0, \tag{4.60}$$

$$\delta^{\rm SSC}\mathcal{M}^{d_\kappa\bar{d}_\kappa H\chi} = -\,\delta_{\kappa L}\, l(s) \sum_{u_i} |V^{\rm CKM}_{u_i d}|^2\, \frac{F_L^{\rm SSC}}{I^Z_{d_\kappa}}\, \mathcal{M}_0. \tag{4.61}$$

Finally, the single-logarithmic corrections are

$$\begin{aligned}\delta^{\rm C}\mathcal{M}^{q_\kappa\bar{q}_\kappa H\chi} = \Bigg\{ &\frac{\alpha}{4\pi}\left[\frac{3}{2s_W^2}\,\frac{m_t^2}{M_W^2}\log\frac{m_t^2}{M_W^2} + \left(\frac{M_Z^2}{8s_W^2 M_W^2} - 2C_\Phi^{\rm ew}\right)\log\frac{M_H^2}{M_W^2}\right] \\ &+ l(s)\left[3C_{q_\kappa}^{\rm ew} + 4C_\Phi^{\rm ew} - \frac{3}{2s_W^2}\,\frac{m_t^2}{M_W^2}\right] + \frac{\alpha}{2\pi}\,Q_q^2\,\log\frac{M_W^2}{\lambda^2}\Bigg\}\,\mathcal{M}_0,\end{aligned} \tag{4.62}$$

$$\begin{aligned}\delta^{\rm PR}\mathcal{M}^{q_\kappa\bar{q}_\kappa H\chi} = \Bigg\{ &\frac{\alpha}{4\pi}\left(\frac{1}{s_W^2} + \frac{\rho_{q_\kappa}}{c_W^2}\right)\left[\frac{5}{6}\log\frac{M_H^2}{M_W^2} - \frac{9+6s_W^2-32s_W^4}{18s_W^2}\log\frac{m_t^2}{M_W^2}\right] \\ &+ l(s)\left[-b_{WW}^{\rm ew} + \rho_{q_\kappa}\frac{s_W}{c_W}\,b_{AZ}^{\rm ew}\right]\Bigg\}\,\mathcal{M}_0.\end{aligned} \tag{4.63}$$

Interchanging the initial-state particles does not modify the results, for the same symmetry reasons explained before.

For $HZ$ production we can easily perform the matching between the $\lambda$-logarithms and the $\epsilon$ poles. In fact, since the only virtual diagram that involves the exchange of a photon is the correction to the quark vertex, we know exactly this correction factor in dimensional regularization. By setting $\mu^2 = s$, all the dominant contributions vanish, and the same must hold for the Sudakov corrections expressed in logarithmic form. To this end, we can neglect all the terms proportional to $\log(M_W^2/\lambda^2)$, and add the following term to the final result,

$$\delta_\lambda^{\rm match}\mathcal{M}^{q_\kappa\bar{q}_\kappa HZ_\lambda} = Q_q^2\,[L(s) - 3l(s)]\,\mathcal{M}_0. \tag{4.64}$$

The double-logarithmic term is needed to cancel the photonic contribution to $C^{\rm ew}$ in the $\delta^{\rm LSC}$ factors, while the single-logarithmic one removes the charge-dependence of $C^{\rm ew}$ in $\delta^{\rm C}$.

## 4.4 The $HZj$ associated production

The last process to be implemented is the $HZj$ associated production process. The quark-initiated partonic process is given by

$$q(p_1)\,\bar{q}(p_2) \to H(p_3)\,Z(k)\,g(p_6) \to H(p_3)\,e^+(p_4)\,e^-(p_5)\,g(p_6), \tag{4.65}$$

plus initial-state particles interchanged and crossing-symmetry processes. The matrix elements for the production of a transverse and a longitudinal $Z$ boson are similar to the ones in $HZ$ production, with the insertion of a gluon,

$$q(p_1)\,\bar{q}(p_2)\,H(-p_3)\,Z_\lambda(-k)\,g(-p_6) \to 0, \tag{4.66}$$

$$\mathcal{M}_0^{q\bar{q}HZ_Tg} = -\frac{i}{q^2}\frac{e^2}{s_W c_W}\,M_Z\,g_s t^a \sum_\kappa I^Z_{q_\kappa}\,S_\kappa^{\mu\nu}\,\epsilon_\mu^T(-k)\,\epsilon_\nu(-p_6), \tag{4.67}$$

$$\mathcal{M}_0^{q\bar{q}HZ_Lg} = i\mathcal{M}_0^{q\bar{q}H\chi g} = -\frac{i}{q^2}\frac{e^2}{2s_W c_W}\,g_s t^a \sum_\kappa I^Z_{q_\kappa}\,S_\kappa^{\mu\nu}\,(-k+p_3)_\mu\,\epsilon_\nu(-p_6). \tag{4.68}$$

The fermionic current $S_\kappa^{\mu\nu}$ is defined in eq. (4.33). The Sudakov corrections are almost equal to the case without the jet, apart from the subleading soft-collinear contributions. For the transverse case we have

$$\delta^{\mathrm{SSC,n}}\mathcal{M}^{q_\kappa\bar{q}_\kappa HZ_T g} = -\left[2\,l(s)\,R_{q_\kappa q_\kappa} + \frac{\alpha}{2\pi}\log\frac{M_W^2}{\lambda^2}\,Q_q^2\right]\log\frac{|r_{12}|}{s}\mathcal{M}_0, \tag{4.69}$$

$$\begin{aligned}\delta^{\mathrm{SSC},\pm}\mathcal{M}^{u_\kappa\bar{u}_\kappa HZ_T g} = \frac{l(s)\,\delta_{\kappa L}}{I^Z_{u_L}}\Bigg\{&-\frac{1}{s_W^2}\left[\frac{1}{2}s_W c_W\left(\log\frac{|r_{13}|}{s}+\log\frac{|r_{23}|}{s}\right)+I^Z_{d_L}\log\frac{|r_{12}|}{s}\right.\\&\left.+\frac{c_W^3}{s_W}\left(\log\frac{|r_{14}|}{s}+\log\frac{|r_{24}|}{s}\right)\right]+2c_W^3\left(\frac{Q_u}{s_W}-\frac{I^Z_{u_L}}{c_W}\right)\log\frac{|r_{34}|}{s}\Bigg\}\mathcal{M}_0,\end{aligned} \tag{4.70}$$

$$\begin{aligned}\delta^{\mathrm{SSC},\pm}\mathcal{M}^{d_\kappa\bar{d}_\kappa HZ_T g} = \frac{l(s)\,\delta_{\kappa L}}{I^Z_{d_L}}\Bigg\{&\frac{1}{s_W^2}\sum_{u_i}|V^{\mathrm{CKM}}_{u_i d}|^2\left[\frac{1}{2}s_W c_W\left(\log\frac{|r_{13}|}{s}+\log\frac{|r_{23}|}{s}\right)\right.\\&\left.-I^Z_{u_L}\log\frac{|r_{12}|}{s}+\frac{c_W^3}{s_W}\left(\log\frac{|r_{14}|}{s}+\log\frac{|r_{24}|}{s}\right)\right]\\&+2c_W^3\left(\frac{Q_d}{s_W}-\frac{I^Z_{d_L}}{c_W}\right)\log\frac{|r_{34}|}{s}\Bigg\}\mathcal{M}_0,\end{aligned} \tag{4.71}$$

having distinguished between up- and down-type initial quarks. The corrections to the longitudinal case take the form

$$\begin{aligned}\delta^{\mathrm{SSC,n}}\mathcal{M}^{q_\kappa\bar{q}_\kappa H\chi g} = &-2l(s)\left[R_{q_\kappa q_\kappa}\log\frac{|r_{12}|}{s}+\left(iI^Z_{H\chi}\right)^2\log\frac{|r_{34}|}{s}\right]\mathcal{M}_0\\&+\frac{\alpha}{2\pi}\,Q_q^2\log\frac{M_W^2}{\lambda^2}\log\frac{|r_{12}|}{s}\mathcal{M}_0,\end{aligned} \tag{4.72}$$

$$\begin{aligned}\delta^{\mathrm{SSC},\pm}\mathcal{M}^{u_\kappa\bar{u}_\kappa H\chi g} = &-\frac{l(s)\delta_{\kappa L}}{s_W^2 I^Z_{u_L}}\left[I^Z_{d_L}\log\frac{|r_{12}|}{s}+\frac{R_{u_L\phi^-}}{iI^Z_{H\chi}}\log\frac{|r_{34}|}{s}\right.\\&\left.+\frac{c_W}{2s_W}\left(\log\frac{|r_{13}|}{s}+\log\frac{|r_{14}|}{s}+\log\frac{|r_{23}|}{s}+\log\frac{|r_{24}|}{s}\right)\right]\mathcal{M}_0,\end{aligned} \tag{4.73}$$

$$\begin{aligned}\delta^{\mathrm{SSC},\pm}\mathcal{M}^{d_\kappa\bar{d}_\kappa H\chi g} = \frac{l(s)\delta_{\kappa L}}{s_W^2 I^Z_{d_L}}\Bigg\{&-\log\frac{|r_{34}|}{s}\frac{R_{d_L\phi^-}}{iI^Z_{H\chi}}+\sum_i|V^{\mathrm{CKM}}_{u_i d}|^2\left[-I^Z_{u_L}\log\frac{|r_{12}|}{s}\right.\\&\left.+\frac{c_W}{2s_W}\left(\log\frac{|r_{13}|}{s}+\log\frac{|r_{14}|}{s}+\log\frac{|r_{23}|}{s}+\log\frac{|r_{24}|}{s}\right)\right]\Bigg\}\mathcal{M}_0.\end{aligned} \tag{4.74}$$

These results also hold for the processes with exchanged initial quarks, because they would require the permutations $r_{13}\leftrightarrow r_{23}$ and $r_{14}\leftrightarrow r_{24}$, but the expressions above are symmetric under it. For this process, the matching of the $\lambda$-logarithms into $\epsilon$ poles is not as straightforward as in the $HZ$ case, and we cannot define a matching contribution analogous to eq. (4.64). Nevertheless, the complete photonic one-loop corrections can be obtained by evaluating the analytic QCD virtual amplitude with $C_F = 1$ and $C_A = 0$. This does not represent the Sudakov photonic corrections, but it is still a result that, in the high-energy limit, gives the correct behaviour. By inserting it in place of the formulae for the Sudakov

photonic corrections, adding also a term

$$\delta_{\lambda}^{\text{match}} \mathcal{M}^{q_\kappa \bar{q}_\kappa H Z_\lambda g} = Q_q^2 \left[ L(s) - 3l(s) + 2l(s) \log \frac{|r_{12}|}{s} \right] \mathcal{M}_0, \tag{4.75}$$

in order to cancel the photonic contributions to $\delta^{\text{LSC}}$, $\delta^{\text{SSC}}$ and $\delta^{\text{C}}$, we can then have more precise predictions than what would be obtained by simply neglecting the $\log(M_W^2/\lambda^2)$ terms without introducing any matching factor.

## 4.5 Input parameters

In this thesis we consider LHC proton-proton collisions at a center-of-mass energy of 13 TeV. As input parameters to study $HV$ and $HVj$ production we use the following masses and widths for the gauge bosons,

$$\begin{aligned} M_Z &= 91.1876 \text{ GeV}, & \Gamma_Z &= 2.509 \text{ GeV}, \\ M_W &= 80.399 \text{ GeV}, & \Gamma_W &= 2.099 \text{ GeV}. \end{aligned} \tag{4.76}$$

The widths of the $W$ and $Z$ bosons are consistently calculated at NLO QCD using the other input parameters. We consider the Higgs boson on shell, with zero width and a mass equal to $M_H = 125$ GeV. Assigning a finite width to the Higgs boson in the final state could invalidate some Ward identities of the electroweak theory: proceeding with zero width, we avoid these possible problems. The treatment of unstable particles is done in the complex-mass scheme [104]. In this scheme the masses are considered as complex quantities,

$$\mu_i^2 = M_i^2 - \mathrm{i}\Gamma_i M_i \qquad \text{for} \quad i = W, Z, t. \tag{4.77}$$

This leads to complex couplings and, in particular, to a complex weak mixing angle. The electroweak couplings are then derived according to the $G_\mu$ scheme, that represents the optimal choice to describe pure SU(2) interactions at the electroweak scale. The fundamental parameters are the (complex-valued) masses of the $W$ and $Z$ bosons and the Fermi constant, $G_\mu = 1.16637 \times 10^{-5}$ GeV$^{-2}$. Starting from them, the Weinberg angle and the electromagnetic coupling constant are given by

$$s_W^2 \equiv 1 - \frac{\mu_W^2}{\mu_Z^2} = 1 - c_W^2, \qquad \alpha = \left| \frac{\sqrt{2} s_W^2 \mu_W^2 G_\mu}{\pi} \right| = \frac{1}{132.28}, \tag{4.78}$$

and all the other couplings can be derived accordingly. In this scheme, the weak corrections to muon decay are included in the renormalization of the electric charge [40]: as a consequence, the electroweak corrections are independent of logarithms of the light-quark masses. Moreover, this definition of $\alpha$ effectively resums the contributions associated with the running of the electromagnetic coupling constant from zero energy transfer to the electroweak scale $M_W$, that correspond to the factor $\Delta\alpha(M_W^2)$ of eq. (3.42). For the values of the CKM matrix we use

$$|V^{\text{CKM}}| = \begin{array}{c} \\ u \\ c \\ t \end{array} \begin{array}{c} \begin{array}{ccc} d & s & b \end{array} \\ \begin{pmatrix} 0.97428 & 0.2253 & 0.00347 \\ 0.2252 & 0.97345 & 0.0410 \\ 0.00862 & 0.0403 & 0.999152 \end{pmatrix} \end{array}. \tag{4.79}$$

We use the NNPDF2.3_as_0119_qed parton distribution set [105], that includes QED contributions to the parton evolution (PDF number 244800 from LHAPDF6 [106]). The value of

$\alpha_s(M_Z)$ from this set is 0.119. Finally, in $HV$ production, the renormalization and factorization scales are set equal to the invariant mass of the $HV$ pair at underlying-Born level,

$$\mu_R = \mu_F = M_{HV}, \qquad M_{HV}^2 = \left(p_H + p_{l_1} + p_{\bar{l}_2}\right)^2, \tag{4.80}$$

while in $HVj$ the `MiNLO` procedure discussed in Sec. 2.5.1 is applied, and the scales are set accordingly.

## 4.6 Validations

We now illustrate several validation checks that we have done. We first compare the NLO EW predictions of the `POWHEG BOX RES` for $HW$ and $HZ$ production with the fixed-order NLO results obtained with `HAWK` [41]. To this end, we set the flag `qed_qcd` to 1 in the input file in order to compute only electroweak corrections. These are obtained by including the virtual contribution and the real emission of a photon, as explained in Sec. 2.1.1. Then, we verify the validity of the leading-pole approximation and carry out some studies on the relevance of the vector-boson polarizations, both at leading order and with the inclusion of NLL EW corrections.

Since in these tests we include different contributions to the virtual electroweak cross section (i.e. the full corrections or their Sudakov approximation), we need to be able to switch between them. The `POWHEG BOX RES` implementation of the processes under study offers this possibility, by changing the value of the flag `select_ew_virt` in the input file. When this flag is set to 1 the full virtual contribution, provided by `OpenLoops`, is evaluated. By setting it to 2, instead, the virtual electroweak cross section is obtained by computing only its high-energy limit, using the formulae derived in Secs. 4.1.7 and 4.2 for the associated production of a Higgs boson, a $W$ boson and eventually a jet, and applying the formulae in Secs. 4.3.4 and 4.4 for $HZ/HZj$. The leading-order and the real terms are obtained by considering the corresponding complete matrix elements, i.e. without applying the leading-pole approximation, as explained in Sec. 3.6.2. The Born amplitudes that enter the Sudakov corrections are instead factorized into production and decay terms, and are computed in the high-energy limit. The corresponding formulae can be found in the previous sections of this chapter. Finally, by choosing 0, the virtual electroweak contribution is completely excluded. If no value is selected, the default behaviour of the code is to perform the full calculation.

### 4.6.1 Comparison of the electroweak corrections to $HV$ production with `HAWK`

In this section we compare the NLO EW `POWHEG BOX RES` implementation of $HV$ production with the NLO results obtained with `HAWK`. This code was originally designed for the description of Higgs boson production via vector boson fusion, but the topology of the two processes is very similar since the same amplitudes appear in a crossed variant. The code has then been adapted by the authors to deal also with the associated production processes.

`HAWK` gives the possibility to include or omit real corrections due to photon-initiated processes: since in the `POWHEG BOX RES` these ones have not been taken into account because of the smallness of the photon PDF, we exclude them accordingly in the `HAWK` computation. The CKM matrix elements are set to

$$|V_{ud}^{\rm CKM}| = |V_{cs}^{\rm CKM}| = 0.974, \qquad |V_{us}^{\rm CKM}| = |V_{cd}^{\rm CKM}| = \sqrt{1 - |V_{ud}^{\rm CKM}|^2}, \tag{4.81}$$

omitting the mixing with the third generation of quarks. Moreover, owing to the smallness of the $b\bar{b}$-initiated contribution in $HZ$ production, this channel has not been included. Finally, since in HAWK the renormalization and factorization scales are by default set to the sum of the Higgs and the vector boson physical masses,

$$\mu_R = \mu_F = M_V + M_H, \qquad V = W, Z, \tag{4.82}$$

in this comparison we set the POWHEG BOX RES scales accordingly. Moving to event selections, photons are recombined with charged leptons if $R_{\gamma l} < 0.1$, where $R_{\gamma l}$ is the angular separation variable in the $y - \phi$ plane, between the photon and the charged lepton,

$$R_{\gamma l} = \sqrt{(y_\gamma - y_l)^2 + \Delta\phi_{\gamma l}^2}. \tag{4.83}$$

Here, $y$ denotes the rapidity, and $\phi_{\gamma l}$ the angle between $l$ and $\gamma$. In case of recombination of the photon with the lepton, we simply add their momenta and consider the resulting particle as a "dressed lepton". If more than one charged lepton is present in the final state, the possible recombination is performed with the lepton having the smallest value of $R_{\gamma l}$. After recombination, we apply the following cuts on the charged leptons,

$$p_T^l > 20\,\text{GeV}, \qquad |y^l| < 2.5, \tag{4.84}$$

while for $HW$ production we also require a missing transverse momentum of

$$\not{E}_T > 25\,\text{GeV}. \tag{4.85}$$

In the following we show the results for this comparison.

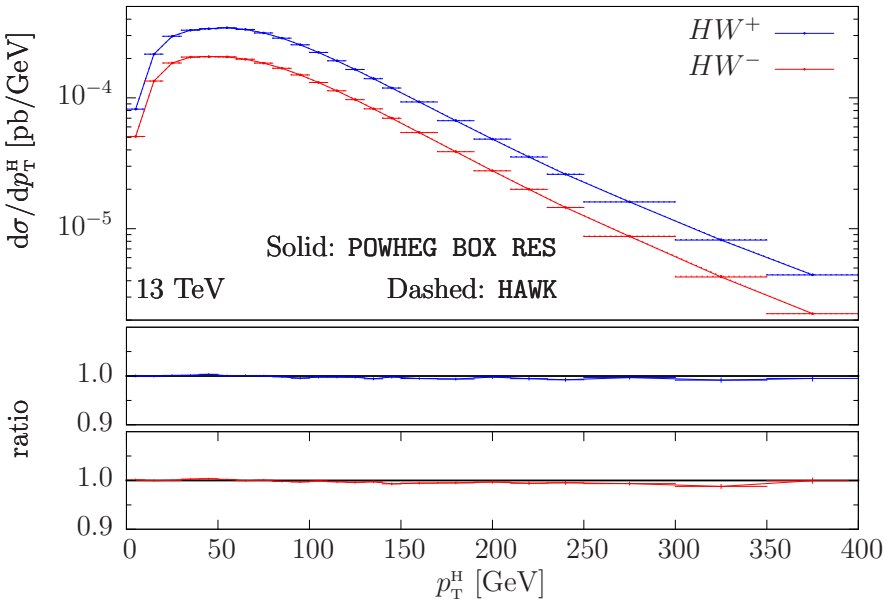


Figure 4.2: NLO EW predictions for the transverse momentum of the Higgs boson in $HW$ production. Comparison between the POWHEG BOX RES (solid lines) and the HAWK (dashed lines) implementations, for both $HW^-$ and $HW^+$ production. Due to the complete overlap of the curves, the dashed lines are hardly visible.

In the figures related to $HW$ production, the POWHEG BOX RES results are plotted with a solid line, while the HAWK ones are plotted with a dashed line. In many plots some lines are

hardly visible: this is due to the complete overlap among the curves. The distributions for $HW^+$ production are reported in blue, and the ones for $HW^-$ production are shown in red. The vertical bars represent the statistical errors associated to the integration procedure.

Figure 4.2 shows this comparison for the Higgs boson transverse-momentum distribution. The agreement between the POWHEG BOX RES and the HAWK implementations is perfect within the statistical uncertainties, such that the two curves are almost indistinguishable. Similar conclusions can be drawn for the Higgs boson rapidity and pseudorapidity, reported in figs. 4.3 and 4.4: the two curves are indistinguishable in the whole $y^H$ and $\eta^H$ ranges considered. Then, in figs. 4.5 and 4.6 we show the missing transverse momentum and the rapidity of the lepton: for these distributions too the agreement between the implementations is remarkable.

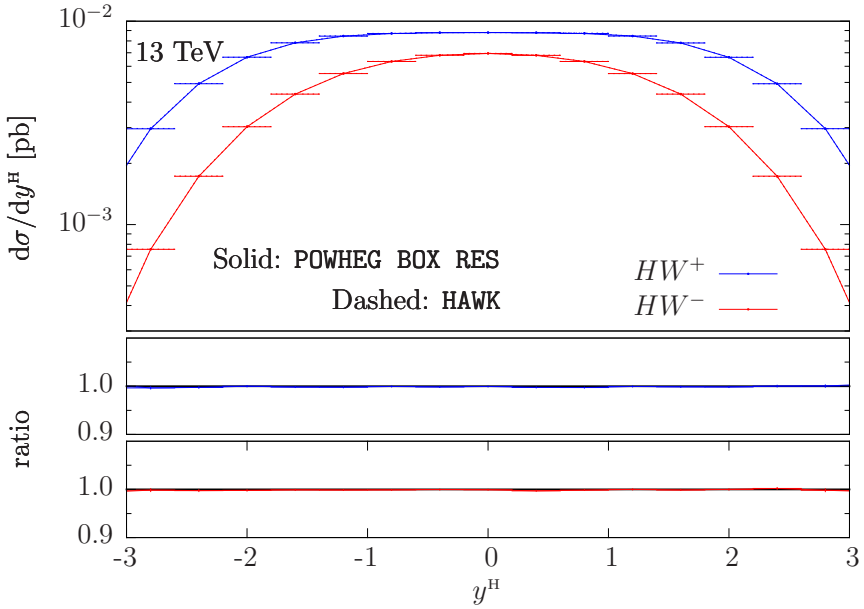


Figure 4.3: NLO EW predictions for the rapidity of the Higgs boson. Same labels as in fig. 4.2.

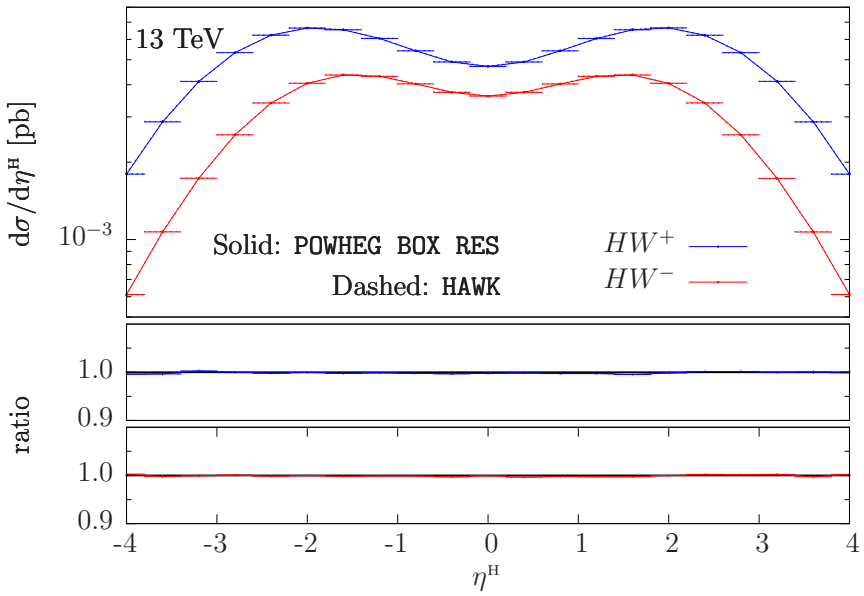


Figure 4.4: NLO EW predictions for the pseudorapidity of the Higgs boson. Same labels as in fig. 4.2.

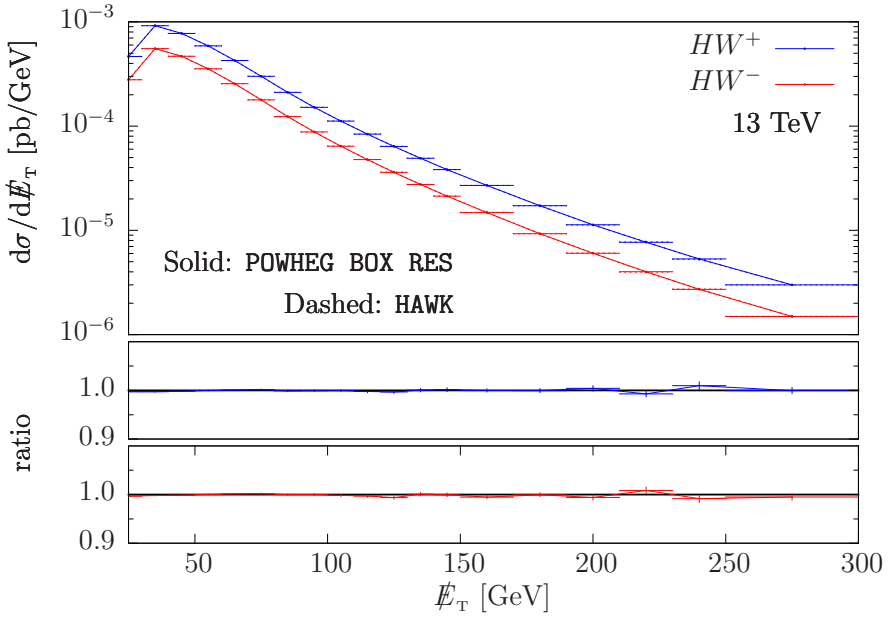


Figure 4.5: NLO EW predictions for the missing transverse momentum. Same labels as in fig. 4.2.

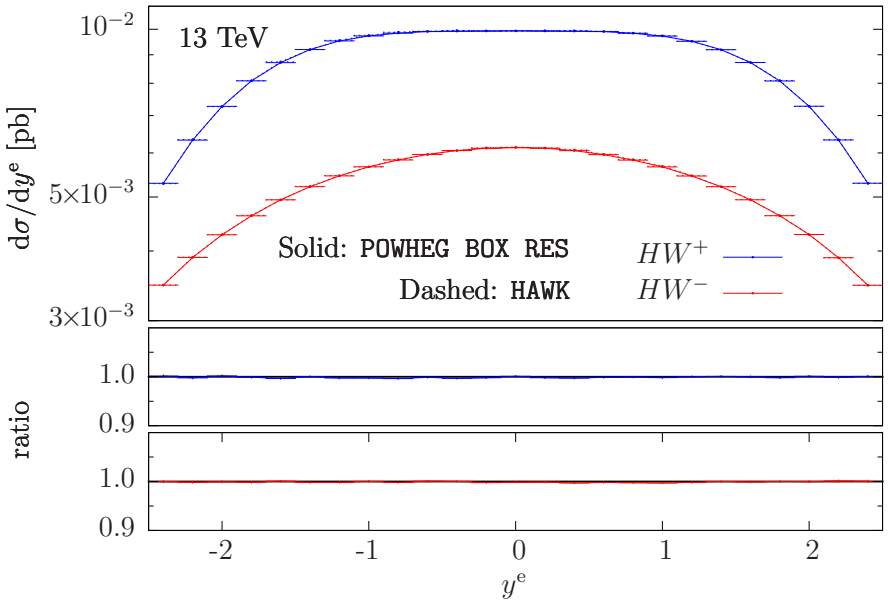


Figure 4.6: NLO EW predictions for the rapidity of the lepton. Same labels as fig. 4.2.

At the end, in figs. 4.7 - 4.11 we repeat this comparison for $HZ$ production, drawing the same conclusions. We remark that, even for this series of plots, the complete overlap between the two results makes one of the curves hardly visible. Nevertheless, each plot contains two curves.

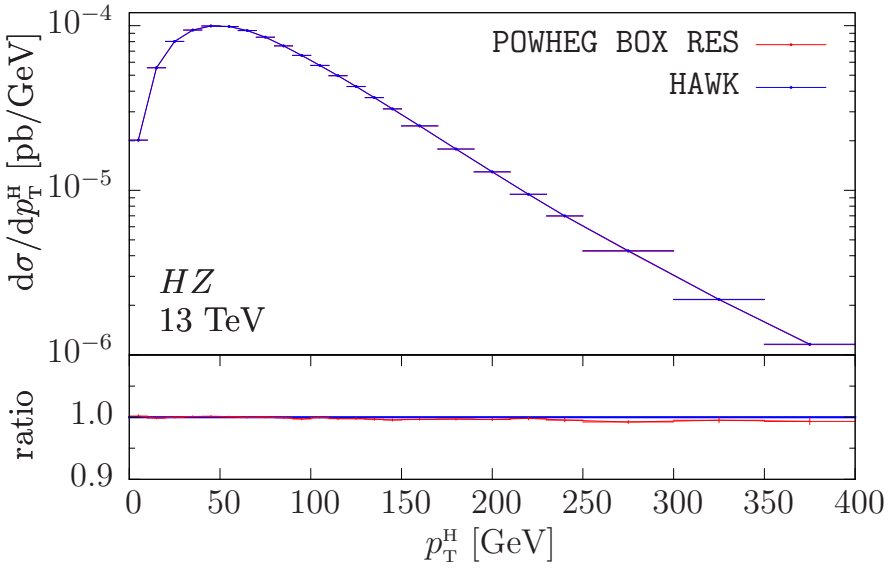


Figure 4.7: NLO EW predictions for the transverse momentum of the Higgs boson in $HZ$ production. Comparison between the POWHEG BOX RES and the HAWK implementations.

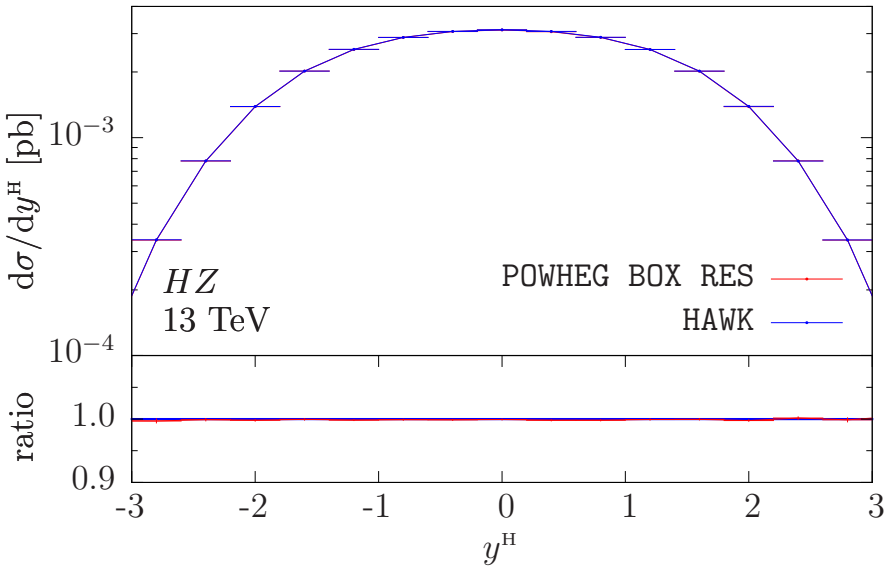


Figure 4.8: NLO EW predictions for the rapidity of the Higgs boson. Same labels as in fig. 4.7.

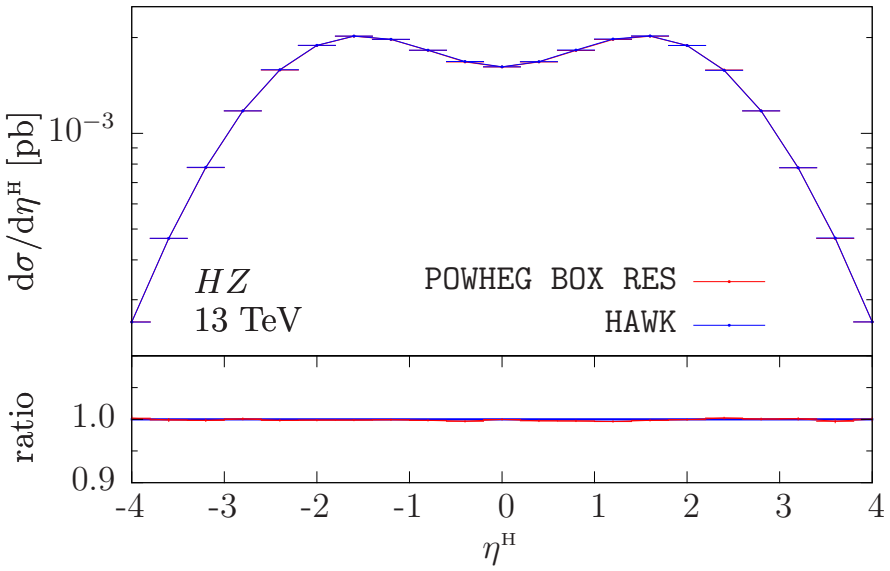


Figure 4.9: NLO EW predictions for the pseudorapidity of the Higgs boson. Same labels as in fig. 4.7.

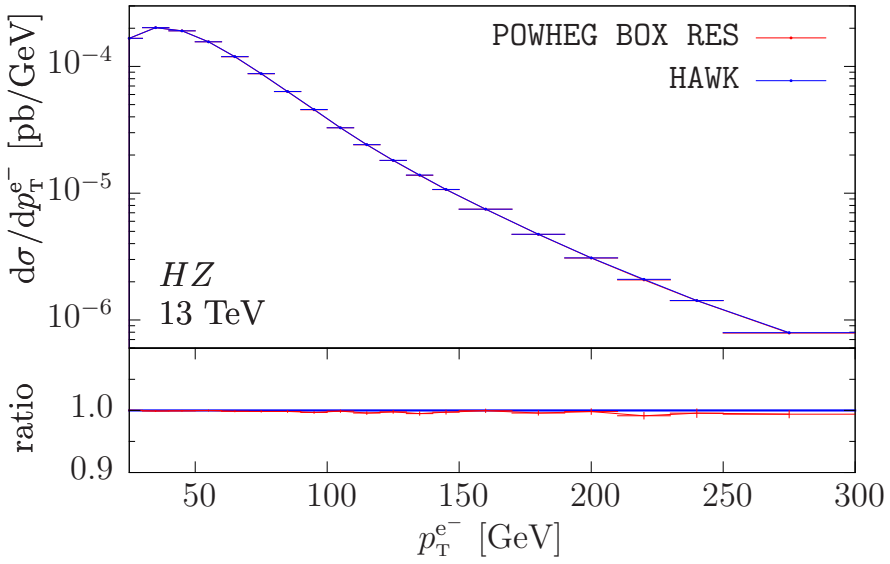


Figure 4.10: NLO EW predictions for the transverse momentum of the electron. Same labels as in fig. 4.7.

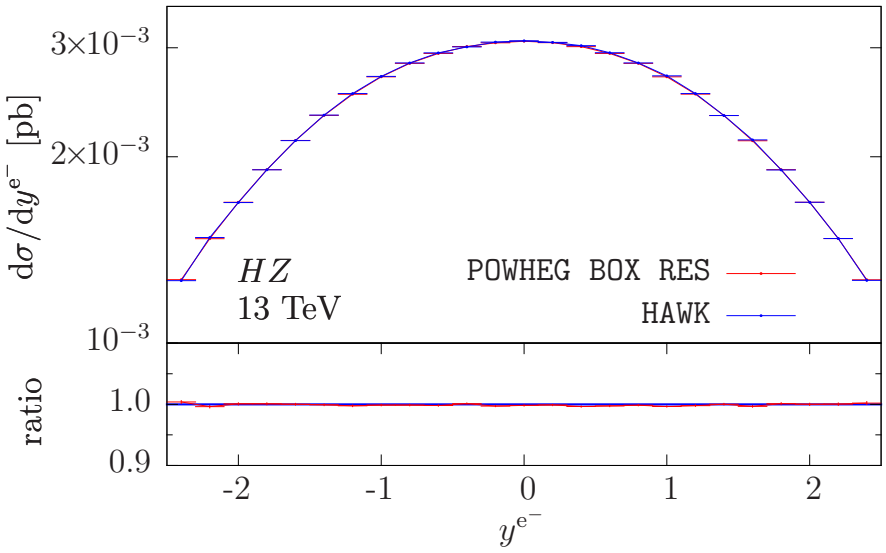


Figure 4.11: NLO EW predictions for the rapidity of the electron. Same labels as in fig. 4.7.

### 4.6.2 Validation of the leading-pole approximation

In order to implement the Sudakov corrections, we first have to make sure that the leading-pole approximation provides a good estimate of the full matrix element. We focus on $HW$ and $HWj$ production: we consider leading-order results, and we compare the complete results with the ones obtained using the approximated matrix elements. For $HWj$, we apply the `MiNLO` procedure described in Sec. 2.5.1 in order not to require a minimum transverse momentum for the leading jet. In the plots, the complete results are reported with a solid line, while the approximated ones are shown with a dashed line. In some plots, due to the overlap between the solid and the dashed curves, the latter is hardly visible. Nevertheless, each plot contains both solid and dashed lines. The vertical bars represent the statistical errors associated to the integration procedure.

| | $HW^-$ | $HW^+$ | $HW^-j$ | $HW^+j$ |
|---|---|---|---|---|
| $\sigma^{\text{LO}}$ [fb] | $51.19 \pm 0.04$ | $80.09 \pm 0.06$ | $44.07 \pm 0.03$ | $69.53 \pm 0.05$ |
| $\sigma^{\text{LO}}_{\text{LPA}}$ [fb] | $50.89 \pm 0.04$ | $79.64 \pm 0.06$ | $43.83 \pm 0.03$ | $69.15 \pm 0.05$ |

Table 4.1: Total leading-order cross section for the $HW$ and $HWj$ production processes at a center-of-mass energy of $\sqrt{s} = 13$ TeV, for the complete calculation and for its leading-pole approximation. The $HWj$ cross sections have been computed with the `MiNLO` procedure active.

We begin by giving the total cross sections in tab. 4.1: the differences between the two implementations are less than 1%. Moving to more differential cross sections, we plot the $W$-boson transverse momentum in fig. 4.12. These distributions disagree for values of $p_T$ below 60 GeV, with discrepancies that reach 10%, while above this value the agreement between the two implementations is remarkable. This is due to the fact that, if the partonic center-of-mass energy is not high enough, when performing the on-shell projection the argument of the square root in eq. (3.67) becomes negative. When this happens, as explained in Sec. 3.6.1, we set the whole matrix element to zero. As a consequence, the low-$p_T$ region,

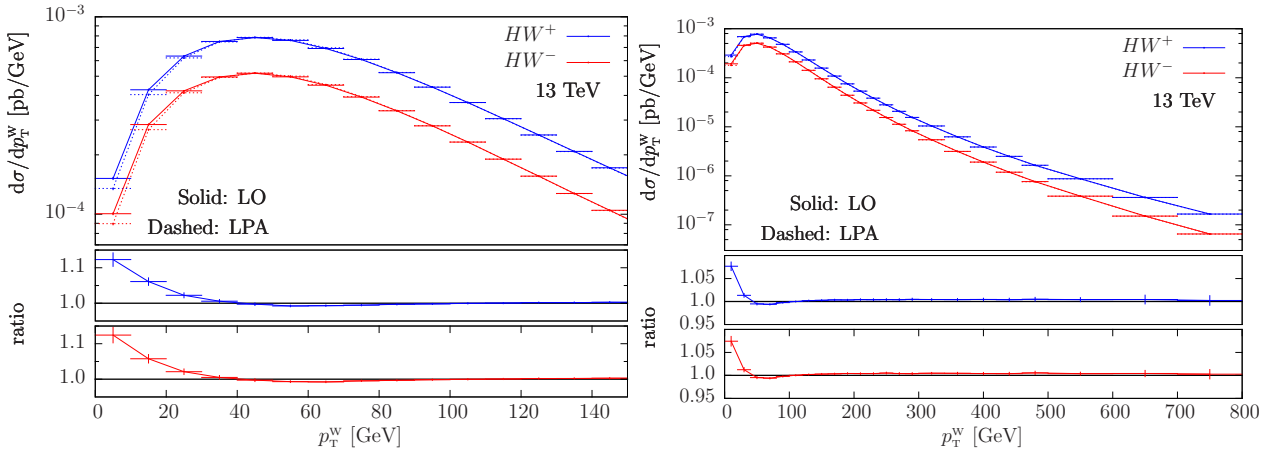


Figure 4.12: Leading-order predictions for the transverse momentum of the $W$ boson in two different ranges of $p_T^W$. Comparison between the full matrix element (solid lines) and its leading-pole approximation (dashed lines), for both $HW^-$ and $HW^+$ production.

generally characterized by a smaller center-of-mass energy, is not described adequately by the leading-pole approximation.

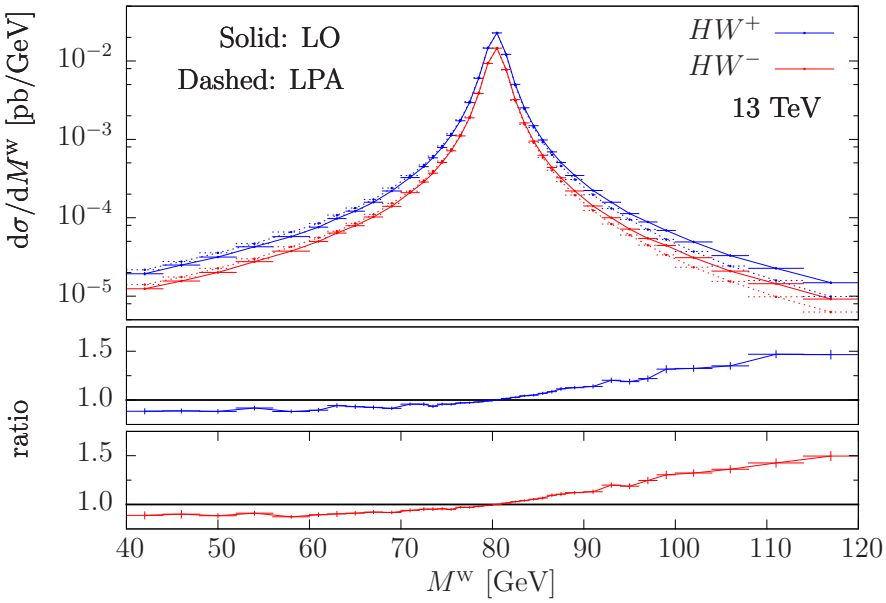


Figure 4.13: Leading-order predictions for the invariant mass of the $W$ boson. Same labels as in fig. 4.12.

The invariant mass distribution of fig. 4.13 shows what one expects from the leading-pole approximation: it agrees with the full result near the resonance peak, while it is not reliable far off resonance.

The same conclusions can be drawn for the lepton transverse momentum, its rapidity and the Higgs boson rapidity, shown in figs. 4.14 - 4.16. Similar results can be obtained for $HWj$ production, as can be seen in figs. 4.17 - 4.21, and for $HZ/HZj$ production, not shown here since they do not differ much from the $W$-boson case.

We can thus conclude that the LPA is a good approximation of the complete calculation, and we can use it to compute the NLL electroweak corrections.

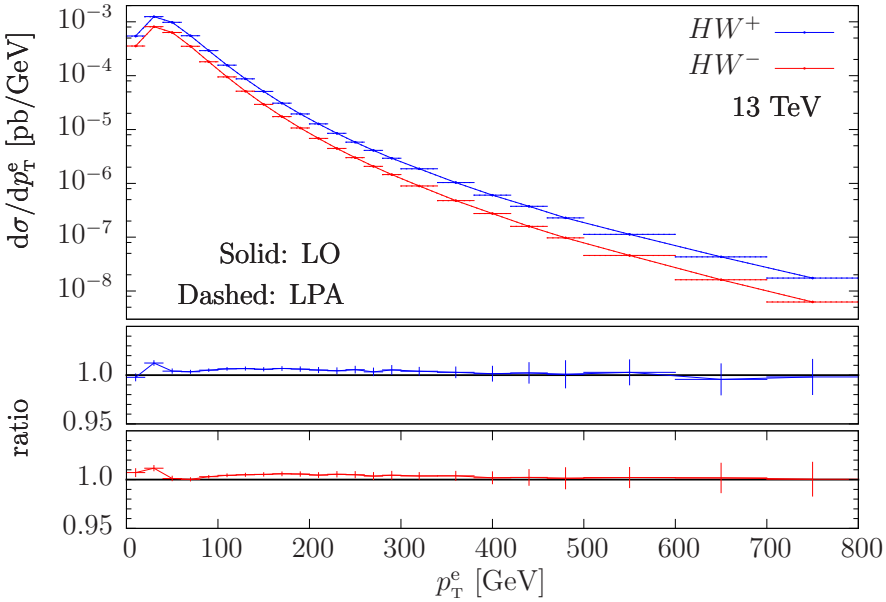


Figure 4.14: Leading-order predictions for the transverse momentum of the lepton. Same labels as in fig. 4.12.

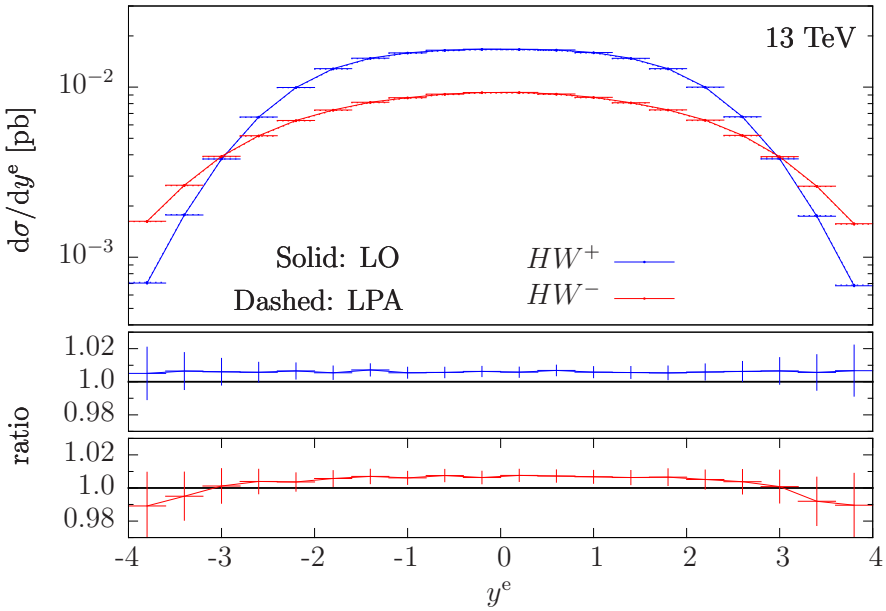


Figure 4.15: Leading-order predictions for the rapidity of the lepton. Same labels as in fig. 4.12.

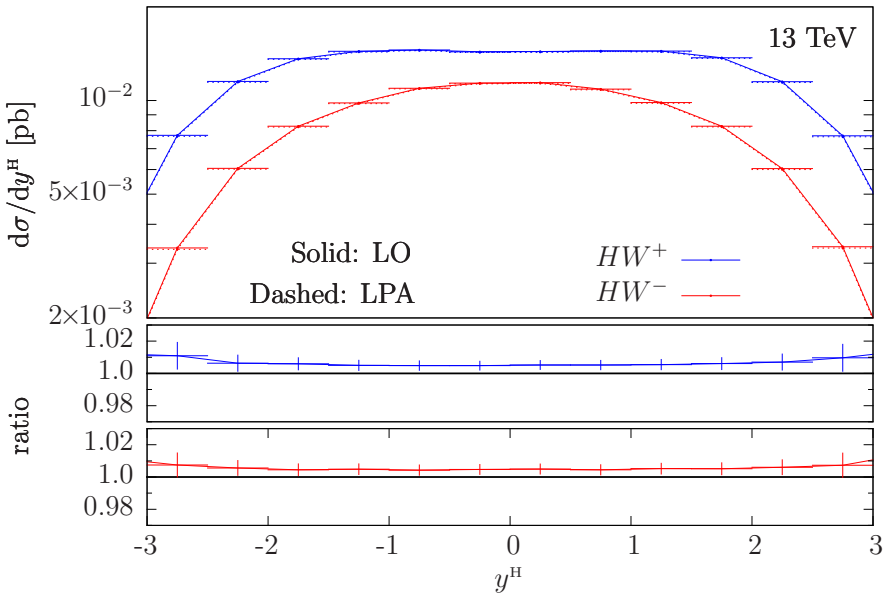


Figure 4.16: Leading-order predictions for the rapidity of the Higgs boson. Same labels as in fig. 4.12.

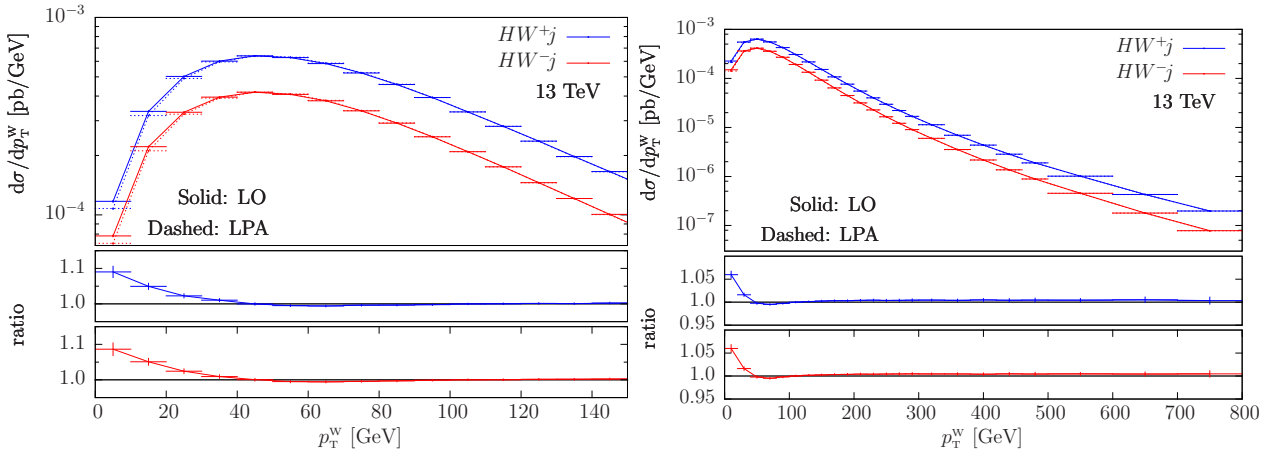


Figure 4.17: Leading-order predictions for the transverse momentum of the $W$ boson in two different ranges of $p_T^W$. Comparison between the full matrix element (solid lines) and its leading-pole approximation (dashed lines), for both $HW^-j$ and $HW^+j$ production.

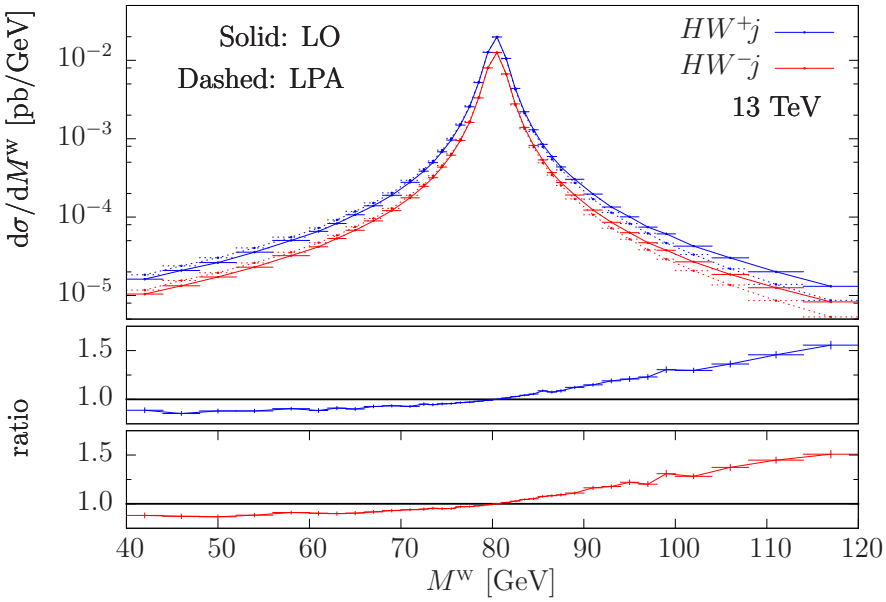


Figure 4.18: Leading-order predictions for the invariant mass of the $W$ boson. Same labels as in fig. 4.17.

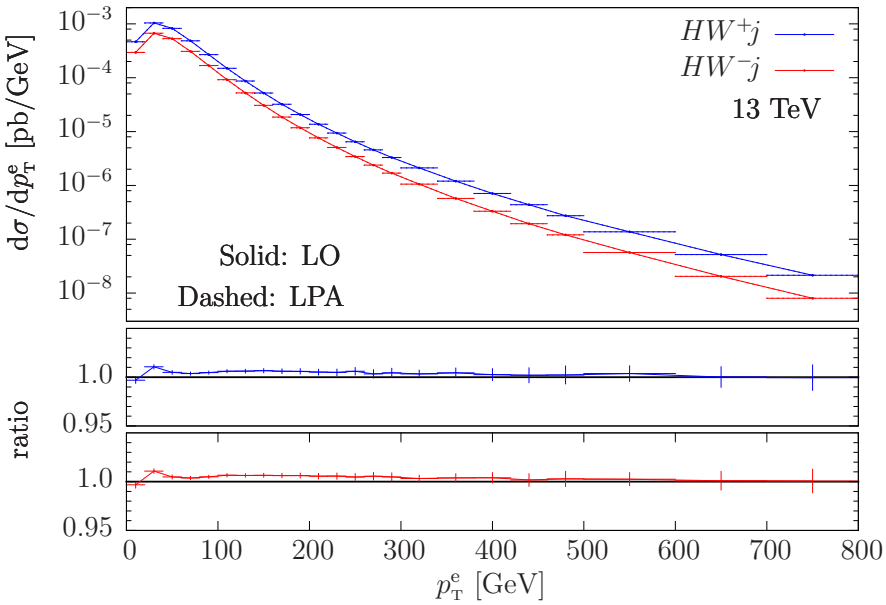


Figure 4.19: Leading-order predictions for the transverse momentum of the lepton. Same labels as in fig. 4.17.

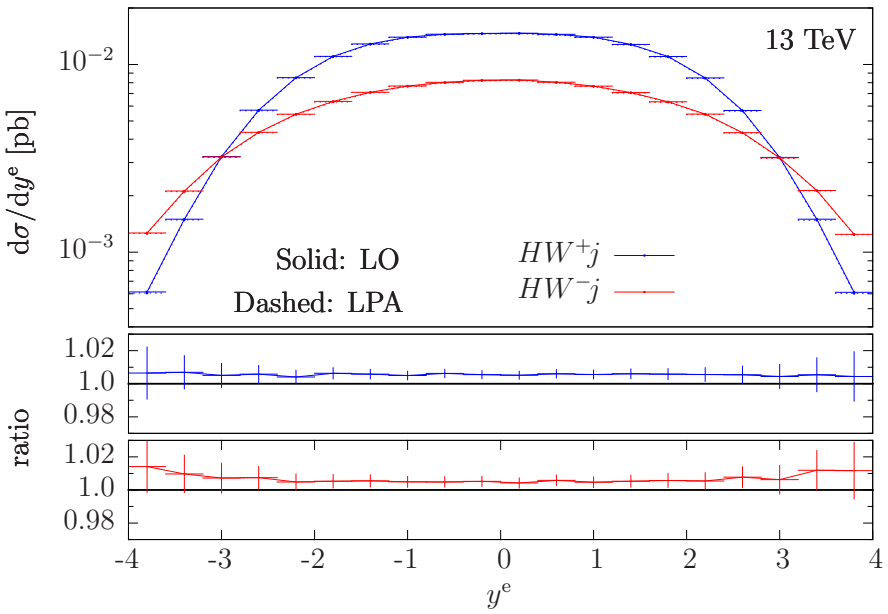


Figure 4.20: Leading-order predictions for the rapidity of the lepton. Same labels as in fig. 4.17.

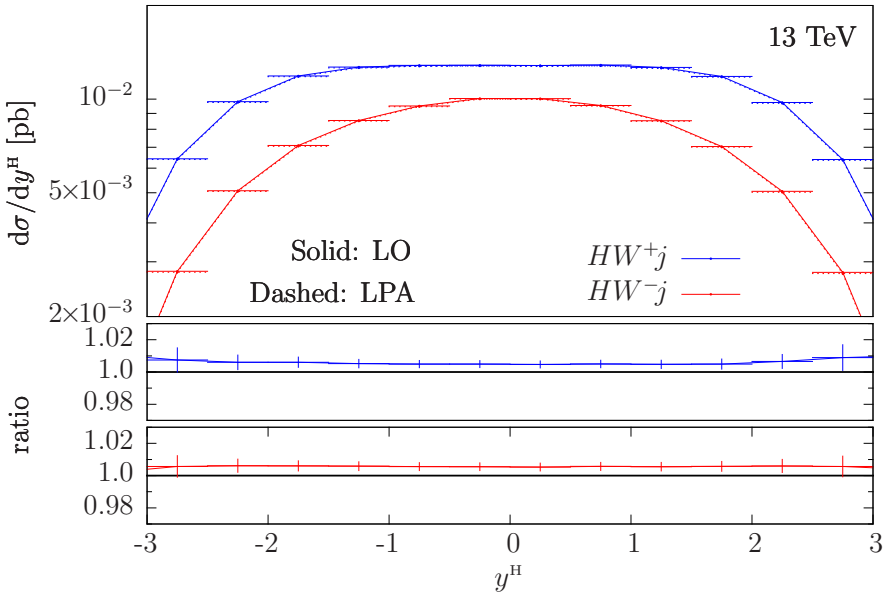


Figure 4.21: Leading-order predictions for the rapidity of the Higgs boson. Same labels as in fig. 4.17.

### 4.6.3 Relevance of the vector-boson polarizations

#### Leading-order results

We now investigate the impact of the different vector-boson polarizations on the total and differential cross sections. As shown before, the matrix element for the production of a transverse vector boson is mass-suppressed, since it contains a factor $M_V$ that is absent in the longitudinal case. When the center-of-mass energy is high enough, then, its contribution to the total result should be negligible. We analyze this energy dependence for $HZ$ and

$HZj$ production. The $W$-boson production processes have the same behaviour, and are not reported.

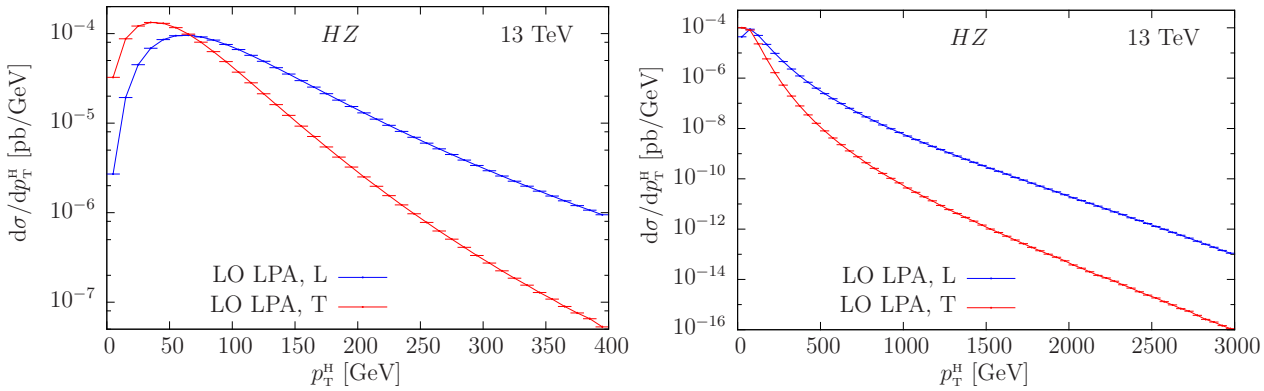


Figure 4.22: Leading-order predictions in leading-pole approximation for the transverse momentum of the Higgs boson in two different ranges of $p_T^H$, for $HZ$ production. Comparison between the results obtained considering a transverse (T) and a longitudinal (L) $Z$ boson.

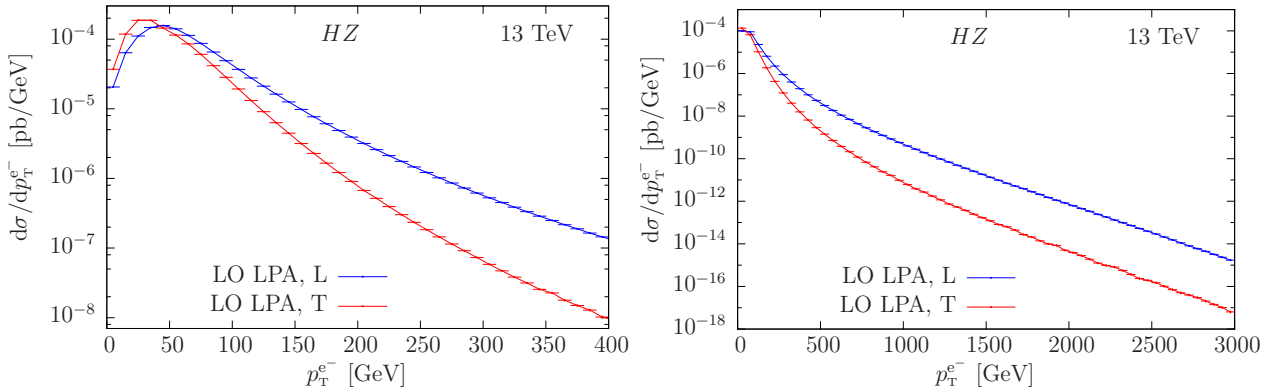


Figure 4.23: Leading-order predictions in leading-pole approximation for the transverse momentum of the electron in two different ranges of $p_T^{e^-}$. Same labels as in fig. 4.22.

By inspecting fig. 4.22, that shows the Higgs boson transverse-momentum distribution in two different ranges of $p_T^H$, we can clearly see that, starting from $p_T^H \sim M_Z$, the contribution coming from the transversely polarized $Z$ boson becomes rapidly subdominant, and in the TeV region it is smaller than the longitudinal one by 2-3 orders of magnitude. Since at leading order the two bosons are produced back-to-back, the partonic center-of-mass energy must be least $\sqrt{s} \gtrsim 2p_T^H$, which in turn means that when $p_T^H > M_Z$ we are approaching the Sudakov region. The same conclusions can be drawn also for the transverse-momentum distribution of the electron, in fig. 4.23. In this case the predominance of the longitudinal polarization becomes manifest at even lower $p_T$ values, around 50 GeV.

In figs. 4.24 and 4.25 we show the same plots for $HZj$ production, for which we can draw very similar conclusions. For this reason, from now on, we focus only on $HZ$ production.

We compare now the leading-order calculation of $HZ$ production performed in leading-pole approximation with the one obtained using only the longitudinal polarization. We expect some discrepancies between the two results, especially in the low-energy region, that decrease when moving towards the Sudakov regime. By analyzing the total cross section, reported in tab. 4.2, we find large differences.

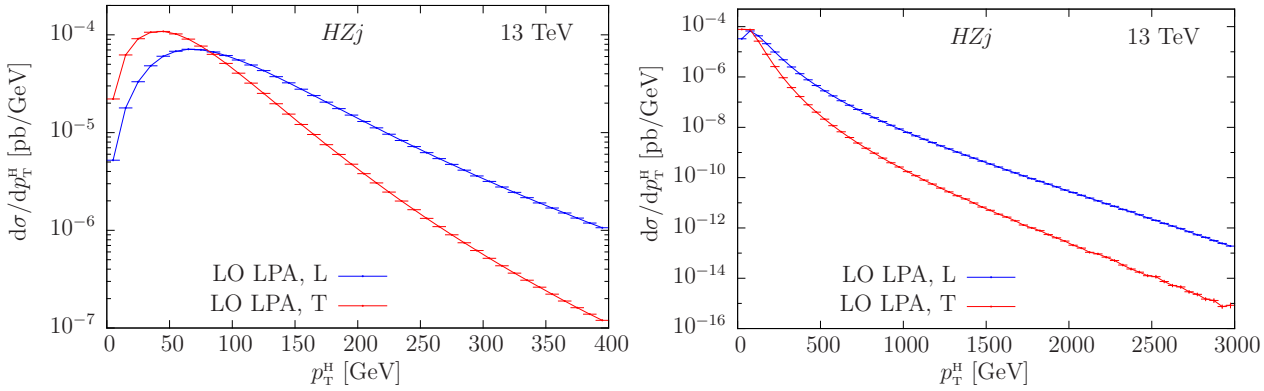


Figure 4.24: Leading-order predictions in leading-pole approximation for the transverse momentum of the Higgs boson in two different ranges of $p_T^H$, for $HZj$ production. Comparison between the results obtained considering a transverse (T) and a longitudinal (L) $Z$ boson.

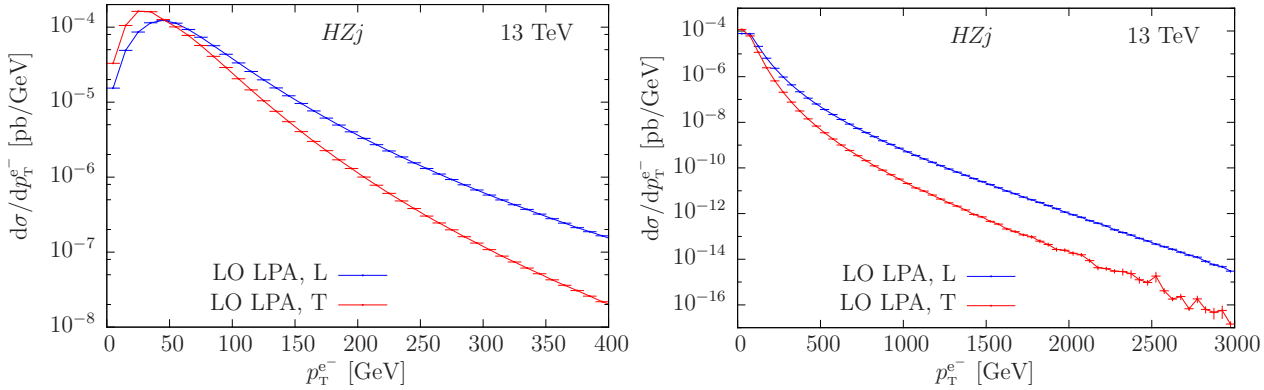


Figure 4.25: Leading-order predictions in leading-pole approximation for the transverse momentum of the electron in two different ranges of $p_T^{e^-}$. Same labels as in fig. 4.24.

| $\sigma_{\text{LPA}}^{\text{LO}}$ [fb] | $\sigma_{\text{LPA,L}}^{\text{LO}}$ [fb] |
|---|---|
| $21.894 \pm 0.005$ | $11.213 \pm 0.002$ |

Table 4.2: Total leading-order cross section in leading-pole approximation for the $HZ$ production process at a center-of-mass energy of $\sqrt{s} = 13$ TeV, and results obtained considering only a longitudinal $Z$ boson.

This result is consistent with the fact that the low-$p_T$ region determines the bulk of the cross section, and here the transverse-polarization contribution is not negligible, being it comparable with the longitudinal one, or even bigger (as shown in fig. 4.22).

The analysis of the Higgs boson transverse momentum, reported in fig. 4.26, confirms this fact. At $p_T^H \sim 500$ GeV (or, in other words, $\sqrt{s} \gtrsim 1$ TeV) the two implementations start overlapping, becoming equal in the TeV region where the transverse component is highly mass-suppressed. The rapidity distribution in fig. 4.27, instead, reflects the striking difference observed at the level of total cross section: here we find differences of order 50% or more between the two implementations.

Summing up, if we limit to leading-order calculations the transverse component cannot be neglected in order to have reliable results, because it contributes to the bulk of the cross section.

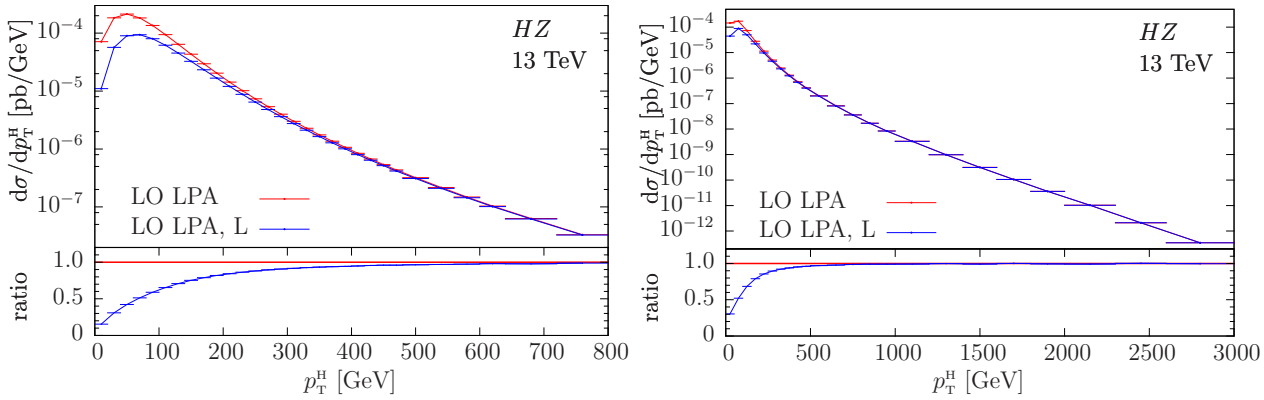


Figure 4.26: Leading-order predictions in leading-pole approximation for the transverse momentum of the Higgs boson in two different ranges of $p_T^H$. Comparison between the results obtained considering the complete process and the ones with a longitudinal $Z$ boson.

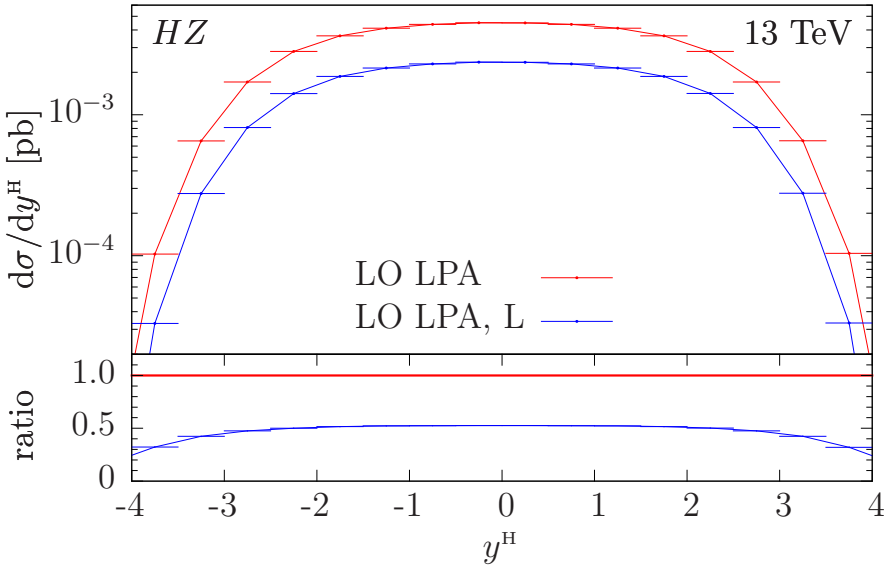


Figure 4.27: Leading-order predictions in leading-pole approximation for the rapidity of the Higgs boson. Same labels as in fig. 4.26.

### Next-to-leading-logarithmic electroweak results

When introducing NLL electroweak corrections, instead, the mass suppression becomes evident also in the low-$p_T$ regions. In the following figures we show the same distributions just analyzed, with the inclusion of the full Born matrix element, the approximated one-loop corrections and real photon radiation.

| $\sigma^{\text{NLL EW}}$ [fb] | $\sigma_{\text{L}}^{\text{NLL EW}}$ [fb] |
|---|---|
| $21.886 \pm 0.005$ | $22.160 \pm 0.005$ |

Table 4.3: Total NLL EW cross section for the $HZ$ production process at a center-of-mass energy of $\sqrt{s} = 13$ TeV, and results obtained considering only a longitudinal $Z$ boson.

We compare the NLL corrections with the ones obtained considering only the longitudinal matrix element. Looking at the total cross sections in tab. 4.3, we find very small differences

between the two implementations. These results are extremely similar to $\sigma^{\rm LO}_{\rm LPA}$ in tab. 4.2: this reflects the small impact of the electroweak corrections on inclusive quantities. The similarity of the results of tab. 4.3, together with the differences between $\sigma^{\rm NLL\,EW}_{\rm L}$ and $\sigma^{\rm LO}_{\rm LPA,L}$ of tab. 4.2, can be ascribed to the fact that, when including NLL EW corrections, the Born term gives the dominant contribution to the total cross section, and it is computed using the full matrix element rather than its expression in leading-pole approximation.

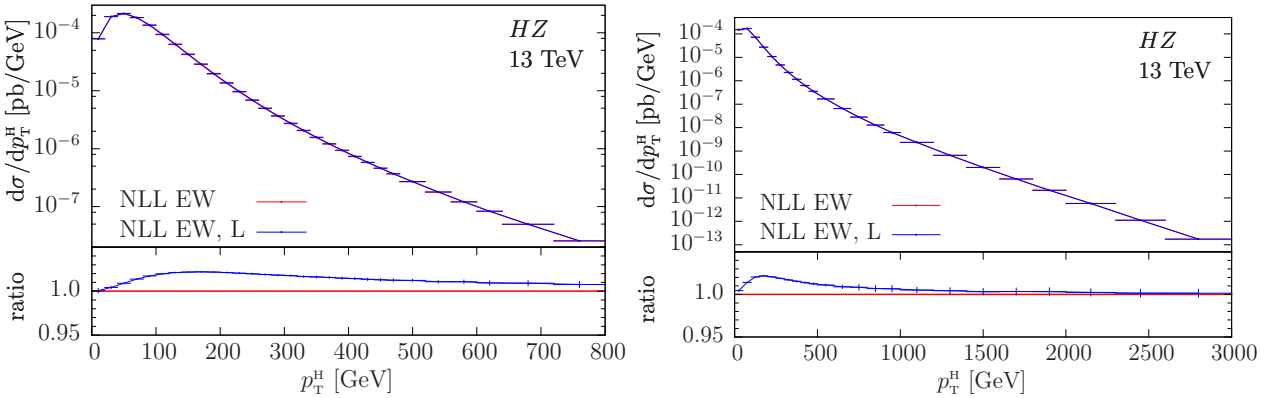


Figure 4.28: NLL EW predictions for the transverse momentum of the Higgs boson in two different ranges of $p_T^H$. Comparison between the results obtained considering the complete process and the ones with a longitudinal $Z$ boson.

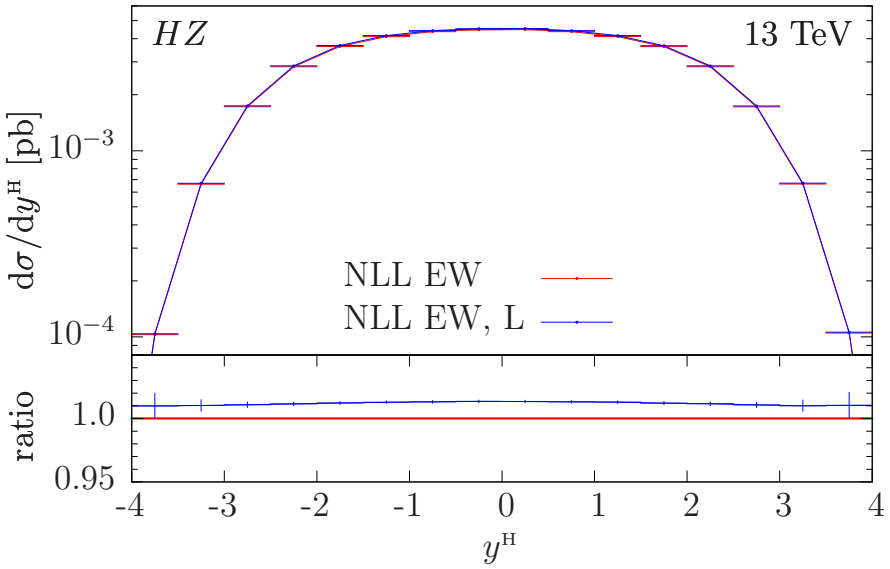


Figure 4.29: NLL EW predictions for the rapidity of the Higgs boson. Same labels as in fig. 4.28.

Moving to more exclusive distributions, in figs. 4.28 and 4.29 we find very good agreement: looking at the transverse momentum of the Higgs boson the low-$p_T$ differences almost vanish, while in the rapidity distribution the differences change from about 50% in fig. 4.27 to 1-2% in fig. 4.29.

In conclusion, since the Sudakov approximation is not fully reliable for mass-suppressed matrix elements, as explained in Sec. 4.1.2, and since their impact on the NLL results is negligible, when considering NLL electroweak calculations we can omit the contribution coming from the transversely polarized vector bosons. In the following, all the results reported with

NLL EW corrections will involve only the longitudinal vector boson. We remark that the contributions from the transverse vector boson are neglected only in the approximated one-loop correction factors, while the Born and real terms are computed considering the full matrix elements.

# Chapter 5

# Phenomenological results

In this chapter we present numerical predictions and kinematic distributions for the associated production of a Higgs boson with a leptonically-decaying vector boson and eventually a jet, in proton-proton collisions at a center-of-mass energy of 13 TeV. We mainly focus on observables that are sensitive to electroweak corrections, since our aim is to investigate their role at hadron colliders. For each process, we first compare fixed-order NLO results: we analyze the differences between the NLO EW corrections and their NLL approximation, and the impact of the electroweak sector on the QCD results. Then, we compare NLO+PS events with QCD and QCD+EW accuracy, applying some kinematic cuts that reproduce the typical experimental setup.

When performing the NLO analysis of processes computed at QCD+EW accuracy, the photon cannot be identified, since all the contributions to the real cross section that share the same underlying Born are collected together by the `POWHEG BOX RES`. Given a Born configuration, then, the radiated particle can be both a photon or a gluon. For this reason photons cannot be recombined with the leptons when the two particles are collinear, and moreover the momentum of the vector boson cannot be reconstructed from its final-state decay products. This limitation could be easily removed in future versions of the `POWHEG BOX RES`, if needed. Nevertheless, the `HEPEVT` common block stores also the momenta of the decaying resonances: we can then have access to the momentum of the vector boson, and we can use it to perform some consistency checks that involve the $HV$ pair. In the rest of the NLO analysis, we focus instead on kinematic distributions that do not involve the photon, namely the total cross section, the Higgs boson distributions and the missing transverse momentum. In case photon distributions are needed at NLO, the code can be run considering only electroweak corrections, as explained in Sec. 2.1.1. In this case, indeed, the radiated particle can only be a photon, and it can easily be identified.

In the ratio plots we use some shorthand notations: the label `QCD` stands for the pure NLO QCD implementation, with `FULL` we refer to the NLO QCD + NLO EW results, and `NLL` denotes the combination of the NLO QCD corrections with the NLL EW ones.

In the generation of events with QCD+EW accuracy, we adopt a variant of the procedure described in Sec. 2.4. To avoid time-consuming computations, we first produce events with NLO QCD + NLL EW accuracy. In this way we obtain events with a weight very similar to the complete QCD+EW cross section. Then, we apply the reweighting procedure starting from these results. In all the plots presented in this chapter, the vertical bars represent the statistical errors associated to the integration procedure.

## 5.1 The interface to the Monte Carlo shower program Pythia 8

In order to generate events with NLO+PS accuracy, including both QCD and QED corrections, we interface our $HV$ and $HVj$ generators to the Monte Carlo shower program `Pythia 8.1`. To this purpose, in the initialization phase we perform the following calls, that are required when interfacing `Pythia 8.1` to NLO+PS generators:

```
pythia.readString("SpaceShower:pTmaxMatch = 1");
pythia.readString("TimeShower:pTmaxMatch = 1");
```

Since we are including also photon-shower effects, we have photon radiation associated with the production process and from the final-state leptons. The subsequent three calls turn on the electromagnetic shower for both cases, while the last one keeps the produced photons stable:

```
pythia.readString("TimeShower:QEDshowerByL = on");
pythia.readString("TimeShower:QEDshowerByQ = on");
pythia.readString("SpaceShower:QEDshowerByQ = on");
pythia.readString("TimeShower:QEDshowerByGamma = off");
```

In this analysis we do not include hadronization effects, by setting the flag `nohad` to 1 in the input file, and we do not consider the decay of the Higgs boson. Being a scalar, its decay can easily be simulated a posteriori.

In the standard behaviour of the `POWHEG BOX RES` only the hardest radiation is stored, so that for each event at most one of the decaying resonances includes a NLO-accurate radiation. Moreover, in case of initial-state radiation, QED emission occurs in competition with QCD. The `POWHEG BOX RES` uses the highest-bid mechanism to decide what kind of radiation (QED or QCD, from the initial or from the final state) has to be generated. Due to the larger center-of-mass energy available at the production stage, initial-state radiation is preferred with respect to the final-state one, and since quarks tend to radiate gluons rather than photons, in the initial state QCD radiation is favoured.

For this reason, QED emission from the decay of the resonance would not take place very often at Les Houches level, and this radiation would be mainly generated by the Monte Carlo shower program. The resonance-aware formalism offers the opportunity to further improve the `POWHEG` radiation formula. In the resonance-unaware version of the `POWHEG BOX`, radiation is generated according to eq. (4.17) of ref. [13],

$$d\sigma = \bar{B}(\Phi_B)\, d\Phi_B \left[ \Delta(q_0^2) + \sum_\alpha \Delta(k_{T,\alpha}^2)\, \frac{R_\alpha(\Phi_\alpha(\Phi_B, \Phi_{\rm rad}))}{B(\Phi_B)}\, d\Phi_{\rm rad} \right]. \tag{5.1}$$

The term $\Delta(q_0^2)$ corresponds to the probability that no radiation is generated with hardness above a cutoff $q_0$, and its kinematics corresponds to the Born one. In the second term, each $\alpha$ labels a collinear singular region of the real cross section, and the real matrix element is decomposed into terms singular only in the region $\alpha$, such that

$$R = \sum_\alpha R_\alpha. \tag{5.2}$$

Finally, even the real phase space $\Phi_\alpha(\Phi_B, \Phi_{\rm rad})$ depends upon the singular region $\alpha$, and is a function of the Born kinematics and of the three radiation variables. For the Sudakov form

factor the following relation holds,

$$\Delta(q^2) = \prod_\alpha \Delta_\alpha(q^2), \tag{5.3}$$

where each term $\Delta_\alpha(q^2)$ has the structure of eq. (2.10) with $R$ replaced by $R_\alpha$. As explained in Sec. 2.1, if resonances are present, the traditional decomposition into singular regions is revised as follows: each $\alpha$ labels a particular singular region with a specific resonance structure, such that collinear partons originate from the same resonance. Moreover, the mapping of the real kinematics into its underlying-Born one is done in such a way that it preserves the virtuality of the resonance associated to that singular region. This formalism offers the possibility to further improve the POWHEG radiation formula: we rewrite eq. (5.1) as

$$d\sigma = \bar{B}(\Phi_B)\, d\Phi_B \prod_\alpha \left[\Delta_\alpha(q_0^2) + \Delta_\alpha(k_{T,\alpha}^2)\, \frac{R_\alpha(\Phi_\alpha(\Phi_B, \Phi_{\rm rad}^\alpha))}{B(\Phi_B)}\, d\Phi_{\rm rad}^\alpha\right], \tag{5.4}$$

where, by writing $\Phi_{\rm rad}^\alpha$, we imply that the radiation variables are now independent for each singular region. By expanding the product, we get a term with no emissions, plus terms with multiple emissions. It can be shown [62, 107] that, as far as the hardest radiation is concerned, this formula is equivalent to eq. (5.1). With this improvement, radiation from each singular region is generated and, instead of keeping only the hardest one, all radiations are stored. As a result, the Les Houches event file will contain a radiated particle for each decaying resonance, plus possibly one emission from the initial state. This radiation has NLO+LL accuracy in each resonance, so that the subsequent shower from each resonance generated by a Monte Carlo shower program like Pythia or Herwig has to be softer than the POWHEG one. The POWHEG BOX RES can be run in this more "general" mode by setting the flag allrad to 1 in the input file. All of our results are obtained by activating this option.

Since the Les Houches Interface does not provide a standard mechanism to veto radiation coming from resonance decays, we do not impose restrictions in the generation of QED radiation from the shower, and we implement a dedicated veto procedure. QCD initial-state radiation, instead, is treated by the shower program in the usual way, with the hardness of the emitted partons limited by the value of scalup, that is passed to Pythia 8.1 via the Les Houches Interface.

We first scan the Les Houches event to identify the photons that have been generated by the POWHEG BOX RES, determining if they come from the production or from the decay subprocess. We repeat the same procedure on the photons after the shower, identifying those produced by the shower algorithm. In $HVj$ production, photons radiated by the jet with the highest transverse momentum are considered as coming from the production stage. We then apply the veto procedure in the following way. For each of the photons produced by the initial-state shower we compute its transverse momentum, and we store the maximum value $p_T^{\rm max}$. If at Les Houches level there are no photons, we veto the event if $p_T^{\rm max}$ is greater than scalup, since in the initial state the emission of a photon competes with QCD radiation. If instead there is already a photon at Les Houches level, the event is vetoed if $p_T^{\rm max}$ is greater than the transverse momentum of this photon. This condition effectively amounts to requiring that no QED radiation is generated by the shower with transverse momentum greater than the one produced by the POWHEG BOX RES.

Since, in order to ensure momentum conservation, the reshuffling procedure that is applied during the shower slightly modifies the momentum of the particles, we also check that $p_T^{\rm max}$ does not exceed the hardness of the Les Houches photon after reshuffling: if this happens, the event is vetoed.

When inspecting particles that come from the decay of a resonance, the variable `scalup` plays no role: we then need to fix the maximum value allowed for the photon hardness. If at Les Houches level there are no photons coming from the decay of the vector boson, it means that the `POWHEG BOX RES` has not been able to generate radiation harder than a minimum value of $10^{-3}$ GeV (`rad_ptsqmin_em = 1e-6`). Since the shower must generate particles softer than the `POWHEG` radiation, we require all the produced photons to have hardness smaller than the square root of `rad_ptsqmin_em`.

If instead a photon is already present, we evaluate its transverse momentum with respect to the emitter in the center-of-mass frame of the mother resonance, and store this result in $p_{T,\mathrm{rel}}^{\mathrm{max}}$. In the $HZ$ and $HZj$ processes, at Les Houches level it is not possible to know if the photon has been emitted by the lepton or by the antilepton: $p_{T,\mathrm{rel}}^{\mathrm{max}}$ will then contain the minimum value between the two relative transverse momenta. At this point we veto the event if, among the produced photons, the maximum relative transverse momentum is greater than $p_{T,\mathrm{rel}}^{\mathrm{max}}$. We also check that this photon is softer than the one already present at Les Houches level after reshuffling.

## 5.2 Phenomenological setup

We use the same settings for the input parameters of Sec. 4.5. In the analysis of Les Houches events, before and after the matching to the shower algorithm, we impose some kinematic cuts that are instead not applied at fixed-order NLO level. The photon cannot be experimentally distinguished from charged leptons or partons if the two particles are too close in phase space. For this reason we apply to the photons a fixed-cone isolation prescription, as described in ref. [108]: for each final-state parton $j$ we compute its transverse energy, defined as

$$E_{T,j} = \frac{E_j}{|\vec{p}_j|}\, p_{T,j}, \tag{5.5}$$

together with the angular separation $R_{\gamma j}$, defined in eq. (4.83), between the parton and the photon. The photon is considered isolated from the partons if the transverse partonic energy inside a cone of half-angle $R_0$ is limited by

$$\sum_{R_{\gamma j}<R_0} E_{T,j} < \epsilon_h\, p_T^{\gamma}, \tag{5.6}$$

being $p_T^{\gamma}$ the transverse momentum of the photon. We use $R_0 = 0.4$ and $\epsilon_h = 0.5$. Then, we consider the photon isolated from charged leptons if $R_{\gamma l} > 0.1$ for each final-state lepton $l$. If this is not the case, we recombine the two particles obtaining a "dressed" lepton. Jets are defined according to the anti-$k_T$ algorithm, as implemented in the `fastjet` package [109, 110], with $R = 0.5$. Moreover, we impose the following kinematic cuts: for every charged lepton we require

$$p_T^l \geq 25 \text{ GeV}, \qquad |y_l| \leq 2.5, \tag{5.7}$$

and for $HW/HWj$ events we also impose

$$\not{E}_T \geq 25 \text{ GeV}, \tag{5.8}$$

where with $\not{E}_T$ we refer to the neutrino momentum, not including the contributions coming from soft jets or photons. In events that involve the production of a $Z$ boson, the invariant mass of the dressed-lepton pair is required to be

$$60 \text{ GeV} \leq m(l^+l^-) \leq 140 \text{ GeV}, \tag{5.9}$$

while in order to obtain the transverse-momentum and the rapidity distributions of the hardest isolated photon we require

$$p_T^\gamma > 10 \text{ GeV}. \tag{5.10}$$

For all the other observables that involve photons (such as the transverse momentum of the charged leptons), instead, we are completely inclusive over photon production. Finally, we reconstruct the vector-boson momentum by combining the momenta of the dressed leptons that come from its decay, and we discuss the impact of the optional additional cuts on the transverse momentum of the Higgs and vector bosons,

$$p_T^H \geq 200 \text{ GeV}, \qquad p_T^V \geq 190 \text{ GeV}. \tag{5.11}$$

The selection of events with a boosted Higgs boson is useful to improve the signal-over-background ratio in the context of $H \to b\bar{b}$ studies. However, symmetric cuts induce large radiative corrections in fixed-order calculations, in the transverse-momentum distributions of the Higgs and vector bosons near the cut. Since, in $HV$ production, at leading order these particles are produced back-to-back, any initial-state radiation decreases $p_T^H$ or $p_T^V$, and the event may not pass the kinematic cut anymore. Therefore, the differential cross section near the cut is sensitive to collinear and soft initial-state radiation. By choosing these slightly asymmetric cuts this large sensitivity to higher-order corrections can be removed. We remark that this potential problem affects only fixed-order NLO results, since with showered events the Sudakov form factor associated to the radiation tames the soft/collinear divergence.

## 5.3 The $HW$ associated production

We begin by verifying the correct implementation of the Sudakov electroweak corrections. Then, we analyze the impact of the complete electroweak corrections on the QCD results, both at NLO and with the inclusion of the parton shower. All the figures in this section contain predictions for $HW^-$ production in the left-hand-side plot, and for $HW^+$ production in the right-hand-side one.

### 5.3.1 Fixed-order NLO results

The total NLO cross sections are reported in tab. 5.1. The inclusion of electroweak corrections decreases the QCD cross sections by about $-6.5\%$ for $HW^-$ production, and by about $-7\%$ for the $HW^+$ case. The Sudakov results, instead, are slightly bigger than the full QCD+EW ones, with differences around 7.5%. However, we do no expect good agreement, since they provide a good approximation of the complete electroweak calculation in the high-energy regime, while, at lower energies, where the bulk of the events is concentrated, they fail to capture the correct behaviour. We also note that the NLO QCD + NLL EW total cross sections are very similar to the NLO QCD ones. This confirms us that this approximation is not reliable for completely inclusive quantities, like the total cross section, as already pointed out in the validation phase.

| | $\sigma^{\text{NLO QCD}}_{\text{NLO EW}}$ [fb] | $\sigma^{\text{NLO QCD}}_{\text{NLL EW}}$ [fb] | $\sigma^{\text{NLO QCD}}$ [fb] |
|---|---|---|---|
| $HW^-$ | $55.31 \pm 0.02$ | $59.49 \pm 0.01$ | $59.25 \pm 0.03$ |
| $HW^+$ | $86.91 \pm 0.02$ | $93.37 \pm 0.02$ | $93.24 \pm 0.05$ |

Table 5.1: Total cross sections for the $HW$ production process at a center-of-mass energy of $\sqrt{s} = 13$ TeV, including NLO QCD + NLO EW, NLO QCD + NLL EW and NLO QCD corrections.

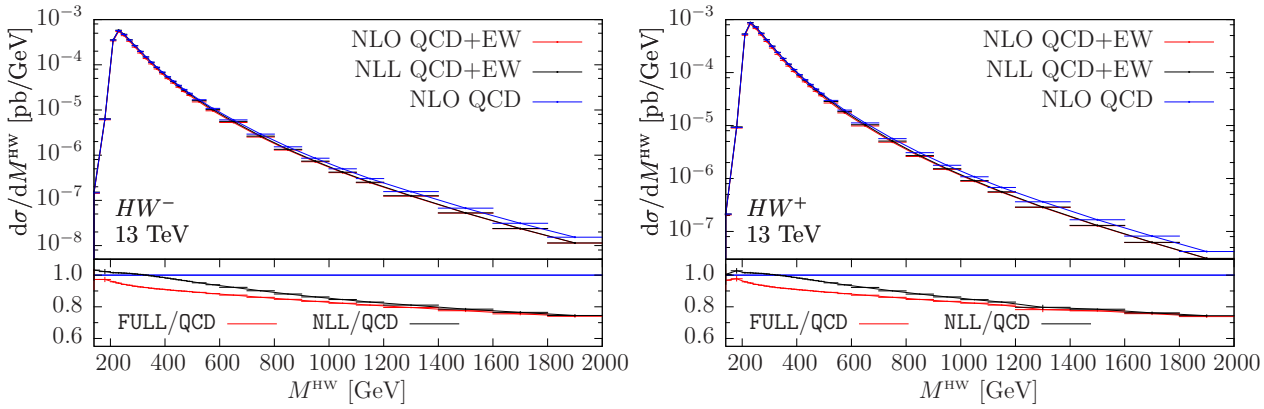


Figure 5.1: NLO predictions for the invariant mass of the $HW$ pair, for both $HW^-$ (left) and $HW^+$ (right) production. Comparison between the full QCD+EW calculation and the QCD results (in red in the ratio panel), and between the approximated QCD+EW calculation and the QCD results (in black in the ratio panel).

In some kinematic distributions, instead, the reliability of the Sudakov approximation can be better investigated. In fig. 5.1 we plot the invariant mass of the $HW$ pair: the lower panel contains the ratio between the `FULL` and the `QCD` implementations, together with the ratio between the `NLL` and the `QCD` results. By inspecting these distributions we can make two comments. First, as expected, the ratio plots overlap when the invariant mass reaches the TeV region. Since for $HV$ production this quantity coincides with the partonic center-of-mass energy, $M^{HW} \gtrsim 1$ TeV means that we are approaching the Sudakov region, where the NLO QCD + NLL EW implementation provides a good approximation of the complete calculation. Secondly, although the impact of electroweak corrections is rather modest on the total cross section, in the tail of this distribution it becomes relevant. Above 1 TeV, indeed, the relative corrections are more than $-15\%$, and they further increase at higher $M^{HW}$ values, reaching $-25\%$ at $M^{HW} \sim 2$ TeV.

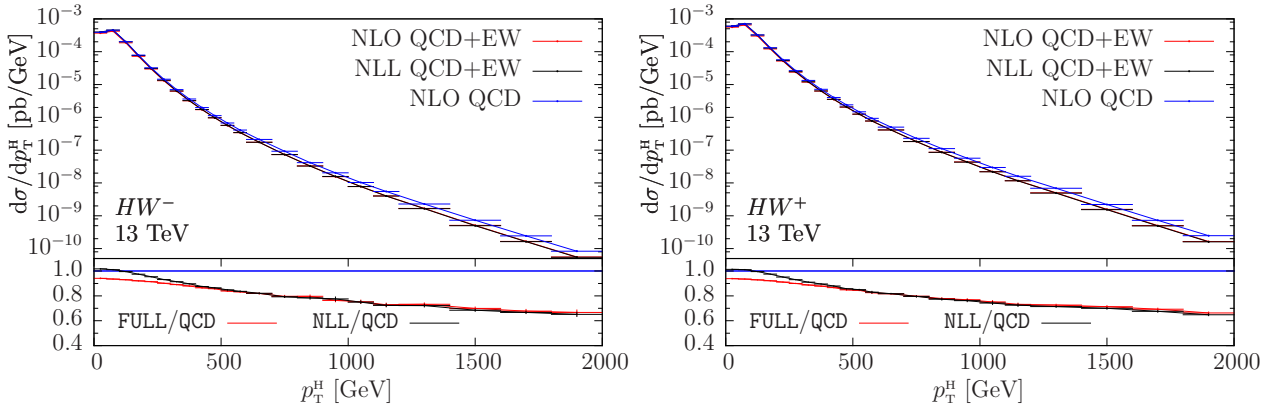


Figure 5.2: NLO predictions for the transverse momentum of the Higgs boson. Same labels as in fig. 5.1.

In fig. 5.2 we show the transverse momentum of the Higgs boson, for which we can draw similar conclusions. The Sudakov approximation converges to the complete calculation for $p_T^H > 500$ GeV, and the effect of the electroweak corrections is more pronounced than in the $HW$ invariant mass. In fact, at $p_T^H \sim 2$ TeV the relative corrections reach $-35\%$, for both $HW^-$ and $HW^+$ production.

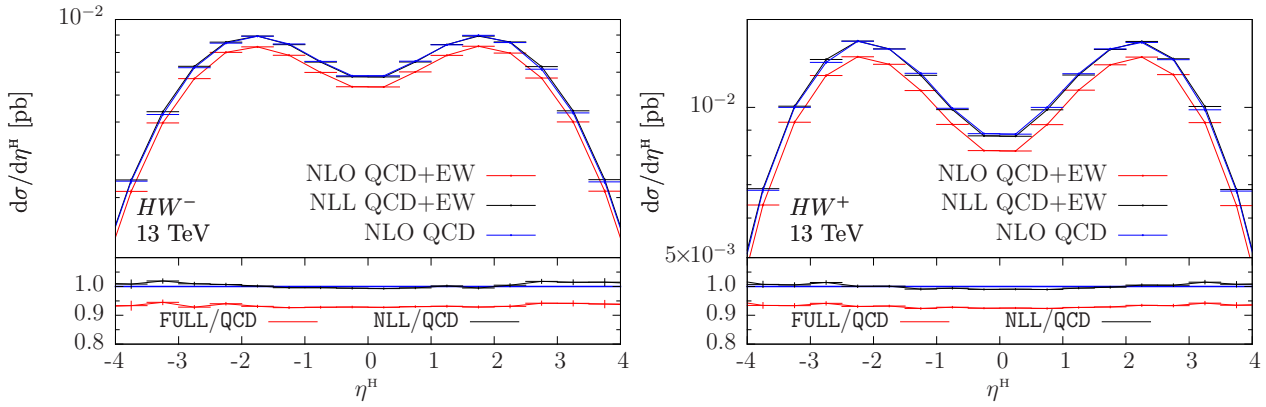


Figure 5.3: NLO predictions for the pseudorapidity of the Higgs boson. Same labels as in fig. 5.1.

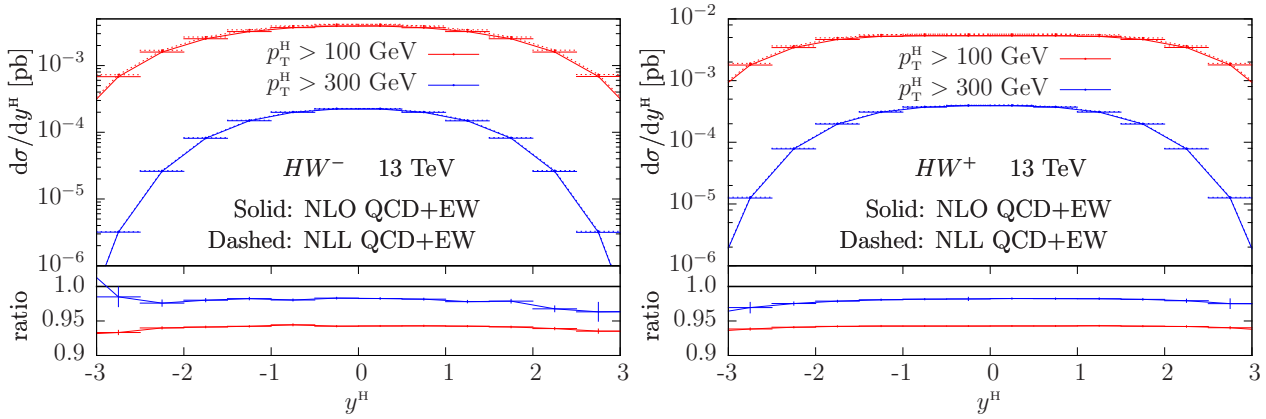


Figure 5.4: NLO rapidity distribution of the Higgs boson, for both $HW^-$ (left) and $HW^+$ (right) production, with kinematic cuts of 100 GeV and 300 GeV on its transverse momentum. Comparison between the complete QCD+EW calculation (solid lines) and its Sudakov approximation (dashed lines).

Figure 5.3 shows the pseudorapidity distribution of the Higgs boson. From the lower panel, we can say that the full electroweak corrections have an almost constant effect on the QCD result. The NLL result, instead, gives a negligible correction: this reflects the problem already pointed out at the level of total cross section, since this quantity is integrated over all emissions. In fig. 5.4 we study in a different way how the approximated result converges to the complete one when moving to the high-energy regime. This plot shows the rapidity of the Higgs boson, comparing the FULL and the NLL calculations with kinematic cuts on its transverse momentum. The blue curves are obtained by applying a 300 GeV cut: the complete implementation and its Sudakov approximation are much more similar than the results obtained with a 100 GeV cut (in red), as can be seen from the ratio plot.

Finally, in fig. 5.5 we see that the electroweak corrections have a sizable impact also on the missing transverse momentum, of the same order as the corrections to the Higgs-boson $p_T$, and that the Sudakov results provide a good approximation in the high-$\not{E}_T$ region.

From the previous plots, it is clear that the inclusion of electroweak corrections is fundamental if one wants to reach a percent-level precision in the high-energy tails of several distributions. In addition, we can conclude that the NLL corrections represent a good approximation of the complete result when focusing on the high-energy tails of the transverse-momentum distributions. On the other hand, for more inclusive distributions such as the total cross section and the rapidity, they are not a good approximation.

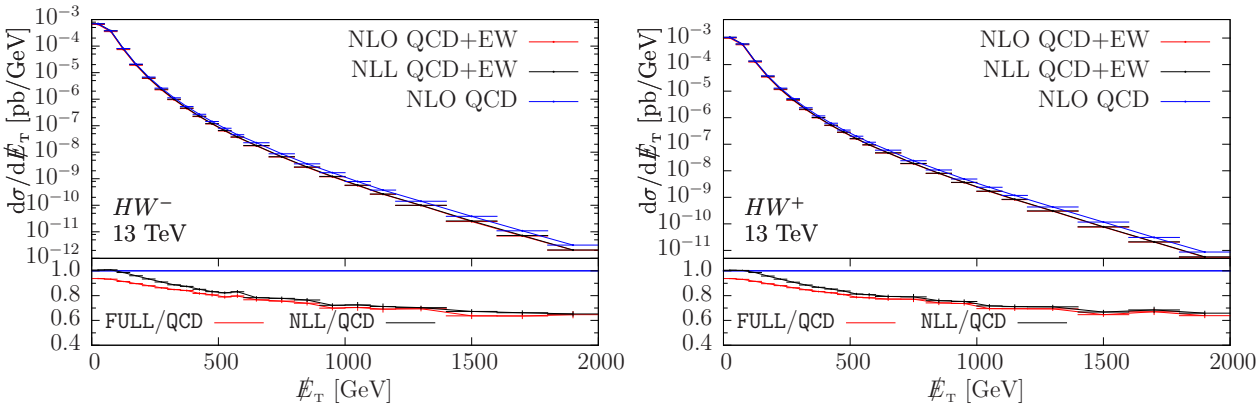


Figure 5.5: NLO predictions for the missing transverse momentum. Same labels as in fig. 5.1.

### 5.3.2 Parton-shower-level predictions

We study now the behaviour of the POWHEG BOX RES results obtained with Monte Carlo Les Houches events, before and after the Pythia 8.1 shower. We compare the QCD+EW distributions at NLO with the corresponding Les Houches events. Then, we study the impact of the electroweak corrections on the QCD results at NLO+PS accuracy.

#### Comparisons among NLO, Les Houches and Pythia results at QCD+EW accuracy

In fig. 5.6 we analyze the rapidity of the $HW$ pair: we clearly see very good agreement, within the integration errors, of the three distributions, as expected in view of the inclusiveness of this NLO quantity.

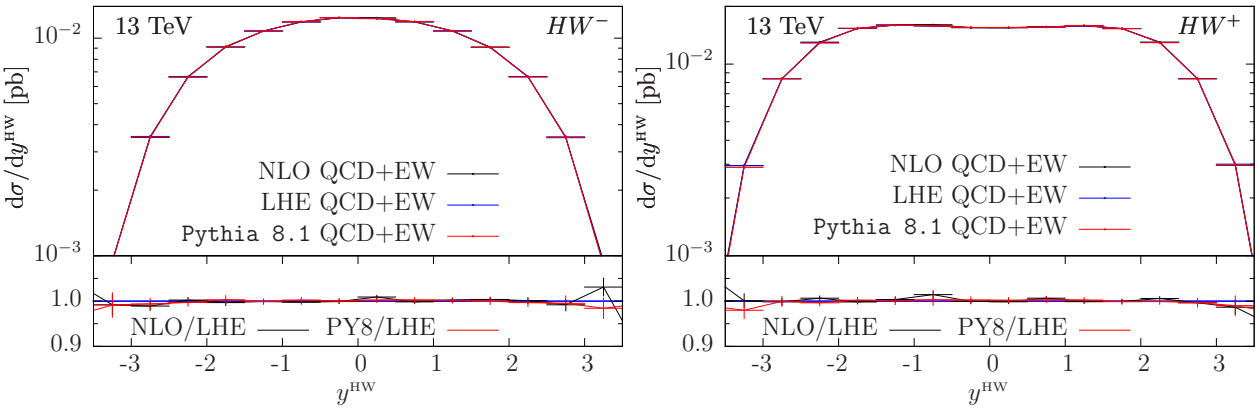


Figure 5.6: Rapidity distribution of the $HW$ pair, for both $HW^-$ (left) and $HW^+$ (right) production. Comparisons among the NLO results, the hardest event produced by the POWHEG BOX RES (LHE) and the NLO+PS predictions, for combined QCD+EW corrections.

Another interesting distribution is the transverse momentum of the $HW$ pair, shown in fig 5.7. As expected, the NLO result displays the typical divergent behaviour at low $p_T$, due to the collinear and soft singularity that affects the real emission. At Les Houches level, instead, the divergence is tamed by the Sudakov form factor. The effect of the parton shower is rather modest in the tail of the distribution, while at low $p_T$ it slightly shifts the position of the Sudakov peak.

We analyze now a few distributions for the hardest photon. Its transverse momentum, to

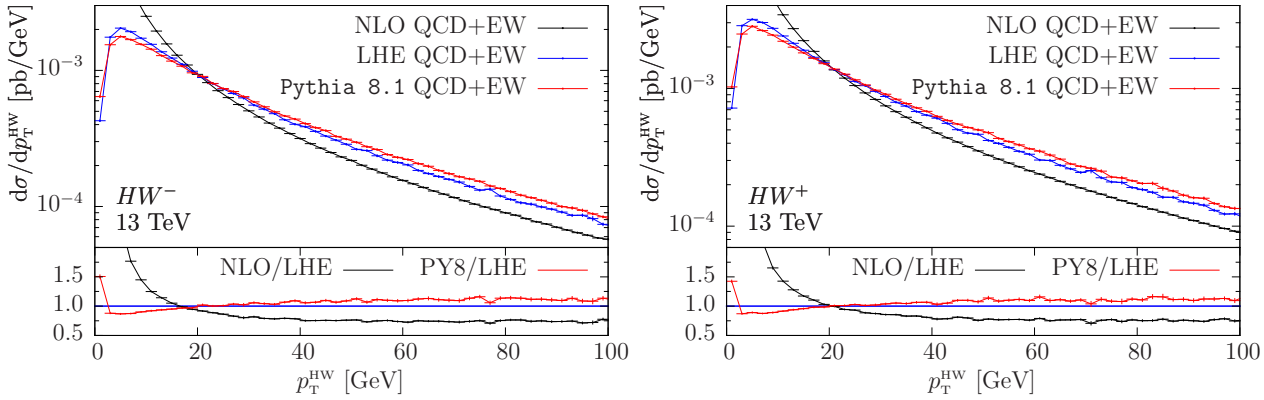


Figure 5.7: Transverse-momentum distribution of the $HW$ pair. Same labels as in fig. 5.6.

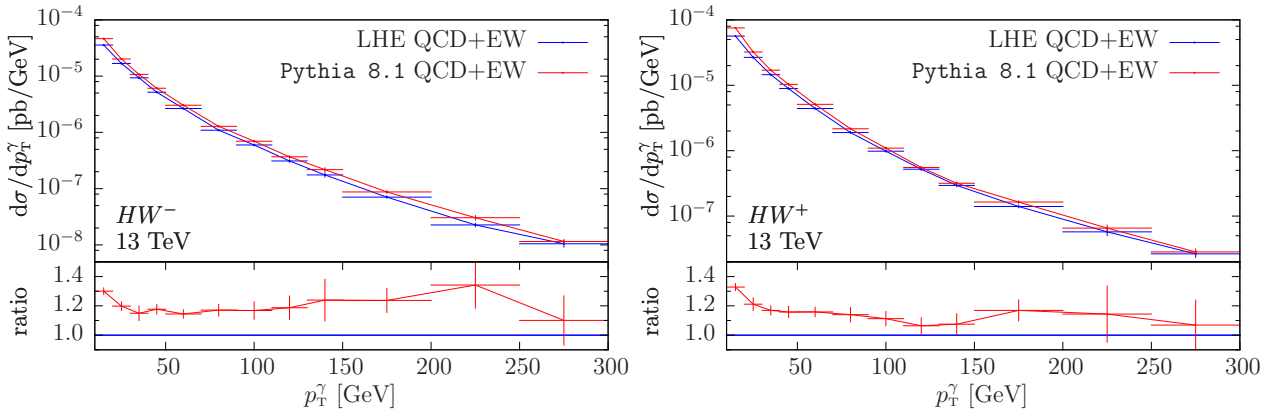


Figure 5.8: Transverse-momentum distribution of the hardest photon, for both $HW^-$ (left) and $HW^+$ (right) production. Comparison between the hardest event produced by the `POWHEG BOX RES` (LHE) and the NLO+PS predictions, for combined QCD+EW corrections.

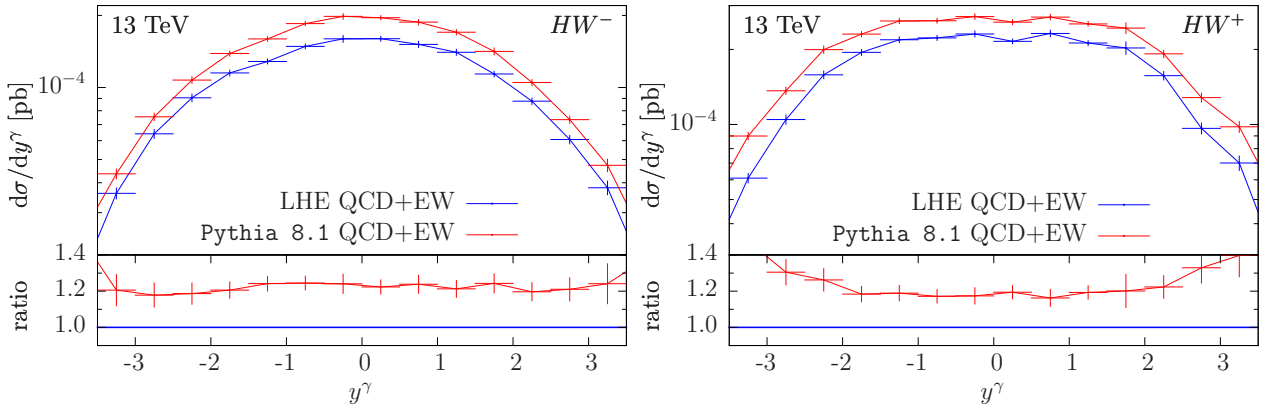


Figure 5.9: Rapidity distribution of the hardest photon, for $HW^-j$ production. Same labels as in fig. 5.8.

which a cut of 10 GeV is applied, as in eq. (5.10), is reported in fig. 5.8: comparing the two results we see that the completion of the shower, provided by `Pythia`, gives a contribution of roughly 20% in the range $p_T^{\gamma} > 30$ GeV, while below this value the increase is slightly more pronounced. Similar conclusions can be drawn by inspecting the photon rapidity, in fig. 5.9: the shower raises the Les Houches distribution by about 20% in the whole $y^{\gamma}$ range.

### Impact of the electroweak corrections in NLO+PS events

The impact of the QCD+EW corrections on the pure QCD results at NLO+PS level is illustrated in the following plots, in which the cuts given in Sec. 5.2 have been applied. The total cross sections, collected in tab. 5.2, totally agree with the NLO results of tab. 5.1. The small differences can be ascribed to the fact that the NLO+PS results contain contributions beyond the NLO.

| | $\sigma^{\text{NLO+PS}}_{\text{QCD+EW}}$ [fb] | $\sigma^{\text{NLO+PS}}_{\text{QCD}}$ [fb] |
|---|---|---|
| $HW^-$ | $55.29 \pm 0.08$ | $59.42 \pm 0.09$ |
| $HW^+$ | $87.3 \pm 0.2$ | $93.2 \pm 0.1$ |

Table 5.2: Total NLO+PS cross sections for the $HW$ production process at a center-of-mass energy of $\sqrt{s} = 13$ TeV, including QCD+EW and QCD corrections.

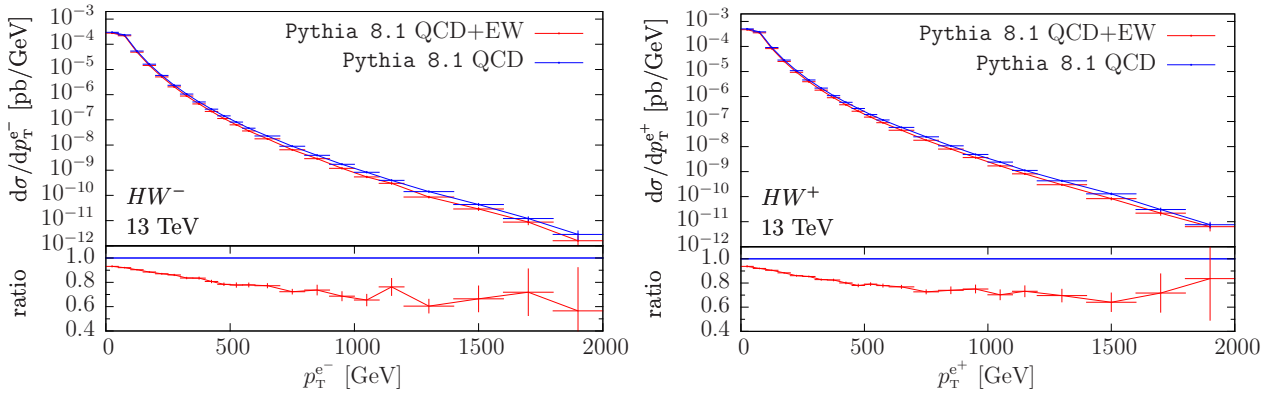


Figure 5.10: NLO+PS predictions for the transverse momentum of the charged lepton, for both $HW^-$ (left) and $HW^+$ (right) production. Comparison between the full QCD+EW calculation and the QCD results.

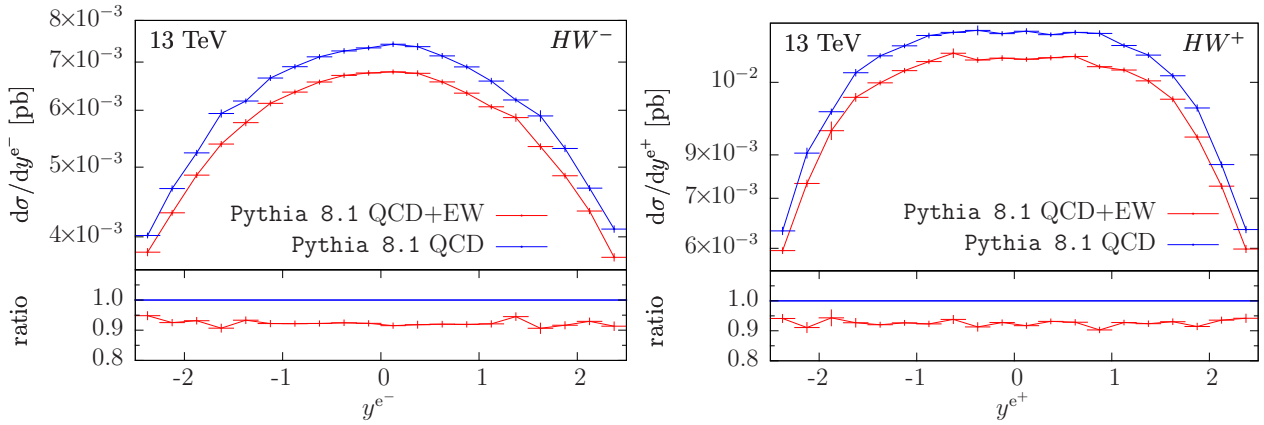


Figure 5.11: NLO+PS predictions for the rapidity of the charged lepton. Same labels as in fig. 5.10.

In figs. 5.10 and 5.11 we show the transverse momentum and the rapidity of the charged lepton, to which the cuts of eq. (5.7) have been imposed. The shape of the $p_T$ distribution changes drastically in the high-$p_T$ region, where differences with respect to the pure QCD

corrections become of the order of $-30\%$ above 1 TeV. In the rapidity distribution, instead, the impact of the electroweak sector is constant and of the order of $-10\%$.

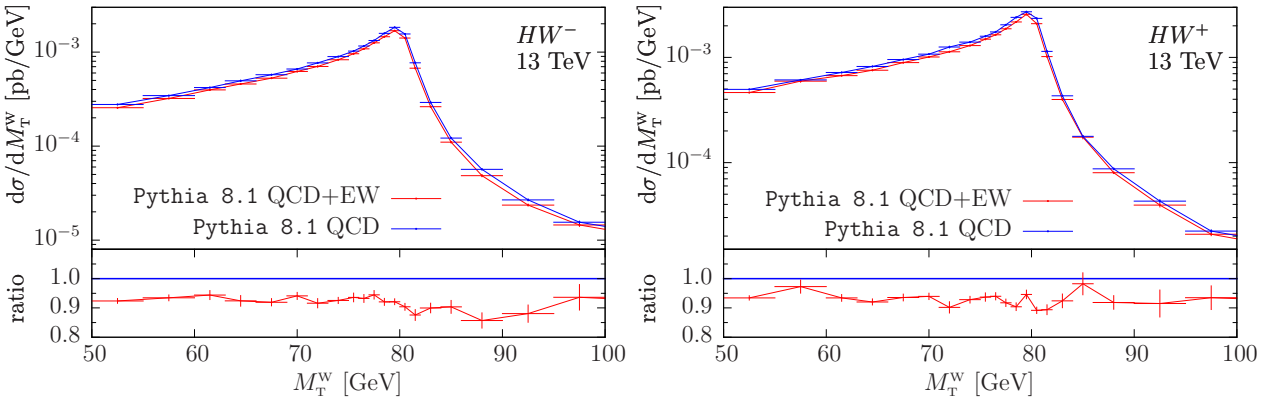


Figure 5.12: NLO+PS predictions for the transverse mass of the $W$ boson. Same labels as in fig. 5.10.

In fig. 5.12 we plot the transverse mass of the $W$ boson,

$$m_T^W = \sqrt{2\, p_T^e \not{E}_T\, (1 - \cos\Delta\phi)}, \tag{5.12}$$

where $\Delta\phi$ is the azimuthal angle between the electron and the missing transverse momentum. For this distribution too, we require a minimum value for $p_T^e$ and $\not{E}_T$, as in eqs. (5.7) and (5.8). As for the lepton rapidity, the electroweak corrections do not change the shape but lower it by roughly 10% with respect to the pure QCD corrections.

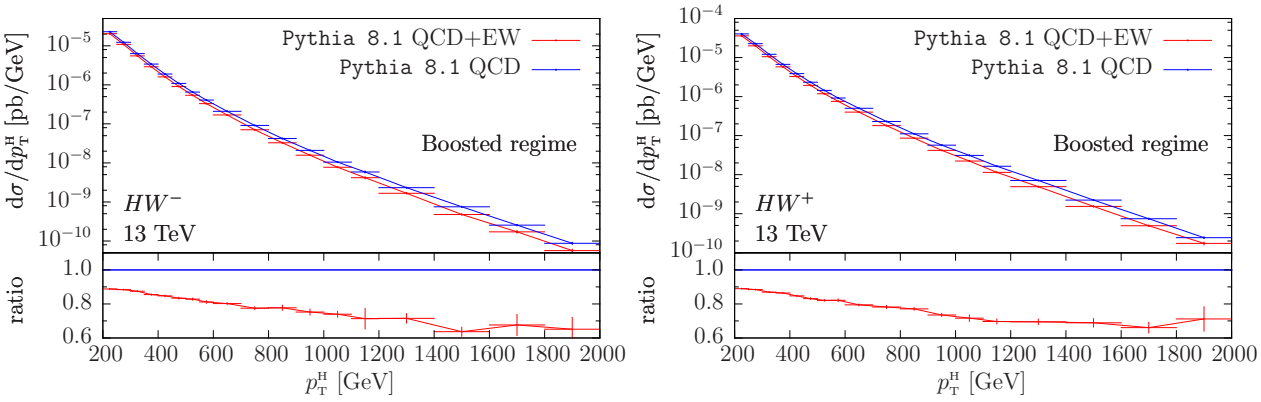


Figure 5.13: NLO+PS predictions for the transverse momentum of the Higgs boson in the boosted regime. Same labels as in fig. 5.10.

Finally, in figs. 5.13 and 5.14 we show the transverse momentum and the rapidity of the Higgs boson, in the boosted regime defined by the cuts of eq. (5.11): for these distributions we can draw similar comments as those for the charged lepton. The same considerations are valid for the $W$ boson, so we do not show the corresponding distributions.

## 5.4 The *HWj* associated production

In this section we study the associated production of a Higgs boson with a $W$ boson and a jet. As shown in the previous section, the behaviour of the $W^-$ and $W^+$ cases is very similar. We then report only the results for $HW^-j$ production.

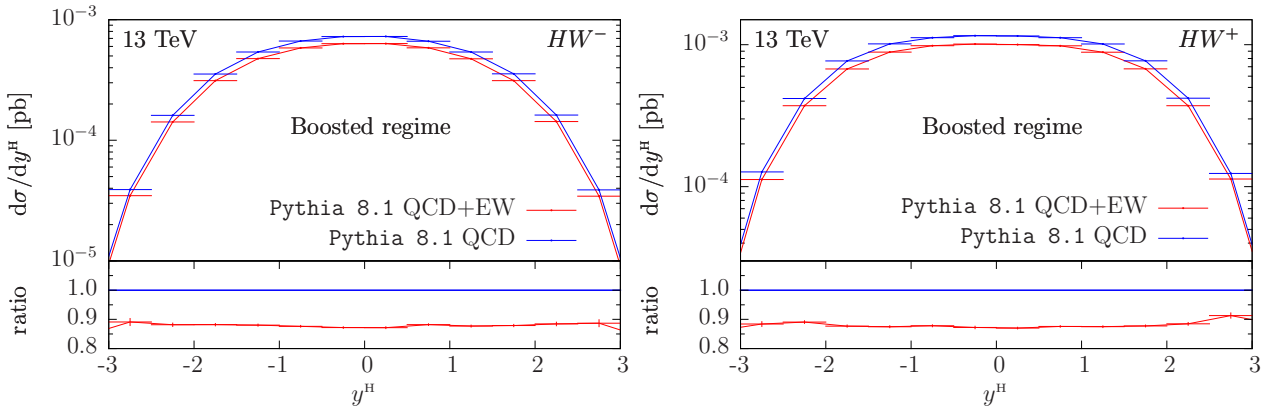


Figure 5.14: NLO+PS predictions for the rapidity of the Higgs boson in the boosted regime. Same labels as in fig. 5.10.

### 5.4.1 Fixed-order NLO results

We begin by giving the total NLO cross section. Table 5.3 contains the results obtained by applying the `MiNLO` procedure to $HWj$ production. In fact, without the inclusion of `MiNLO`, we should need a minimal cut on the transverse momentum of the leading jet, i.e. the jet with the highest transverse momentum. In tab. 5.4, instead, we report the total cross section obtained by requiring a minimum transverse momentum of 20 GeV for the leading jet. The differences between the full QCD+EW results and the QCD implementation are of about $-4\%$ when the `MiNLO` procedure is applied, and of $-2\%$ with the minimal cut. The approximated NLL results give instead a positive contribution to the QCD cross section, increasing it of 4% in both cases.

| $\sigma^{\text{NLO QCD}}_{\text{NLO EW}}$ [fb] | $\sigma^{\text{NLO QCD}}_{\text{NLL EW}}$ [fb] | $\sigma^{\text{NLO QCD}}$ [fb] |
|---|---|---|
| $55.3 \pm 0.1$ | $59.6 \pm 0.1$ | $57.46 \pm 0.02$ |

Table 5.3: Total cross sections for the $HW^-j$ production process at a center-of-mass energy of $\sqrt{s} = 13$ TeV, including NLO QCD + NLO EW, NLO QCD + NLL EW and NLO QCD corrections, computed with the `MiNLO` procedure active.

| $\sigma^{\text{NLO QCD}}_{\text{NLO EW}}$ [fb] | $\sigma^{\text{NLO QCD}}_{\text{NLL EW}}$ [fb] | $\sigma^{\text{NLO QCD}}$ [fb] |
|---|---|---|
| $26.19 \pm 0.04$ | $27.82 \pm 0.04$ | $26.720 \pm 0.008$ |

Table 5.4: Total cross sections for the $HW^-j$ production process at a center-of-mass energy of $\sqrt{s} = 13$ TeV, including NLO QCD + NLO EW, NLO QCD + NLL EW and NLO QCD corrections, with a minimum transverse-momentum cut of 20 GeV on the leading jet.

In fig. 5.15 we show the transverse momentum and the invariant mass of the $HW^-$ pair, comparing both the full QCD+EW and the NLL computations with the QCD results. As the energy increases, we approach the region where $p_T^{HW}$ and $M^{HW}$ are much greater than the Higgs- and $W$-boson masses. In this regime, the NLL result provides a good approximation of the full correction: from the ratio plots, indeed, we see that the distributions overlap.

In fig. 5.16 we show the transverse momentum of the Higgs boson. As in $HW^-$ production, for values of $p_T$ near 500 GeV the Sudakov approximation converges to the full calculation.

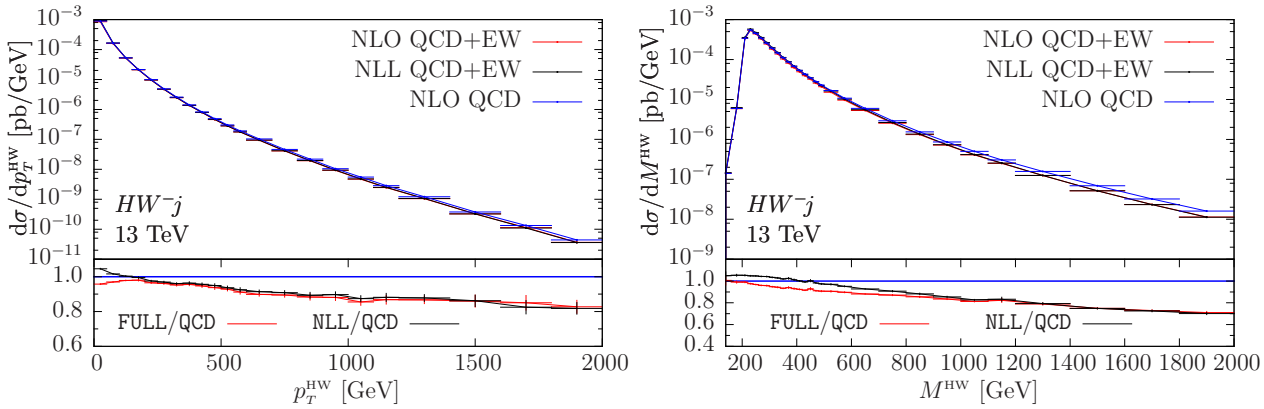


Figure 5.15: NLO predictions for the transverse momentum (left) and the invariant mass (right) of the $HW$ pair, for $HW^-j$ production. Comparison between the full QCD+EW calculation and the QCD results (in red in the ratio panel), and between the approximated QCD+EW calculation and the QCD results (in black in the ratio panel).

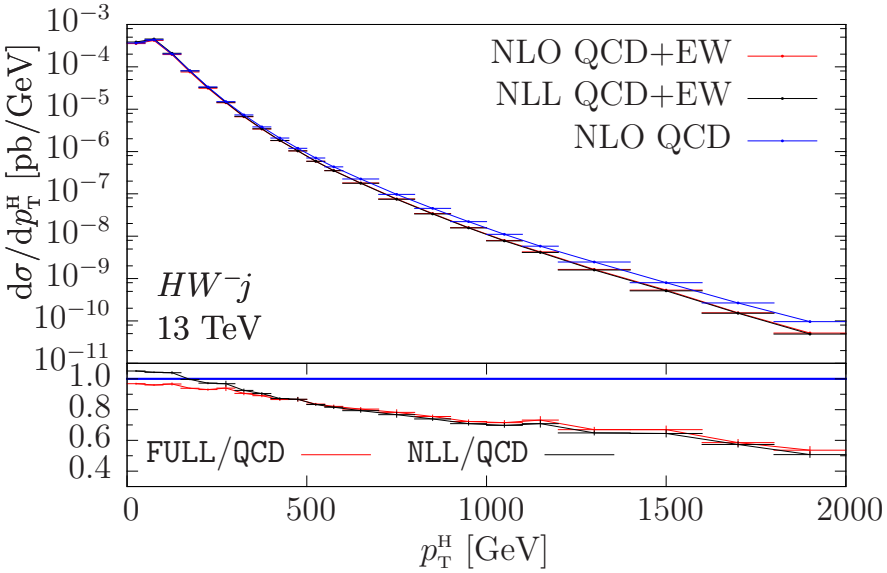


Figure 5.16: NLO predictions for the transverse momentum of the Higgs boson. Same labels as in fig. 5.15.

The relative corrections with respect to the pure QCD implementation are more pronounced, reaching $-50\%$ around 2 TeV. This is due to the fact that, thanks to the inclusion of MiNLO, the electroweak corrections can be applied in the full phase space, including also the contributions coming from the Born-level jet. These contributions are not present in the $HW$ implementation, since in that case the jet does not receive NLO QCD+EW corrections.

The pseudorapidity distribution of the Higgs boson is reported in fig. 5.17: the effect of the full electroweak corrections on the QCD results is constant, and of the order of $-5\%$. The ratio NLL/QCD, instead, reflects the fact that the approximated cross section is bigger than the QCD one. Then, in fig. 5.18, we analyze the rapidity of the Higgs boson, comparing the FULL and the NLL calculations with kinematic cuts on the transverse momentum of the Higgs boson. The blue curves are obtained by applying a 300 GeV cut, while the red ones are obtained with a 100 GeV cut. The lower panel shows that the discrepancies between the complete implementation and its Sudakov approximation decrease when increasing the cut.

We compare now some distributions for the leading jet. Figure 5.19 shows its transverse

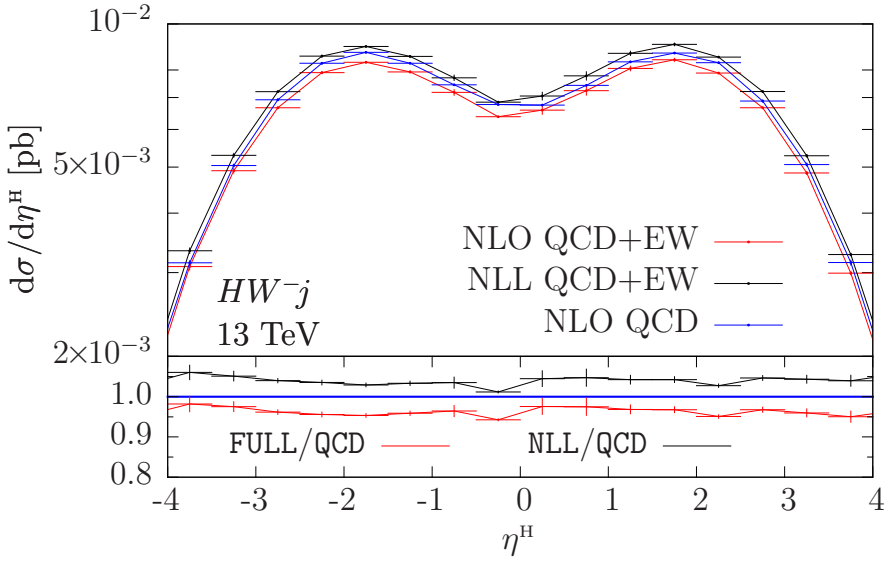


Figure 5.17: NLO predictions for the pseudorapidity of the Higgs boson. Same labels as in fig. 5.15.

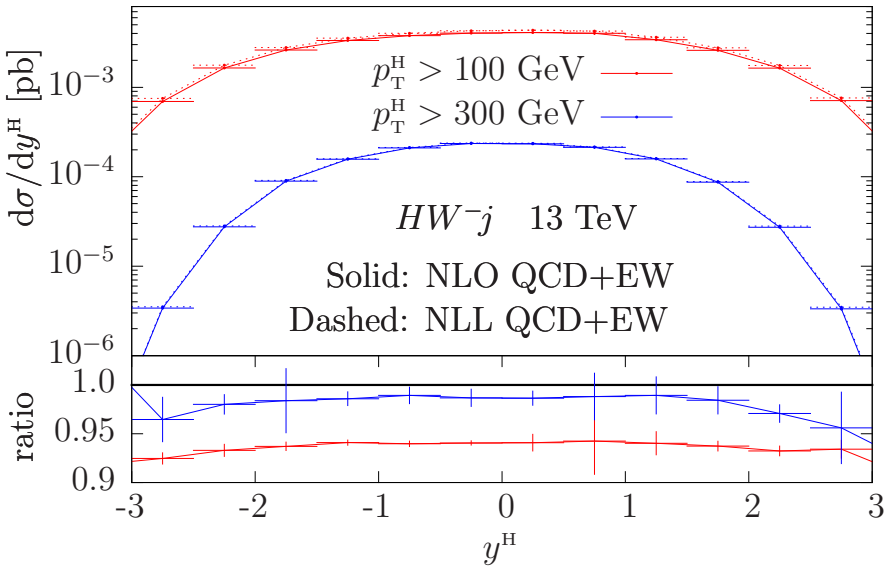


Figure 5.18: NLO rapidity distribution of the Higgs boson, for $HW^-j$ production, with kinematic cuts of 100 GeV and 300 GeV on its transverse momentum. Comparison between the complete QCD+EW calculation (solid lines) and its Sudakov approximation (dashed lines).

momentum in two different $p_T^{j_1}$ ranges. For this distribution, the electroweak corrections give the most relevant contributions in the low-$p_T$ region, while starting from $p_T^{j_1} \sim 25$ GeV their effect becomes of order $-5\%$. The `NLL` results, instead, converge to the `FULL` ones for values of $p_T^{j_1}$ around 200 GeV, while below 150 GeV they give a positive contribution to the differential cross section. We also note that these distributions are not divergent: this is due to the inclusion of the `MiNLO` prescription, that tames the collinear singularity. By inspecting the leading-jet rapidity in fig. 5.20, instead, we see that the electroweak corrections are distributed rather uniformly over the full $y^{j_1}$ range, for both the complete and the approximated calculation.

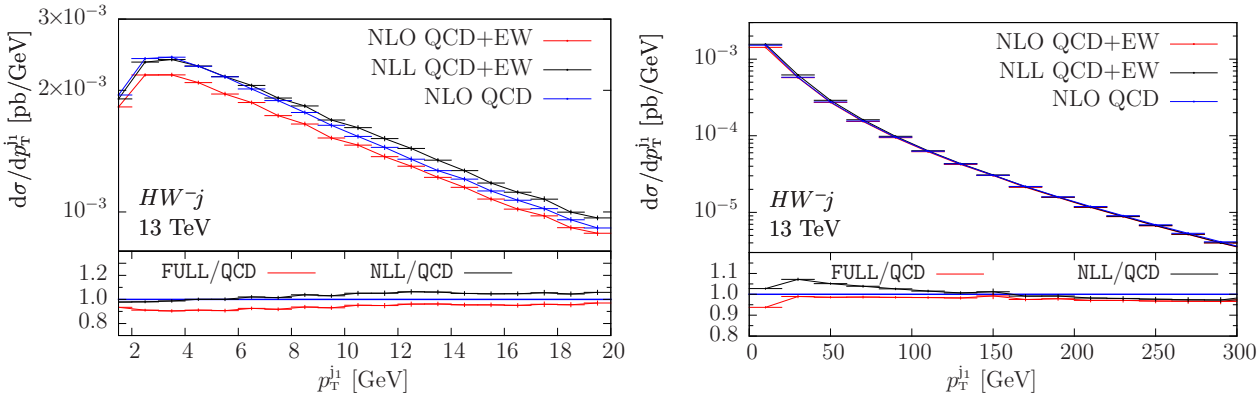


Figure 5.19: NLO predictions for the transverse momentum of the leading jet in two different $p_T^{j_1}$ ranges. Same labels as in fig. 5.15.

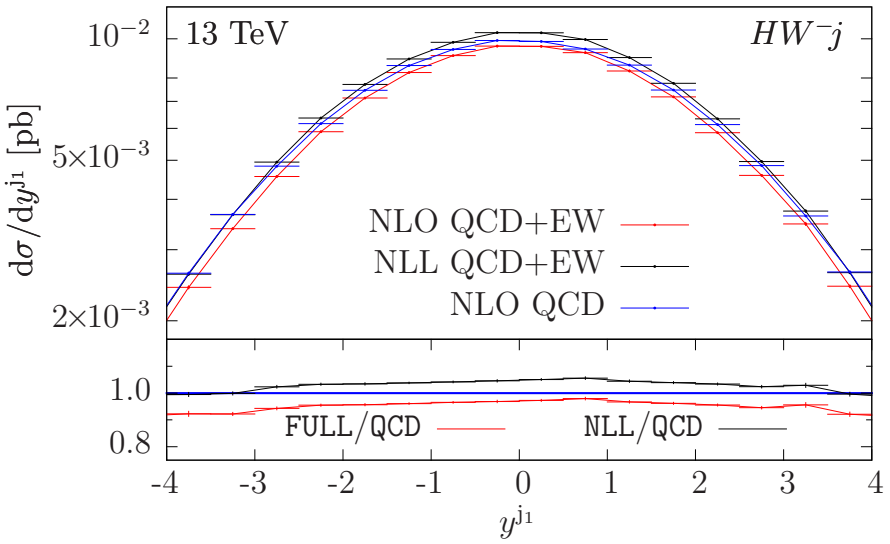


Figure 5.20: NLO predictions for the rapidity of the leading jet. Same labels as in fig. 5.15.

### 5.4.2 Parton-shower-level predictions

As we have done for $HW$ production, in this section we present a few results for the full showered final state, comparing them with the ones obtained with the POWHEG BOX RES hardest event (LHE) and with the fixed-order NLO results. We applied the cuts of eqs. (5.7) and (5.8) to the decay products of the $W$ boson, and we required a minimum transverse momentum of 10 GeV for the hardest photon, as in eq. (5.10).

#### Comparisons among NLO, Les Houches and Pythia results at QCD+EW accuracy

In fig. 5.21 we analyze the rapidity distribution of the $HW$ system: due to the presence of MiNLO, this quantity is finite and we find very good agreement among the three curves.

In fig. 5.22 we plot the transverse momentum of the $HW$ pair, that at leading order recoils against the jet. There are no divergences in the small-$p_T$ region, due to the use of the MiNLO procedure. As far as the subleading jet is concerned, in fig. 5.23 we see that the NLO result

is divergent at small transverse momenta. The LHE results, and consequently the NLO+PS ones, display instead the typical Sudakov shoulder of the resummed results.

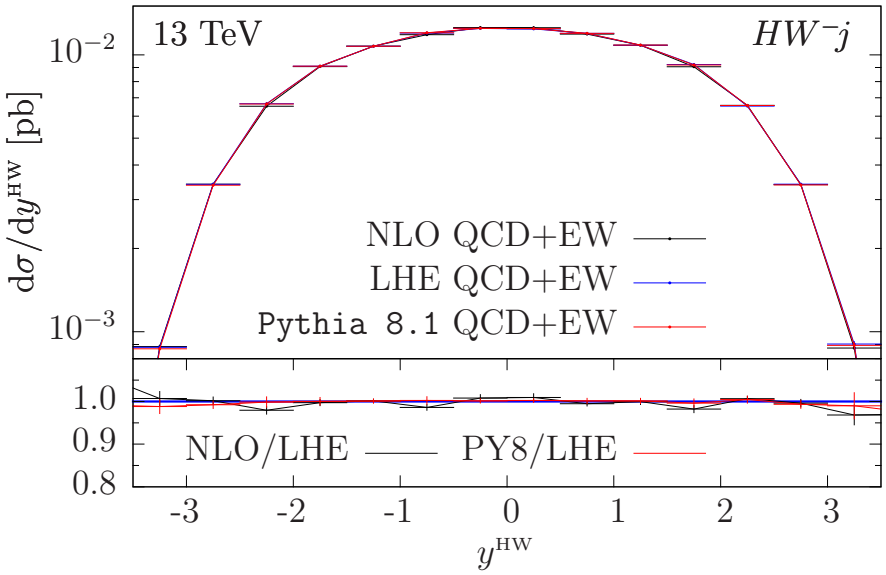


Figure 5.21: Rapidity distribution of the $HW$ pair, for $HW^-j$ production. Comparisons among the NLO results, the hardest event produced by the `POWHEG BOX RES` (LHE) and the NLO+PS predictions, for combined QCD+EW corrections.

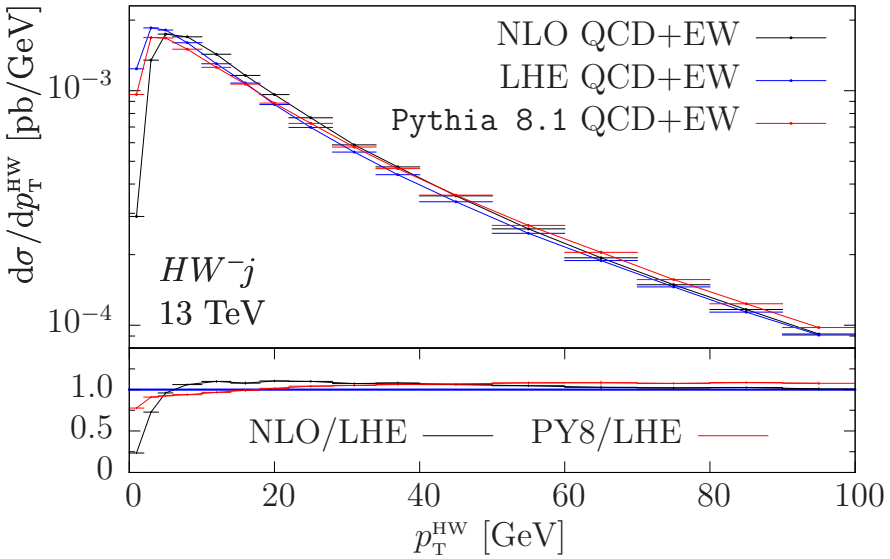


Figure 5.22: Transverse-momentum distribution of the $HW$ pair. Same labels as in fig. 5.21.

In fig. 5.24 the rapidity distribution of the hardest photon is reported. This plot presents some differences with respect to the $HW^-$ case (shown in fig. 5.9). Here, the contribution coming from the shower is almost negligible on the whole $y^\gamma$ range. Similar conclusions can be drawn for the transverse-momentum distribution of the photon, shown in fig. 5.25.

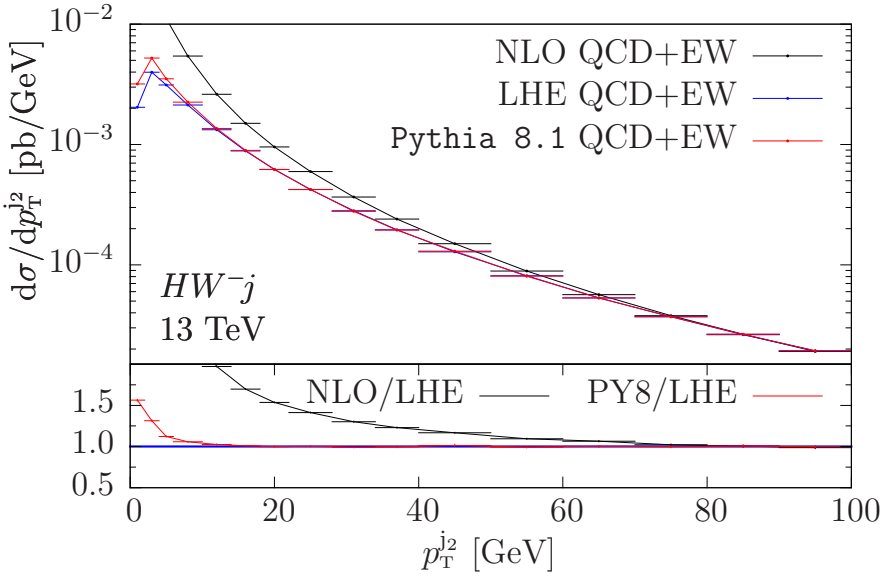


Figure 5.23: Transverse-momentum distribution of the subleading jet. Same labels as in fig. 5.21.

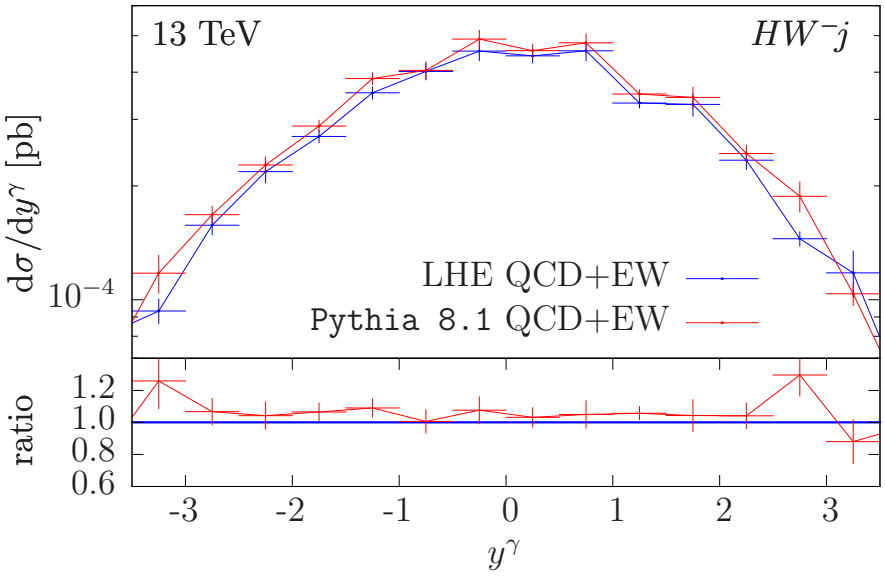


Figure 5.24: Rapidity distribution of the hardest photon. Comparison between the hardest event produced by the `POWHEG BOX RES` (LHE) and the NLO+PS predictions, for combined QCD+EW corrections.

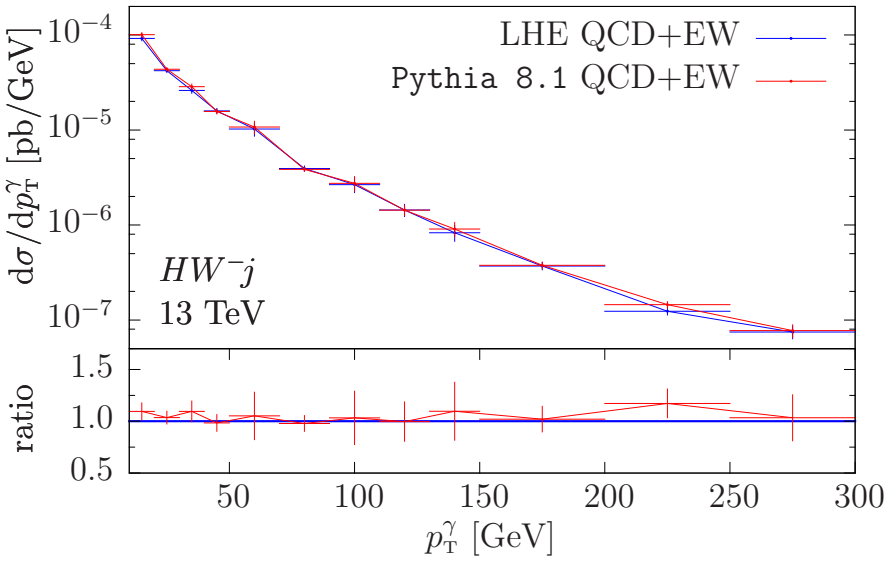


Figure 5.25: Transverse-momentum distribution of the hardest photon. Same labels as in fig. 5.24.

### Impact of the electroweak corrections in NLO+PS events

At the end, we study the impact of the electroweak corrections on the QCD results at NLO+PS level. The values of the total cross section are reported in tabs. 5.5 and 5.6. The former collects the results obtained by applying the `MiNLO` procedure, while in the latter a minimum transverse-momentum cut of 20 GeV on the leading jet is imposed. By inspecting tabs. 5.3 and 5.4, that contain the corresponding NLO results, we find good agreement.

| $\sigma^{\text{NLO+PS}}_{\text{QCD+EW}}$ [fb] | $\sigma^{\text{NLO+PS}}_{\text{QCD}}$ [fb] |
|---|---|
| $55.29 \pm 0.08$ | $57.49 \pm 0.04$ |

Table 5.5: Total NLO+PS cross sections for the $HW^-j$ production process at a center-of-mass energy of $\sqrt{s} = 13$ TeV, including QCD+EW and QCD corrections, computed with the `MiNLO` procedure active.

| $\sigma^{\text{NLO+PS}}_{\text{QCD+EW}}$ [fb] | $\sigma^{\text{NLO+PS}}_{\text{QCD}}$ [fb] |
|---|---|
| $25.46 \pm 0.04$ | $26.90 \pm 0.03$ |

Table 5.6: Total NLO+PS cross sections for the $HW^-j$ production process at a center-of-mass energy of $\sqrt{s} = 13$ TeV, including QCD+EW and QCD corrections, with a minimum transverse-momentum cut of 20 GeV on the leading jet.

Turning to exclusive kinematic quantities, in fig. 5.26 we show the missing transverse momentum, to which the cut of eq. (5.8) has been imposed, and in fig. 5.27 the $p_T$ of the leading jet. Then, in figs. 5.28 and 5.29 we plot the transverse momentum and the rapidity of the Higgs boson in the boosted regime defined by the cuts of eq. (5.11). While the missing transverse momentum and the Higgs-boson distributions behave in a similar way as in $HW$ production, giving corrections that reach $-30\%$ at high-$p_T$ values and constant corrections of about $-10\%$ in the whole $y^H$ range considered, the leading-jet transverse momentum receives small corrections from the electroweak sector. We have checked that for several other typical

kinematic distributions involving the jet we can draw similar conclusions. For this reason, we do not show them in here.

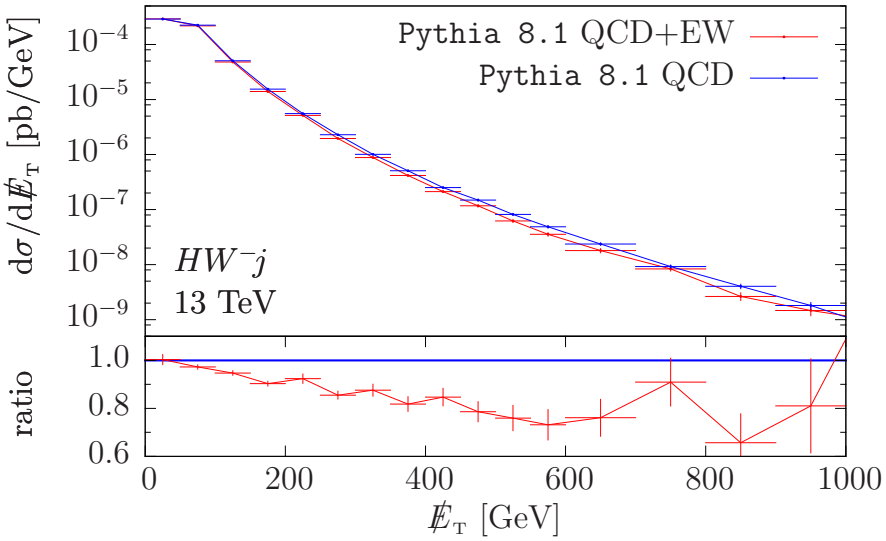


Figure 5.26: NLO+PS predictions for the missing transverse momentum, for $HW^-j$ production. Comparison between the full QCD+EW calculation and the QCD results.

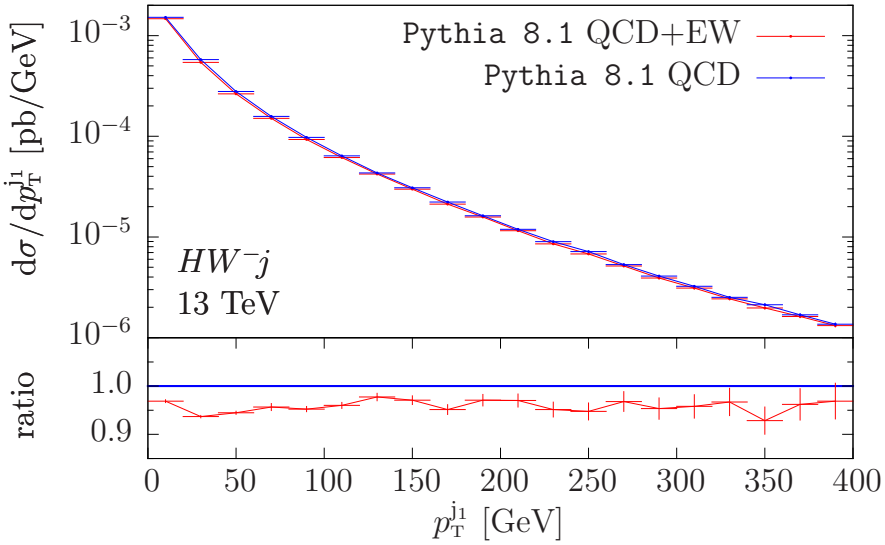


Figure 5.27: NLO+PS predictions for the transverse momentum of the leading jet. Same labels as in fig. 5.26.

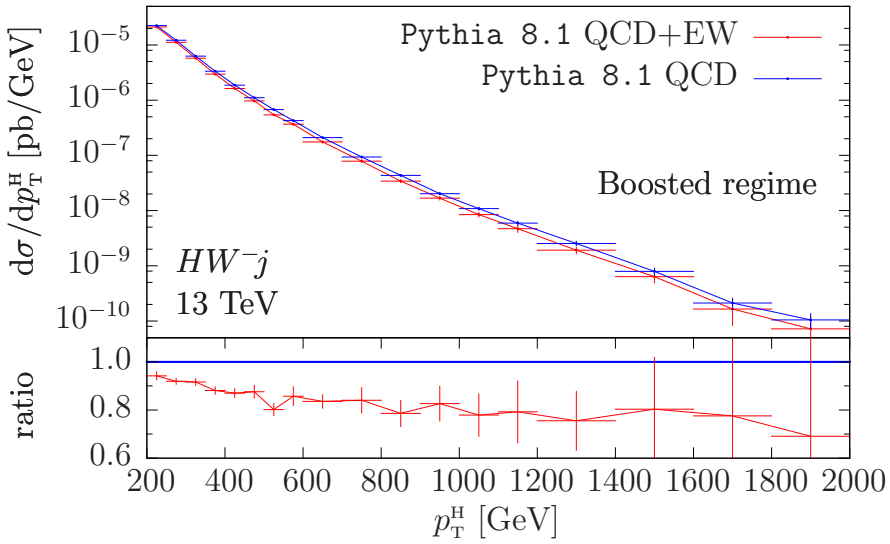


Figure 5.28: NLO+PS predictions for the transverse momentum of the Higgs boson in the boosted regime. Same labels as in fig. 5.26.

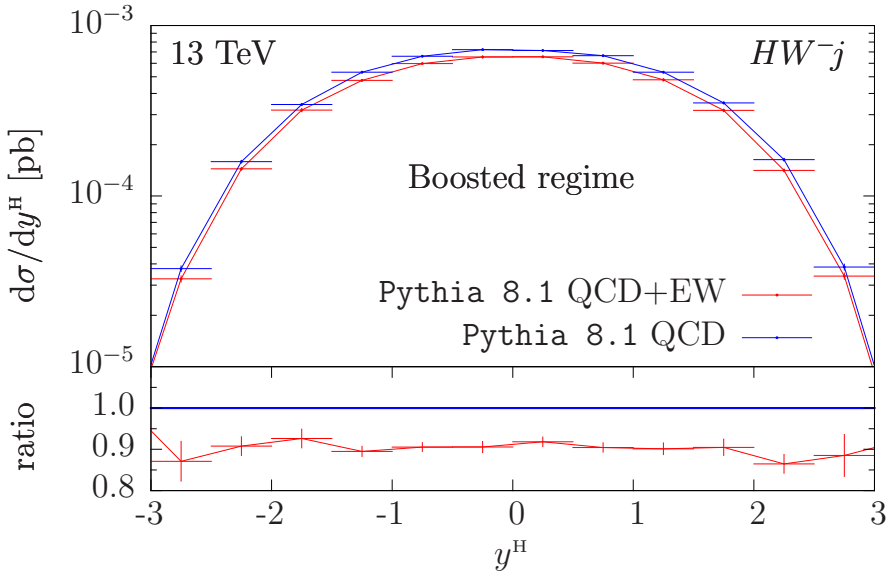


Figure 5.29: NLO+PS predictions for the rapidity of the Higgs boson in the boosted regime. Same labels as in fig. 5.26.

## 5.5 The $HZ$ associated production

We now move to the discussion of the associated production of a Higgs boson and a $Z$ boson. Considering that the $HW$ and $HZ$ results are very similar, in the following we show fewer plots with respect to the previous sections. Nevertheless, differently from the $HW$ and $HWj$ processes, the momentum of the vector boson can be experimentally reconstructed, due to its decay into charged leptons. We then show also NLO+PS predictions for quantities that directly involve the $Z$ boson, like its invariant mass, since it is known that the electroweak corrections slightly change its shape.

### 5.5.1 Fixed-order NLO results

The NLO QCD+NLO EW, NLO QCD+NLL EW and NLO QCD total cross sections for $HZ$ production are reported in tab. 5.7. The full electroweak corrections have a modest impact on the QCD result, of less than 5%, while the NLL corrections give a negligible contribution.

| $\sigma^{\text{NLO QCD}}_{\text{NLO EW}}$ [fb] | $\sigma^{\text{NLO QCD}}_{\text{NLL EW}}$ [fb] | $\sigma^{\text{NLO QCD}}$ [fb] |
|---|---|---|
| $24.382 \pm 0.008$ | $25.457 \pm 0.008$ | $25.551 \pm 0.005$ |

Table 5.7: Total cross sections for the $HZ$ production process at a center-of-mass energy of $\sqrt{s} = 13$ TeV, including NLO QCD + NLO EW, NLO QCD + NLL EW and NLO QCD corrections.

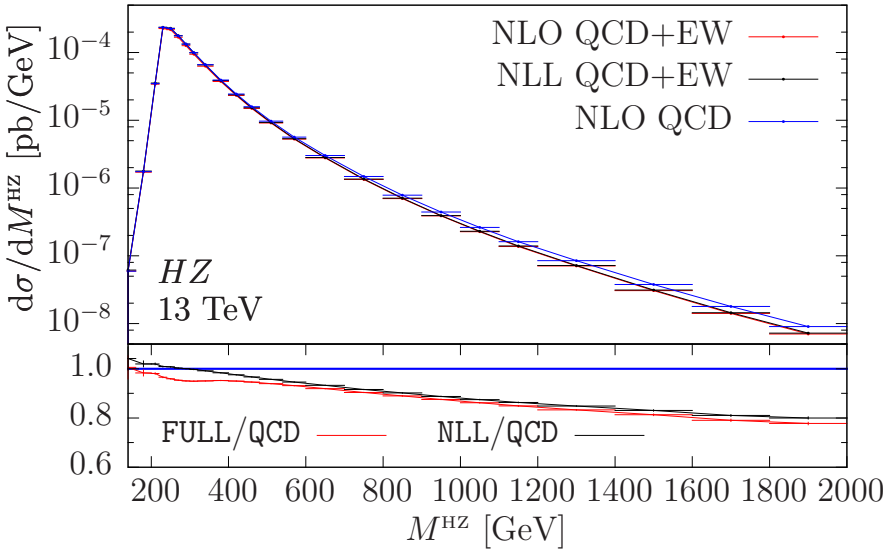


Figure 5.30: NLO predictions for the invariant mass of the $HZ$ pair, for $HZ$ production. Comparison between the full QCD+EW calculation and the QCD results (in red in the ratio panel), and between the approximated QCD+EW calculation and the QCD results (in black in the ratio panel).

In fig. 5.30 we study the validity of the Sudakov approximation, and the impact of the electroweak corrections on the QCD results, for the invariant mass of the $HZ$ pair. We find a behaviour similar to $HW$ production (shown in fig. 5.1): the electroweak corrections decrease the differential cross section by about 15% in the TeV region, while the NLL result converges to the full one around 700 GeV, with small differences at the percent level.

In fig. 5.31 we inspect the transverse-momentum distribution of the Higgs boson. The effect of the electroweak corrections on the high-energy tail is more pronounced than in the invariant mass of the $HZ$ system, reaching $-30\%$ at 2 TeV. The NLL corrections overlap at rather low values of $p_T^H$: already around 250 GeV the agreement between the two implementations is remarkable.

The predictions for the Higgs boson pseudorapidity and rapidity further clarify the role of the approximated Sudakov corrections. In the pseudorapidity distribution, shown in fig. 5.32, the ratio `NLL/QCD` reflects the fact that the Sudakov corrections give a negligible contribution to inclusive quantities, as pointed out at the level of total cross section. Looking at the impact of the full electroweak corrections, instead, we find again a constant contribution on the whole $\eta^H$ range, of about $-5\%$. In fig. 5.33 we inspect the rapidity distribution of the

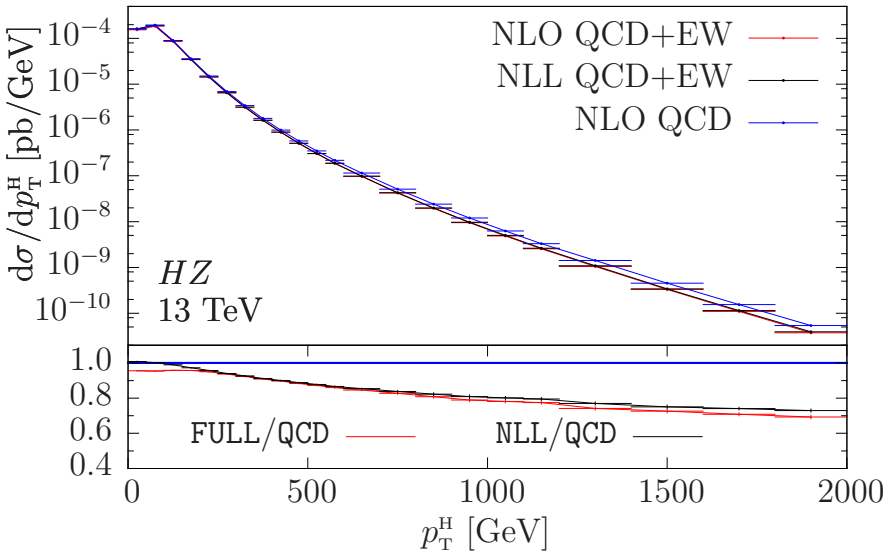


Figure 5.31: NLO predictions for the transverse momentum of the Higgs boson. Same labels as in fig. 5.30.

Higgs boson, applying two kinematic cuts on $p_T^H$ and comparing the FULL results with the NLL ones. With a 100 GeV cut the discrepancy between the two implementations is less than 3%, while with a 300 GeV cut the two results are almost indistinguishable.

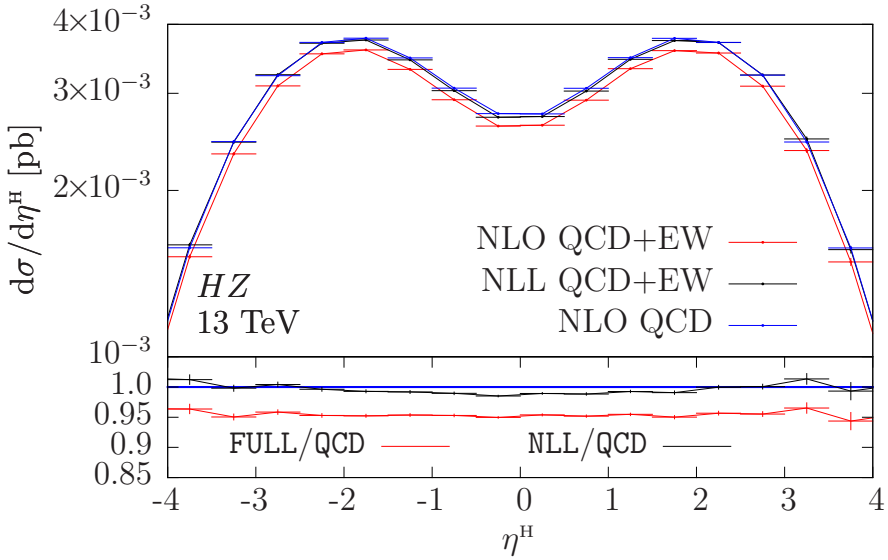


Figure 5.32: NLO predictions for the pseudorapidity of the Higgs boson. Same labels as in fig. 5.30.

### 5.5.2 Parton-shower-level predictions

We now discuss the POWHEG BOX RES results, before and after the shower performed by Pythia 8.1. As done in Sec. 5.3.2 for $HW$ production, we first compare QCD+EW differential cross sections at NLO level with the corresponding ones at Les Houches and shower level. Then, we discuss the role of the electroweak corrections at NLO+PS accuracy.

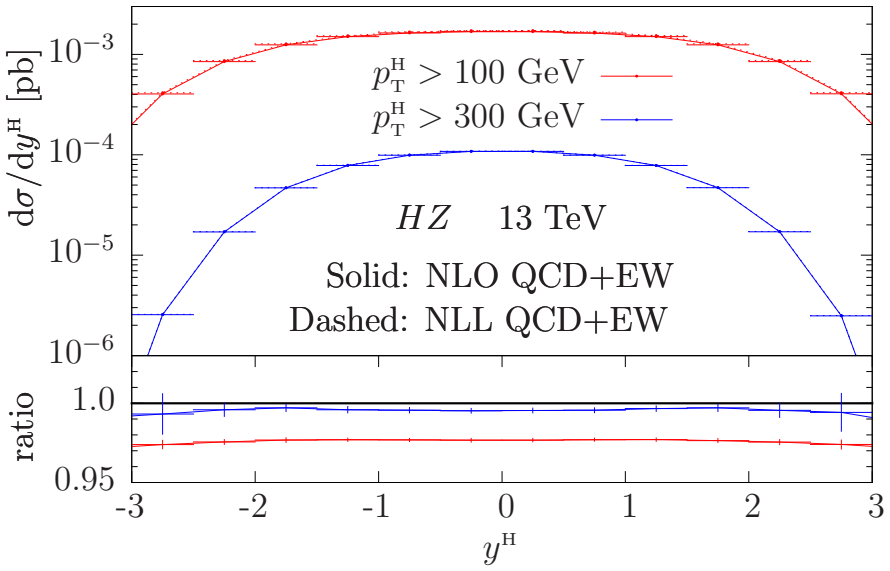


Figure 5.33: NLO rapidity distribution of the Higgs boson, for $HZ$ production, with kinematic cuts of 100 GeV and 300 GeV on its transverse momentum. Comparison between the complete QCD+EW calculation (solid lines) and its Sudakov approximation (dashed lines).

### Comparisons among NLO, Les Houches and `Pythia` results at QCD+EW accuracy

One of the most inclusive distributions is the rapidity of the $HZ$ pair, shown in fig. 5.34: by inspecting the lower panel we see a very good agreement among the three distributions.

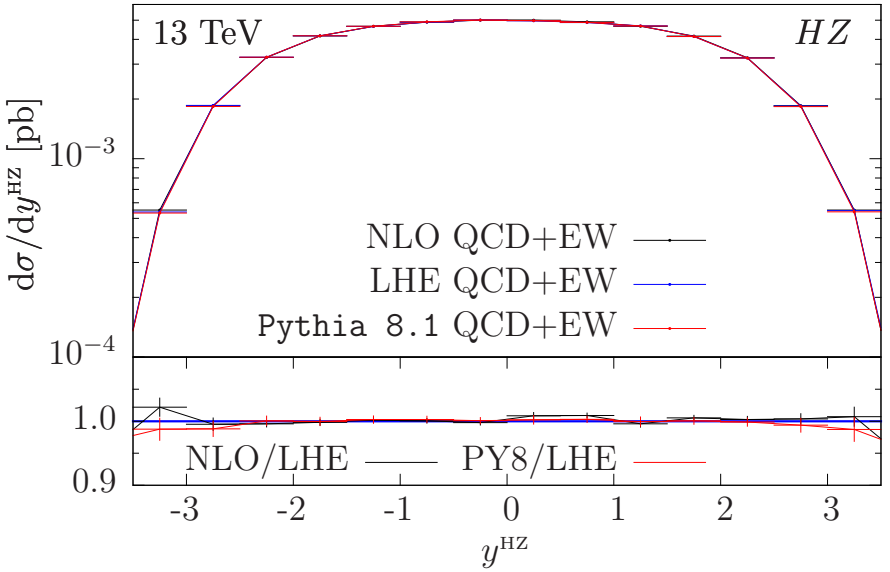


Figure 5.34: Rapidity distribution of the $HZ$ pair, for $HZ$ production. Comparisons among the NLO results, the hardest event produced by the `POWHEG BOX RES` (LHE) and the NLO+PS predictions, for combined QCD+EW corrections.

The transverse-momentum distribution of the $HZ$ system, reported in fig. 5.35, is affected by the typical NLO divergence that vanishes when adding the Sudakov form factor. The effect of the shower is more visible in the low-$p_T$ region, where it completes the `POWHEG`-initiated shower with the rest of the shower.

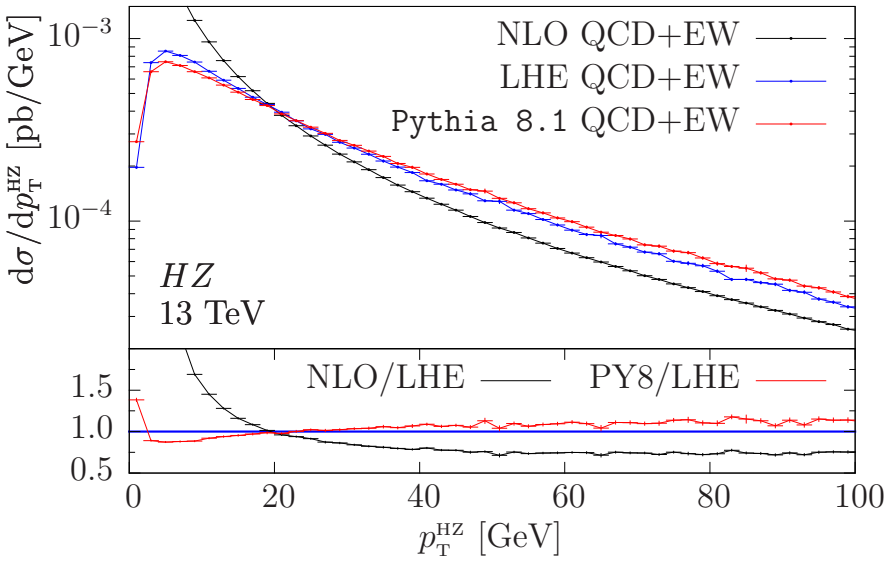


Figure 5.35: Transverse-momentum distribution of the $HZ$ pair. Same labels as in fig. 5.34.

In figs. 5.36 and 5.37 we plot the rapidity and the transverse momentum of the hardest photon, obtained imposing a 10 GeV cut on its transverse momentum, as in eq. (5.10). In both the distributions we see an increase of about 10% in the whole $p_T^\gamma$ and $y^\gamma$ ranges when moving from Les Houches to NLO+PS events. The effect of the shower is more moderate with respect to $HW$ production (figs. 5.8 and 5.9), where it amounts to roughly 20%.

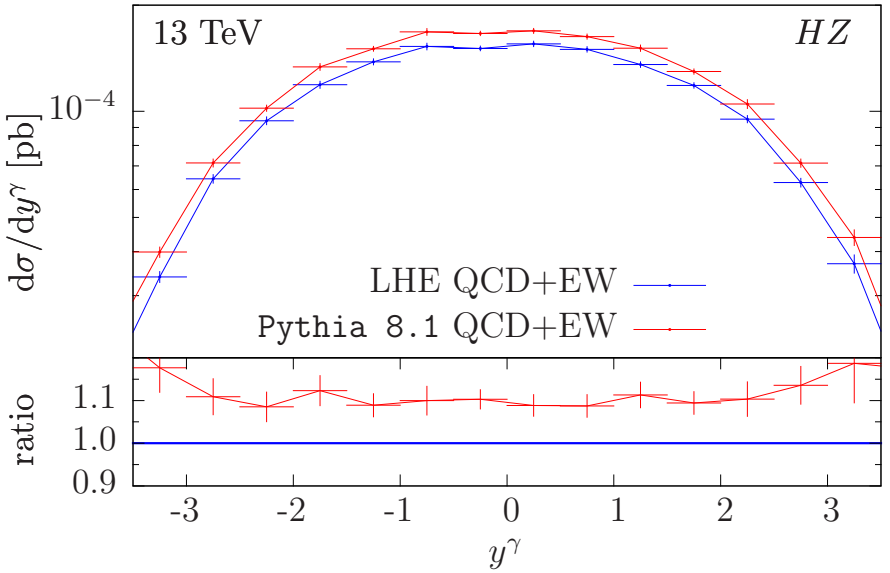


Figure 5.36: Rapidity distribution of the hardest photon, for $HZ$ production. Comparison between the hardest event produced by the `POWHEG BOX RES` (LHE) and the NLO+PS predictions, for combined QCD+EW corrections.

### Impact of the electroweak corrections in NLO+PS events

In the following we focus on complete NLO+PS events, evaluating the impact of the electroweak corrections on the QCD results. The typical experimental setup is reproduced by

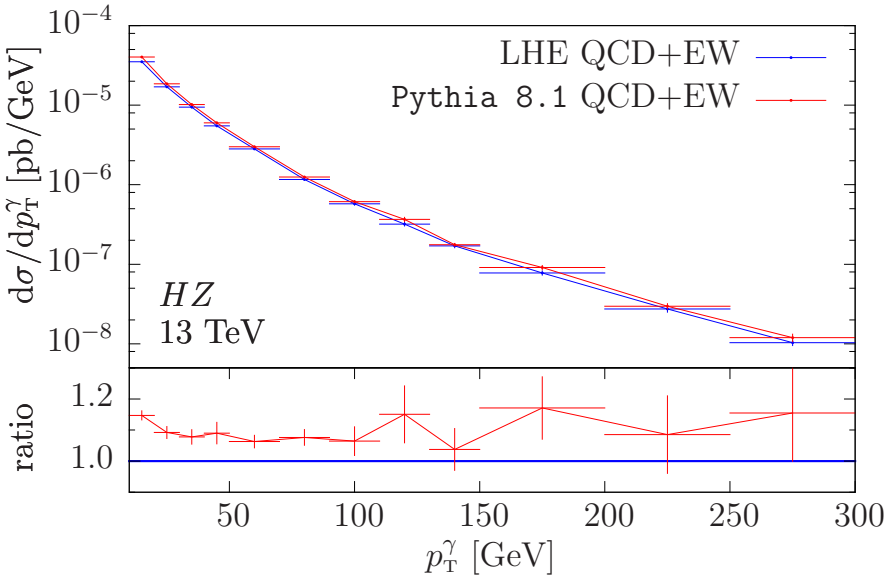


Figure 5.37: Transverse-momentum distribution of the hardest photon. Same labels as in fig. 5.36.

| $\sigma^{\text{NLO+PS}}_{\text{QCD+EW}}$ [fb] | $\sigma^{\text{NLO+PS}}_{\text{QCD}}$ [fb] |
|---|---|
| $24.34 \pm 0.03$ | $25.60 \pm 0.03$ |

Table 5.8: Total NLO+PS cross sections for the $HZ$ production process at a center-of-mass energy of $\sqrt{s} = 13$ TeV, including QCD+EW and QCD corrections.

applying the cuts of eqs. (5.7) and (5.9) to the leptons. The values of the total cross sections are reported in tab. 5.8. These results are in remarkable agreement with the ones obtained at NLO level, collected in tab. 5.7, and show a decrease of about 5% due to the electroweak sector.

In fig. 5.38 we show the transverse-momentum distributions of the two charged leptons, together with their rapidities in fig. 5.39. In the high-energy tails of the $p_T$ distributions, the electroweak corrections decrease the differential cross section by roughly $-30\%$, and in the rapidity range considered the electroweak corrections give a constant contribution of about $-5\%$.

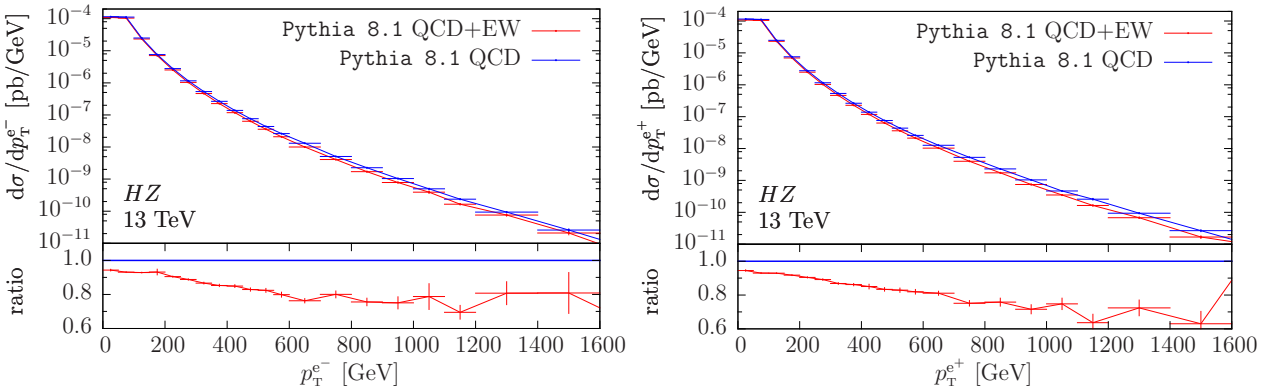


Figure 5.38: NLO+PS predictions for the transverse momentum of the electron (left) and of the positron (right), for $HZ$ production. Comparison between the full QCD+EW calculation and the QCD results.

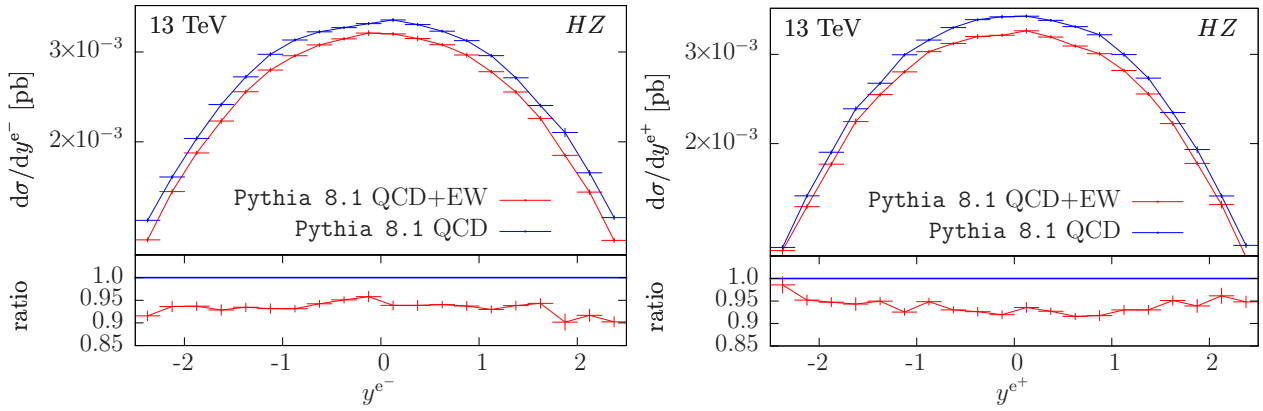


Figure 5.39: NLO+PS predictions for rapidity of the electron (left) and of the positron (right). Same labels as in fig. 5.38.

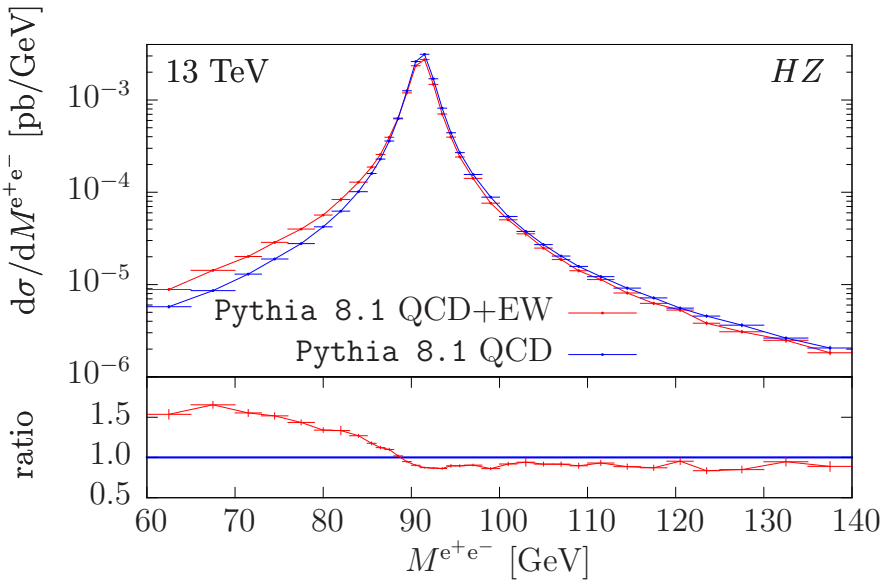


Figure 5.40: NLO+PS predictions for the invariant mass of the lepton pair. Same labels as in fig. 5.38.

The invariant mass of the lepton pair changes considerably when considering QCD+EW events. In fig. 5.40 we see an increase of the differential cross section in the low-mass region, that reaches 50% around the lower limit for $M^z$ imposed by the kinematic cut of eq. (5.9) on the $Z$-boson decay products. Around the peak and at higher values of invariant mass, instead, the contribution from the electroweak sector amounts to roughly $-10\%$. This distortion is due to the fact that we are considering the invariant mass of the "dressed" leptons. In the QCD case, all the photons are produced by the shower algorithm, and for this reason they are likely to be near in phase space to the leptons. They are then often recombined, and the momentum of the dressed-lepton pair quite resembles the momentum of the $Z$-boson resonance. When including QCD+EW corrections, instead, the hardest photon emission is produced by the `POWHEG BOX RES`, and this particle can be well separated from the lepton. Since in this case it is not recombined with its emitter, the shape of the invariant mass changes.

Finally, in figs. 5.41 and 5.42 we analyze the transverse-momentum and rapidity distributions of the $Z$ boson in the boosted regime defined by the cuts of eq. (5.11). These results are

very similar to the ones obtained for the Higgs boson in $HW$ production (figs. 5.13 and 5.14). While the electroweak corrections have a constant impact on the rapidity distribution, of about $-10\%$ in the whole $y^z$ range, the high-energy tail of the transverse momentum shows differences with respect to the pure QCD results of the order of $-25\%$ for $p_T > 1$ TeV.

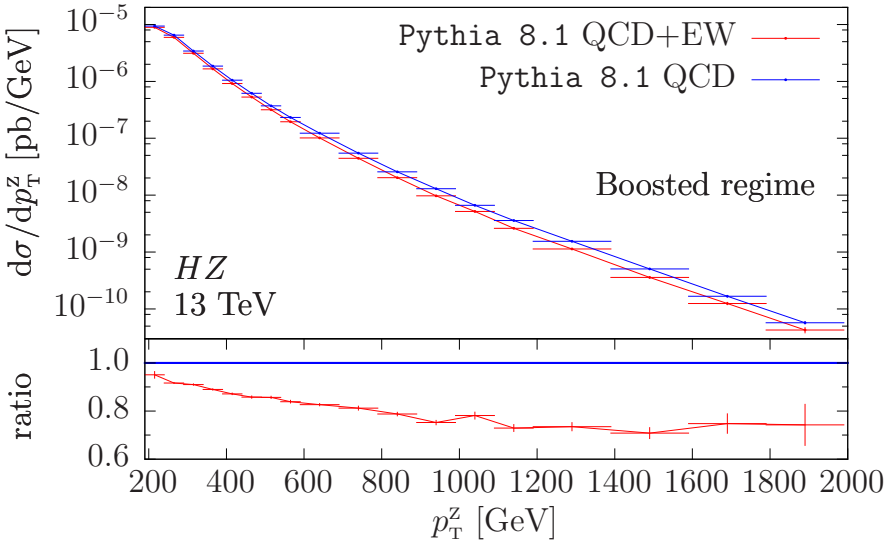


Figure 5.41: NLO+PS predictions for the transverse momentum of the $Z$ boson in the boosted regime. Same labels as in fig. 5.38.

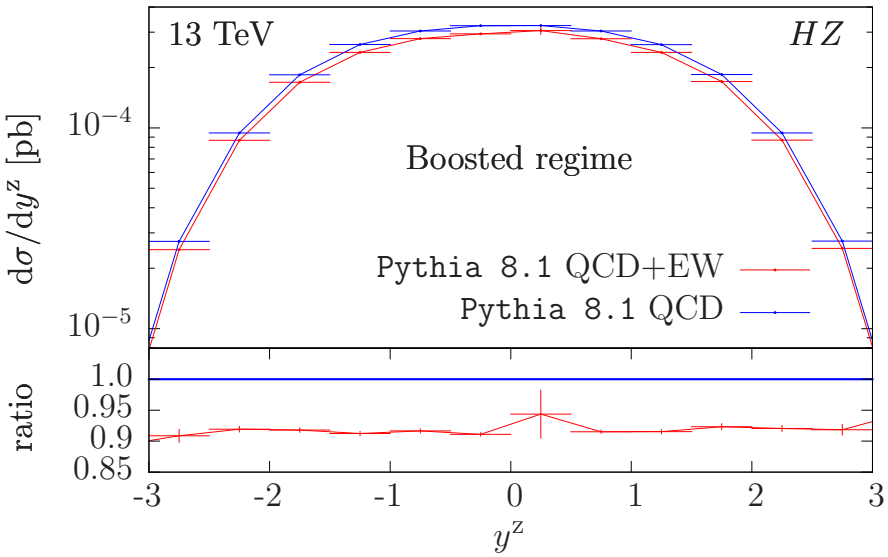


Figure 5.42: NLO+PS predictions for the rapidity of the $Z$ boson in the boosted regime. Same labels as in fig. 5.38.

## 5.6 The $HZj$ associated production

In this section we analyze the associated production of a Higgs boson with a $Z$ boson and a jet. As done for $HWj$ production, we apply the MiNLO procedure in order not to require a minimum transverse momentum for the leading jet and to leave to MiNLO the choice of scales at underlying-Born level.

### 5.6.1 Fixed-order NLO results

The total NLO cross sections are reported in tabs. 5.9 and 5.10. The former shows the results obtained by applying the `MiNLO` prescription, while for the latter we applied a cut of 20 GeV on the transverse momentum of the leading jet. The differences between the full QCD+EW

| $\sigma^{\text{NLO QCD}}_{\text{NLO EW}}$ [fb] | $\sigma^{\text{NLO QCD}}_{\text{NLL EW}}$ [fb] | $\sigma^{\text{NLO QCD}}$ [fb] |
|---|---|---|
| $24.59 \pm 0.07$ | $25.84 \pm 0.07$ | $24.801 \pm 0.009$ |

Table 5.9: Total cross sections for the *HZj* production process at a center-of-mass energy of $\sqrt{s} = 13$ TeV, including NLO QCD + NLO EW, NLO QCD + NLL EW and NLO QCD corrections, computed with the `MiNLO` procedure active.

| $\sigma^{\text{NLO QCD}}_{\text{NLO EW}}$ [fb] | $\sigma^{\text{NLO QCD}}_{\text{NLL EW}}$ [fb] | $\sigma^{\text{NLO QCD}}$ [fb] |
|---|---|---|
| $12.13 \pm 0.03$ | $12.69 \pm 0.01$ | $11.720 \pm 0.004$ |

Table 5.10: Total cross sections for the *HZj* production process at a center-of-mass energy of $\sqrt{s} = 13$ TeV, including NLO QCD + NLO EW, NLO QCD + NLL EW and NLO QCD corrections, with a minimum transverse-momentum cut of 20 GeV on the leading jet.

results and the QCD implementation are very small when the `MiNLO` procedure is activated, of the order of 1.5%, while the approximated NLL cross section is bigger than the QCD one of 5%. When a minimum transverse momentum is required, instead, both the full QCD+EW results and their NLL approximation are bigger than the QCD ones by about 4%. A similar behaviour occurred in *HWj* production (see tabs. 5.3 and 5.4): we can then conclude that for the *HVj* processes the Sudakov approximation does not give a good estimate of the NLO EW correction to the inclusive cross section.

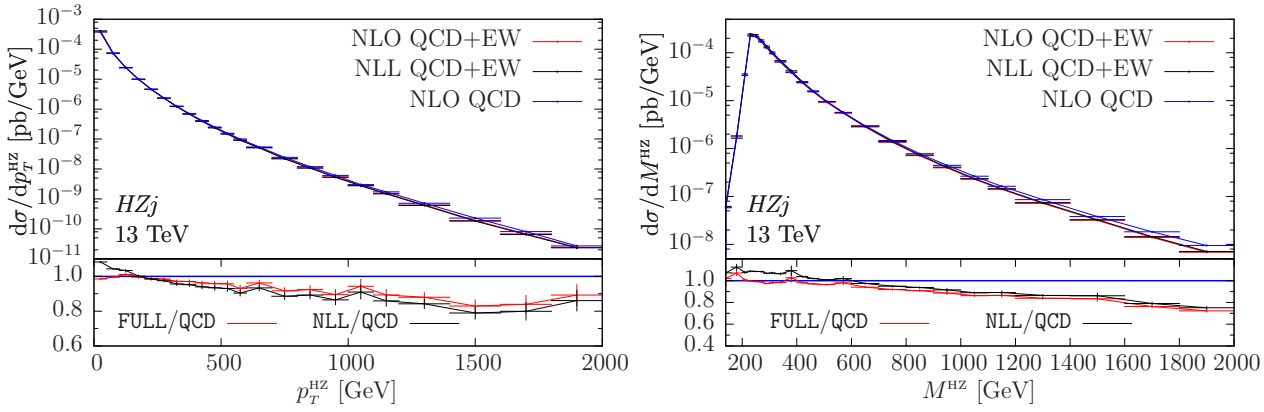


Figure 5.43: NLO predictions for the transverse momentum (left) and the invariant mass (right) of the $HZ$ pair, for *HZj* production. Comparison between the full QCD+EW calculation and the QCD results (in red in the ratio panel), and between the approximated QCD+EW calculation and the QCD results (in black in the ratio panel).

Figure 5.43 shows the transverse momentum and the invariant mass of the $HZ$ system: the lower panel displays the ratio between the `FULL` and the `QCD` implementations, and the ratio between the `NLL` and the `QCD` results. The high-energy behaviour of $M^{HZ}$ is similar to $HZ$ production: the decrease of the invariant mass due to the inclusion of the electroweak

corrections is around $-20\%$ above 1.5 TeV, and in this region the FULL and the NLL results converge to the same behaviour. Looking at the transverse-momentum distribution, instead, this overlap is visible starting from $p_T^{HZ} \sim 300$ GeV.

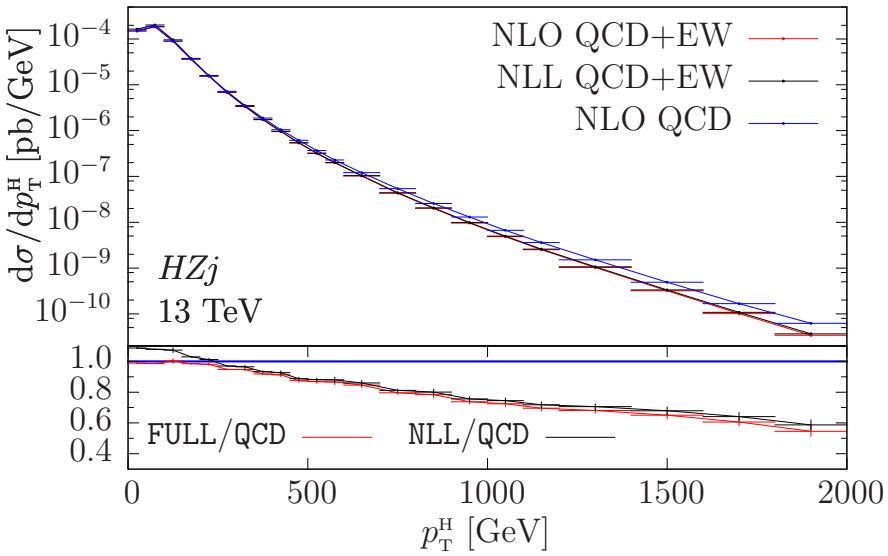


Figure 5.44: NLO predictions for the transverse momentum of the Higgs boson. Same labels as in fig. 5.43.

In fig. 5.44 we plot the transverse momentum of the Higgs boson. The effect of the electroweak corrections on the QCD predictions is about $-50\%$ around 2 TeV, while below 200 GeV, where the bulk of the events is concentrated, is almost negligible. As remarked in Sec. 5.4.1 when analyzing $HWj$ production, the electroweak corrections give a more pronounced effect with respect to $HZ$ production. This is due to the inclusion of the MiNLO prescription, that allows to apply the electroweak corrections in the full phase space, including also the contributions coming from the Born-level jet that are absent in the $HZ$ case.

As far as the pseudorapidity of the Higgs boson is concerned we see, in fig. 5.45, that the full electroweak corrections have a constant and very small impact on this distribution, while

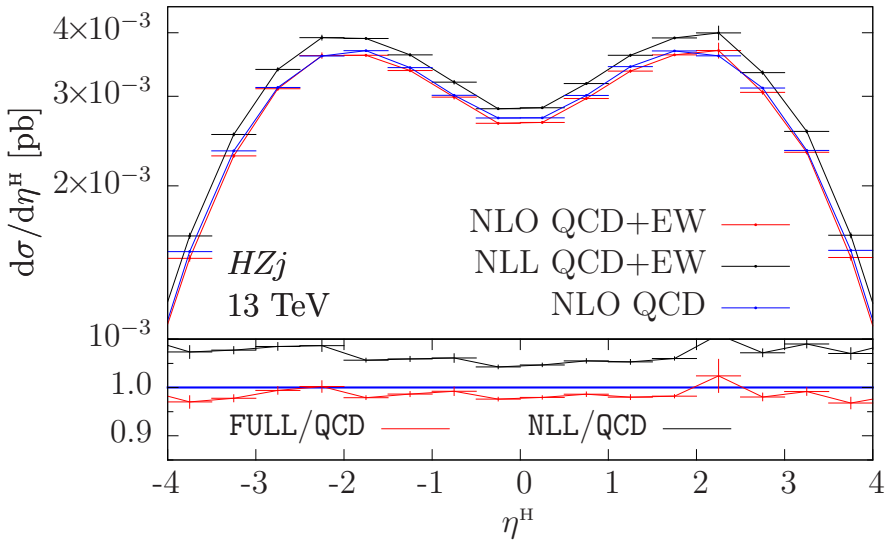


Figure 5.45: NLO predictions for the pseudorapidity of the Higgs boson. Same labels as in fig. 5.43.

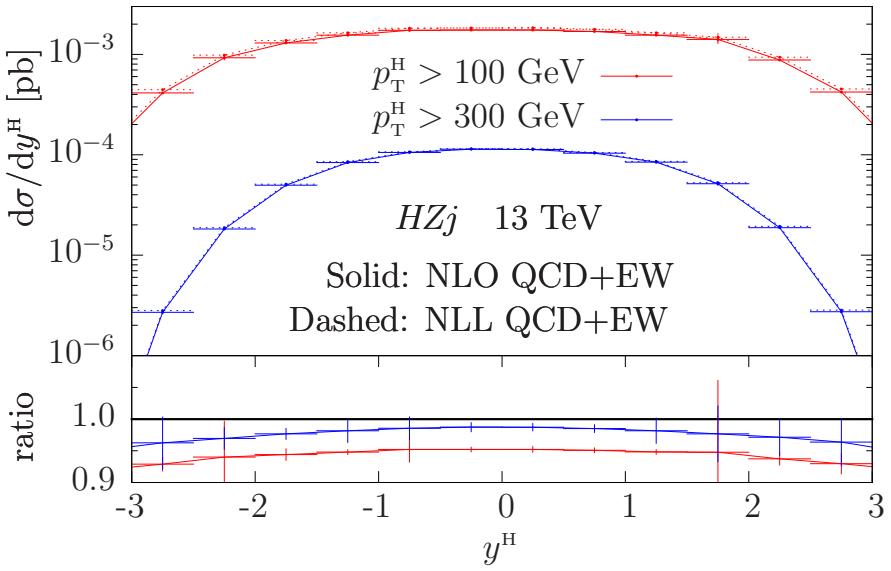


Figure 5.46: NLO rapidity distribution of the Higgs boson, for $HZj$ production, with kinematic cuts of 100 GeV and 300 GeV on its transverse momentum. Comparison between the complete QCD+EW calculation (solid lines) and its Sudakov approximation (dashed lines).

the NLL approximation gives a positive contribution, as remarked in the analysis of the total cross sections. Figure 5.46, instead, shows the Higgs-boson rapidity distribution obtained with kinematic cuts of 100 GeV and 300 GeV on its transverse momentum, and compares the NLO QCD+EW results with their NLL approximation. By inspecting the lower panel we see that, while with the lower cut the FULL results are smaller than the NLL ones by about 5%, with a 300 GeV cut this difference decreases, reaching 1-2%.

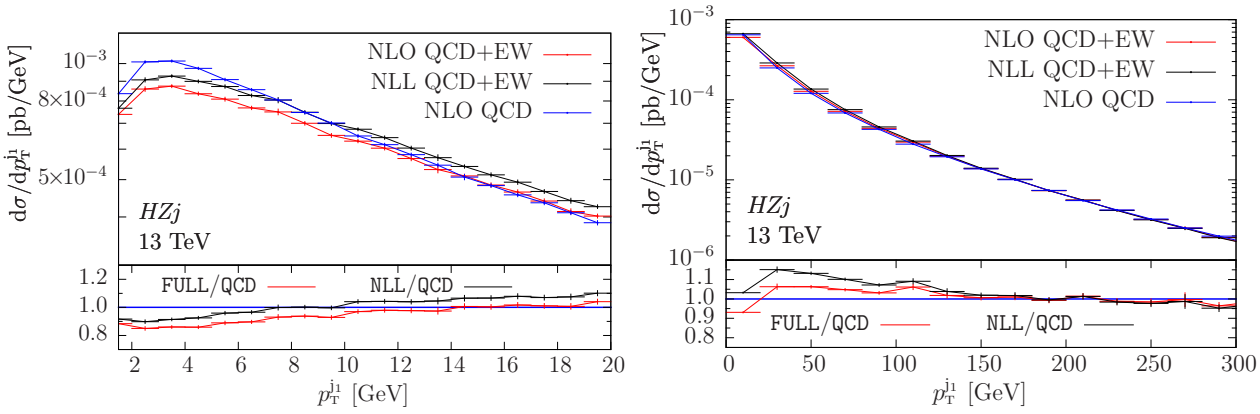


Figure 5.47: NLO predictions for the transverse momentum of the leading jet in two different $p_T^{j1}$ ranges. Same labels as in fig. 5.43.

We now analyze some distributions for the leading jet: in fig. 5.47 we show its transverse momentum in two different $p_T^{j1}$ ranges. As already pointed out in $HWj$ production, both the full and the approximated electroweak corrections give the most relevant contributions in the low-$p_T$ region: from 20 GeV up to 150 GeV, their contribution increases the differential cross section, while at higher values of $p_T^{j1}$ their contribution becomes negligible. Looking at the leading-jet rapidity in fig. 5.48, instead, we find a negligible contribution in the range $|y^{j_1}| < 3$, and a contribution of the order of $-5\%$ for $|y^{j_1}| > 3$.

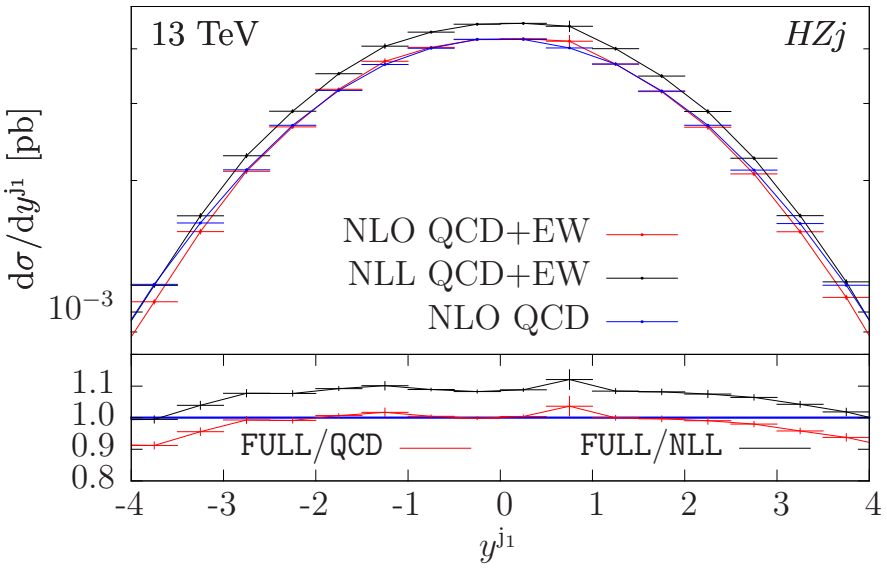


Figure 5.48: NLO predictions for the rapidity of the leading jet. Same labels as in fig. 5.43.

### 5.6.2 Parton-shower-level predictions

In this section we compare three outputs: the showered `POWHEG BOX RES` results, the events at Les Houches level, and the fixed-order NLO predictions.

#### Comparisons among NLO, Les Houches and `Pythia` results at QCD+EW accuracy

Similarly to what done in the previous sections, we first inspect the rapidity of the $HZ$ system, shown in fig. 5.49. Due to the presence of `MiNLO`, this quantity is finite and we see a very good agreement, within the integration errors, of the three distributions.

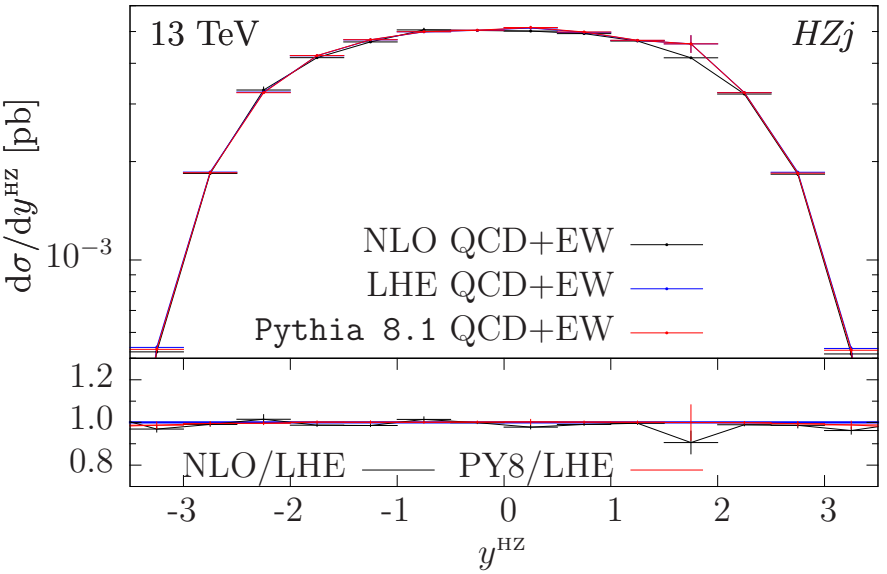


Figure 5.49: Rapidity distribution of the $HZ$ pair, for $HZj$ production. Comparisons among the NLO results, the hardest event produced by the `POWHEG BOX RES` (LHE) and the NLO+PS predictions, for combined QCD+EW corrections.

In fig. 5.50 we plot the transverse momentum of the $HZ$ pair. At leading order, this

system recoils against the leading jet: the inclusion of the MiNLO prescription tames the NLO divergence associated to the small-$p_T$ region.

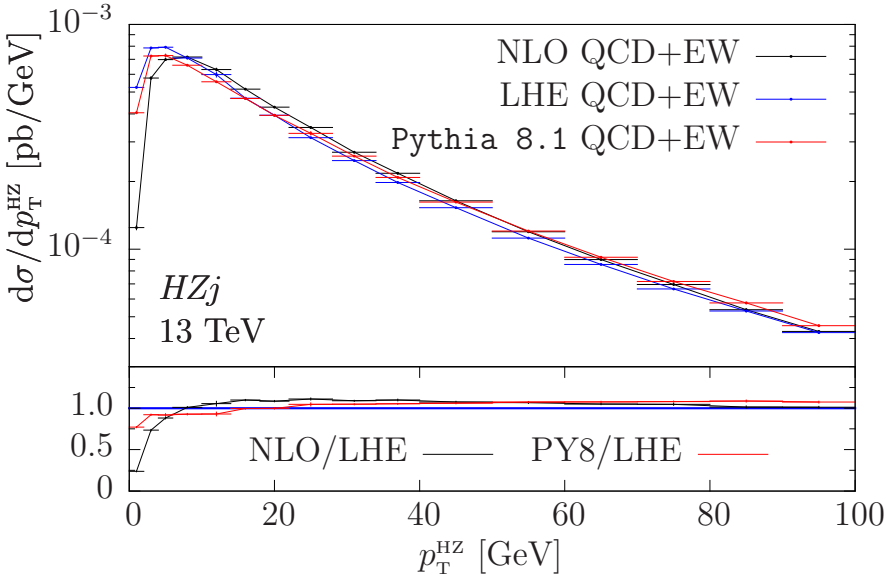


Figure 5.50: Transverse-momentum distribution of the $HZ$ pair. Same labels as in fig. 5.49.

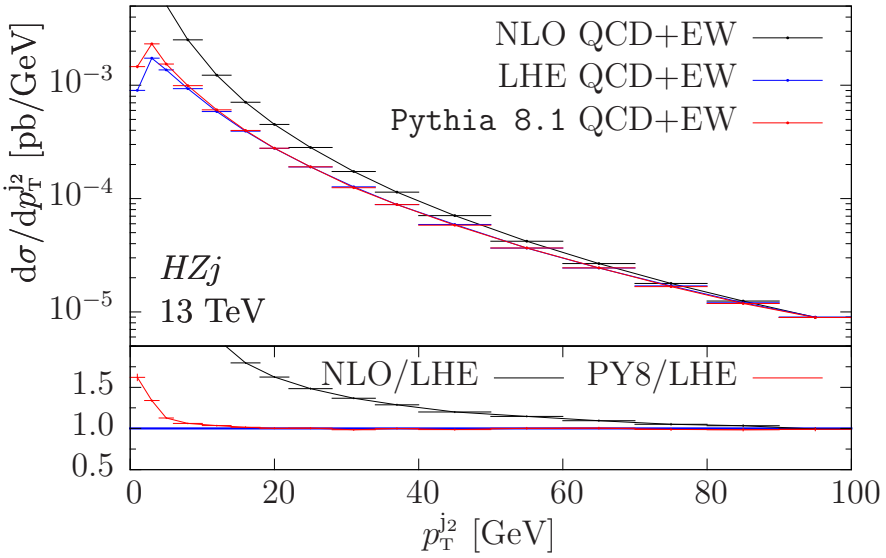


Figure 5.51: Transverse-momentum distribution of the subleading jet. Same labels as in fig. 5.49.

The NLO singularity is instead visible in the transverse momentum of the subleading jet, in fig. 5.51. The Les Houches and showered results are finite at low $p_T$, due to the POWHEG BOX Sudakov form factor associated with the radiated parton.

In fig. 5.52 we show the rapidity distribution of the hardest photon, obtained with a cut of 10 GeV on its transverse momentum, as explained in Sec. 5.2. This plot presents some differences with respect to the $HZ$ case (in fig. 5.36): here, the contribution coming from the shower is almost negligible on the whole $y^\gamma$ range. Similar conclusions can be drawn for the transverse-momentum distribution of the photon, shown in fig. 5.53.

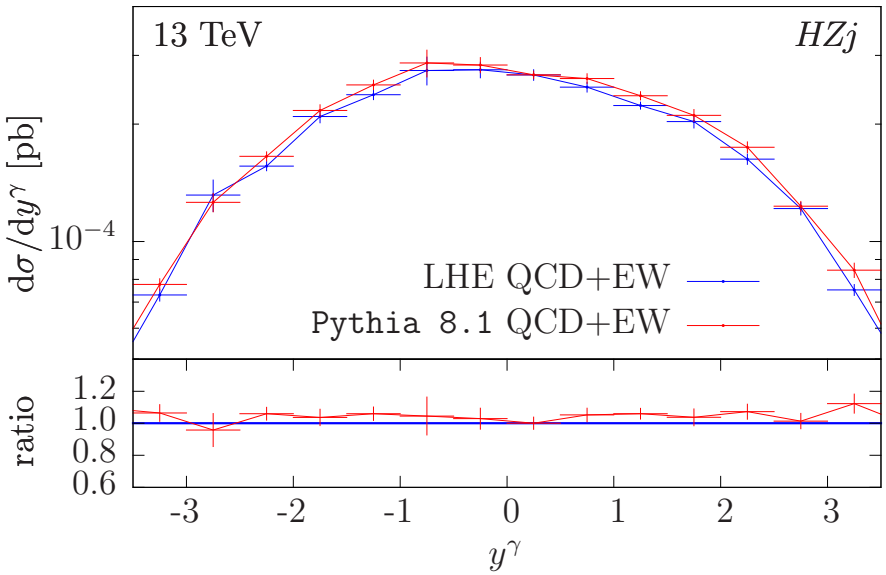


Figure 5.52: Rapidity distribution of the hardest photon, for *HZj* production. Comparison between the hardest event produced by the `POWHEG BOX RES` (LHE) and the NLO+PS predictions, for combined QCD+EW corrections.

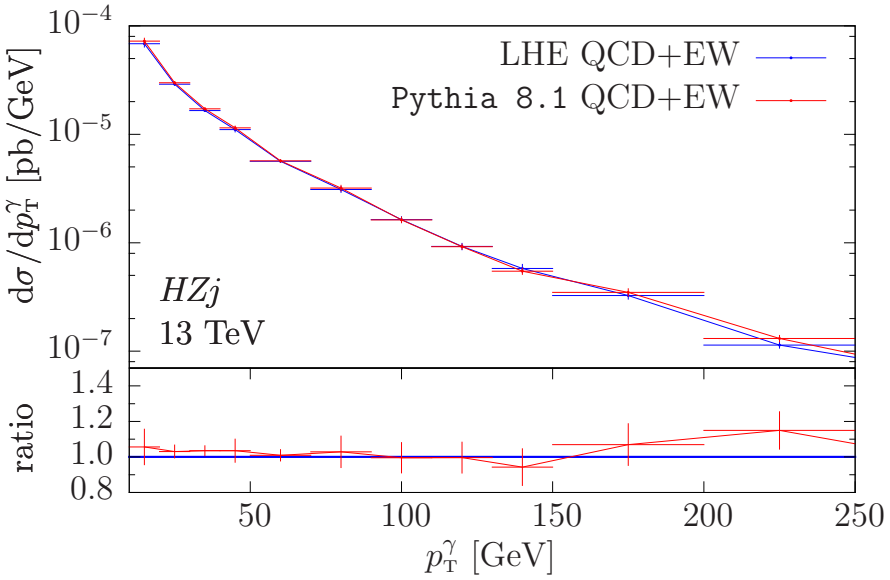


Figure 5.53: Transverse-momentum distribution of the hardest photon. Same labels as in fig. 5.52.

### Impact of the electroweak corrections in NLO+PS events

We conclude this section by studying the impact of the electroweak sector on the QCD one at NLO+PS level. For the total NLO+PS cross section the results obtained with the inclusion of the `MiNLO` prescription are collected in tab. 5.11, while tab. 5.12 contains the results for the cross section with a cut of 20 GeV on the transverse momentum of the leading jet. If we compare these results with the NLO cross sections, we can find a good agreement, with small differences that can be ascribed to the fact that the NLO+PS results contain contributions beyond the NLO.

| $\sigma^{\text{NLO+PS}}_{\text{QCD+EW}}$ [fb] | $\sigma^{\text{NLO+PS}}_{\text{QCD}}$ [fb] |
|---|---|
| $25.0 \pm 0.2$ | $24.84 \pm 0.02$ |

Table 5.11: Total NLO+PS cross sections for the $HZj$ production process at a center-of-mass energy of $\sqrt{s} = 13$ TeV, including QCD+EW and QCD corrections, computed with the `MiNLO` procedure active.

| $\sigma^{\text{NLO+PS}}_{\text{QCD+EW}}$ [fb] | $\sigma^{\text{NLO+PS}}_{\text{QCD}}$ [fb] |
|---|---|
| $11.46 \pm 0.01$ | $11.84 \pm 0.01$ |

Table 5.12: Total NLO+PS cross sections for the $HZj$ production process, at a center-of-mass energy of $\sqrt{s} = 13$ TeV, including QCD+EW and QCD corrections, computed with a minimum transverse-momentum cut of 20 GeV on the leading jet.

Looking at less inclusive quantities, the transverse momentum of the leading jet, reported in fig. 5.54, receives very small corrections in the whole $p_T^{j_1}$ range, as pointed out in $HWj$ production. The same behaviour holds for other typical kinematic distributions involving the jet, that therefore we do not show.

In fig. 5.55, instead, we show the transverse momentum of the $Z$ boson in the boosted regime, for which we can draw conclusions similar to the ones of the previous sections. The electroweak corrections give a negative contribution, that in the tail of the distribution reaches $-40\%$. The rapidity and invariant mass of the $Z$ boson, together with the transverse momentum of the charged leptons, do not have appreciable differences with respect to the $HZ$ case, so they are not reported here.

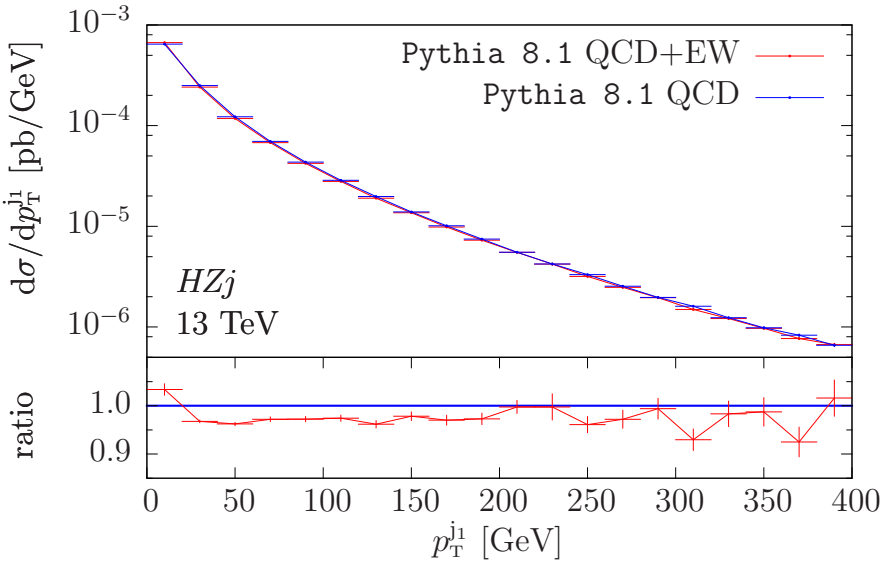


Figure 5.54: NLO+PS predictions for the transverse momentum of the leading jet, for $HZj$ production. Comparison between the full QCD+EW calculation and the QCD results.

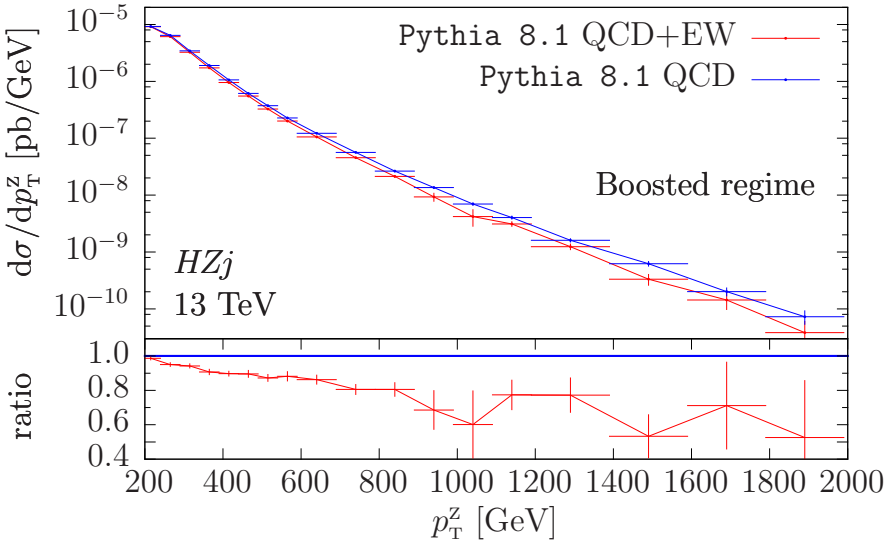


Figure 5.55: NLO+PS predictions for the transverse momentum of the $Z$ boson in the boosted regime. Same labels as in fig. 5.54.

## 5.7 Parton-shower-level comparison between the *HV* and *HVj* generators

After analyzing the four classes of processes separately, in this section we discuss and compare the NLO+PS QCD+EW results for $HV$ and $HVj$ production, reproducing the analysis performed in ref. [12], where only QCD corrections were considered. This comparison is motivated by the fact that the improved `MiNLO` prescription applied in $HVj$ production achieves NLO accuracy for observables that are inclusive in the $HV$ production, i.e. when the associated jet is not resolved. For $HW$ and $HWj$ production, we show results for the production of a $W^-$ boson only. Similar results can be obtained for the $W^+$ case.

In tab. 5.13 we collect the total cross sections for the considered processes at NLO+PS QCD+EW level, for different scale combinations. The scale variations are obtained by multiplying the renormalization and factorization scales $\mu_R$ and $\mu_F$, whose central value for $HV$ production is defined in eq. (4.80), by the factors $K_R$ and $K_F$ respectively, where

$$(K_R, K_F) = \left(\frac{1}{2}, \frac{1}{2}\right), \left(\frac{1}{2}, 1\right), \left(1, \frac{1}{2}\right), (1,1), (2,1), (1,2), (2,2), \tag{5.13}$$

and by taking the envelope of the resulting predictions. In the $HVj$ case, due to the inclusion of the `MiNLO` prescription, this multiplication is performed for each of the several renormalization scales that appear in the process. The Sudakov form factor is also changed, according to this prescription, as explained in Sec. 2.5.1.

The results are fairly consistent: the central-scale cross sections are slightly bigger in the $HVj$ processes than in $HV$, with differences of the order of 1% for the $W$ case and of about 3% for the $Z$ case. The scale variation is larger in the $HVj$ implementations, and it shrinks if a symmetric scale variation is performed, as can be seen by inspecting the last two rows of the table. Since in the `POWHEG BOX RES` the scale variation is performed only in the inclusive NLO cross section (the $\bar{B}$ function in the `POWHEG` jargon), and not in the scale associated to the radiation, these uncertainty bands are narrower than what would be obtained by varying all the scales in a fixed-order NLO computation.

| $(K_R, K_F)$ | $\sigma^{\text{NLO+PS}}_{HW^-}$ [fb] | $\sigma^{\text{NLO+PS}}_{HW^-j}$ [fb] | $\sigma^{\text{NLO+PS}}_{HZ}$ [fb] | $\sigma^{\text{NLO+PS}}_{HZj}$ [fb] |
|---|---|---|---|---|
| $(1, 1)$ | $55.29 \pm 0.08$ | $55.25 \pm 0.08$ | $24.34 \pm 0.03$ | $24.9 \pm 0.2$ |
| $(1, 2)$ | $56.06 \pm 0.08$ | $56.50 \pm 0.09$ | $24.66 \pm 0.03$ | $25.4 \pm 0.2$ |
| $(2, 1)$ | $54.63 \pm 0.08$ | $53.50 \pm 0.07$ | $24.06 \pm 0.03$ | $24.0 \pm 0.2$ |
| $\left(1, \frac{1}{2}\right)$ | $54.55 \pm 0.08$ | $52.68 \pm 0.08$ | $24.03 \pm 0.03$ | $23.8 \pm 0.2$ |
| $\left(\frac{1}{2}, 1\right)$ | $56.09 \pm 0.08$ | $55.7 \pm 0.1$ | $24.68 \pm 0.03$ | $25.5 \pm 0.3$ |
| $\left(\frac{1}{2}, \frac{1}{2}\right)$ | $55.44 \pm 0.08$ | $55.9 \pm 0.1$ | $24.41 \pm 0.03$ | $25.5 \pm 0.3$ |
| $(2, 2)$ | $55.45 \pm 0.08$ | $55.52 \pm 0.08$ | $24.40 \pm 0.03$ | $24.8 \pm 0.2$ |

Table 5.13: Total NLO+PS cross sections for the $HV$ and $HVj$ production processes at a center-of-mass energy of $\sqrt{s} = 13$ TeV, for different scale combinations. The $HVj$ processes are computed with the `MiNLO` procedure active.

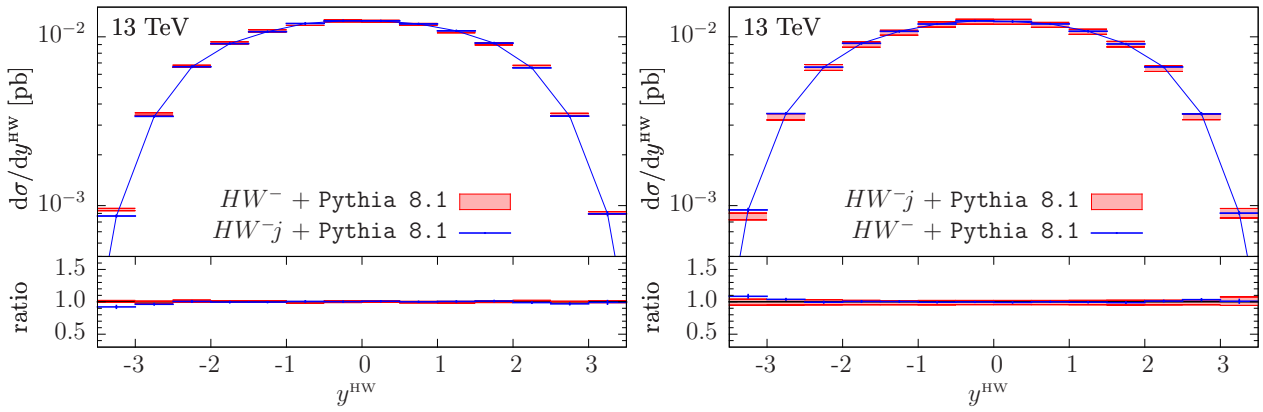


Figure 5.56: NLO+PS comparison between the $HW^-$ rapidity distributions in the $HW$ and in the $HWj$ computation. The left-hand-side plot shows the 7-point scale-variation band for the $HW$ generator, while the right-hand-side plot shows the $HWj$ 7-point band.

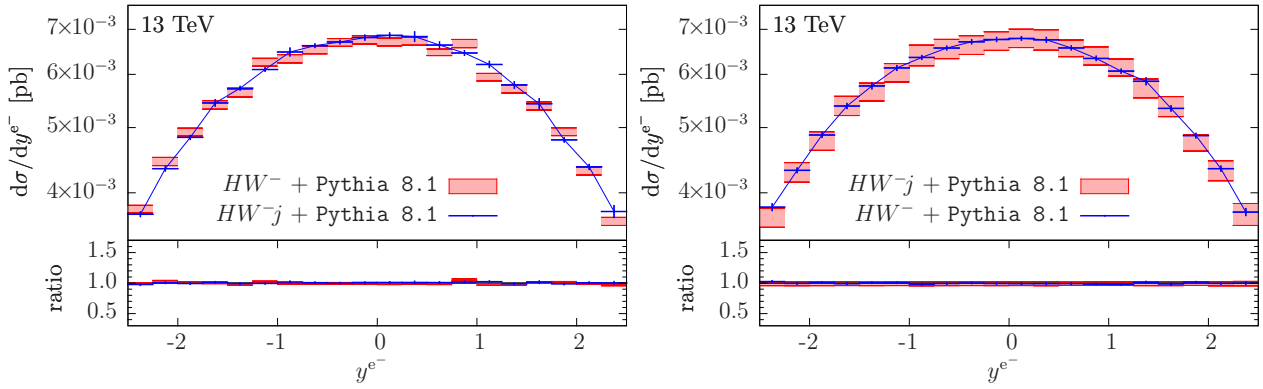


Figure 5.57: NLO+PS comparison between the electron rapidity distributions in the $HW$ and in the $HWj$ computation. The bands are obtained as in fig. 5.56.

Moving to more exclusive quantities, we first analyze in fig. 5.56 the rapidity distribution of the $HW$ system. In this and in the following plots, the red bands represent the uncertainty associated to the scale variations, while the blue bars represent the statistical uncertainties of the integration procedure. The plot on the left-hand side shows the uncertainty band of the $HW$ process, while the right-hand-side one shows the uncertainty band of the $HWj$ generator. Since this quantity is predicted at NLO by both processes, we find very good agreement. The uncertainty band is larger in the $HWj$ case: this is due to the fact that for $HW$ production there is no renormalization-scale dependence at leading order, while in $HWj$ such dependence is present. The same agreement can be found in another inclusive quantity, i.e. the rapidity of the electron, shown in fig. 5.57.

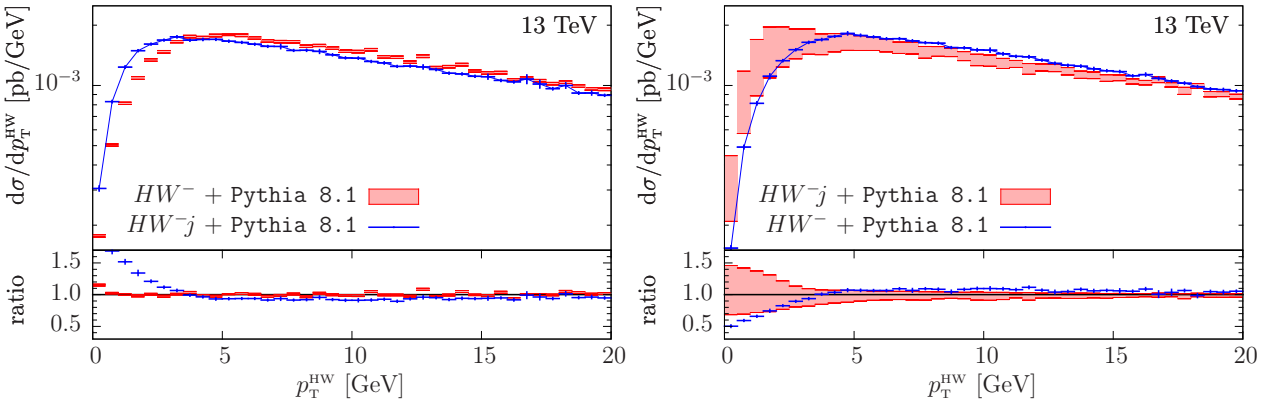


Figure 5.58: NLO+PS comparison between the $HW$ transverse-momentum distributions in the $HW$ and in the $HWj$ computation. The bands are obtained as in fig. 5.56.

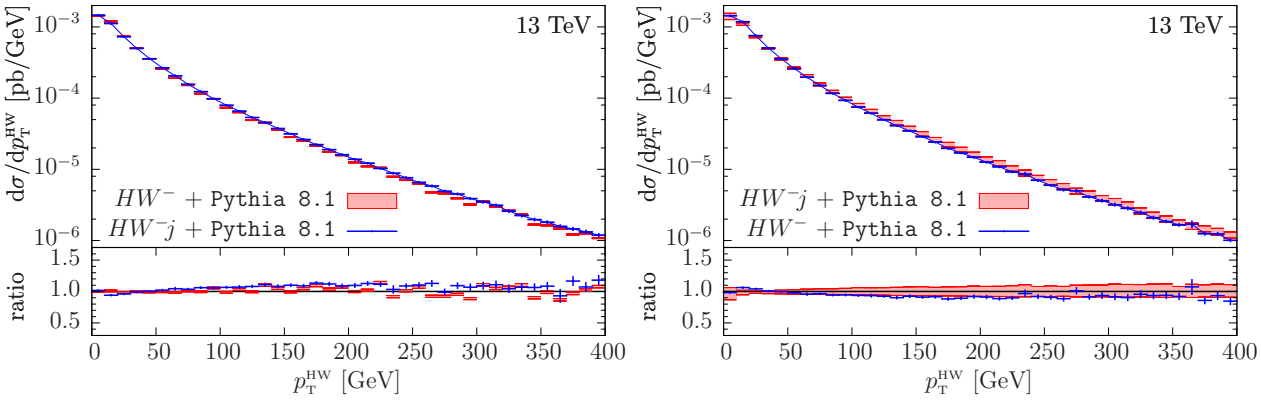


Figure 5.59: Same comparison as in fig. 5.58, in a different $p_T^{HW}$ range.

In figs. 5.58 and 5.59 we compare the transverse momentum of the $HW$ pair, in two different $p_T$ ranges. Here we observe some differences, as discussed in the original paper, due to the fact that this distribution is only computed at leading order in $HW$ production, while it has NLO accuracy in the other case. Since we included also electroweak corrections, in our plots these differences are slightly more pronounced than in the pure QCD implementation. We can also note that the uncertainty band for the $HW$ generator is smaller than the $HWj$ one. This is due to the fact that, at Born level, $HW$ production does not depend upon $\alpha_s$, while $HWj$ production does, and this dependence amplifies the bands.

In figs. 5.60 - 5.63 we repeat these comparisons for $HZ$ and $HZj$ production, for which we can draw similar conclusions as for the $HW/HWj$ comparison.

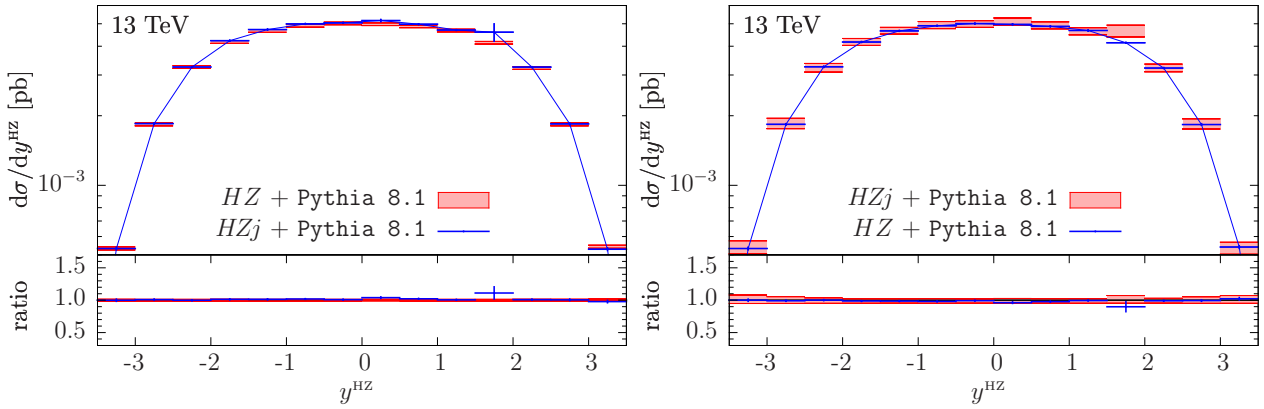


Figure 5.60: NLO+PS comparison between the $HZ$ rapidity distributions in the $HZ$ and in the $HZj$ computation. The left-hand-side plot shows the 7-point scale-variation band for the $HZ$ generator, while the right-hand-side plot shows the $HZj$ 7-point band.

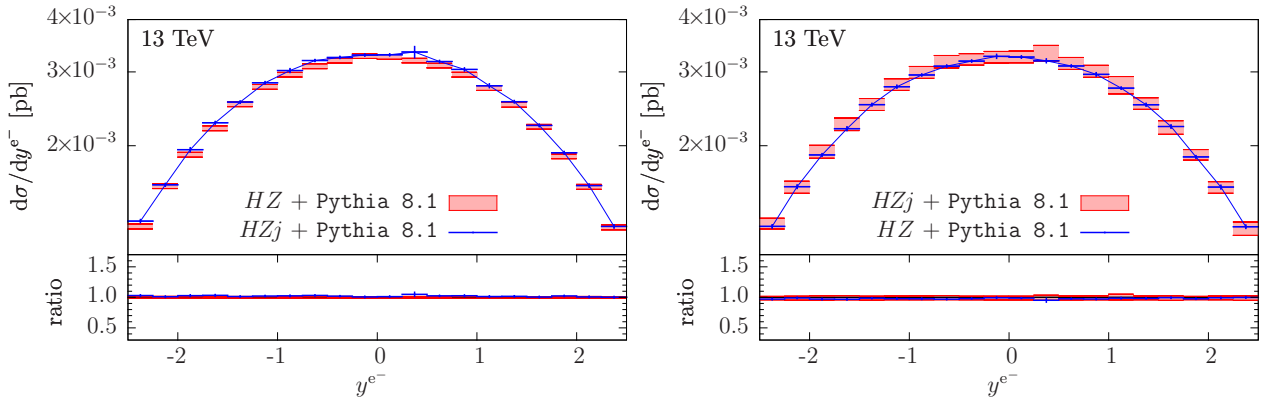


Figure 5.61: NLO+PS comparison between the electron rapidity distributions in the $HZ$ and in the $HZj$ computation. The bands are obtained as in fig. 5.60.

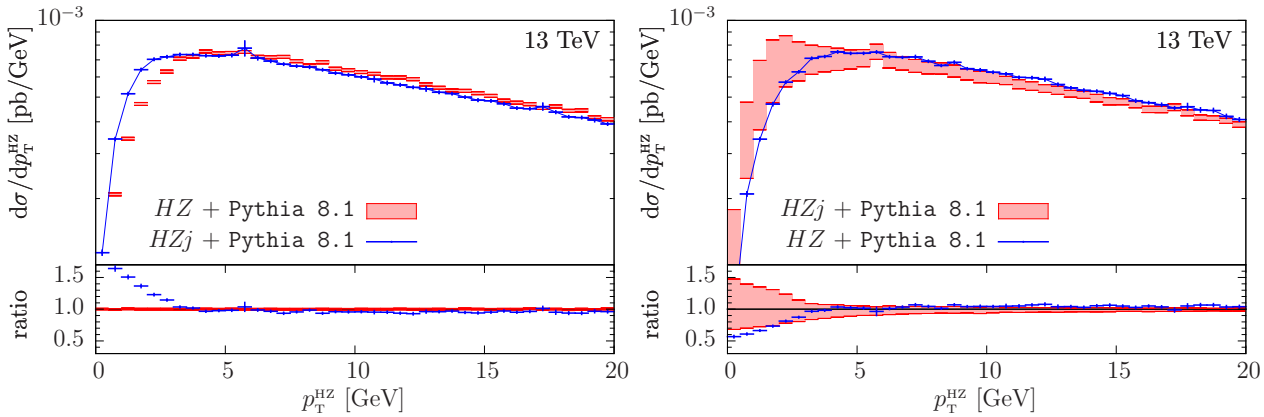


Figure 5.62: NLO+PS comparison between the $HZ$ transverse-momentum distributions in the $HZ$ and in the $HZj$ computation. The bands are obtained as in fig. 5.60.

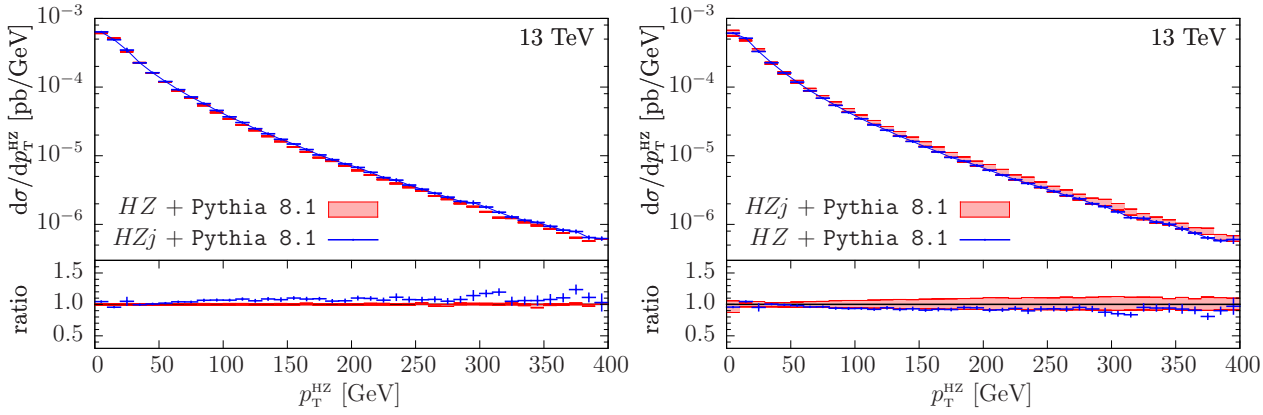


Figure 5.63: Same comparison as in fig. 5.62, in a different $p_T^{HW}$ range.

# Conclusions

In this thesis we have presented original theoretical results on the combined QCD+EW corrections to the associated production of a Higgs boson with a leptonically-decaying vector boson and eventually a jet ($HV/HVj$) in hadronic collisions, at NLO + parton-shower level.

To describe the associated production processes at combined QCD+EW accuracy, we extended a previous NLO+PS QCD calculation, including also the full electroweak corrections and their Sudakov approximation. We implemented them in the `POWHEG BOX RES`, a Monte Carlo event generator with NLO accuracy that can be interfaced to parton- and photon-shower generators according to the `POWHEG` method. This program is an extension of the `POWHEG BOX`: it considerably improves the precision in the description of processes where the radiation can originate from the decay of massive resonances. Photon radiation from massive leptons was already introduced in this framework, and we have added the treatment of photon radiation from final-state massless charged particles.

In the first part of this thesis we computed the Sudakov corrections to the associated production processes $HV$ and $HVj$. We distinguished between the production of transverse and longitudinal vector bosons, since they behave in different ways in the high-energy limit. We found a negligible contribution coming from the transversely polarized vector boson, in the high-energy region $\sqrt{s} \gtrsim 1$ TeV. This can be ascribed to the fact that the corresponding matrix element is mass-suppressed with respect to the longitudinal one, so at high energies it gives contributions of less than 1% to the total result.

Then, we analyzed $HV$ and $HVj$ production in proton-proton collisions at a center-of-mass energy of 13 TeV. We focused on the transverse momentum of the final-state particles, in the high-energy regime. The discrepancies between the approximated NLL and the complete calculations turned out to be of the order of 1-2% in $HW$ and $HWj$ production, and of 5% for the $Z$-boson case. When inspecting more inclusive quantities, like the total cross section and the rapidity distributions, the NLL approximation has not provided reliable results, presenting differences with respect to the complete calculation of 8% for $HW$ and $HWj$ production, and of 5% for $HZ$ and $HZj$. Moreover we found that, while the full electroweak corrections always decrease the pure QCD predictions, in $HWj$ and $HZj$ production the Sudakov approximation gives a positive contribution to the total cross sections and to the rapidity distributions. However, we did not expect the NLL approximation to be good for these inclusive quantities.

The electroweak corrections have sizable impact on several transverse-momentum distributions at high $p_T$. For example, in $HV$ production we found that the electroweak corrections decrease the QCD results of 15% at $p_T$ values of the vector boson of 1 TeV, while around 2 TeV the corrections amount to $-30\%$. For $HVj$ production, the effect is even more pronounced, reaching $-20\%$ at 1 TeV and $-40\%$ at 2 TeV. The rapidity distributions, the transverse mass of the vector boson and the typical kinematic distributions involving the jets, instead, receive constant negative contributions in the whole rapidity ranges considered, of the order of 5-10%, depending on the process.

It is then important to include the electroweak corrections when computing collider observables in the high-energy regime, since they change in a non-negligible way the shape of many kinematic distributions.

A good approximation of the complete result can be obtained by including the NLL approximated results, i.e. those that contain the Sudakov logarithms up to order next-to-leading. Using approximated expressions for the full one-loop electroweak virtual amplitudes drastically reduces the computational cost. While this approximation is valid in the tails of some transverse-momentum distributions, starting from $p_T$-values of the order of 500 GeV, it differs with respect to the full electroweak results for more inclusive quantities.

The work presented in this thesis provides the first NLO+PS simulation of the associated production of a Higgs boson with a leptonically-decaying vector boson and eventually a jet at hadron colliders, with combined QCD+EW accuracy and with the possibility to include the complete one-loop electroweak corrections or their high-energy limit. Thanks to the improvements introduced in the `POWHEG BOX RES` for the treatment of photon radiation, and to the interface to the `OpenLoops` generator, this framework can consistently simulate Standard Model processes at NLO+PS EW accuracy. This is a good starting point for future works, towards the automation of the generation of Standard Model processes at NLO+PS QCD+EW accuracy, to comply with the experimental results that are coming from the LHC Run 2.

# Appendix A

# Representations of the gauge group

In this appendix we define the generators of the SU(2) × U(1) gauge group, and we list some useful group-theoretical quantities that are used in the calculation of the electroweak corrections in Sudakov approximation.

## A.1 SU(2) × U(1) generators

The infinitesimal global SU(2) × U(1) transformations of the fields $\varphi_i$ are determined by

$$\delta\varphi_i = ie \sum_{V^a=A,\,Z,\,W^\pm} \sum_{\varphi_{i'}} I^{V^a}_{\varphi_i\varphi_{i'}} \delta\theta^{V^a} \varphi_{i'}, \tag{A.1}$$

where $\delta\theta^{V^a}$ are the infinitesimal gauge parameters, and the matrices $I^{V^a}_{\varphi_i\varphi_{i'}}$ are the generators that determine the gauge couplings. In other words, $ieI^{V^a}_{\varphi_i\varphi_{i'}}$ is the coupling corresponding to the gauge vertex $V^a\bar{\varphi}_i\varphi_{i'}$, with all fields incoming. The representation of these matrices depends on $\varphi$: in general it is not irreducible.

Since the transformation rule for the complex-conjugate fields is fixed by the complex conjugation of eq. (A.1), the following relation holds,

$$\left(I^{V^a}_{\varphi_i\varphi_j}\right)^* = -I^{\bar{V}^a}_{\varphi_i^+\varphi_j^+}, \tag{A.2}$$

where $\bar{V}^a$ and $\varphi_i^+$ are the charge-conjugated fields of $V^a$ and $\varphi_i$. Owing to the unitarity of representations, in a real basis in which $\bar{V}^a = V^a$ the generators are self-adjoint, so that

$$I^{\bar{V}^a}_{\varphi_i\varphi_j} = \left(I^{V^a}_{\varphi_j\varphi_i}\right)^*, \tag{A.3}$$

and combining these two relations we obtain

$$I^{V^a}_{\varphi_i\varphi_j} = -I^{V^a}_{\varphi_j^+\varphi_i^+}. \tag{A.4}$$

The generators in the adjoint representation are connected to the structure constants through a set of commutation relations,

$$\left[I^{V^a}, I^{V^b}\right]_{\varphi_i\varphi_j} = \frac{i}{s_W} \sum_{V^c} \varepsilon^{V^aV^bV^c}\, I^{\bar{V}^c}_{\varphi_i\varphi_j}. \tag{A.5}$$

## A.2 Bases for gauge fields

Group-theoretical quantities can be expressed in two different bases. The symmetric basis is formed by the U(1) and SU(2) gauge bosons $\tilde{V} = (B, W^3, W^1, W^2)^T$. The physical basis, instead, can be obtained by considering the charge and mass eigenstates, $V = (A, Z, W^+, W^-)^T$. The relation between these two bases is

$$A = c_W B - s_W W^3, \tag{A.6}$$

$$Z = s_W B + c_W W^3, \tag{A.7}$$

$$W^\pm = \frac{W^1 \mp i W^2}{\sqrt{2}}, \tag{A.8}$$

or, in matrix notation, $V = U(\theta_W)\tilde{V}$, where

$$U(\theta_W) = \begin{pmatrix} c_W & -s_W & 0 & 0 \\ s_W & c_W & 0 & 0 \\ 0 & 0 & \frac{1}{\sqrt{2}} & -\frac{i}{\sqrt{2}} \\ 0 & 0 & \frac{1}{\sqrt{2}} & \frac{i}{\sqrt{2}} \end{pmatrix}. \tag{A.9}$$

We can then express the generators of the gauge group, and some other useful group-theoretical quantities, in the two different bases. The generators of the gauge group in the symmetric basis can be written in terms of the components of the weak isospin $T^a$, the hypercharge $Y$ and the relation with the electric charge $Q = T^3 + Y/2$, according to

$$\tilde{I}^B = -\frac{1}{c_W}\frac{Y}{2}, \quad \tilde{I}^{W^a} = \frac{1}{s_W} T^a, \quad a = 1, 2, 3. \tag{A.10}$$

Defining a vector $\tilde{I}^{\tilde{V}} = (\tilde{I}^B, \tilde{I}^{W^3}, \tilde{I}^{W^1}, \tilde{I}^{W^2})$, the generators $I^V = (I^A, I^Z, I^{W^+}, I^{W^-})$ of the physical basis can be obtained employing the matrix (A.9), through $I^V = \tilde{I}^{\tilde{V}} U^\dagger(\theta_W)$, where

$$U^\dagger(\theta_W) = U^{-1}(\theta_W) = \begin{pmatrix} c_W & s_W & 0 & 0 \\ -s_W & c_W & 0 & 0 \\ 0 & 0 & \frac{1}{\sqrt{2}} & \frac{1}{\sqrt{2}} \\ 0 & 0 & \frac{i}{\sqrt{2}} & -\frac{i}{\sqrt{2}} \end{pmatrix}. \tag{A.11}$$

The result is

$$I^A = -Q, \qquad I^Z = \frac{T^3 - Q s_W^2}{s_W c_W}, \qquad I^\pm = \frac{1}{s_W} T^\pm = \frac{1}{s_W}\frac{T^1 \pm i T^2}{\sqrt{2}}. \tag{A.12}$$

## A.3 Relevant group-theoretical quantities

We first introduce the electroweak Casimir operator, defined as the sum over the squared SU(2) and U(1) generators,

$$C^{\text{ew}}_{\varphi_i \varphi_{i'}} = \sum_{V^a = A,\, Z,\, W^\pm} \left( I^{V^a} I^{\bar{V}^a} \right)_{\varphi_i \varphi_{i'}} = \frac{1}{c_W^2} \left( \frac{Y}{2} \right)^2_{\varphi_i \varphi_{i'}} + \frac{1}{s_W^2} C^{\text{SU(2)}}_{\varphi_i \varphi_{i'}}, \tag{A.13}$$

where the SU(2) Casimir operator is

$$C^{\text{SU(2)}} = \sum_{a=1}^{3} (T^a)^2 . \tag{A.14}$$

For fermions and scalars the electroweak Casimir operator is diagonal,

$$C^{\rm ew}_{\varphi_i\varphi_{i'}} = \delta_{\varphi_i\varphi_{i'}} \left[ \frac{Y^2_{\varphi_i}}{4c_W^2} + \frac{|T^3_{\varphi_i}| \left( |T^3_{\varphi_i}| + 1 \right)}{s_W^2} \right], \tag{A.15}$$

while for gauge bosons it is non-diagonal in the neutral components of the physical basis, and reads

$$C^{\rm ew}_{V^a V^b} = \frac{2}{s_W^2} \begin{pmatrix} s_W^2 & -s_W c_W & 0 & 0 \\ -s_W c_W & c_W^2 & 0 & 0 \\ 0 & 0 & 1 & 0 \\ 0 & 0 & 0 & 1 \end{pmatrix}, \qquad V^a = A, Z, W^+, W^-. \tag{A.16}$$

### A.3.1 Fermions

The fermionic doublets $f_\kappa = (f_{\kappa,+}, f_{\kappa,-})^T$ transform according to the fundamental representation, depending on the chirality $\kappa = L, R$. The only non-diagonal operators are $I^\pm$, because the coupling with a $W^\pm$ boson changes the flavour of the fermion. For the lepton and quark doublets, $L_\kappa = (\nu_\kappa, l_\kappa)^T$ and $Q_\kappa = (u_\kappa, d_\kappa)^T$, the eigenvalues of the operators are listed in tab. A.1.

| | $Y/2$ | $Q$ | $T^3$ | $C^{\rm SU(2)}$ | $\left(I^A\right)^2$ | $\left(I^Z\right)^2$ | $C^{\rm ew}$ |
|---|---|---|---|---|---|---|---|
| $\nu_L, \bar\nu_L$ | $\mp\frac{1}{2}$ | $0$ | $\pm\frac{1}{2}$ | $\frac{3}{4}$ | $0$ | $\frac{1}{4s_W^2 c_W^2}$ | $\frac{1+2c_W^2}{4s_W^2 c_W^2}$ |
| $l_L, \bar l_L$ | $\mp\frac{1}{2}$ | $\mp1$ | $\mp\frac{1}{2}$ | $\frac{3}{4}$ | $1$ | $\frac{(c_W^2-s_W^2)^2}{4s_W^2 c_W^2}$ | $\frac{1+2c_W^2}{4s_W^2 c_W^2}$ |
| $l_R, \bar l_R$ | $\mp1$ | $\mp1$ | $0$ | $0$ | $1$ | $\frac{s_W^2}{c_W^2}$ | $\frac{1}{c_W^2}$ |
| $u_L, \bar u_L$ | $\pm\frac{1}{6}$ | $\pm\frac{2}{3}$ | $\pm\frac{1}{2}$ | $\frac{3}{4}$ | $\frac{4}{9}$ | $\frac{(3c_W^2-s_W^2)^2}{36s_W^2 c_W^2}$ | $\frac{s_W^2+27c_W^2}{36s_W^2 c_W^2}$ |
| $d_L, \bar d_L$ | $\pm\frac{1}{6}$ | $\mp\frac{1}{3}$ | $\mp\frac{1}{2}$ | $\frac{3}{4}$ | $\frac{1}{9}$ | $\frac{(3c_W^2+s_W^2)^2}{36s_W^2 c_W^2}$ | $\frac{s_W^2+27c_W^2}{36s_W^2 c_W^2}$ |
| $u_R, \bar u_R$ | $\pm\frac{2}{3}$ | $\pm\frac{2}{3}$ | $0$ | $0$ | $\frac{4}{9}$ | $\frac{4s_W^2}{9c_W^2}$ | $\frac{4}{9c_W^2}$ |
| $d_R, \bar d_R$ | $\mp\frac{1}{3}$ | $\mp\frac{1}{3}$ | $0$ | $0$ | $\frac{1}{9}$ | $\frac{s_W^2}{9c_W^2}$ | $\frac{1}{9c_W^2}$ |

Table A.1: Eigenvalues of the relevant SU(2) × U(1) operators for the lepton and quark doublets.

For $I^\pm$ instead we have

$$I^\sigma_{f_{\kappa',\sigma'} f_{\kappa,-\sigma'}} = -\, I^\sigma_{\bar f_{\kappa',-\sigma'} \bar f_{\kappa,\sigma'}} = \delta_{\kappa L}\delta_{\kappa' L}\, \frac{\delta_{\sigma\sigma'}}{\sqrt{2} s_W}. \tag{A.17}$$

If the particles involved are quarks, this operator has to be multiplied by the corresponding CKM matrix element.

### A.3.2 Scalar fields

The symmetric scalar doublet, $\Phi = (\phi^+, \phi_0)^T$ and $\Phi^* = (\phi^-, \phi_0^*)^T$, transforms like fermions, according to the fundamental representation. Its quantum numbers correspond to those of the left-handed leptons in the previous table, with

$$\phi^+ \leftrightarrow \bar l_L, \quad \phi^- \leftrightarrow l_L, \quad \phi_0 \leftrightarrow \bar\nu_L, \quad \phi_0^* \leftrightarrow \nu_L. \tag{A.18}$$

In the physical basis, after symmetry breaking the $\phi_0$ component is parametrized by the mass eigenstates

$$\phi_0 = \frac{1}{\sqrt{2}}(v + H + i\chi). \tag{A.19}$$

In this basis, $S = (H, \chi)$, the operators $Q, C^{\mathrm{SU}(2)}, \left(I^A\right)^2, \left(I^Z\right)^2$ and $C^{\mathrm{ew}}$ remain unchanged (in particular $I^Z_H = I^Z_\chi = I^Z_{\bar{\nu}_L}$), while $T^3$ and $Y$ become non-diagonal,

$$T^3_{SS'} = -\left(\frac{Y}{2}\right)_{SS'} = -\frac{1}{2}\begin{pmatrix} 0 & i \\ -i & 0 \end{pmatrix}, \tag{A.20}$$

so that

$$I^Z_{H\chi} = -I^Z_{\chi H} = -\frac{i}{2 s_W c_W}. \tag{A.21}$$

The $I^\pm$ couplings take the values

$$I^\sigma_{S\phi^{-\sigma'}} = -I^\sigma_{\phi^{\sigma'}S} = \delta_{\sigma\sigma'} I^\sigma_S, \qquad I^\sigma_H = -\frac{\sigma}{2 s_W}, \quad I^\sigma_\chi = -\frac{i}{2 s_W}. \tag{A.22}$$

### A.3.3 Gauge fields

In the adjoint representation, under which gauge bosons transform, the generators are fixed by the structure constants of the gauge group through eq. (A.5),

$$I^{V^a}_{\bar{V}^c V^b} = \frac{i}{s_W}\,\varepsilon^{V^a V^b V^c} = \begin{cases} (-1)^{p+1} & \text{if} \quad V^a V^b V^c = \pi(A W^+ W^-), \\ (-1)^p \, \frac{c_W}{s_W} & \text{if} \quad V^a V^b V^c = \pi(Z W^+ W^-), \\ 0 & \text{otherwise.} \end{cases} \tag{A.23}$$

The symbol $\pi$ denotes a permutation, and $(-1)^p$ represents the sign of this permutation. In the symmetric basis the diagonal operators have the eigenvalues reported in tab. A.2.

| | $Y/2$ | $Q$ | $T^3$ | $C^{\mathrm{SU}(2)}$ | $\left(I^A\right)^2$ | $\left(I^Z\right)^2$ | $C^{\mathrm{ew}}$ |
|---|---|---|---|---|---|---|---|
| $W^\pm$ | 0 | $\pm1$ | $\pm1$ | 2 | 1 | $\frac{c_W^2}{s_W^2}$ | $\frac{2}{s_W^2}$ |
| $W^3$ | 0 | 0 | 0 | 2 | 0 | 0 | $\frac{2}{s_W^2}$ |
| $B$ | 0 | 0 | 0 | 0 | 0 | 0 | 0 |

Table A.2: Eigenvalues of the relevant SU(2) × U(1) operators for gauge fields in the symmetric basis.

In the physical basis, the operators that have vanishing eigenvalues in the neutral sector remain unchanged: their values can be found in tab. A.3.

| | $Y/2$ | $Q$ | $T^3$ | $\left(I^A\right)^2$ | $\left(I^Z\right)^2$ |
|---|---|---|---|---|---|
| $W^\pm$ | 0 | $\pm1$ | $\pm1$ | 1 | $\frac{c_W^2}{s_W^2}$ |
| $Z$ | 0 | 0 | 0 | 0 | 0 |
| $A$ | 0 | 0 | 0 | 0 | 0 |

Table A.3: Eigenvalues of the relevant SU(2) × U(1) operators for gauge fields in the physical basis.

The remaining operators become non-diagonal in the neutral sector $N = (A, Z)$, and read

$$C^{\rm ew}_{NN'} = \frac{1}{s_W^2}\, C^{\rm SU(2)}_{NN'} = \frac{2}{s_W^2} \begin{pmatrix} s_W^2 & -s_W c_W \\ -s_W c_W & c_W^2 \end{pmatrix}. \tag{A.24}$$

At the end, in the physical basis the non-vanishing components of the $I^{\pm}$ couplings are

$$I^{\sigma}_{NW^{-\sigma'}} = -\, I^{\sigma}_{W^{\sigma'}N} = \delta_{\sigma\sigma'} I^{\sigma}_{N}, \qquad\qquad I^{\sigma}_{A} = -\,\sigma, \quad I^{\sigma}_{Z} = \sigma\, \frac{c_W}{s_W}. \tag{A.25}$$

### A.3.4 Dynkin operator

The group-theoretical object that appears in gauge boson self-energies is the Dynkin operator,

$$D^{\rm ew}_{V^a V^b}(\varphi) \equiv {\rm Tr}\left\{ I^{\bar{V}^a}(\varphi) I^{V^b}(\varphi) \right\} = \sum_{\varphi_i, \varphi_{i'}} I^{\bar{V}^a}_{\varphi_i \varphi_{i'}}\, I^{V^b}_{\varphi_{i'} \varphi_i}. \tag{A.26}$$

The indices $a, b$ are those of the gauge group. The trace is performed over the isospin doublet for $\varphi = \Phi, f_L, f_R$, and over the gauge group for $\varphi = V$. In the latter case the Dynkin operator corresponds to the electroweak Casimir operator,

$$D^{\rm ew}_{V^a V^b}(V) = C^{\rm ew}_{V^a V^b}. \tag{A.27}$$

In the symmetric basis $\tilde{D}^{\rm ew}$ is diagonal,

$$\tilde{D}^{\rm ew}_{V^a V^b}(\varphi) = \delta_{V^a V^b}\, \tilde{D}^{\rm ew}_{a}(\varphi). \tag{A.28}$$

The SU(2) and U(1) eigenvalues of the fundamental representation, $\varphi = \Phi, f_L$, are

$$\tilde{D}^{\rm ew}_{B}(\varphi) = \frac{Y_\varphi^2}{2c_W^2}\, \xi, \qquad \tilde{D}^{\rm ew}_{W}(\varphi) = \frac{1}{2s_W^2}\, \xi, \tag{A.29}$$

where $\xi = 1$ for fermions, and $\xi = 2$ for the scalar doublet. For right-handed fermions instead we have

$$\tilde{D}^{\rm ew}_{B}(f_R) = \frac{Y_{f_{R,+}}^2 + Y_{f_{R,-}}^2}{4c_W^2}, \qquad \tilde{D}^{\rm ew}_{W}(f_R) = 0. \tag{A.30}$$

In the physical basis, the charged components are

$$D^{\rm ew}_{W^\sigma W^{\sigma'}}(\varphi) = \delta_{\sigma\sigma'}\, \tilde{D}^{\rm ew}_{W}(\varphi). \tag{A.31}$$

For the neutral components, instead, the eigenvalues for the scalar doublet and the left-handed fermion doublet read

$$\tilde{D}^{\rm ew}_{NN'}(\varphi) = \left[ U(\theta_W) \tilde{D}^{\rm ew}(\varphi) U(\theta_W)^{-1} \right]_{NN'} = \frac{1}{2} \begin{pmatrix} 1 + Y_\varphi^2 & \frac{Y_\varphi^2 s_W^2 - c_W^2}{s_W c_W} \\ \frac{Y_\varphi^2 s_W^2 - c_W^2}{s_W c_W} & \frac{Y_\varphi^2 s_W^4 + c_W^4}{s_W^2 c_W^2} \end{pmatrix}, \tag{A.32}$$

while for right-handed fermions

$$\tilde{D}^{\rm ew}_{NN'}(f_R) = \tilde{D}^{\rm ew}_{B}(f_R) \begin{pmatrix} c_W^2 & c_W s_W \\ c_W s_W & s_W^2 \end{pmatrix}. \tag{A.33}$$

The explicit values of the Dynkin operator are listed in tab. A.4.

| | $D^{\rm ew}_{AA}$ | $D^{\rm ew}_{AZ}$ | $D^{\rm ew}_{ZZ}$ | $D^{\rm ew}_{W}$ |
|---|---|---|---|---|
| $\Phi$ | 2 | $\frac{s_W^2-c_W^2}{s_W c_W}$ | $\frac{s_W^4+c_W^4}{s_W^2 c_W^2}$ | $\frac{1}{s_W^2}$ |
| $L_L$ | 1 | $\frac{s_W^2-c_W^2}{2s_W c_W}$ | $\frac{s_W^4+c_W^4}{2s_W^2 c_W^2}$ | $\frac{1}{2s_W^2}$ |
| $L_R$ | 1 | $\frac{s_W}{c_W}$ | $\frac{s_W^2}{c_W^2}$ | 0 |
| $Q_L$ | $\frac{5}{9}$ | $\frac{s_W^2-9c_W^2}{18s_W c_W}$ | $\frac{s_W^4+9c_W^4}{18s_W^2 c_W^2}$ | $\frac{1}{2s_W^2}$ |
| $Q_R$ | $\frac{5}{9}$ | $\frac{5s_W}{9c_W}$ | $\frac{5s_W^2}{9c_W^2}$ | 0 |

Table A.4: Eigenvalues of the Dynkin operator for the scalar doublet and for fermions.

### A.3.5 $\beta$-function coefficients

In gauge boson self-energies, the sums of gauge-boson, scalar and fermionic loops give the following combination of Dynkin operators,

$$b^{\rm ew}_{V^aV^b} \equiv \frac{11}{3} D^{\rm ew}_{V^aV^b}(V) - \frac{1}{6} D^{\rm ew}_{V^aV^b}(\Phi) - \frac{2}{3} \sum_{f=Q,L} \sum_{j=1}^{3} N_C^f \sum_{\kappa=L,R} D^{\rm ew}_{V^aV^b}(f_\kappa^j), \tag{A.34}$$

which is proportional to the one-loop coefficients of the $\beta$-function. In the symmetric basis $\tilde{b}^{\rm ew}_{V^aV^b}$ is diagonal, and its eigenvalues are

$$\tilde{b}^{\rm ew}_B = -\frac{41}{6c_W^2}, \qquad \tilde{b}^{\rm ew}_W = \frac{19}{6s_W^2}. \tag{A.35}$$

They describe the running of the hypercharge and weak-isospin coupling constants. In the physical basis the single components read

$$b^{\rm ew}_{AA} = c_W^2 \tilde{b}^{\rm ew}_B + s_W^2 \tilde{b}^{\rm ew}_W = -\frac{11}{3}, \tag{A.36}$$

$$b^{\rm ew}_{AZ} = s_W c_W (\tilde{b}^{\rm ew}_B - \tilde{b}^{\rm ew}_W) = -\frac{19+22s_W^2}{6s_W c_W}, \tag{A.37}$$

$$b^{\rm ew}_{ZZ} = s_W^2 \tilde{b}^{\rm ew}_B + c_W^2 \tilde{b}^{\rm ew}_W = \frac{19-38s_W^2-22s_W^4}{6s_W^2 c_W^2}, \tag{A.38}$$

$$b^{\rm ew}_{W^\sigma W^{\sigma'}} = \delta_{\sigma\sigma'} \tilde{b}^{\rm ew}_B = \frac{19}{6s_W^2}. \tag{A.39}$$

The $AA$ component determines the running of the electric charge, while the $AZ$ component is associated with the running of the weak mixing angle.

# Appendix B

# Computation of the Sudakov corrections

In this appendix we derive the results reported in Chap. 4 for the computation of the Sudakov electroweak corrections to the $HW$ and $HZ$ associated production processes in leading-pole approximation, distinguishing between transverse and longitudinal vector bosons. All the relevant group-theoretical quantities that appear in the formulae can be found in App. A, while the Feynman rules used to obtain these results are taken from App. C of ref. [8]. We report here, for completeness, the high-energy logarithms defined in eq. (3.10),

$$L(s) \equiv \frac{\alpha}{4\pi} \log^2 \frac{s}{M_W^2}, \qquad l(s) \equiv \frac{\alpha}{4\pi} \log \frac{s}{M_W^2}. \tag{B.1}$$

As explained in Sec. 4.1.7, the logarithmic corrections containing the fictitious photon mass $\lambda$ and the light fermion masses $m_f$ are not included. We neglect also the factors $\delta_{b_\kappa}^{\mathrm{LSC,h}}$ and $\delta_{b_\kappa}^{\mathrm{C,h}}$, since we are considering the bottom quark as massless.

In the following, $u$ and $d$ denote generic up- and down-type quarks, regardless of their generation, unless specified. The intermediate and final results are written in such a way that they can be easily adapted to the $HVj$ processes. In more detail, the subleading soft-collinear corrections can be obtained from the ones computed here by including the terms proportional to $\log(|r_{12}|/s)$ and $\log(|r_{34}|/s)$. Moreover, with more than four particles involved, $r_{13} \neq r_{24}$ and $r_{14} \neq r_{23}$. For the $W$ boson, we focus on $W^-$ production, since the $W^+$ results can be obtained from the ones we derive here through simple relations. For all the processes under study, the relation $q = p_1 + p_2$ holds.

## B.1 The $HW_T^-$ associated production

The leading-order process, with all the particles incoming, is

$$d_L(p_1)\, \bar{u}_L(p_2)\, H(-p_3)\, W_T^+(-k) \to 0, \tag{B.2}$$

and its matrix element reads

$$\mathcal{M}_0^{d_L \bar{u}_L H W_T^+} = \bar{v}_L(p_2)\, V_{d\bar{u}W^+}^{\mu}\, u_L(p_1)\, \frac{(-i)}{q^2 - M_W^2}\, ie^2 v \left\{ I^-, I^+ \right\}_{HH} \epsilon_\mu^T(-k). \tag{B.3}$$

$V_{d\bar{u}W^+}^{\mu}$ represents the vertex $duW$,

$$V_{d\bar{u}W^+}^{\mu} = (-ie\gamma^\mu)\, \frac{1-\gamma_5}{2}\, I_{ud}^+\, V_{ud}^{\mathrm{CKM}}, \tag{B.4}$$

while the $WWH$ vertex gives a factor

$$ie^2 v \left\{I^-, I^+\right\}_{HH} = ie^2 v \, \frac{1}{2s_W^2}. \tag{B.5}$$

We can simplify eq. (B.3) inserting the vacuum expectation value $v = 2M_W s_W/e$, the value of $I^+_{ud}$ taken from eq. (A.17), neglecting $M_W^2$ in the denominator of the propagator and considering that the helicity projector acts on left-handed spinors, so that $(1-\gamma_5)u_L = 2u_L$,

$$\mathcal{M}_0^{d_L \bar{u}_L H W_T^+} = -\frac{i}{q^2}\frac{e^2}{\sqrt{2}s_W^2} M_W \, V_{ud}^{\rm CKM} \, \bar{v}_L(p_2)\gamma^\mu u_L(p_1)\, \epsilon_\mu^T(-k) = \frac{e^2}{\sqrt{2}s_W^2} M_W \, V_{ud}^{\rm CKM} \, \frac{A_{T-}}{q^2}, \tag{B.6}$$

having grouped the spinorial part of the matrix element in

$$A_{T-} = -i \, \bar{v}_L(p_2)\gamma^\mu u_L(p_1)\, \epsilon_\mu^T(-k). \tag{B.7}$$

### B.1.1 Leading soft-collinear contributions

In order to obtain these correction factors we apply the formulae (3.25) and (3.26). For the process under consideration we have:

$$\begin{aligned}
k=1: \quad & \varphi_1 = \varphi_{1'} = d_L \\
\delta^{\rm LSC}_{d_L d_L} &= -\frac{1}{2}L(s)\, C^{\rm ew}_{d_L} + l(s)\, \log\frac{M_Z^2}{M_W^2}\,(I^Z_{d_L})^2 - \frac{1}{2}\,Q_d^2\, L_{\rm em}(s,\lambda^2,m_d^2),
\end{aligned} \tag{B.8}$$

$$\begin{aligned}
k=2: \quad & \varphi_2 = \varphi_{2'} = \bar{u}_L \\
\delta^{\rm LSC}_{\bar{u}_L \bar{u}_L} &= -\frac{1}{2}L(s)\, C^{\rm ew}_{\bar{u}_L} + l(s)\, \log\frac{M_Z^2}{M_W^2}\,(I^Z_{\bar{u}_L})^2 - \frac{1}{2}\,Q_u^2\, L_{\rm em}(s,\lambda^2,m_u^2),
\end{aligned} \tag{B.9}$$

$$\begin{aligned}
k=3: \quad & \varphi_3 = \varphi_{3'} = H \\
\delta^{\rm LSC}_{HH} &= -\frac{1}{2}L(s)\, C^{\rm ew}_{\Phi} + l(s)\, \log\frac{M_Z^2}{M_W^2}\,(I^Z_{H})^2 + \delta_H^{\rm LSC,h},
\end{aligned} \tag{B.10}$$

$$\begin{aligned}
k=4: \quad & \varphi_4 = \varphi_{4'} = W_T^+ \\
\delta^{\rm LSC}_{W^+W^+} &= -\frac{1}{2}L(s)\, C^{\rm ew}_{W^+} + l(s)\, \log\frac{M_Z^2}{M_W^2}\,(I^Z_{W^+})^2 - \frac{1}{2}\,Q_W^2\, L_{\rm em}(s,\lambda^2,M_W^2),
\end{aligned} \tag{B.11}$$

with $\delta_H^{\rm LSC,h}$, relevant only for external Higgs bosons, defined in eq. (3.31). Summing these contributions, and considering that $C^{\rm ew}_{d_L} = C^{\rm ew}_{\bar{u}_L} \equiv C^{\rm ew}_q$, we obtain

$$\begin{aligned}
\delta^{\rm LSC}\mathcal{M}^{d_L \bar{u}_L H W_T^+} &= \Bigg\{ -\frac{1}{2}L(s)\left[2C^{\rm ew}_q + C^{\rm ew}_\Phi + C^{\rm ew}_W\right] + \delta_H^{\rm LSC,h} \\
&\quad + l(s)\log\frac{M_Z^2}{M_W^2}\left[(I^Z_{d_L})^2 + (I^Z_{\bar{u}_L})^2 + (I^Z_H)^2 + (I^Z_W)^2\right] - \frac{1}{2}\left[Q_d^2\, L_{\rm em}(s,\lambda^2,m_d^2)\right. \\
&\quad \left. + Q_u^2\, L_{\rm em}(s,\lambda^2,m_u^2) + Q_W^2\, L_{\rm em}(s,\lambda^2,M_W^2)\right]\Bigg\}\mathcal{M}_0.
\end{aligned} \tag{B.12}$$

### B.1.2 Subleading soft-collinear contributions

When considering processes that involve four particles, the subleading soft-collinear corrections take the form of eq. (4.17). Since $r_{12} = r_{34} = s$, all the terms multiplied by $\log(|r_{12}|/s)$

and $\log(|r_{34}|/s)$ vanish. Nevertheless, in $HWj$ production they may become relevant, because of the switch of the kinematic invariants required by crossing symmetry. For this reason we include them in our computation: from these results, then, it is possible to easily obtain the correction factors for $HWj$ production. This procedure is adopted for all the other processes described in this appendix. In the following we list the relevant terms.

**Photon exchange**

$$\sum I^A_{\varphi_{1'}d_L}\, I^A_{\varphi_{2'}\bar{u}_L}\, \mathcal{M}_0^{\varphi_{1'}\varphi_{2'}HW_T^+} = I^A_{d_Ld_L}\, I^A_{\bar{u}_L\bar{u}_L}\, \mathcal{M}_0 = -Q_d\, Q_u\, \mathcal{M}_0, \tag{B.13}$$

$$\sum I^A_{\varphi_{2'}\bar{u}_L}\, I^A_{\varphi_{4'}W_T^+}\, \mathcal{M}_0^{d_L\varphi_{2'}H\varphi_{4'}} = I^A_{\bar{u}_L\bar{u}_L}\, I^A_{W^+W^+}\, \mathcal{M}_0 = -Q_u\, Q_{W^+}\, \mathcal{M}_0, \tag{B.14}$$

$$\sum I^A_{\varphi_{1'}d_L}\, I^A_{\varphi_{4'}W_T^+}\, \mathcal{M}_0^{\varphi_{1'}\bar{u}_LH\varphi_{4'}} = I^A_{d_Ld_L}\, I^A_{W^+W^+}\, \mathcal{M}_0 = Q_d\, Q_{W^+}\, \mathcal{M}_0. \tag{B.15}$$

***Z*-boson exchange**

$$\sum I^Z_{\varphi_{1'}d_L}\, I^Z_{\varphi_{2'}\bar{u}_L}\, \mathcal{M}_0^{\varphi_{1'}\varphi_{2'}HW_T^+} = I^Z_{d_Ld_L}\, I^Z_{\bar{u}_L\bar{u}_L}\, \mathcal{M}_0 = -I^Z_{d_L}\, I^Z_{u_L}\, \mathcal{M}_0, \tag{B.16}$$

$$\sum I^Z_{\varphi_{1'}d_L}\, I^Z_{\varphi_{3'}H}\, \mathcal{M}_0^{\varphi_{1'}\bar{u}_L\varphi_{3'}W_T^+} = I^Z_{d_Ld_L}\, I^Z_{\chi H}\, \mathcal{M}_0^{d_L\bar{u}_L\chi W_T^+} = 0, \tag{B.17}$$

$$\sum I^Z_{\varphi_{2'}\bar{u}_L}\, I^Z_{\varphi_{4'}W_T^+}\, \mathcal{M}_0^{d_L\varphi_{2'}H\varphi_{4'}} = I^Z_{\bar{u}_L\bar{u}_L}\, I^Z_{W^+W^+}\, \mathcal{M}_0 = -I^Z_{u_L}\, I^Z_{W^+}\, \mathcal{M}_0, \tag{B.18}$$

$$\sum I^Z_{\varphi_{1'}d_L}\, I^Z_{\varphi_{4'}W_T^+}\, \mathcal{M}_0^{\varphi_{1'}\bar{u}_LH\varphi_{4'}} = I^Z_{d_Ld_L}\, I^Z_{W^+W^+}\, \mathcal{M}_0 = I^Z_{d_L}\, I^Z_{W^+}\, \mathcal{M}_0, \tag{B.19}$$

$$\sum I^Z_{\varphi_{2'}\bar{u}_L}\, I^Z_{\varphi_{3'}H}\, \mathcal{M}_0^{d_L\varphi_{2'}\varphi_{3'}W_T^+} = I^Z_{\bar{u}_L\bar{u}_L}\, I^Z_{\chi H}\, \mathcal{M}_0^{d_L\bar{u}_L\chi W_T^+} = 0, \tag{B.20}$$

$$\sum I^Z_{\varphi_{3'}H}\, I^Z_{\varphi_{4'}W_T^+}\, \mathcal{M}_0^{d_L\bar{u}_L\varphi_{3'}\varphi_{4'}} = I^Z_{\chi H}\, I^Z_{W^+W^+}\, \mathcal{M}_0^{d_L\bar{u}_L\chi W_T^+} = 0. \tag{B.21}$$

The terms that multiply $\mathcal{M}_0^{d_L\bar{u}_L\chi W_T^+}$ vanish, since in this matrix element the Goldstone boson is coupled to massless fermions, and this coupling is proportional to the fermion mass.

***W*$^+$-boson exchange**

$$\begin{aligned}\sum I^+_{\varphi_{1'}d_L}\, I^-_{\varphi_{3'}H}\, \mathcal{M}_0^{\varphi_{1'}\bar{u}_L\varphi_{3'}W_T^+} &= I^+_{ud}\, I^-_{\phi^-H}\, \mathcal{M}_0^{u_L\bar{u}_L\phi^-W_T^+} \\ &= -\frac{1}{2\sqrt{2}s_W^2}\, V_{ud}^{\rm CKM}\, \mathcal{M}_0^{u_L\bar{u}_L\phi^-W_T^+},\end{aligned} \tag{B.22}$$

$$\begin{aligned}\sum I^+_{\varphi_{2'}\bar{u}_L}\, I^-_{\varphi_{4'}W_T^+}\, \mathcal{M}_0^{d_L\varphi_{2'}H\varphi_{4'}} &= I^+_{\bar{d}\bar{u}}\left(I^-_{AW^+}\, \mathcal{M}_0^{d_L\bar{d}_LHA} + I^-_{ZW^+}\, \mathcal{M}_0^{d_L\bar{d}_LHZ}\right) \\ &= \frac{c_W}{\sqrt{2}s_W^2}\, V_{ud}^{\rm CKM}\, \mathcal{M}_0^{d_L\bar{d}_LHZ},\end{aligned} \tag{B.23}$$

$$\begin{aligned}\sum I^+_{\varphi_{1'}d_L}\, I^-_{\varphi_{4'}W_T^+}\, \mathcal{M}_0^{\varphi_{1'}\bar{u}_LH\varphi_{4'}} &= I^+_{ud}\left(I^-_{AW^+}\, \mathcal{M}_0^{u_L\bar{u}_LHA} + I^-_{ZW^+}\, \mathcal{M}_0^{u_L\bar{u}_LHZ}\right) \\ &= -\frac{c_W}{\sqrt{2}s_W^2}\, V_{ud}^{\rm CKM}\, \mathcal{M}_0^{u_L\bar{u}_LHZ},\end{aligned} \tag{B.24}$$

$$\sum I^{+}_{\varphi_{2'}\bar{u}_L}\, I^{-}_{\varphi_{3'}H}\, \mathcal{M}_0^{d_L\varphi_{2'}\varphi_{3'}W_T^+} = I^{+}_{\bar{d}\bar{u}}\, I^{-}_{\phi^-H}\, \mathcal{M}_0^{d_L\bar{d}_L\phi^-W_T^+}$$
$$= \frac{1}{2\sqrt{2}s_W^2}\, V_{ud}^{\rm CKM}\, \mathcal{M}_0^{d_L\bar{d}_L\phi^-W_T^+}, \tag{B.25}$$

$$\sum I^{+}_{\varphi_{3'}H}\, I^{-}_{\varphi_{4'}W_T^+}\, \mathcal{M}_0^{d_L\bar{u}_L\varphi_{3'}\varphi_{4'}} = I^{+}_{\phi^+H}\left(I^{-}_{AW^+}\, \mathcal{M}_0^{d_L\bar{u}_L\phi^+A} + I^{-}_{ZW^+}\, \mathcal{M}_0^{d_L\bar{u}_L\phi^+Z}\right)$$
$$= \frac{1}{2s_W}\left(\mathcal{M}_0^{d_L\bar{u}_L\phi^+A} - \frac{c_W}{s_W}\, \mathcal{M}_0^{d_L\bar{u}_L\phi^+Z}\right). \tag{B.26}$$

$\mathcal{M}_0^{q_L\bar{q}_LHA}$ vanishes because of the Higgs boson coupling to massless quarks. The processes $\mathcal{M}_0^{q_L\bar{q}_L\phi^-W_T^+}$ occur through an intermediate photon or $Z$ boson: they are related to $\mathcal{M}_0$ by

$$\mathcal{M}_0^{q_L\bar{q}_L\phi^-W_T^+} = \frac{2\sqrt{2}s_W^3}{V_{ud}^{\rm CKM}}\left[\frac{Q_q}{2s_W} - \frac{I^Z_{q_L}}{2c_W}\right]\mathcal{M}_0. \tag{B.27}$$

The processes $\mathcal{M}_0^{q_L\bar{q}_LHZ}$, instead, can be written in terms of $\mathcal{M}_0$ as

$$\mathcal{M}_0^{q_L\bar{q}_LHZ} = \frac{\sqrt{2}s_W}{c_W^2}\, \frac{I^Z_{q_L}}{V_{ud}^{\rm CKM}}\, \mathcal{M}_0. \tag{B.28}$$

Finally, for the matrix elements $\mathcal{M}_0^{d_L\bar{u}_L\phi^+A}$ and $\mathcal{M}_0^{d_L\bar{u}_L\phi^+Z}$ we obtain

$$\mathcal{M}_0^{d_L\bar{u}_L\phi^+A} = -\, s_W\mathcal{M}_0, \qquad \mathcal{M}_0^{d_L\bar{u}_L\phi^+Z} = -\,\frac{s_W^2}{c_W}\mathcal{M}_0, \tag{B.29}$$

so that the term multiplying $\log(|r_{34}|/s)$ vanishes independently of the value assumed by $r_{34}$.

### $W^-$-boson exchange

No contributions come from the exchange of a $W^-$ boson.

### Final results

We can write the subleading soft-collinear corrections grouping the neutral- and charged-boson terms, as

$$\delta^{\rm SSC}\mathcal{M}^{d_L\bar{u}_LHW_T^+} = \delta^{\rm SSC,n}\mathcal{M}^{d_L\bar{u}_LHW_T^+} + \delta^{\rm SSC,\pm}\mathcal{M}^{d_L\bar{u}_LHW_T^+}. \tag{B.30}$$

Defining $t = r_{13}$ and $u = r_{14}$ these correction factors take the form

$$\delta^{\rm SSC,n}\mathcal{M}^{d_L\bar{u}_LHW_T^+} = \left[2l(s)\left(R_{d_LW^+}\log\frac{|u|}{s} - R_{u_LW^+}\log\frac{|t|}{s}\right)\right.$$
$$\left. + \frac{\alpha}{2\pi}\log\frac{M_W^2}{\lambda^2}\left(Q_d\log\frac{|u|}{s} - Q_u\log\frac{|t|}{s}\right)Q_{W^+}\right]\mathcal{M}_0, \tag{B.31}$$

$$\delta^{\rm SSC,\pm}\mathcal{M}^{d_L\bar{u}_LHW_T^+} = 2l(s)\, s_W\left[\log\frac{|t|}{s}\left(\frac{I^Z_{u_L}}{2c_W} - \frac{Q_u}{2s_W} + \frac{I^Z_{d_L}}{s_W^2c_W}\right)\right.$$
$$\left. - \log\frac{|u|}{s}\left(\frac{I^Z_{d_L}}{2c_W} - \frac{Q_d}{2s_W} + \frac{I^Z_{u_L}}{s_W^2c_W}\right)\right]\mathcal{M}_0, \tag{B.32}$$

in which $R_{\phi_1\phi_2}$ is related to the charge and to the weak isospin of the involved particles according to

$$R_{\phi_1\phi_2} = Q_{\phi_1}Q_{\phi_2} + I^Z_{\phi_1}I^Z_{\phi_2}. \tag{B.33}$$

### B.1.3 Single-logarithmic corrections: external particles

The corrections associated to external particles take the form described in Sec. 3.5. For this process we obtain

$$\begin{aligned} k=1: \quad & \varphi_1=\varphi_{1'}=d_L \\ \delta^{\rm C}_{d_Ld_L} &= \frac{3}{2}\,l(s)\,C^{\rm ew}_{d_L}+\frac{\alpha}{4\pi}\,Q_d^2\log\frac{M_W^2}{\lambda}, \end{aligned} \tag{B.34}$$

$$\begin{aligned} k=2: \quad & \varphi_2=\varphi_{2'}=\bar{u}_L \\ \delta^{\rm C}_{\bar{u}_L\bar{u}_L} &= \frac{3}{2}\,l(s)\,C^{\rm ew}_{\bar{u}_L}+\frac{\alpha}{4\pi}\,Q_u^2\log\frac{M_W^2}{\lambda}, \end{aligned} \tag{B.35}$$

$$\begin{aligned} k=3: \quad & \varphi_3=\varphi_{3'}=H \\ \delta^{\rm C}_{HH} &= \frac{\alpha}{4\pi}\left(2C^{\rm ew}_{\Phi}\log\frac{s}{M_H^2}-\frac{3}{4s_W^2}\,\frac{m_t^2}{M_W^2}\log\frac{s}{m_t^2}\right), \end{aligned} \tag{B.36}$$

$$\begin{aligned} k=4: \quad & \varphi_4=\varphi_{4'}=W_T^+ \\ \delta^{\rm C}_{W^+W^+} &= \frac{1}{2}\,b^{\rm ew}_{WW}\,l(s)+\frac{\alpha}{4\pi}\left(\frac{1}{24s_W^2}\log\frac{M_H^2}{M_W^2}+T_{WW}\log\frac{m_t^2}{M_W^2}+Q_W^2\log\frac{M_W^2}{\lambda^2}\right), \end{aligned} \tag{B.37}$$

where $T_{WW}$ is taken from eq. (3.43). Manipulating the logarithms in eq. (B.36) in order to isolate $l(s)$, the result is

$$\begin{aligned} \delta^{\rm C}\mathcal{M}^{d_L\bar{u}_LHW_T^+} &= \left\{\frac{\alpha}{4\pi}\left[\left(\frac{3}{4s_W^2}\frac{m_t^2}{M_W^2}+T_{WW}\right)\log\frac{m_t^2}{M_W^2}+\left(\frac{1}{24s_W^2}-2C^{\rm ew}_{\Phi}\right)\log\frac{M_H^2}{M_W^2}\right]\right. \\ &\quad + l(s)\left[3C^{\rm ew}_q+2C^{\rm ew}_{\Phi}+\frac{1}{2}b^{\rm ew}_{WW}-\frac{3}{4s_W^2}\,\frac{m_t^2}{M_W^2}\right] \\ &\quad \left.+\frac{\alpha}{4\pi}\log\frac{M_W^2}{\lambda^2}(Q_d^2+Q_u^2+Q_W^2)\right\}\mathcal{M}_0. \end{aligned} \tag{B.38}$$

### B.1.4 Single-logarithmic corrections: parameter renormalization

The parameters appearing in the leading-order process, that have to be renormalized, are $e$, $s_W$ and $M_W$. In principle the last parameter should not be considered, carrying it a mass dimension. Since the original matrix element is mass-suppressed, however, the factor $(\partial\mathcal{M}_0/\partial M_W^2)\,\delta M_W^2$ has the same energy dependence of $\mathcal{M}_0$, so it has to be included. These corrections are then given by

$$\delta^{\rm PR}\mathcal{M}^{d_L\bar{u}_LHW_T^+}=\left(\frac{\partial\mathcal{M}_0}{\partial e}\,\delta e+\frac{\partial\mathcal{M}_0}{\partial c_W^2}\,\delta c_W^2+\frac{\partial\mathcal{M}_0}{\partial M_W^2}\,\delta M_W^2\right)\Bigg|_{\mu^2=s}, \tag{B.39}$$

with

$$\frac{\partial\mathcal{M}_0}{\partial e} = \frac{2}{e}\mathcal{M}_0, \tag{B.40}$$

$$\frac{\partial\mathcal{M}_0}{\partial c_W^2} = -\frac{\partial\mathcal{M}_0}{\partial s_W^2}=\frac{\mathcal{M}_0}{s_W^2}, \tag{B.41}$$

$$\frac{\partial\mathcal{M}_0}{\partial M_W^2} = \frac{\mathcal{M}_0}{2M_W^2}. \tag{B.42}$$

The factors $\delta e$, $\delta c_W^2$ and $\delta M_W^2$ can be obtained from eqs. (3.56), (3.57) and (3.60). Grouping together the various terms, and considering that

$$\frac{c_W}{s_W} b_{AZ}^{\rm ew} - b_{AA}^{\rm ew} = -b_{WW}^{\rm ew}, \tag{B.43}$$

we get

$$\begin{aligned}\delta^{\rm PR}\mathcal{M}^{d_L\bar{u}_L H W_T^+} \;=\; & \left\{ \frac{\alpha}{4\pi}\left[\frac{5}{12 s_W^2}\log\frac{M_H^2}{M_W^2} - \left(\frac{9+6s_W^2-32s_W^4}{18 s_W^4} + T_{WW} - \frac{3}{4s_W^2}\frac{m_t^2}{M_W^2}\right)\log\frac{m_t^2}{M_W^2}\right]\right. \\ & \left. + l(s)\left(-\frac{3}{2}\, b_{WW}^{\rm ew} + 2C_\Phi^{\rm ew} - \frac{3}{4s_W^2}\frac{m_t^2}{M_W^2}\right)\right\}\mathcal{M}_0. \end{aligned} \tag{B.44}$$

## B.2 The $HW_L^-$ associated production

For the production of a longitudinal $W^-$ boson,

$$d_L(p_1)\,\bar{u}_L(p_2)\,H(-p_3)\,W_L^+(-k) \to 0, \tag{B.45}$$

the GBET has to be applied, giving $\mathcal{M}_0^{d_L\bar{u}_L H W_L^+} = \mathcal{M}_0^{d_L\bar{u}_L H\phi^+}$. The $HW\phi$ vertex gives a factor $ieI^-_{H\phi^+}(-k+p_3)_\mu$. The matrix element can then be written as

$$\begin{aligned}\mathcal{M}_0^{d_L\bar{u}_L H W_L^+} = \mathcal{M}_0^{d_L\bar{u}_L H\phi^+} &= \bar{v}_L(p_2) V^\mu_{d\bar{u}W^+} u_L(p_1)\,\frac{(-i)}{q^2-M_W^2}\, ieI^-_{H\phi^+}\,(-k+p_3)_\mu \\ &= -\frac{i}{q^2}\,\frac{e^2}{2\sqrt{2}s_W^2}\,V_{ud}^{\rm CKM}\,\bar{v}_L(p_2)\gamma^\mu u_L(p_1)\,(-k+p_3)_\mu \\ &= \frac{e^2}{2\sqrt{2}s_W^2}\,V_{ud}^{\rm CKM}\,\frac{A_{L-}}{q^2}, \end{aligned} \tag{B.46}$$

having defined $V^\mu_{d\bar{u}W^+}$ in eq. (B.4) and

$$A_{L-} = -\,i\,\bar{v}_L(p_2)\gamma^\mu u_L(p_1)\,(-k+p_3)_\mu. \tag{B.47}$$

### B.2.1 Leading soft-collinear contributions

To obtain these corrections we apply the same formulae used in the transverse case. Apart from the Goldstone boson, the factors for the other particles remain unchanged and are not reported.

$$\delta^{\rm LSC}_{\phi^+\phi^+} \;=\; -\frac{1}{2}L(s)\,C_\Phi^{\rm ew} + l(s)\,\log\frac{M_Z^2}{M_W^2}\,(I^Z_{\phi^+})^2 + \delta^{\rm LSC,h}_{\phi^\pm} - \frac{1}{2}\,Q_\phi^2\,L_{\rm em}(s,\lambda^2,M_W^2), \tag{B.48}$$

with $\delta^{\rm LSC,h}_{\phi^\pm}$ defined in eq. (3.32). We then get

$$\begin{aligned}\delta^{\rm LSC}\mathcal{M}^{d_L\bar{u}_L H\phi^+} \;=\; & \left\{ -L(s)\left(C_q^{\rm ew} + C_\Phi^{\rm ew}\right) + \delta_H^{\rm LSC,h} + \delta_{\phi^\pm}^{\rm LSC,h}\right. \\ & + l(s)\log\frac{M_Z^2}{M_W^2}\left[(I^Z_{d_L})^2 + (I^Z_{\bar{u}_L})^2 + (I^Z_H)^2 + (I^Z_{\phi^+})^2\right] - \frac{1}{2}\left[Q_d^2\,L_{\rm em}(s,\lambda^2,m_d^2)\right. \\ & \left.\left. + Q_u^2\,L_{\rm em}(s,\lambda^2,m_u^2) + Q_\phi^2\,L_{\rm em}(s,\lambda^2,M_W^2)\right]\right\}\mathcal{M}_0. \end{aligned} \tag{B.49}$$

### B.2.2 Subleading soft-collinear contributions

**Photon exchange**

$$\sum I^A_{\varphi_{1'}d_L}\, I^A_{\varphi_{2'}\bar{u}_L}\, \mathcal{M}_0^{\varphi_{1'}\varphi_{2'}H\phi^+} = I^A_{d_Ld_L}\, I^A_{\bar{u}_L\bar{u}_L}\, \mathcal{M}_0 = -Q_d\, Q_u\, \mathcal{M}_0, \tag{B.50}$$

$$\sum I^A_{\varphi_{2'}\bar{u}_L}\, I^A_{\varphi_{4'}\phi^+}\, \mathcal{M}_0^{d_L\varphi_{2'}H\varphi_{4'}} = I^A_{\bar{u}_L\bar{u}_L}\, I^A_{\phi^+\phi^+}\, \mathcal{M}_0 = -Q_u\, Q_{\phi^+}\, \mathcal{M}_0, \tag{B.51}$$

$$\sum I^A_{\varphi_{1'}d_L}\, I^A_{\varphi_{4'}\phi^+}\, \mathcal{M}_0^{\varphi_{1'}\bar{u}_LH\varphi_{4'}} = I^A_{d_Ld_L}\, I^A_{\phi^+\phi^+}\, \mathcal{M}_0 = Q_d\, Q_{\phi^+}\, \mathcal{M}_0. \tag{B.52}$$

***Z*-boson exchange**

$$\sum I^Z_{\varphi_{1'}d_L}\, I^Z_{\varphi_{2'}\bar{u}_L}\, \mathcal{M}_0^{\varphi_{1'}\varphi_{2'}H\phi^+} = I^Z_{d_Ld_L}\, I^Z_{\bar{u}_L\bar{u}_L}\, \mathcal{M}_0 = -I^Z_{d_L}\, I^Z_{u_L}\, \mathcal{M}_0, \tag{B.53}$$

$$\sum I^Z_{\varphi_{1'}d_L}\, I^Z_{\varphi_{3'}H}\, \mathcal{M}_0^{\varphi_{1'}\bar{u}_L\varphi_{3'}\phi^+} = I^Z_{d_Ld_L}\, I^Z_{\chi H}\, \mathcal{M}_0^{d_L\bar{u}_L\chi\phi^+} = -I^Z_{d_L}\, I^Z_{H\chi}\, \mathcal{M}_0^{d_L\bar{u}_L\chi\phi^+}, \tag{B.54}$$

$$\sum I^Z_{\varphi_{2'}\bar{u}_L}\, I^Z_{\varphi_{4'}\phi^+}\, \mathcal{M}_0^{d_L\varphi_{2'}H\varphi_{4'}} = I^Z_{\bar{u}_L\bar{u}_L}\, I^Z_{\phi^+\phi^+}\, \mathcal{M}_0 = -I^Z_{u_L}\, I^Z_{\phi^+}\, \mathcal{M}_0, \tag{B.55}$$

$$\sum I^Z_{\varphi_{1'}d_L}\, I^Z_{\varphi_{4'}\phi^+}\, \mathcal{M}_0^{\varphi_{1'}\bar{u}_LH\varphi_{4'}} = I^Z_{d_Ld_L}\, I^Z_{\phi^+\phi^+}\, \mathcal{M}_0 = I^Z_{d_L}\, I^Z_{\phi^+}\, \mathcal{M}_0, \tag{B.56}$$

$$\sum I^Z_{\varphi_{2'}\bar{u}_L}\, I^Z_{\varphi_{3'}H}\, \mathcal{M}_0^{d_L\varphi_{2'}\varphi_{3'}\phi^+} = I^Z_{\bar{u}_L\bar{u}_L}\, I^Z_{\chi H}\, \mathcal{M}_0^{d_L\bar{u}_L\chi\phi^+} = I^Z_{u_L}\, I^Z_{H\chi}\, \mathcal{M}_0^{d_L\bar{u}_L\chi\phi^+}, \tag{B.57}$$

$$\sum I^Z_{\varphi_{3'}H}\, I^Z_{\varphi_{4'}\phi^+}\, \mathcal{M}_0^{d_L\bar{u}_L\varphi_{3'}\varphi_{4'}} = I^Z_{\chi H}\, I^Z_{\phi^+\phi^+}\, \mathcal{M}_0^{d_L\bar{u}_L\chi\phi^+} = -I^Z_{H\chi}\, I^Z_{\phi^+}\, \mathcal{M}_0^{d_L\bar{u}_L\chi\phi^+}. \tag{B.58}$$

The process $\mathcal{M}_0^{d_L\bar{u}_L\chi\phi^+}$ occurs through an intermediate $W^-$ boson, and is related to $\mathcal{M}_0$ by

$$\mathcal{M}_0^{d_L\bar{u}_L\chi\phi^+} = -i\mathcal{M}_0. \tag{B.59}$$

***W*$^+$-boson exchange**

$$\sum I^+_{\varphi_{1'}d_L}\, I^-_{\varphi_{3'}H}\, \mathcal{M}_0^{\varphi_{1'}\bar{u}_L\varphi_{3'}\phi^+} = I^+_{ud}\, I^-_{\phi^-H}\, \mathcal{M}_0^{u_L\bar{u}_L\phi^-\phi^+} = -\frac{1}{2\sqrt{2}s_W^2}\, V_{ud}^{\rm CKM}\, \mathcal{M}_0^{u_L\bar{u}_L\phi^-\phi^+}, \tag{B.60}$$

$$\begin{aligned}\sum I^+_{\varphi_{2'}\bar{u}_L}\, I^-_{\varphi_{4'}\phi^+}\, \mathcal{M}_0^{d_L\varphi_{2'}H\varphi_{4'}} &= I^+_{\bar{d}\bar{u}}\left(I^-_{H\phi^+}\, \mathcal{M}_0^{d_L\bar{d}_LHH} + I^-_{\chi\phi^+}\, \mathcal{M}_0^{d_L\bar{d}_LH\chi}\right)\\ &= \frac{i}{2\sqrt{2}s_W^2}\, V_{ud}^{\rm CKM}\, \mathcal{M}_0^{d_L\bar{d}_LH\chi},\end{aligned} \tag{B.61}$$

$$\begin{aligned}\sum I^+_{\varphi_{1'}d_L}\, I^-_{\varphi_{4'}\phi^+}\, \mathcal{M}_0^{\varphi_{1'}\bar{u}_LH\varphi_{4'}} &= I^+_{ud}\left(I^-_{H\phi^+}\, \mathcal{M}_0^{u_L\bar{u}_LHH} + I^-_{\chi\phi^+}\, \mathcal{M}_0^{u_L\bar{u}_LH\chi}\right)\\ &= -\frac{i}{2\sqrt{2}s_W^2}\, V_{ud}^{\rm CKM}\, \mathcal{M}_0^{u_L\bar{u}_LH\chi},\end{aligned} \tag{B.62}$$

$$\sum I^+_{\varphi_{2'}\bar{u}_L}\, I^-_{\varphi_{3'}H}\, \mathcal{M}_0^{d_L\varphi_{2'}\varphi_{3'}\phi^+} = I^+_{\bar{d}\bar{u}}\, I^-_{\phi^-H}\, \mathcal{M}_0^{d_L\bar{d}_L\phi^-\phi^+} = \frac{1}{2\sqrt{2}s_W^2}\, V_{ud}^{\rm CKM}\, \mathcal{M}_0^{d_L\bar{d}_L\phi^-\phi^+}, \tag{B.63}$$

$$\begin{aligned}\sum I^+_{\varphi_{3'}H}\, I^-_{\varphi_{4'}\phi^+}\, \mathcal{M}_0^{d_L\bar{u}_L\varphi_{3'}\varphi_{4'}} &= I^+_{\phi^+H}\left(I^-_{H\phi^+}\, \mathcal{M}_0^{d_L\bar{u}_L\phi^+H} + I^-_{\chi\phi^+}\, \mathcal{M}_0^{d_L\bar{u}_L\phi^+\chi}\right)\\ &= \frac{1}{4s_W^2}\left(\mathcal{M}_0^{d_L\bar{u}_L\phi^+H} - i\mathcal{M}_0^{d_L\bar{u}_L\phi^+\chi}\right).\end{aligned} \tag{B.64}$$

$\mathcal{M}_0^{q_L\bar{q}_L HH}$ vanishes, because it can only be realized through Higgs bosons that couple to massless quarks. The processes $\mathcal{M}_0^{q_L\bar{q}_L\phi^-\phi^+}$, instead, occur with an intermediate photon or $Z$ boson, and they are related to $\mathcal{M}_0$ through

$$\mathcal{M}_0^{q_L\bar{q}_L\phi^-\phi^+} = \frac{2\sqrt{2}s_W^2}{V_{ud}^{\rm CKM}}\, R_{q_L\phi^+}\, \mathcal{M}_0. \tag{B.65}$$

The processes $\mathcal{M}_0^{q_L\bar{q}_L H\chi}$ have an intermediate $Z$ boson, and can be written in terms of $\mathcal{M}_0$ according to

$$\mathcal{M}_0^{q_L\bar{q}_L H\chi} = \frac{2\sqrt{2}s_W^2}{V_{ud}^{\rm CKM}}\, I^Z_{q_L}\, I^Z_{H\chi}\, \mathcal{M}_0. \tag{B.66}$$

The matrix element with an intermediate $\chi$ boson, and the one with the final state particles directly connected to the quark current, vanish because of the coupling between these particles and the quarks. Finally, for $\mathcal{M}_0^{d_L\bar{u}_L\phi^+H}$ and $\mathcal{M}_0^{d_L\bar{u}_L\phi^+\chi}$ we obtain

$$\mathcal{M}_0^{d_L\bar{u}_L\phi^+H} = -\mathcal{M}_0, \qquad\qquad \mathcal{M}_0^{d_L\bar{u}_L\phi^+\chi} = i\mathcal{M}_0, \tag{B.67}$$

so that the terms that multiply $\log(|r_{34}|/s)$ vanish.

#### $W^-$-boson exchange

No contributions come from the exchange of a $W^-$ boson.

#### Final results

We combine the subleading soft-collinear corrections into neutral- and charged-boson terms,

$$\begin{aligned}\delta^{\rm SSC,n}\mathcal{M}^{d_L\bar{u}_L H\phi^+} \;=\; & \frac{\alpha}{2\pi}\log\frac{M_W^2}{\lambda^2}\left(Q_d\log\frac{|u|}{s} - Q_u\log\frac{|t|}{s}\right) Q_{\phi^+}\mathcal{M}_0 \\ & + 2l(s)\left[\log\frac{|t|}{s}\left(iI^Z_{H\chi}\, I^Z_{d_L} - R_{u_L\phi^+}\right) - \log\frac{|u|}{s}\left(iI^Z_{H\chi}\, I^Z_{u_L} - R_{d_L\phi^+}\right)\right]\mathcal{M}_0,\end{aligned} \tag{B.68}$$

$$\delta^{\rm SSC,\pm}\mathcal{M}^{d_L\bar{u}_L H\phi^+} \;=\; 2l(s)\left[\log\frac{|t|}{s}\left(iI^Z_{H\chi}\, I^Z_{d_L} - R_{u_L\phi^+}\right) - \log\frac{|u|}{s}\left(iI^Z_{H\chi}\, I^Z_{u_L} - R_{d_L\phi^+}\right)\right]\mathcal{M}_0. \tag{B.69}$$

The non-photonic part of these correction factors turns out to be the same: this is due to the fact that, for this process, the exchange of $Z$ bosons gives diagrams that are topologically equivalent to the ones obtained by exchanging charged gauge bosons.

### B.2.3 Single-logarithmic corrections: external particles

The correction factors for the quarks and for the Higgs boson are the same as the transverse case. For the Goldstone boson, instead, we have

$$\delta^{\rm C}_{\phi^+\phi^+} = 2C_\Phi^{\rm ew}\, l(s) + \frac{\alpha}{4\pi}\left(-\frac{3}{4s_W^2}\frac{m_t^2}{M_W^2}\log\frac{s}{m_t^2} + \frac{1}{8s_W^2}\log\frac{M_H^2}{M_W^2} + Q_\phi^2\log\frac{M_W^2}{\lambda^2}\right). \tag{B.70}$$

Summing the contributions and making $l(s)$ explicit,

$$\begin{aligned}\delta^{\rm C}\mathcal{M}^{d_L\bar{u}_L H\phi^+} \;=\; & \left\{\frac{\alpha}{4\pi}\left[\frac{3}{2s_W^2}\frac{m_t^2}{M_W^2}\log\frac{m_t^2}{M_W^2} + \left(\frac{1}{8s_W^2} - 2C_\Phi^{\rm ew}\right)\log\frac{M_H^2}{M_W^2}\right]\right. \\ & \left. + l(s)\left[3C_q^{\rm ew} + 4C_\Phi^{\rm ew} - \frac{3}{2s_W^2}\frac{m_t^2}{M_W^2}\right] + \log\frac{M_W^2}{\lambda^2}(Q_d^2 + Q_u^2 + Q_\phi^2)\right\}\mathcal{M}_0.\end{aligned} \tag{B.71}$$

### B.2.4 Single-logarithmic corrections: parameter renormalization

The matrix element involves the same parameters as the transverse case apart from $M_W$. The corrections due to parameter renormalization are then given by the renormalization of $e$ and $s_W$, and the combination of these factors gives

$$\delta^{\rm PR}\mathcal{M}^{d_L\bar{u}_L H\phi^+} = \left[\frac{\alpha}{4\pi}\left(\frac{5}{6s_W^2}\log\frac{M_H^2}{M_W^2} - \frac{9+6s_W^2-32s_W^4}{18s_W^4}\log\frac{m_t^2}{M_W^2}\right) - b_{WW}^{\rm ew}\,l(s)\right]\mathcal{M}_0. \quad \text{(B.72)}$$

## B.3 The $HZ_T$ associated production

For the associated production of a Higgs boson and a transverse $Z$ boson the leading-order process is

$$q(p_1)\,\bar{q}(p_2)\,H(-p_3)\,Z_T(-k) \to 0, \quad \text{(B.73)}$$

and its matrix element can be written as

$$\mathcal{M}_0^{q\bar{q}HZ_T} = \bar{v}(p_2)\,V^\mu_{q\bar{q}Z}\,u(p_1)\,\frac{(-i)}{q^2-M_Z^2}\,ie^2v\,\left\{I^Z,I^Z\right\}_{HH}\,\epsilon_\mu^T(-k). \quad \text{(B.74)}$$

In this case $V^\mu_{q\bar{q}Z}$, representing the vertex $q\bar{q}Z$, contains both the helicity projectors: for a generic fermion $f$ its value is

$$V^\mu_{f\bar{f}Z} = (-ie\gamma^\mu)\left[\frac{1-\gamma_5}{2}I^Z_{f_L} + \frac{1+\gamma_5}{2}I^Z_{f_R}\right]. \quad \text{(B.75)}$$

The vertex $ZZH$ instead gives a factor

$$ie^2v\left\{I^Z,I^Z\right\}_{HH} = i\,\frac{eM_Z}{s_Wc_W}. \quad \text{(B.76)}$$

Inserting these results into eq. (B.74) we can split it into two contributions, coming from the different chiralities involved, due to the action of the helicity projectors on the quark current,

$$\begin{aligned}\mathcal{M}_0^{q\bar{q}HZ_T} &= -\frac{i}{q^2}\,\frac{e^2M_Z}{s_Wc_W}\,\bar{v}(p_2)\,\gamma^\mu\left[\frac{1-\gamma_5}{2}I^Z_{q_L}+\frac{1+\gamma_5}{2}I^Z_{q_R}\right]u(p_1)\,\epsilon_\mu^T(-k)\\ &= -\frac{i}{q^2}\,\frac{e^2M_Z}{s_Wc_W}\sum_\kappa I^Z_{q_\kappa}\,\bar{v}_\kappa(p_2)\gamma^\mu u_\kappa(p_1)\,\epsilon_\mu^T(-k)\frac{e^2M_Z}{s_Wc_W}\sum_\kappa I^Z_{q_\kappa}\,\frac{A^\kappa_{TZ}}{q^2}. \quad \text{(B.77)}\end{aligned}$$

The spinorial part has been collected in

$$A^\kappa_{TZ} = -i\,\bar{v}_\kappa(p_2)\gamma^\mu u_\kappa(p_1)\,\epsilon_\mu^T(-k). \quad \text{(B.78)}$$

### B.3.1 Leading soft-collinear contributions

We compute the correction factors for both left- and right-handed quarks, that multiply the corresponding part of the leading-order matrix element: in the following we then write explicitly their chirality. The application of the formulae for the leading soft-collinear corrections gives

$$\begin{aligned}k=1: \qquad & \varphi_1=\varphi_{1'}=q_\kappa\\ \delta^{\rm LSC}_{q_\kappa q_\kappa} &= -\frac{1}{2}\,L(s)\,C^{\rm ew}_{q_\kappa} + l(s)\,\log\frac{M_Z^2}{M_W^2}\,(I^Z_{q_\kappa})^2 - \frac{1}{2}\,Q_q^2\,L_{\rm em}(s,\lambda^2,m_q^2), \quad \text{(B.79)}\end{aligned}$$

$$
\begin{aligned}
k=2: \qquad & \varphi_2 = \varphi_{2'} = \bar{q}_\kappa \\
\delta^{\rm LSC}_{\bar{q}_\kappa \bar{q}_\kappa} &= -\frac{1}{2}\,L(s)\,C^{\rm ew}_{\bar{q}_\kappa} + l(s)\,\log\frac{M_Z^2}{M_W^2}\,(I^Z_{\bar{q}_\kappa})^2 - \frac{1}{2}\,Q_q^2\,L_{\rm em}(s,\lambda^2,m_q^2), \qquad \text{(B.80)} \\
k=3: \qquad & \varphi_3 = \varphi_{3'} = H \\
\delta^{\rm LSC}_{HH} &= -\frac{1}{2}\,L(s)\,C^{\rm ew}_{\Phi} + l(s)\,\log\frac{M_Z^2}{M_W^2}\,(I^Z_{H})^2 + \delta^{\rm LSC,h}_{H}, \qquad \text{(B.81)} \\
k=4: \qquad & \varphi_4 = A, Z_T \\
\delta^{\rm LSC}_{AZ}\,\mathcal{M}_0^{q_\kappa\bar{q}_\kappa HA} &= -\frac{1}{2}\,L(s)\,C^{\rm ew}_{AZ}\,\mathcal{M}_0^{q_\kappa\bar{q}_\kappa HA} = 0, \qquad \text{(B.82)} \\
\delta^{\rm LSC}_{ZZ} &= -\frac{1}{2}\,L(s)\,C^{\rm ew}_{ZZ}. \qquad \text{(B.83)}
\end{aligned}
$$

The correction factor in eq. (B.82) vanishes because of the topology of the process, since the Higgs boson couples with fermions that are considered as massless. Since $C^{\rm ew}_{q_\kappa} = C^{\rm ew}_{\bar{q}_\kappa}$ and $\left(I^Z_{q_\kappa}\right)^2 = \left(I^Z_{\bar{q}_\kappa}\right)^2$, we obtain

$$
\begin{aligned}
\delta^{\rm LSC}\mathcal{M}^{q_\kappa\bar{q}_\kappa HZ_T} &= \Bigg\{-\frac{1}{2}\,L(s)\left[2C^{\rm ew}_{q_\kappa} + C^{\rm ew}_{\Phi} + C^{\rm ew}_{ZZ}\right] + \delta^{\rm LSC,h}_{H} \\
&\quad + l(s)\log\frac{M_Z^2}{M_W^2}\left[2\left(I^Z_{q_\kappa}\right)^2 + (I^Z_H)^2\right] - Q_q^2\,L_{\rm em}(s,\lambda^2,m_q^2)\Bigg\}\mathcal{M}_0. \qquad \text{(B.84)}
\end{aligned}
$$

### B.3.2 Subleading soft-collinear contributions

For the subleading soft-collinear corrections we apply the same procedure adopted in the $HW$ process, distinguishing between up- and down-type quarks. The corrections coming from the exchange of charged gauge bosons are non-vanishing only if the quarks involved are left-handed.

**Photon exchange**

$$
\sum I^A_{\varphi_{1'}q_\kappa}\,I^A_{\varphi_{2'}\bar{q}_\kappa}\,\mathcal{M}_0^{\varphi_{1'}\varphi_{2'}HZ_T} = I^A_{q_\kappa q_\kappa}\,I^A_{\bar{q}_\kappa\bar{q}_\kappa}\,\mathcal{M}_0 = -Q_q^2\,\mathcal{M}_0. \qquad \text{(B.85)}
$$

***Z*-boson exchange**

$$
\begin{aligned}
\sum I^Z_{\varphi_{1'}q_\kappa}\,I^Z_{\varphi_{2'}\bar{q}_\kappa}\,\mathcal{M}_0^{\varphi_{1'}\varphi_{2'}HZ_T} &= I^Z_{q_\kappa q_\kappa}\,I^Z_{\bar{q}_\kappa\bar{q}_\kappa}\,\mathcal{M}_0 = -(I^Z_{q_\kappa})^2\,\mathcal{M}_0, \qquad \text{(B.86)} \\
\sum I^Z_{\varphi_{1'}q_\kappa}\,I^Z_{\varphi_{3'}H}\,\mathcal{M}_0^{\varphi_{1'}\bar{q}_\kappa\varphi_{3'}Z_T} &= I^Z_{q_\kappa q_\kappa}\,I^Z_{\chi H}\,\mathcal{M}_0^{q_\kappa\bar{q}_\kappa\chi Z_T} = 0, \qquad \text{(B.87)} \\
\sum I^Z_{\varphi_{2'}\bar{q}_\kappa}\,I^Z_{\varphi_{3'}H}\,\mathcal{M}_0^{q_\kappa\varphi_{2'}\varphi_{3'}Z_T} &= I^Z_{\bar{q}_\kappa\bar{q}_\kappa}\,I^Z_{\chi H}\,\mathcal{M}_0^{q_\kappa\bar{q}_\kappa\chi Z_T} = 0. \qquad \text{(B.88)}
\end{aligned}
$$

The terms that involve $\mathcal{M}_0^{q_\kappa\bar{q}_\kappa\chi Z_T}$ vanish because of the coupling between massless quarks and the Goldstone boson $\chi$.

**$W^+$-boson exchange with initial-state up-type quarks**

$$\begin{aligned}
\sum I^+_{\varphi_{2'}\bar{u}_L}\, I^-_{\varphi_{3'}H}\, \mathcal{M}_0^{u_L\varphi_{2'}\varphi_{3'}Z_T} &= \sum_i I^+_{\bar{d}_i\bar{u}}\, I^-_{\phi^-H}\, \mathcal{M}_0^{u_L\bar{d}_{iL}\phi^-Z_T} \\
&= \frac{1}{2\sqrt{2}s_W^2}\sum_i V_{ud_i}^{\rm CKM}\, \mathcal{M}_0^{u_L\bar{d}_{iL}\phi^-Z_T}, \qquad \text{(B.89)} \\
\sum I^+_{\varphi_{2'}\bar{u}_L}\, I^-_{\varphi_{4'}Z_T}\, \mathcal{M}_0^{u_L\varphi_{2'}H\varphi_{4'}} &= \sum_i I^+_{\bar{d}_i\bar{u}} I^-_{W^-Z}\, \mathcal{M}_0^{u_L\bar{d}_{iL}HW^-} \\
&= -\frac{c_W}{\sqrt{2}s_W^2}\sum_i V_{ud_i}^{\rm CKM}\, \mathcal{M}_0^{u_L\bar{d}_{iL}HW^-}, \qquad \text{(B.90)} \\
\sum I^+_{\varphi_{3'}H}\, I^-_{\varphi_{4'}Z_T}\, \mathcal{M}_0^{u_L\bar{u}_L\varphi_{3'}\varphi_{4'}} &= I^+_{\phi^+H} I^-_{W^-Z}\, \mathcal{M}_0^{u_L\bar{u}_L\phi^+W^-} = \frac{c_W}{2s_W^2}\, \mathcal{M}_0^{u_L\bar{u}_L\phi^+W^-}. \qquad \text{(B.91)}
\end{aligned}$$

**$W^-$-boson exchange with initial-state up-type quarks**

$$\begin{aligned}
\sum I^-_{\varphi_{1'}u_L}\, I^+_{\varphi_{2'}\bar{u}_L}\, \mathcal{M}_0^{\varphi_{1'}\varphi_{2'}HZ_T} &= \sum_i I^-_{d_iu}\, I^+_{\bar{d}_i\bar{u}}\, \mathcal{M}_0^{d_{iL}\bar{d}_{iL}HZ_T} \\
&= -\frac{1}{2s_W^2}\sum_i |V_{ud_i}^{\rm CKM}|^2 \mathcal{M}_0^{d_{iL}\bar{d}_{iL}HZ_T} = -\frac{1}{2s_W^2}\mathcal{M}_0^{d_L\bar{d}_LHZ_T}, \qquad \text{(B.92)} \\
\sum I^-_{\varphi_{1'}u_L}\, I^+_{\varphi_{3'}H}\, \mathcal{M}_0^{\varphi_{1'}\bar{u}_L\varphi_{3'}Z_T} &= \sum_i I^-_{d_iu}\, I^+_{\phi^+H}\, \mathcal{M}_0^{d_{iL}\bar{u}_L\phi^+Z_T} \\
&= \frac{1}{2\sqrt{2}s_W^2}\sum_i V_{ud_i}^{\rm CKM}\, \mathcal{M}_0^{d_{iL}\bar{u}_L\phi^+Z_T}, \qquad \text{(B.93)} \\
\sum I^-_{\varphi_{1'}u_L}\, I^+_{\varphi_{4'}Z_T}\, \mathcal{M}_0^{\varphi_{1'}\bar{u}_LH\varphi_{4'}} &= \sum_i I^-_{d_iu} I^+_{W^+Z}\, \mathcal{M}_0^{d_{iL}\bar{u}_LHW^+} \\
&= -\frac{c_W}{\sqrt{2}s_W^2}\sum_i V_{ud_i}^{\rm CKM}\, \mathcal{M}_0^{d_{iL}\bar{u}_LHW^+}, \qquad \text{(B.94)} \\
\sum I^-_{\varphi_{3'}H}\, I^+_{\varphi_{4'}Z_T}\, \mathcal{M}_0^{u_L\bar{u}_L\varphi_{3'}\varphi_{4'}} &= I^-_{\phi^-H} I^+_{W^+Z}\, \mathcal{M}_0^{u_L\bar{u}_L\phi^-W^+} = \frac{c_W}{2s_W^2}\, \mathcal{M}_0^{u_L\bar{u}_L\phi^-W^+}. \qquad \text{(B.95)}
\end{aligned}$$

In eq. (B.92), since the sum runs over the three down-type quark generations we have used the unitarity property of the CKM matrix, $\sum_i |V_{ud_i}^{\rm CKM}|^2 = 1$, to simplify the result. The resulting correction factor involves then a generic down-type quark, choosing a particular generation does not produce any change.

**$W^+$-boson exchange with initial-state down-type quarks**

With initial-state down-type quarks the mixing among the quark generations due to the exchange of charged bosons does not include the top quark. The sum over the generations runs then only over $u_i = u, c$. Therefore, in this case we cannot use the unitarity property of

the CKM matrix anymore.

$$\begin{aligned}
\sum I^{+}_{\varphi_{1'}d_L}\, I^{-}_{\varphi_{2'}\bar{d}_L}\, \mathcal{M}_0^{\varphi_{1'}\varphi_{2'}HZ_T} &= \sum_i I^{+}_{u_i d}\, I^{-}_{\bar{u}_i\bar{d}}\, \mathcal{M}_0^{u_{iL}\bar{u}_{iL}HZ_T} \\
&= -\frac{1}{2s_W^2}\sum_i |V^{\mathrm{CKM}}_{u_i d}|^2 \mathcal{M}_0^{u_{iL}\bar{u}_{iL}HZ_T}, \qquad \text{(B.96)} \\
\sum I^{+}_{\varphi_{1'}d_L}\, I^{-}_{\varphi_{3'}H}\, \mathcal{M}_0^{\varphi_{1'}\bar{d}_L\varphi_{3'}Z_T} &= \sum_i I^{+}_{u_i d}\, I^{-}_{\phi^- H}\, \mathcal{M}_0^{u_{iL}\bar{d}_L\phi^- Z_T} \\
&= -\frac{1}{2\sqrt{2}s_W^2}\sum_i V^{\mathrm{CKM}}_{u_i d}\, \mathcal{M}_0^{u_{iL}\bar{d}_L\phi^- Z_T}, \qquad \text{(B.97)} \\
\sum I^{+}_{\varphi_{1'}d_L}\, I^{-}_{\varphi_{4'}Z_T}\, \mathcal{M}_0^{\varphi_{1'}\bar{d}_L H\varphi_{4'}} &= \sum_i I^{+}_{u_i d}\, I^{-}_{W^- Z}\, \mathcal{M}_0^{u_{iL}\bar{d}_L HW^-} \\
&= \frac{c_W}{\sqrt{2}s_W^2}\sum_i V^{\mathrm{CKM}}_{u_i d}\, \mathcal{M}_0^{u_{iL}\bar{d}_L HW^-}, \qquad \text{(B.98)} \\
\sum I^{+}_{\varphi_{3'}H}\, I^{-}_{\varphi_{4'}Z_T}\, \mathcal{M}_0^{d_L\bar{d}_L\varphi_{3'}\varphi_{4'}} &= I^{+}_{\phi^+ H} I^{-}_{W^- Z}\, \mathcal{M}_0^{d_L\bar{d}_L\phi^+W^-} = \frac{c_W}{2s_W^2}\, \mathcal{M}_0^{d_L\bar{d}_L\phi^+W^-}. \qquad \text{(B.99)}
\end{aligned}$$

**$W^-$-boson exchange with initial-state down-type quarks**

$$\begin{aligned}
\sum I^{-}_{\varphi_{2'}\bar{d}_L}\, I^{+}_{\varphi_{3'}H}\, \mathcal{M}_0^{d_L\varphi_{2'}\varphi_{3'}Z_T} &= \sum_i I^{-}_{\bar{u}_i\bar{d}}\, I^{+}_{\phi^+ H}\, \mathcal{M}_0^{d_L\bar{u}_{iL}\phi^+ Z_T} \\
&= -\frac{1}{2\sqrt{2}s_W^2}\sum_i V^{\mathrm{CKM}}_{u_i d}\, \mathcal{M}_0^{d_L\bar{u}_{iL}\phi^+ Z_T}, \qquad \text{(B.100)} \\
\sum I^{-}_{\varphi_{2'}\bar{d}_L}\, I^{+}_{\varphi_{4'}Z_T}\, \mathcal{M}_0^{d_L\varphi_{2'}H\varphi_{4'}} &= \sum_i I^{-}_{\bar{u}_i\bar{d}}\, I^{+}_{W^+ Z}\, \mathcal{M}_0^{d_L\bar{u}_{iL}HW^+} \\
&= \frac{c_W}{\sqrt{2}s_W^2}\sum_i V^{\mathrm{CKM}}_{u_i d}\, \mathcal{M}_0^{d_L\bar{u}_{iL}HW^+}, \qquad \text{(B.101)} \\
\sum I^{-}_{\varphi_{3'}H}\, I^{+}_{\varphi_{4'}Z_T}\, \mathcal{M}_0^{d_L\bar{d}_L\varphi_{3'}\varphi_{4'}} &= I^{-}_{\phi^- H} I^{+}_{W^+ Z}\, \mathcal{M}_0^{d_L\bar{d}_L\phi^-W^+} = \frac{c_W}{2s_W^2}\, \mathcal{M}_0^{d_L\bar{d}_L\phi^-W^+}. \qquad \text{(B.102)}
\end{aligned}$$

**Transformed matrix elements**

The matrix elements $\mathcal{M}_0^{u_L\bar{d}_L\phi^- Z_T}$ and $\mathcal{M}_0^{d_L\bar{u}_L\phi^+ Z_T}$ are related to the original matrix element with initial-state quarks $q_L$ by

$$\mathcal{M}_0^{u_L\bar{d}_L\phi^- Z_T} = \mathcal{M}_0^{d_L\bar{u}_L\phi^+ Z_T} = -\frac{s_W c_W}{\sqrt{2}}\,\frac{V^{\mathrm{CKM}}_{ud}}{I^Z_{q_L}}\,\mathcal{M}_0^{q_L\bar{q}_L HZ_T}. \qquad \text{(B.103)}$$

For the matrix elements $\mathcal{M}_0^{u_L\bar{d}_L HW^-}$ and $\mathcal{M}_0^{d_L\bar{u}_L HW^+}$, instead, we can write

$$\mathcal{M}_0^{u_L\bar{d}_L HW^-} = \mathcal{M}_0^{d_L\bar{u}_L HW^+} = \frac{c_W^2}{\sqrt{2}s_W}\,\frac{V^{\mathrm{CKM}}_{ud}}{I^Z_{q_L}}\,\mathcal{M}_0^{q_L\bar{q}_L HZ_T}. \qquad \text{(B.104)}$$

The processes $\mathcal{M}_0^{q_L\bar{q}_L\phi^+W^-}$ and $\mathcal{M}_0^{q_L\bar{q}_L\phi^-W^+}$ occur through an intermediate photon or $Z$ boson: they can be written in terms of the original matrix element as

$$\mathcal{M}_0^{q_L\bar{q}_L\phi^+W^-} = \mathcal{M}_0^{q_L\bar{q}_L\phi^-W^+} = \frac{s_W^2 c_W^2}{I_{q_L}^Z}\left(\frac{Q_q}{s_W} - \frac{I_{q_L}^Z}{c_W}\right)\mathcal{M}_0. \tag{B.105}$$

Finally, the $HZ$ production processes with up- and down-type initial quarks can be related one to each other by

$$\frac{\mathcal{M}_0^{u_L\bar{u}_L HZ_T}}{I_{u_L}^Z} = \frac{\mathcal{M}_0^{d_L\bar{d}_L HZ_T}}{I_{d_L}^Z}. \tag{B.106}$$

**Final results**

Since the corrections coming from the exchange of neutral gauge bosons include only terms that multiply $\log(|r_{12}|/s)$, for this process they do not give any contribution. The only relevant corrections arise from the exchange of charged gauge bosons: defining a common factor

$$F_T^{\rm SSC} = -\left[\log\frac{|t|}{s} + \log\frac{|u|}{s}\right]\frac{c_W(1+c_W^2)}{2s_W^3}, \tag{B.107}$$

the corrections for up- and down-type quarks are

$$\delta^{\rm SSC}\mathcal{M}^{u_\kappa\bar{u}_\kappa HZ_T} = \delta_{\kappa L}\, l(s)\,\frac{F_T^{\rm SSC}}{I_{u_\kappa}^Z}\,\mathcal{M}_0, \tag{B.108}$$

$$\delta^{\rm SSC}\mathcal{M}^{d_\kappa\bar{d}_\kappa HZ_T} = -\,\delta_{\kappa L}\, l(s)\sum_{u_i}|V_{u_i d}^{\rm CKM}|^2\,\frac{F_T^{\rm SSC}}{I_{d_\kappa}^Z}\,\mathcal{M}_0. \tag{B.109}$$

In the derivation of the result (B.108) we used again the unitarity property of the CKM matrix: indeed, combining the transformed matrix elements with their prefactors, we obtain $\sum_i |V_{ud_i}^{\rm CKM}|^2$.

### B.3.3 Single-logarithmic corrections: external particles

For the process in which the incoming particles are quarks $q$ with chirality $\kappa$ the corrections associated to the external particles are

$$k=1: \quad \varphi_1 = \varphi_{1'} = q_\kappa$$

$$\delta_{q_\kappa q_\kappa}^{\rm C} = \frac{3}{2}\,l(s)\,C_{q_\kappa}^{\rm ew} + \frac{\alpha}{4\pi}\,Q_q^2\,\log\frac{M_W^2}{\lambda^2}, \tag{B.110}$$

$$k=2: \quad \varphi_2 = \varphi_{2'} = \bar{q}_\kappa$$

$$\delta_{\bar{q}_L\bar{q}_L}^{\rm C} = \frac{3}{2}\,l(s)\,C_{\bar{q}_\kappa}^{\rm ew} + \frac{\alpha}{4\pi}\,Q_q^2\,\log\frac{M_W^2}{\lambda^2}, \tag{B.111}$$

$$k=3: \quad \varphi_3 = \varphi_{3'} = H$$

$$\delta_{HH}^{\rm C} = \frac{\alpha}{4\pi}\left(2C_\Phi^{\rm ew}\log\frac{s}{M_H^2} - \frac{3}{4s_W^2}\,\frac{m_t^2}{M_W^2}\log\frac{s}{m_t^2}\right), \tag{B.112}$$

$$k=4: \quad \varphi_4 = A, Z_T$$

$$\delta_{AZ}^{\rm C}\mathcal{M}_0^{q_\kappa\bar{q}_\kappa HA} = 0, \tag{B.113}$$

$$\delta_{ZZ}^{\rm C} = \frac{1}{2}\,b_{ZZ}^{\rm ew}\,l(s) + \frac{\alpha}{4\pi}\left(\frac{M_Z^2}{24s_W^2M_W^2}\log\frac{M_H^2}{M_W^2} + T_{ZZ}\log\frac{m_t^2}{M_W^2}\right), \tag{B.114}$$

in which $T_{ZZ}$ is taken from eq. (3.43) and the contribution in eq. (B.113) vanishes for the same reasons explained in the computation of $\delta^{\rm LSC}$. The result is then

$$\delta^{\rm C}\mathcal{M}^{q_\kappa\bar{q}_\kappa HZ_T} = \left\{\frac{\alpha}{4\pi}\left[\left(\frac{3}{4s_W^2}\frac{m_t^2}{M_W^2}+T_{ZZ}\right)\log\frac{m_t^2}{M_W^2}+\left(\frac{M_Z^2}{24s_W^2M_W^2}-2C_\Phi^{\rm ew}\right)\log\frac{M_H^2}{M_W^2}\right]\right.$$
$$\left.+\,l(s)\left[3C_{q_\kappa}^{\rm ew}+2C_\Phi^{\rm ew}+\frac{1}{2}b_{ZZ}^{\rm ew}-\frac{3}{4s_W^2}\frac{m_t^2}{M_W^2}\right]+\frac{\alpha}{2\pi}Q_q^2\log\frac{M_W^2}{\lambda^2}\right\}\mathcal{M}_0. \quad \text{(B.115)}$$

### B.3.4 Single-logarithmic corrections: parameter renormalization

The parameters appearing in the leading-order process, that have to be renormalized, are $e$, $c_W$ and $M_Z$, the latter for the same reasons explained in $HW$ production. The Weinberg angle also appears in the definition of $I_{q_\kappa}^Z$: the matrix element can be rewritten as

$$\mathcal{M}_0^{q\bar{q}HZ_T}=\sum_\kappa\frac{e^2M_Z}{s_Wc_W}\frac{T_{q_\kappa}^3-Q_qs_W^2}{s_Wc_W}\frac{A_{TZ}^\kappa}{q^2}=\sum_\kappa g_2^2\,M_Z\frac{T_{q_\kappa}^3-Q_qs_W^2}{1-s_W^2}\frac{A_{TZ}^\kappa}{q^2}. \quad \text{(B.116)}$$

We then get

$$\delta^{\rm PR}\mathcal{M}^{q\bar{q}HZ_T}=\left(\frac{\partial\mathcal{M}_0}{\partial g_2}\,\delta g_2+\frac{\partial\mathcal{M}_0}{\partial c_W^2}\,\delta c_W^2+\frac{\partial\mathcal{M}_0}{\partial M_Z^2}\,\delta M_Z^2\right)\Big|_{\mu^2=s}. \quad \text{(B.117)}$$

The partial derivatives with respect to the involved parameters are

$$\frac{\partial\mathcal{M}_0}{\partial g_2} = \frac{2}{g_2}\mathcal{M}_0, \quad \text{(B.118)}$$

$$\frac{\partial\mathcal{M}_0}{\partial c_W^2} = -\frac{\partial\mathcal{M}_0}{\partial s_W^2}=\frac{\mathcal{M}_0}{c_W^2}\frac{Q_q-T_{q_\kappa}^3}{T_{q_\kappa}^3-Q_qs_W^2}=\frac{\mathcal{M}_0}{c_W^2}\rho_\kappa, \quad \text{(B.119)}$$

$$\frac{\partial\mathcal{M}_0}{\partial M_Z^2} = \frac{\mathcal{M}_0}{2M_Z^2}, \quad \text{(B.120)}$$

having defined

$$\rho_\kappa=\frac{Q_q-T_{q_\kappa}^3}{T_{q_\kappa}^3-Q_qs_W^2}. \quad \text{(B.121)}$$

Adding up the various contributions, for the corrections from parameter renormalization we obtain

$$\delta^{\rm PR}\mathcal{M}^{q_\kappa\bar{q}_\kappa HZ_T} = \left\{\frac{\alpha}{4\pi}\left[\left(\frac{5}{6s_W^2}+\frac{5\rho_{q_\kappa}}{6c_W^2}-\frac{5M_Z^2}{12s_W^2M_W^2}\right)\log\frac{M_H^2}{M_W^2}\right.\right.$$
$$\left.-\left(\frac{9+6s_W^2-32s_W^4}{18s_W^2}\left(\frac{1}{s_W^2}+\frac{\rho_{q_\kappa}}{c_W^2}\right)+T_{ZZ}-\frac{3}{4s_W^2}\frac{m_t^2}{M_W^2}\right)\log\frac{m_t^2}{M_W^2}\right]$$
$$\left.+\,l(s)\left[-b_{WW}^{\rm ew}+\rho_{q_\kappa}\frac{s_W}{c_W}b_{AZ}^{\rm ew}+2C_\Phi^{\rm ew}-\frac{1}{2}b_{ZZ}^{\rm ew}-\frac{3}{4s_W^2}\frac{m_t^2}{M_W^2}\right]\right\}\mathcal{M}_0. \quad \text{(B.122)}$$

## B.4 The $HZ_L$ associated production

For the process

$$q_\kappa(p_1)\,\bar{q}_\kappa(p_2)\,H(-p_3)\,Z_{\scriptscriptstyle L}(-k)\to 0, \tag{B.123}$$

the application of the GBET gives $\mathcal{M}_0^{q_\kappa\bar{q}_\kappa HZ_L}=i\mathcal{M}_0^{q_\kappa\bar{q}_\kappa H\chi}$. The $HZ\chi$ vertex contributes to the matrix element with a factor $ieI^Z_{H\chi}(-k+p_3)_\mu$, giving

$$\begin{aligned}
\mathcal{M}_0^{q\bar{q}H\chi} &= \bar{v}(p_2)\,V^\mu_{q\bar{q}Z}\,u(p_1)\,\frac{(-i)}{q^2-M_W^2}\,ieI^Z_{H\chi}\,(-k+p_3)_\mu \\
&= -\frac{1}{q^2}\,\frac{e^2}{2s_{\scriptscriptstyle W}c_{\scriptscriptstyle W}}\,\bar{v}(p_2)\,\gamma^\mu\left[\frac{1-\gamma_5}{2}I^Z_{q_L}+\frac{1+\gamma_5}{2}I^Z_{q_R}\right]u(p_1)\,(-k+p_3)_\mu \\
&= -\frac{1}{q^2}\,\frac{e^2}{2s_{\scriptscriptstyle W}c_{\scriptscriptstyle W}}\sum_\kappa I^Z_{q_\kappa}\,\bar{v}_\kappa(p_2)\gamma^\mu u_\kappa(p_1)\,(-k+p_3)_\mu.
\end{aligned} \tag{B.124}$$

Combining these relations, we obtain

$$\begin{aligned}
\mathcal{M}_0^{q\bar{q}HZ_L} &= i\mathcal{M}_0^{q\bar{q}H\chi}=-\frac{i}{q^2}\,\frac{e^2}{2s_{\scriptscriptstyle W}c_{\scriptscriptstyle W}}\sum_\kappa I^Z_{q_\kappa}\,\bar{v}_\kappa(p_2)\gamma^\mu u_\kappa(p_1)\,(-k+p_3)_\mu \\
&= \frac{e^2}{2s_{\scriptscriptstyle W}c_{\scriptscriptstyle W}}\sum_\kappa I^Z_{q_\kappa}\frac{A^\kappa_{LZ}}{q^2},
\end{aligned} \tag{B.125}$$

in which

$$A^\kappa_{LZ}=-i\,\bar{v}_\kappa(p_2)\gamma^\mu u_\kappa(p_1)\,(-k+p_3)_\mu. \tag{B.126}$$

### B.4.1 Leading soft-collinear contributions

We apply the same formulae used in the transverse case. Apart from the Goldstone boson, the factors for the other particles remain unchanged,

$$\delta^{\rm LSC}_{\chi\chi} = -\frac{1}{2}\,L(s)\,C^{\rm ew}_\Phi+l(s)\,\log\frac{M_Z^2}{M_W^2}\,(I^Z_\chi)^2+\delta^{\rm LSC,h}_\chi, \tag{B.127}$$

with $\delta^{\rm LSC,h}_\chi$ defined in eq. (3.33). We then obtain

$$\begin{aligned}
\delta^{\rm LSC}\mathcal{M}^{q_\kappa\bar{q}_\kappa H\chi} = \Big\{&-L(s)\left[C^{\rm ew}_{q_\kappa}+C^{\rm ew}_\Phi\right]+2l(s)\log\frac{M_Z^2}{M_W^2}\left[(I^Z_{q_\kappa})^2+(I^Z_H)^2\right] \\
&+\delta^{\rm LSC,h}_H+\delta^{\rm LSC,h}_\chi-Q_q^2\,L_{\rm em}(s,\lambda^2,m_q^2)\Big\}\mathcal{M}_0.
\end{aligned} \tag{B.128}$$

### B.4.2 Subleading soft-collinear contributions

**Photon exchange**

$$\sum I^A_{\varphi_{1'}q_\kappa}\,I^A_{\varphi_{2'}\bar{q}_\kappa}\,\mathcal{M}_0^{\varphi_{1'}\varphi_{2'}H\chi} = I^A_{q_\kappa q_\kappa}\,I^A_{\bar{q}_\kappa\bar{q}_\kappa}\,\mathcal{M}_0=-Q_q^2\,\mathcal{M}_0. \tag{B.129}$$

**$Z$-boson exchange**

$$\sum I^Z_{\varphi_{1'}q_\kappa}\, I^Z_{\varphi_{2'}\bar{q}_\kappa}\, \mathcal{M}_0^{\varphi_{1'}\varphi_{2'}H\chi} = I^Z_{q_\kappa q_\kappa}\, I^Z_{\bar{q}_\kappa\bar{q}_\kappa}\, \mathcal{M}_0 = -(I^Z_{q_\kappa})^2\, \mathcal{M}_0, \tag{B.130}$$

$$\sum I^Z_{\varphi_{1'}q_\kappa}\, I^Z_{\varphi_{3'}H}\, \mathcal{M}_0^{\varphi_{1'}\bar{q}_\kappa\varphi_{3'}\chi} = I^Z_{q_\kappa q_\kappa}\, I^Z_{\chi H}\, \mathcal{M}_0^{q_\kappa\bar{q}_\kappa\chi\chi} = 0, \tag{B.131}$$

$$\sum I^Z_{\varphi_{1'}q_\kappa}\, I^Z_{\varphi_{4'}\chi}\, \mathcal{M}_0^{\varphi_{1'}\bar{q}_\kappa H\varphi_{4'}} = I^Z_{q_\kappa q_\kappa}\, I^Z_{H\chi}\, \mathcal{M}_0^{q_\kappa\bar{q}_\kappa HH} = 0, \tag{B.132}$$

$$\sum I^Z_{\varphi_{2'}\bar{q}_\kappa}\, I^Z_{\varphi_{3'}H}\, \mathcal{M}_0^{q_\kappa\varphi_{2'}\varphi_{3'}\chi} = I^Z_{\bar{q}_\kappa\bar{q}_\kappa}\, I^Z_{\chi H}\, \mathcal{M}_0^{q_\kappa\bar{q}_\kappa\chi\chi} = 0, \tag{B.133}$$

$$\sum I^Z_{\varphi_{2'}\bar{q}_\kappa}\, I^Z_{\varphi_{4'}\chi}\, \mathcal{M}_0^{q_\kappa\varphi_{2'}H\varphi_{4'}} = I^Z_{\bar{q}_\kappa\bar{q}_\kappa}\, I^Z_{H\chi}\, \mathcal{M}_0^{q_\kappa\bar{q}_\kappa HH} = 0, \tag{B.134}$$

$$\sum I^Z_{\varphi_{3'}H}\, I^Z_{\varphi_{4'}\chi}\, \mathcal{M}_0^{q_\kappa\bar{q}_\kappa\varphi_{3'}\varphi_{4'}} = I^Z_{\chi H}\, I^Z_{H\chi}\, \mathcal{M}_0^{q_\kappa\bar{q}_\kappa\chi H} = (iI^Z_{H\chi})^2 \mathcal{M}_0^{q_\kappa\bar{q}_\kappa\chi H}. \tag{B.135}$$

The terms that involve $\mathcal{M}_0^{q_\kappa\bar{q}_\kappa\chi\chi}$ and $\mathcal{M}_0^{q_\kappa\bar{q}_\kappa HH}$ vanish, since these matrix elements contain a coupling between massless quarks and the Goldstone boson $\chi$ or the Higgs boson. $\mathcal{M}_0^{q_\kappa\bar{q}_\kappa\chi H}$ is instead related to the original matrix element by

$$\mathcal{M}_0^{q_\kappa\bar{q}_\kappa\chi H} = -\mathcal{M}_0. \tag{B.136}$$

**$W^+$-boson exchange with initial-state up-type quarks**

$$\begin{aligned}\sum I^+_{\varphi_{2'}\bar{u}_L}\, I^-_{\varphi_{3'}H}\, \mathcal{M}_0^{u_L\varphi_{2'}\varphi_{3'}\chi} &= \sum_i I^+_{\bar{d}_i\bar{u}}\, I^-_{\phi^-H}\, \mathcal{M}_0^{u_L\bar{d}_{iL}\phi^-\chi} \\ &= \frac{1}{2\sqrt{2}s_W^2} \sum_i V^{\rm CKM}_{ud_i}\, \mathcal{M}_0^{u_L\bar{d}_{iL}\phi^-\chi},\end{aligned} \tag{B.137}$$

$$\begin{aligned}\sum I^+_{\varphi_{2'}\bar{u}_L}\, I^-_{\varphi_{4'}\chi}\, \mathcal{M}_0^{u_L\varphi_{2'}H\varphi_{4'}} &= \sum_i I^+_{\bar{d}_i\bar{u}} I^-_{\phi^-\chi}\, \mathcal{M}_0^{u_L\bar{d}_{iL}H\phi^-} \\ &= -\frac{i}{2\sqrt{2}s_W^2} \sum_i V^{\rm CKM}_{ud_i}\, \mathcal{M}_0^{u_L\bar{d}_{iL}H\phi^-},\end{aligned} \tag{B.138}$$

$$\sum I^+_{\varphi_{3'}H}\, I^-_{\varphi_{4'}\chi}\, \mathcal{M}_0^{u_L\bar{u}_L\varphi_{3'}\varphi_{4'}} = I^+_{\phi^+H} I^-_{\phi^-\chi}\, \mathcal{M}_0^{u_L\bar{u}_L\phi^+\phi^-} = \frac{i}{4s_W^2}\, \mathcal{M}_0^{u_L\bar{u}_L\phi^+\phi^-}. \tag{B.139}$$

**$W^-$-boson exchange with initial-state up-type quarks**

$$\begin{aligned}\sum I^-_{\varphi_{1'}u_L}\, I^+_{\varphi_{2'}\bar{u}_L}\, \mathcal{M}_0^{\varphi_{1'}\varphi_{2'}H\chi} &= \sum_i I^-_{d_iu}\, I^+_{\bar{d}_i\bar{u}}\, \mathcal{M}_0^{d_{iL}\bar{d}_{iL}H\chi} \\ &= -\frac{1}{2s_W^2} \sum_i |V^{\rm CKM}_{ud_i}|^2 \mathcal{M}_0^{d_{iL}\bar{d}_{iL}H\chi} = -\frac{1}{2s_W^2} \mathcal{M}_0^{d_L\bar{d}_LH\chi},\end{aligned} \tag{B.140}$$

$$\begin{aligned}\sum I^-_{\varphi_{1'}u_L}\, I^+_{\varphi_{3'}H}\, \mathcal{M}_0^{\varphi_{1'}\bar{u}_L\varphi_{3'}\chi} &= \sum_i I^-_{d_iu}\, I^+_{\phi^+H}\, \mathcal{M}_0^{d_{iL}\bar{u}_L\phi^+\chi} \\ &= \frac{1}{2\sqrt{2}s_W^2} \sum_i V^{\rm CKM}_{ud_i}\, \mathcal{M}_0^{d_{iL}\bar{u}_L\phi^+\chi},\end{aligned} \tag{B.141}$$

$$\sum I^-_{\varphi_{1'}u_L}\, I^+_{\varphi_{4'}\chi}\, \mathcal{M}_0^{\varphi_{1'}\bar{u}_L H\varphi_{4'}} = \sum_i I^-_{d_i u} I^+_{\phi^+\chi}\, \mathcal{M}_0^{d_{iL}\bar{u}_L H\phi^+}$$
$$= \frac{i}{2\sqrt{2}s_W^2} \sum_i V^{\rm CKM}_{ud_i}\, \mathcal{M}_0^{d_{iL}\bar{u}_L H\phi^+}, \tag{B.142}$$

$$\sum I^-_{\varphi_{3'}H}\, I^+_{\varphi_{4'}\chi}\, \mathcal{M}_0^{u_L\bar{u}_L\varphi_{3'}\varphi_{4'}} = I^-_{\phi^-H} I^+_{\phi^+\chi}\, \mathcal{M}_0^{u_L\bar{u}_L\phi^-\phi^+} = -\frac{i}{4s_W^2}\, \mathcal{M}_0^{u_L\bar{u}_L\phi^-\phi^+}. \tag{B.143}$$

In these computations too we used the unitarity property of the CKM matrix to simplify the results.

**$W^+$-boson exchange with initial-state down-type quarks**

$$\sum I^+_{\varphi_{1'}d_L}\, I^-_{\varphi_{2'}\bar{d}_L}\, \mathcal{M}_0^{\varphi_{1'}\varphi_{2'}H\chi} = \sum_i I^+_{u_i d}\, I^-_{\bar{u}_i\bar{d}}\, \mathcal{M}_0^{u_{iL}\bar{u}_{iL}H\chi}$$
$$= -\frac{1}{2s_W^2} \sum_i |V^{\rm CKM}_{u_i d}|^2 \mathcal{M}_0^{u_{iL}\bar{u}_{iL}H\chi}, \tag{B.144}$$

$$\sum I^+_{\varphi_{1'}d_L}\, I^-_{\varphi_{3'}H}\, \mathcal{M}_0^{\varphi_{1'}\bar{d}_L\varphi_{3'}\chi} = \sum_i I^+_{u_i d}\, I^-_{\phi^-H}\, \mathcal{M}_0^{u_{iL}\bar{d}_L\phi^-\chi}$$
$$= -\frac{1}{2\sqrt{2}s_W^2} \sum_i V^{\rm CKM}_{u_i d}\, \mathcal{M}_0^{u_{iL}\bar{d}_L\phi^-\chi}, \tag{B.145}$$

$$\sum I^+_{\varphi_{1'}d_L}\, I^-_{\varphi_{4'}\chi}\, \mathcal{M}_0^{\varphi_{1'}\bar{d}_L H\varphi_{4'}} = \sum_i I^+_{u_i d}\, I^-_{\phi^-\chi}\, \mathcal{M}_0^{u_{iL}\bar{d}_L H\phi^-}$$
$$= \frac{i}{2\sqrt{2}s_W^2} \sum_i V^{\rm CKM}_{u_i d}\, \mathcal{M}_0^{u_{iL}\bar{d}_L H\phi^-}, \tag{B.146}$$

$$\sum I^+_{\varphi_{3'}H}\, I^-_{\varphi_{4'}\chi}\, \mathcal{M}_0^{d_L\bar{d}_L\varphi_{3'}\varphi_{4'}} = I^+_{\phi^+H} I^-_{\phi^-\chi}\, \mathcal{M}_0^{d_L\bar{d}_L\phi^+\phi^-} = \frac{i}{4s_W^2}\, \mathcal{M}_0^{d_L\bar{d}_L\phi^+\phi^-}. \tag{B.147}$$

**$W^-$-boson exchange with initial-state down-type quarks**

$$\sum I^-_{\varphi_{2'}\bar{d}_L}\, I^+_{\varphi_{3'}H}\, \mathcal{M}_0^{d_L\varphi_{2'}\varphi_{3'}\chi} = \sum_i I^-_{\bar{u}_i\bar{d}}\, I^+_{\phi^+H}\, \mathcal{M}_0^{d_L\bar{u}_{iL}\phi^+\chi}$$
$$= -\frac{1}{2\sqrt{2}s_W^2} \sum_i V^{\rm CKM}_{u_i d}\, \mathcal{M}_0^{d_L\bar{u}_{iL}\phi^+\chi}, \tag{B.148}$$

$$\sum I^-_{\varphi_{2'}\bar{d}_L}\, I^+_{\varphi_{4'}\chi}\, \mathcal{M}_0^{d_L\varphi_{2'}H\varphi_{4'}} = \sum_i I^-_{\bar{u}_i\bar{d}}\, I^+_{\phi^+\chi}\, \mathcal{M}_0^{d_L\bar{u}_{iL}H\phi^+}$$
$$= -\frac{i}{2\sqrt{2}s_W^2} \sum_i V^{\rm CKM}_{u_i d}\, \mathcal{M}_0^{d_L\bar{u}_{iL}H\phi^+}, \tag{B.149}$$

$$\sum I^-_{\varphi_{3'}H}\, I^+_{\varphi_{4'}\chi}\, \mathcal{M}_0^{d_L\bar{d}_L\varphi_{3'}\varphi_{4'}} = I^-_{\phi^-H} I^+_{\phi^+\chi}\, \mathcal{M}_0^{d_L\bar{d}_L\phi^-\phi^+} = -\frac{i}{4s_W^2}\, \mathcal{M}_0^{d_L\bar{d}_L\phi^-\phi^+}. \tag{B.150}$$

**Transformed matrix elements**

$\mathcal{M}_0^{u_L\bar{d}_L\phi^-\chi}$ and $\mathcal{M}_0^{d_L\bar{u}_L\phi^+\chi}$ are related to the original matrix element with initial-state quarks $q_L$ by

$$\mathcal{M}_0^{u_L\bar{d}_L\phi^-\chi} = \mathcal{M}_0^{d_L\bar{u}_L\phi^+\chi} = -\frac{c_W}{\sqrt{2}s_W}\frac{V_{ud}^{\rm CKM}}{I_{q_L}^Z}\,\mathcal{M}_0^{q_L\bar{q}_L H\chi}. \tag{B.151}$$

Calling this result $\overline{\mathcal{M}}_0$, for the matrix elements $\mathcal{M}_0^{u_L\bar{d}_L H\phi^-}$ and $\mathcal{M}_0^{d_L\bar{u}_L H\phi^+}$ we obtain

$$\mathcal{M}_0^{u_L\bar{d}_L H\phi^-} = -\mathcal{M}_0^{d_L\bar{u}_L H\phi^+} = i\overline{\mathcal{M}}_0. \tag{B.152}$$

The processes $\mathcal{M}_0^{q_L\bar{q}_L\phi^+\phi^-}$ and $\mathcal{M}_0^{q_L\bar{q}_L\phi^-\phi^+}$ occur through an intermediate photon or $Z$ boson: they can be written in terms of the original matrix element as

$$\mathcal{M}_0^{q_L\bar{q}_L\phi^+\phi^-} = -\,\mathcal{M}_0^{q_L\bar{q}_L\phi^-\phi^+} = \frac{R_{q_L\phi^-}}{I_{q_L}^Z I_{H\chi}^Z}\,\mathcal{M}_0. \tag{B.153}$$

Finally, the $H\chi$ production processes with up- and down-type initial quarks are related one to each other by

$$\frac{\mathcal{M}_0^{u_L\bar{u}_L H\chi}}{I_{u_L}^Z} = \frac{\mathcal{M}_0^{d_L\bar{d}_L H\chi}}{I_{d_L}^Z}. \tag{B.154}$$

**Final results**

For the production of a longitudinal $Z$ boson too, the corrections coming from the exchange of neutral gauge bosons do not give any contribution. Defining a factor

$$F_L^{\rm SSC} = -\frac{c_W}{s_W^3}\left[\log\frac{|t|}{s} + \log\frac{|u|}{s}\right], \tag{B.155}$$

the corrections for up- and down-type quarks are

$$\delta^{\rm SSC}\mathcal{M}^{u_\kappa\bar{u}_\kappa H\chi} = \delta_{\kappa L}\,l(s)\,\frac{F_L^{\rm SSC}}{I_{u_\kappa}^Z}\,\mathcal{M}_0, \tag{B.156}$$

$$\delta^{\rm SSC}\mathcal{M}^{d_\kappa\bar{d}_\kappa H\chi} = -\,\delta_{\kappa L}\,l(s)\sum_{u_i}|V_{u_i d}^{\rm CKM}|^2\,\frac{F_L^{\rm SSC}}{I_{d_\kappa}^Z}\,\mathcal{M}_0. \tag{B.157}$$

### B.4.3 Single-logarithmic corrections: external particles

Even for this type of corrections the only difference with respect to the transverse case is in the Goldstone-boson term,

$$\delta_{\chi\chi}^{\rm C} = 2\,C_\Phi^{\rm ew}\,l(s) + \frac{\alpha}{4\pi}\left(-\frac{3}{4s_W^2}\frac{m_t^2}{M_W^2}\log\frac{s}{m_t^2} + \frac{M_Z^2}{8s_W^2M_W^2}\log\frac{M_H^2}{M_W^2}\right). \tag{B.158}$$

Summing the contributions,

$$\begin{aligned}\delta^{\rm C}\mathcal{M}^{q_\kappa\bar{q}_\kappa H\chi} = \Bigg\{&\frac{\alpha}{4\pi}\left[\frac{3}{2s_W^2}\frac{m_t^2}{M_W^2}\log\frac{m_t^2}{M_W^2} + \left(\frac{M_Z^2}{8s_W^2M_W^2} - 2C_\Phi^{\rm ew}\right)\log\frac{M_H^2}{M_W^2}\right]\\ &+ l(s)\left[3C_{q_\kappa}^{\rm ew} + 4C_\Phi^{\rm ew} - \frac{3}{2s_W^2}\frac{m_t^2}{M_W^2}\right] + \frac{\alpha}{2\pi}\,Q_q^2\,\log\frac{M_W^2}{\lambda^2}\Bigg\}\,\mathcal{M}_0.\end{aligned} \tag{B.159}$$

### B.4.4 Single-logarithmic corrections: parameter renormalization

The matrix element involves the same parameters as the transverse case apart from $M_Z$: the corrections due to parameter renormalization are then given by the renormalization of $e$ and $c_W$ derived in the previous section. The combination of these factors gives

$$\begin{aligned}\delta^{\mathrm{PR}}\mathcal{M}^{q_\kappa\bar{q}_\kappa HZ_T} &= \left\{\frac{\alpha}{4\pi}\left(\frac{1}{s_W^2}+\frac{\rho_{q_\kappa}}{c_W^2}\right)\left[\frac{5}{6}\log\frac{M_H^2}{M_W^2}-\frac{9+6s_W^2-32s_W^4}{18s_W^2}\log\frac{m_t^2}{M_W^2}\right]\right. \\ &\quad \left.+\,l(s)\left[-b_{WW}^{\mathrm{ew}}+\rho_{q_\kappa}\frac{s_W}{c_W}b_{AZ}^{\mathrm{ew}}\right]\right\}\mathcal{M}_0. \qquad \text{(B.160)}\end{aligned}$$

# Bibliography


[1] **ATLAS** Collaboration, G. Aad et al., *Observation of a new particle in the search for the Standard Model Higgs boson with the ATLAS detector at the LHC*, Phys. Lett. **B716** (2012) 1–29, [1207.7214].

[2] **CMS** Collaboration, S. Chatrchyan et al., *Observation of a new boson at a mass of 125 GeV with the CMS experiment at the LHC*, Phys. Lett. **B716** (2012) 30–61, [1207.7235].

[3] V. V. Sudakov, *Vertex parts at very high-energies in quantum electrodynamics*, Sov. Phys. JETP **3** (1956) 65–71. [Zh. Eksp. Teor. Fiz.30,87(1956)].

[4] R. Jackiw, *Dynamics at high momentum and the vertex function of spinor electrodynamics*, Annals Phys. **48** (1968) 292–321.

[5] P. Ciafaloni and D. Comelli, *Sudakov enhancement of electroweak corrections*, Phys. Lett. **B446** (1999) 278–284, [hep-ph/9809321].

[6] M. Beccaria, G. Montagna, F. Piccinini, F. M. Renard, and C. Verzegnassi, *Rising bosonic electroweak virtual effects at high-energy e+ e- colliders*, Phys. Rev. **D58** (1998) 093014, [hep-ph/9805250].

[7] V. S. Fadin, L. N. Lipatov, A. D. Martin, and M. Melles, *Resummation of double logarithms in electroweak high-energy processes*, Phys. Rev. **D61** (2000) 094002, [hep-ph/9910338].

[8] S. Pozzorini, Electroweak radiative corrections at high-energies. PhD thesis, Zurich U., Inst. Math., 2001. hep-ph/0201077.

[9] A. Denner and S. Pozzorini, *One loop leading logarithms in electroweak radiative corrections. 1. Results*, Eur. Phys. J. **C18** (2001) 461–480, [hep-ph/0010201].

[10] A. Denner and S. Pozzorini, *One loop leading logarithms in electroweak radiative corrections. 2. Factorization of collinear singularities*, Eur. Phys. J. **C21** (2001) 63–79, [hep-ph/0104127].

[11] S. Frixione and B. R. Webber, *The MC@NLO 3.1 event generator*, hep-ph/0506182.

[12] G. Luisoni, P. Nason, C. Oleari, and F. Tramontano, *$HW^{\pm}$/HZ + 0 and 1 jet at NLO with the POWHEG BOX interfaced to GoSam and their merging within MiNLO*, JHEP **10** (2013) 083, [1306.2542].

[13] S. Frixione, P. Nason, and C. Oleari, *Matching NLO QCD computations with Parton Shower simulations: the POWHEG method*, JHEP **11** (2007) 070, [0709.2092].

[14] S. Alioli, P. Nason, C. Oleari, and E. Re, *A general framework for implementing NLO calculations in shower Monte Carlo programs: the POWHEG BOX*, JHEP **06** (2010) 043, [1002.2581].

[15] P. Nason, *A New method for combining NLO QCD with shower Monte Carlo algorithms*, JHEP **11** (2004) 040, [hep-ph/0409146].

[16] T. Ježo and P. Nason, *On the Treatment of Resonances in Next-to-Leading Order Calculations Matched to a Parton Shower*, JHEP **12** (2015) 065, [1509.09071].

[17] L. Barze, G. Montagna, P. Nason, O. Nicrosini, and F. Piccinini, *Implementation of electroweak corrections in the POWHEG BOX: single W production*, JHEP **04** (2012) 037, [1202.0465].

[18] K. Hamilton, P. Nason, and G. Zanderighi, *MINLO: Multi-Scale Improved NLO*, JHEP **10** (2012) 155, [1206.3572].

[19] K. Hamilton, P. Nason, C. Oleari, and G. Zanderighi, *Merging H/W/Z + 0 and 1 jet at NLO with no merging scale: a path to parton shower + NNLO matching*, JHEP **05** (2013) 082, [1212.4504].

[20] **CMS** Collaboration, S. Chatrchyan et al., *Measurement of the properties of a Higgs boson in the four-lepton final state*, Phys. Rev. **D89** (2014), no. 9 092007, [1312.5353].

[21] **CMS** Collaboration, V. Khachatryan et al., *Observation of the diphoton decay of the Higgs boson and measurement of its properties*, Eur. Phys. J. **C74** (2014), no. 10 3076, [1407.0558].

[22] **ATLAS** Collaboration, G. Aad et al., *Measurement of the Higgs boson mass from the $H \to \gamma\gamma$ and $H \to ZZ^* \to 4\ell$ channels with the ATLAS detector using 25 $fb^{-1}$ of pp collision data*, Phys. Rev. **D90** (2014), no. 5 052004, [1406.3827].

[23] P. W. Higgs, *Broken symmetries, massless particles and gauge fields*, Phys. Lett. **12** (1964) 132–133.

[24] P. W. Higgs, *Broken Symmetries and the Masses of Gauge Bosons*, Phys. Rev. Lett. **13** (1964) 508–509.

[25] F. Englert and R. Brout, *Broken symmetry and the mass of gauge vector mesons*, Phys. Rev. Lett. **13** (Aug, 1964) 321–323.

[26] **LHC Higgs Cross Section Working Group** Collaboration, D. de Florian et al., *Handbook of LHC Higgs Cross Sections: 4. Deciphering the Nature of the Higgs Sector*, 1610.07922.

[27] J. M. Butterworth, A. R. Davison, M. Rubin, and G. P. Salam, *Jet substructure as a new Higgs search channel at the LHC*, Phys. Rev. Lett. **100** (2008) 242001, [0802.2470].

[28] **ATLAS, CMS** Collaboration, G. Aad et al., *Combined Measurement of the Higgs Boson Mass in pp Collisions at $\sqrt{s} = 7$ and 8 TeV with the ATLAS and CMS Experiments*, Phys. Rev. Lett. **114** (2015) 191803, [1503.07589].

[29] **CMS** Collaboration, S. Chatrchyan et al., *Evidence for the direct decay of the 125 GeV Higgs boson to fermions*, Nature Phys. **10** (2014) 557–560, [1401.6527].

[30] **ATLAS** Collaboration, G. Aad et al., *Evidence for the Higgs-boson Yukawa coupling to tau leptons with the ATLAS detector*, JHEP **04** (2015) 117, [1501.04943].

[31] **ATLAS** Collaboration, G. Aad et al., *Search for the $b\bar{b}$ decay of the Standard Model Higgs boson in associated $(W/Z)H$ production with the ATLAS detector*, JHEP **01** (2015) 069, [1409.6212].

[32] **ATLAS, CMS** Collaboration, G. Aad et al., *Measurements of the Higgs boson production and decay rates and constraints on its couplings from a combined ATLAS and CMS analysis of the LHC pp collision data at $\sqrt{s} = 7$ and 8 TeV*, JHEP **08** (2016) 045, [1606.02266].

[33] **Particle Data Group** Collaboration, K. A. Olive et al., *Review of Particle Physics*, Chin. Phys. **C38** (2014) 090001.

[34] O. Brein, A. Djouadi, and R. Harlander, *NNLO QCD corrections to the Higgs-strahlung processes at hadron colliders*, Phys. Lett. **B579** (2004) 149–156, [hep-ph/0307206].

[35] G. Ferrera, M. Grazzini, and F. Tramontano, *Associated WH production at hadron colliders: a fully exclusive QCD calculation at NNLO*, Phys. Rev. Lett. **107** (2011) 152003, [1107.1164].

[36] G. Ferrera, M. Grazzini, and F. Tramontano, *Associated ZH production at hadron colliders: the fully differential NNLO QCD calculation*, Phys. Lett. **B740** (2015) 51–55, [1407.4747].

[37] G. Ferrera, M. Grazzini, and F. Tramontano, *Higher-order QCD effects for associated WH production and decay at the LHC*, JHEP **04** (2014) 039, [1312.1669].

[38] J. M. Campbell, R. K. Ellis, and C. Williams, *Associated production of a Higgs boson at NNLO*, JHEP **06** (2016) 179, [1601.00658].

[39] L. Altenkamp, S. Dittmaier, R. V. Harlander, H. Rzehak, and T. J. E. Zirke, *Gluon-induced Higgs-strahlung at next-to-leading order QCD*, JHEP **02** (2013) 078, [1211.5015].

[40] M. L. Ciccolini, S. Dittmaier, and M. Kramer, *Electroweak radiative corrections to associated WH and ZH production at hadron colliders*, Phys. Rev. **D68** (2003) 073003, [hep-ph/0306234].

[41] A. Denner, S. Dittmaier, S. Kallweit, and A. Muck, *Electroweak corrections to Higgs-strahlung off W/Z bosons at the Tevatron and the LHC with HAWK*, JHEP **03** (2012) 075, [1112.5142].

[42] A. Denner, S. Dittmaier, S. Kallweit, and A. Mück, *HAWK 2.0: A Monte Carlo program for Higgs production in vector-boson fusion and Higgs strahlung at hadron colliders*, Comput. Phys. Commun. **195** (2015) 161–171, [1412.5390].

[43] O. Brein, R. V. Harlander, and T. J. E. Zirke, *VH@NNLO - Higgs Strahlung at hadron colliders*, Comput. Phys. Commun. **184** (2013) 998–1003, [1210.5347].

[44] K. Hamilton, P. Nason, E. Re, and G. Zanderighi, *NNLOPS simulation of Higgs boson production*, JHEP **10** (2013) 222, [1309.0017].

[45] W. Astill, W. Bizon, E. Re, and G. Zanderighi, *NNLOPS accurate associated HW production*, JHEP **06** (2016) 154, [1603.01620].

[46] T. Sjöstrand, S. Ask, J. R. Christiansen, R. Corke, N. Desai, P. Ilten, S. Mrenna, S. Prestel, C. O. Rasmussen, and P. Z. Skands, *An Introduction to PYTHIA 8.2*, Comput. Phys. Commun. **191** (2015) 159–177, [1410.3012].

[47] J. Bellm et al., *Herwig 7.0/Herwig++ 3.0 release note*, Eur. Phys. J. **C76** (2016), no. 4 196, [1512.01178].

[48] T. Kinoshita, *Mass singularities of Feynman amplitudes*, J. Math. Phys. **3** (1962) 650–677.

[49] T. D. Lee and M. Nauenberg, *Degenerate systems and mass singularities*, Phys. Rev. **133** (Mar, 1964) B1549–B1562.

[50] S. Catani and M. H. Seymour, *A General algorithm for calculating jet cross-sections in NLO QCD*, Nucl. Phys. **B485** (1997) 291–419, [hep-ph/9605323]. [Erratum: Nucl. Phys.B510,503(1998)].

[51] S. Frixione, Z. Kunszt, and A. Signer, *Three jet cross-sections to next-to-leading order*, Nucl. Phys. **B467** (1996) 399–442, [hep-ph/9512328].

[52] L. Barze, G. Montagna, P. Nason, O. Nicrosini, F. Piccinini, and A. Vicini, *Neutral current Drell-Yan with combined QCD and electroweak corrections in the POWHEG BOX*, Eur. Phys. J. **C73** (2013), no. 6 2474, [1302.4606].

[53] The OpenLoops one-loop generator by F. Cascioli, J. Lindert, P. Maierhöfer and S. Pozzorini is publicly available at http://openloops.hepforge.org.

[54] F. Cascioli, P. Maierhofer, and S. Pozzorini, *Scattering Amplitudes with Open Loops*, Phys. Rev. Lett. **108** (2012) 111601, [1111.5206].

[55] G. Ossola, C. G. Papadopoulos, and R. Pittau, *Reducing full one-loop amplitudes to scalar integrals at the integrand level*, Nucl. Phys. **B763** (2007) 147–169, [hep-ph/0609007].

[56] G. Ossola, C. G. Papadopoulos, and R. Pittau, *CutTools: A Program implementing the OPP reduction method to compute one-loop amplitudes*, JHEP **03** (2008) 042, [0711.3596].

[57] A. van Hameren, *OneLOop: For the evaluation of one-loop scalar functions*, Comput. Phys. Commun. **182** (2011) 2427–2438, [1007.4716].

[58] A. Denner and S. Dittmaier, *Reduction of one loop tensor five point integrals*, Nucl. Phys. **B658** (2003) 175–202, [hep-ph/0212259].

[59] A. Denner and S. Dittmaier, *Reduction schemes for one-loop tensor integrals*, Nucl. Phys. **B734** (2006) 62–115, [hep-ph/0509141].

[60] A. Denner and S. Dittmaier, *Scalar one-loop 4-point integrals*, Nucl. Phys. **B844** (2011) 199–242, [1005.2076].

[61] A. Denner, S. Dittmaier, and L. Hofer, *Collier: a fortran-based Complex One-Loop LIbrary in Extended Regularizations*, 1604.06792.

[62] T. Ježo, J. M. Lindert, P. Nason, C. Oleari, and S. Pozzorini, *An NLO+PS generator for $t\bar{t}$ and $Wt$ production and decay including non-resonant and interference effects*, 1607.04538.

[63] J. M. Campbell, R. K. Ellis, R. Frederix, P. Nason, C. Oleari, and C. Williams, *NLO Higgs Boson Production Plus One and Two Jets Using the POWHEG BOX, MadGraph4 and MCFM*, JHEP **07** (2012) 092, [1202.5475].

[64] T. Stelzer and W. F. Long, *Automatic generation of tree level helicity amplitudes*, Comput. Phys. Commun. **81** (1994) 357–371, [hep-ph/9401258].

[65] J. Alwall, P. Demin, S. de Visscher, R. Frederix, M. Herquet, F. Maltoni, T. Plehn, D. L. Rainwater, and T. Stelzer, *MadGraph/MadEvent v4: The New Web Generation*, JHEP **09** (2007) 028, [0706.2334].

[66] S. Catani, F. Krauss, R. Kuhn, and B. R. Webber, *QCD matrix elements + parton showers*, JHEP **11** (2001) 063, [hep-ph/0109231].

[67] F. Krauss, *Matrix elements and parton showers in hadronic interactions*, JHEP **08** (2002) 015, [hep-ph/0205283].

[68] S. Mrenna and P. Richardson, *Matching matrix elements and parton showers with HERWIG and PYTHIA*, JHEP **05** (2004) 040, [hep-ph/0312274].

[69] J. Kodaira and L. Trentadue, *Summing Soft Emission in QCD*, Phys. Lett. **B112** (1982) 66.

[70] C. T. H. Davies and W. J. Stirling, *Nonleading Corrections to the Drell-Yan Cross-Section at Small Transverse Momentum*, Nucl. Phys. **B244** (1984) 337–348.

[71] C. T. H. Davies, B. R. Webber, and W. J. Stirling, *Drell-Yan Cross-Sections at Small Transverse Momentum*, Nucl. Phys. **B256** (1985) 413. [1,I.95(1984)].

[72] S. Frixione and B. R. Webber, *Matching NLO QCD computations and parton shower simulations*, JHEP **06** (2002) 029, [hep-ph/0204244].

[73] T. Gleisberg, S. Hoeche, F. Krauss, M. Schonherr, S. Schumann, F. Siegert, and J. Winter, *Event generation with SHERPA 1.1*, JHEP **02** (2009) 007, [0811.4622].

[74] G. Cullen, N. Greiner, G. Heinrich, G. Luisoni, P. Mastrolia, G. Ossola, T. Reiter, and F. Tramontano, *Automated One-Loop Calculations with GoSam*, Eur. Phys. J. **C72** (2012) 1889, [1111.2034].

[75] C. F. Berger, Z. Bern, L. J. Dixon, F. Febres Cordero, D. Forde, H. Ita, D. A. Kosower, and D. Maitre, *An Automated Implementation of On-Shell Methods for One-Loop Amplitudes*, Phys. Rev. **D78** (2008) 036003, [0803.4180].

[76] S. Actis, A. Denner, L. Hofer, A. Scharf, and S. Uccirati, *Recursive generation of one-loop amplitudes in the Standard Model*, JHEP **04** (2013) 037, [1211.6316].

[77] J. Alwall, R. Frederix, S. Frixione, V. Hirschi, F. Maltoni, O. Mattelaer, H. S. Shao, T. Stelzer, P. Torrielli, and M. Zaro, *The automated computation of tree-level and next-to-leading order differential cross sections, and their matching to parton shower simulations*, JHEP **07** (2014) 079, [1405.0301].

[78] U. Baur and D. Wackeroth, *Electroweak radiative corrections to weak boson production at hadron colliders*, Nucl. Phys. Proc. Suppl. **116** (2003) 159–163, [hep-ph/0211089]. [,159(2002)].

[79] M. Chiesa, G. Montagna, L. Barzè, M. Moretti, O. Nicrosini, F. Piccinini, and F. Tramontano, *Electroweak Sudakov Corrections to New Physics Searches at the LHC*, Phys. Rev. Lett. **111** (2013), no. 12 121801, [1305.6837].

[80] J. R. Andersen et al., *Les Houches 2013: Physics at TeV Colliders: Standard Model Working Group Report*, 1405.1067.

[81] F. Bloch and A. Nordsieck, *Note on the radiation field of the electron*, Phys. Rev. **52** (Jul, 1937) 54–59.

[82] A. Nordsieck, *The low frequency radiation of a scattered electron*, Phys. Rev. **52** (Jul, 1937) 59–62.

[83] G. Grammer and D. R. Yennie, *Improved treatment for the infrared-divergence problem in quantum electrodynamics*, Phys. Rev. D **8** (Dec, 1973) 4332–4344.

[84] D. Yennie, S. Frautschi, and H. Suura, *The infrared divergence phenomena and high-energy processes*, Annals of Physics **13** (1961), no. 3 379 – 452.

[85] M. Ciafaloni, P. Ciafaloni, and D. Comelli, *Bloch-Nordsieck violating electroweak corrections to inclusive TeV scale hard processes*, Phys. Rev. Lett. **84** (2000) 4810–4813, [hep-ph/0001142].

[86] U. Baur, *Weak Boson Emission in Hadron Collider Processes*, Phys. Rev. **D75** (2007) 013005, [hep-ph/0611241].

[87] W. J. Stirling and E. Vryonidou, *Electroweak corrections and Bloch-Nordsieck violations in 2-to-2 processes at the LHC*, JHEP **04** (2013) 155, [1212.6537].

[88] A. Manohar, B. Shotwell, C. Bauer, and S. Turczyk, *Non-cancellation of electroweak logarithms in high-energy scattering*, Phys. Lett. **B740** (2015) 179–187, [1409.1918].

[89] P. Ciafaloni and D. Comelli, *The Importance of weak bosons emission at LHC*, JHEP **09** (2006) 055, [hep-ph/0604070].

[90] S. Frixione, V. Hirschi, D. Pagani, H. S. Shao, and M. Zaro, *Weak corrections to Higgs hadroproduction in association with a top-quark pair*, JHEP **09** (2014) 065, [1407.0823].

[91] S. Frixione, V. Hirschi, D. Pagani, H. S. Shao, and M. Zaro, *Electroweak and QCD corrections to top-pair hadroproduction in association with heavy bosons*, JHEP **06** (2015) 184, [150 4.03446].

[92] G. Bell, J. H. Kuhn, and J. Rittinger, *Electroweak Sudakov Logarithms and Real Gauge-Boson Radiation in the TeV Region*, Eur. Phys. J. **C70** (2010) 659–671, [1004.4117].

[93] J.-y. Chiu, R. Kelley, and A. V. Manohar, *Electroweak Corrections using Effective Field Theory: Applications to the LHC*, Phys. Rev. **D78** (2008) 073006, [0806.1240].

[94] C. Becchi, A. Rouet, and R. Stora, *The Abelian Higgs-Kibble Model. Unitarity of the S Operator*, Phys. Lett. **B52** (1974) 344–346.

[95] J. M. Cornwall, D. N. Levin, and G. Tiktopoulos, *Derivation of gauge invariance from high-energy unitarity bounds on the S matrix*, Phys. Rev. D **10** (Aug, 1974) 1145–1167.

[96] C. E. Vayonakis, *Born helicity amplitudes and cross-sections in non-abelian gauge theories*, Lettere al Nuovo Cimento (1971-1985) **17** (1976), no. 11 383–387.

[97] M. S. Chanowitz and M. K. Gaillard, *The TeV physics of strongly interacting W's and Z's*, Nuclear Physics B **261** (1985) 379 – 431.

[98] A. Denner, *Techniques for the calculation of electroweak radiative corrections at the one-loop level and results for W-physics at LEP 200*, Fortschritte der Physik/Progress of Physics **41** (1993), no. 4 307–420.

[99] W. Beenakker, F. A. Berends, and A. P. Chapovsky, *Radiative corrections to pair production of unstable particles: results for $e^+e^- \to$ four fermions*, Nucl. Phys. **B548** (1999) 3–59, [hep-ph/9811481].

[100] W. Beenakker, A. P. Chapovsky, and F. A. Berends, *Nonfactorizable corrections to W pair production*, Phys. Lett. **B411** (1997) 203–210, [hep-ph/9706339].

[101] A. Denner, S. Dittmaier, and M. Roth, *Nonfactorizable photonic corrections to $e^+e^- \to WW \to$ four fermions*, Nucl. Phys. **B519** (1998) 39–84, [hep-ph/9710521].

[102] A. Denner, S. Dittmaier, and M. Roth, *Further numerical results on nonfactorizable corrections to $e^+e^- \to$ four fermions*, Phys. Lett. **B429** (1998) 145–150, [hep-ph/9803306].

[103] S. Dittmaier, A. Huss, and C. Schwinn, *Mixed QCD-electroweak $\mathcal{O}(\alpha_s\alpha)$ corrections to Drell-Yan processes in the resonance region: pole approximation and non-factorizable corrections*, Nucl. Phys. **B885** (2014) 318–372, [1403.3216].

[104] A. Denner, S. Dittmaier, M. Roth, and L. H. Wieders, *Electroweak corrections to charged-current $e^+e^- \to 4$ fermion processes: Technical details and further results*, Nucl. Phys. **B724** (2005) 247–294, [hep-ph/0505042]. [Erratum: Nucl. Phys.B854,504(2012)].

[105] **NNPDF** Collaboration, R. D. Ball, V. Bertone, S. Carrazza, L. Del Debbio, S. Forte, A. Guffanti, N. P. Hartland, and J. Rojo, *Parton distributions with QED corrections*, Nucl. Phys. **B877** (2013) 290–320, [1308.0598].

[106] A. Buckley, J. Ferrando, S. Lloyd, K. Nordström, B. Page, M. Rüfenacht, M. Schönherr, and G. Watt, *LHAPDF6: parton density access in the LHC precision era*, Eur. Phys. J. **C75** (2015) 132, [1412.7420].

[107] J. M. Campbell, R. K. Ellis, P. Nason, and E. Re, *Top-pair production and decay at NLO matched with parton showers*, JHEP **04** (2015) 114, [1412.1828].

[108] S. Frixione, *Isolated photons in perturbative QCD*, Phys. Lett. **B429** (1998) 369–374, [hep-ph/9801442].

[109] M. Cacciari and G. P. Salam, *Dispelling the $N^3$ myth for the $k_T$ jet-finder*, Phys. Lett. **B641** (2006) 57–61, [hep-ph/0512210].

[110] M. Cacciari, G. P. Salam, and G. Soyez, *The Anti-$k_T$ jet clustering algorithm*, JHEP **04** (2008) 063, [0802.1189].